

5.2 WAVES IN UNBOUNDED MEDIA

The propagation of stress waves is most easily understood by first considering an unbounded, or “infinite,” medium [i.e., one that extends infinitely in the direction(s) of wave propagation]. A simple, one-dimensional idealization of an unbounded medium is that of an infinitely long rod or bar. Using the basic requirements of equilibrium of forces and compatibility of displacements, and using strain–displacement and stress–strain relationships, a one-dimensional wave equation can be derived and solved. The process can be repeated, using the same requirements and relationships, for the more general case of wave propagation in a medium that extends infinitely in three orthogonal directions.

5.2.1 One-Dimensional Wave Propagation

Three different types of vibration can occur in a thin rod: longitudinal vibration during which the axis of the rod extends and contracts without lateral displacement; torsional vibration in which the rod rotates about its axis without lateral displacement of the axis; and flexural vibration during which the axis itself moves laterally. The flexural vibration problem has little application in soil dynamics and will not be considered further. For the first two cases, however, the operative wave equations are easily derived and solved.

5.2.1.1 Longitudinal Waves in an Infinitely Long Rod

Consider the free vibration of an infinitely long, linear elastic, constrained rod with cross-sectional area A , Young’s modulus E , Poisson’s ratio ν , and density ρ , as shown in Figure 5.1. If the rod is constrained against radial straining, then particle displacements caused by a longitudinal wave must be parallel to the axis of the rod. Assume that cross-sectional planes will remain planar and that stresses will be distributed uniformly over each cross section. As a stress wave travels along the rod and passes through the small element shown in Figure 5.2, the axial stress at the left end of the element ($x = x_0$) is σ_{x_0} . At the right end ($x = x_0 + dx$), the axial stress is $\sigma_{x_0} + (\partial\sigma_x / \partial x) dx$. Then dynamic equilibrium of the element requires that

$$\left(\sigma_{x_0} + \frac{\partial\sigma_x}{\partial x} dx \right) A - \sigma_{x_0} A = \rho A dx \frac{\partial^2 u}{\partial t^2} \quad (5.1)$$

where u is the displacement in the x -direction. This simply states that the unbalanced external forces acting on the ends of the element [the left side of Equation (5.1)] must equal the inertial force induced by acceleration of the mass of the element (the right side). Simplifying yields the one-dimensional *equation of motion*

$$\frac{\partial\sigma_x}{\partial x} = \rho \frac{\partial^2 u}{\partial t^2} \quad (5.2)$$

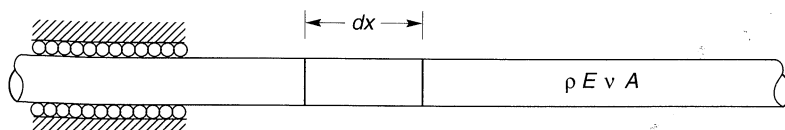


Figure 5.1 Constrained, infinite rod for one-dimensional wave propagation. Constraint against radial straining schematically represented by rollers.

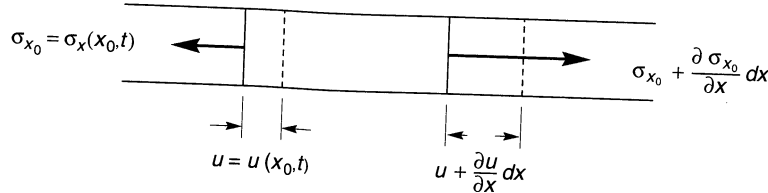


Figure 5.2 Stresses and displacements at ends of element of length dx and cross-sectional area, A .

In this form, the equation of motion is valid for any stress-strain behavior but cannot be solved directly because it mixes stresses [on the left side of equation (5.2)] with displacements (on the right side). To simplify the equation of motion, the left side can be expressed in terms of displacement by using the *stress-strain relationship*, $\sigma_x = M\epsilon_x$, where the *constrained modulus* $M = \{(1 - v)/[(1 + v)(1 - 2v)]\}E$, and the *strain-displacement relationship*, $\epsilon_x = \partial u / \partial x$. These substitutions allow the one-dimensional equation of motion to be written in the familiar form of the one-dimensional *longitudinal wave equation* for a constrained rod:

$$\frac{\partial^2 u}{\partial t^2} = \frac{M}{\rho} \frac{\partial^2 u}{\partial x^2} \quad (5.3)$$

The one-dimensional wave equation can be written in the alternative form

$$\frac{\partial^2 u}{\partial t^2} = v_p^2 \frac{\partial^2 u}{\partial x^2} \quad (5.4)$$

where v_p is the *wave propagation velocity*; for this case, the wave travels at $v_p = \sqrt{M/\rho}$. Note that the wave propagation velocity depends only on the properties of the rod material (its stiffness and density) and is independent of the amplitude of the stress wave. The wave propagation velocity increases with increasing stiffness and with decreasing density. The wave propagation velocity is an extremely important material property that is relied upon heavily in soil dynamics and geotechnical earthquake engineering.

The wave propagation velocity is the velocity at which a stress wave would travel along the rod. It is not the same as the *particle velocity*, which is the velocity at which a single point within the rod would move as the wave passes through it. Knowing that $\partial u = \epsilon_x \partial x$ (from the strain-displacement relationship), $\epsilon_x = \sigma_x/M$ (from the stress-strain relationship), and $\partial x = v_p \partial t$ (from the definition of wave propagation velocity), the particle velocity \dot{u} can be shown to be

$$\dot{u} = \frac{\partial u}{\partial t} = \frac{\epsilon_x \partial x}{\partial t} = \frac{\sigma_x v_p \partial t}{M \partial t} = \frac{\sigma_x}{M} v_p = \frac{\sigma_x}{\rho v_p^2} v_p = \frac{\sigma_x}{\rho v_p} \quad (5.5)$$

Equation (5.5) shows that the particle velocity is proportional to the axial stress in the rod. The coefficient of proportionality, ρv_p , is called the *specific impedance* of the material. The specific impedance is another important property that influences the behavior of waves at boundaries (Section 5.4).

Example 5.1

Compute v_p for steel, vulcanized rubber, and water.

Solution The constrained moduli and specific gravities of steel, rubber, and water can be found in a number of reference books; typical values are summarized below:

MATERIAL	SPECIFIC GRAVITY, SG	M (PSI)
Steel	7.85	40.4×10^6
Vulcanized Rubber	1.2	167×10^6
Water	1.0	0.34×10^6

With this information, the v_p -values can be calculated from:

$$v_p = \sqrt{\frac{M}{\rho}} = \sqrt{\frac{M}{(SG)\rho_w}} = \sqrt{\frac{Mg}{(SG)\gamma_w}}$$

For steel,

$$v_p = \sqrt{\frac{(40.4 \times 10^6 \text{ psi})(144 \text{ in}^2/\text{ft}^2)(32.2 \text{ ft/sec}^2)}{(7.85)(62.4 \text{pcf})}} = 19556 \text{ ft/sec}$$

For vulcanized rubber,

$$v_p = \sqrt{\frac{(167 \times 10^6 \text{ psi})(144 \text{ in}^2/\text{ft}^2)(32.2 \text{ ft/sec}^2)}{(1.20)(62.4 \text{pcf})}} = 101691 \text{ ft/sec}$$

For water,

$$v_p = \sqrt{\frac{(0.34 \times 10^6 \text{ psi})(144 \text{ in}^2/\text{ft}^2)(32.2 \text{ ft/sec}^2)}{(1.00)(62.4 \text{pcf})}} = 5026 \text{ ft/sec}$$

5.2.1.2 Torsional Waves in an Infinitely Long Rod

Torsional waves involve rotation of the rod about its own axis. In the case of the longitudinal wave, the direction of particle motion was parallel to the direction of wave propagation. For torsional waves, particle motion is constrained to planes perpendicular to the direction of wave propagation. Development of a wave equation for torsional vibrations, however, follows exactly the same steps as for longitudinal vibration. Consider the short segment of a cylindrical rod shown in Figure 5.3 as a torsional wave of torque amplitude T travels along the rod. Dynamic torsional equilibrium requires that the unbalanced external torque [left side of equation (5.6)] is equal to the inertial torque (right side):

$$\left(T_{x_0} + \frac{\partial T}{\partial x} dx \right) - T_{x_0} = \rho J dx \frac{\partial^2 \theta}{\partial t^2} \quad (5.6)$$

where J is the polar moment of inertia of the rod about its axis. This equilibrium equation can be simplified to produce the equation of motion

$$\frac{\partial T}{\partial x} = \rho J \frac{\partial^2 \theta}{\partial t^2} \quad (5.7)$$

Now, incorporating the torque–rotation relationship

$$T = GJ \frac{\partial \theta}{\partial x} \quad (5.8)$$

where G is the *shear modulus* of the rod, the *torsional wave equation* can be written as

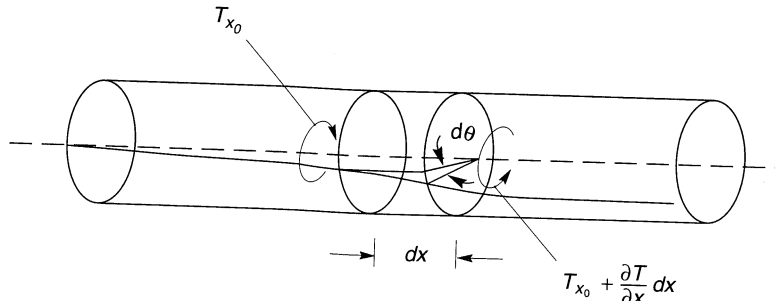


Figure 5.3 Torque and rotation at ends of element of length dx and cross-sectional area, A .

$$\frac{\partial^2 \theta}{\partial t^2} = \frac{G}{\rho} \frac{\partial^2 \theta}{\partial x^2} = v_s^2 \frac{\partial^2 \theta}{\partial x^2} \quad (5.9)$$

where $v_s = \sqrt{G/\rho}$ is the velocity of propagation of the torsional wave. Note that the form of the wave equation for torsional waves [equation (5.9)] is identical to that for longitudinal waves [equation (5.3)], but the wave propagation velocities are different. The wave propagation velocity depends both on the stiffness of the rod in the mode of deformation induced by the wave and on the material density but is independent of the amplitude of the stress wave.

Example 5.2

Compute v_s for steel, vulcanized rubber, and water.

Solution The shear moduli of steel, rubber, and water can be found in a number of reference books; typical values are summarized below:

MATERIAL	G (PSI)
Steel	11.5×10^6
Vulcanized Rubber	0.167×10^6
Water	0

With this information, the v_s -values can be calculated from

$$v_s = \sqrt{\frac{G}{\rho}} = \sqrt{\frac{G g}{(\text{SG}) \gamma_w}}$$

For steel,

$$v_s = \sqrt{\frac{(11.5 \times 10^6 \text{ psi}) (144 \text{ in}^2/\text{ft}^2) (32.2 \text{ ft/sec}^2)}{(7.85) (62.4 \text{pcf})}} = 10434 \text{ ft/sec}$$

For vulcanized rubber,

$$v_s = \sqrt{\frac{(0.167 \times 10^6 \text{ psi}) (144 \text{ in}^2/\text{ft}^2) (32.2 \text{ ft/sec}^2)}{(1.20) (62.4 \text{pcf})}} = 3216 \text{ ft/sec}$$

For water,

$$v_s = 0$$

The last result is obvious—as an inviscid fluid, water can produce no resistance to shear stresses and consequently cannot transmit torsional waves.

5.2.1.3 Solution of the One-Dimensional Equation of Motion

The one-dimensional wave equation is a partial differential equation of the form

$$\frac{\partial^2 u}{\partial t^2} = v^2 \frac{\partial^2 u}{\partial x^2} \quad (5.10)$$

where v represents the wave propagation velocity corresponding to the type of stress wave of interest. The solution of such an equation can be written in the form

$$u(x, t) = f(vt - x) + g(vt + x) \quad (5.11)$$

where f and g can be any arbitrary functions of $(vt - x)$ and $(vt + x)$ that satisfy equation (5.10). Note that the argument of f remains constant when x increases with time (at velocity v), and the argument of g remains constant when x decreases with time. Therefore, the solution of equation (5.11) describes a displacement wave [$f(vt - x)$] traveling at velocity v in the positive x -direction and another [$g(vt + x)$] traveling at the same speed in the negative x -direction. It also implies that the shapes of the waves do not change with position or time.

If the rod is subjected to some steady-state harmonic stress $\sigma(t) = \sigma_0 \cos \omega t$ where σ_0 is the stress wave amplitude and $\bar{\omega}$ is the circular frequency of the applied loading, the solution can be expressed using the *wave number*, $k = \bar{\omega}/v$, in the form

$$u(x, t) = A \cos(\bar{\omega}t - kx) + B \cos(\bar{\omega}t + kx) \quad (5.12)$$

Here the first and second terms describe harmonic waves propagating in the positive and negative x -directions, respectively. The wave number is related to the *wavelength*, λ , of the motion by

$$\lambda = v\bar{T} = \frac{v}{\bar{f}} = \frac{2\pi}{\bar{\omega}}v = \frac{2\pi}{k} \quad (5.13)$$

where \bar{T} is the period of the applied loading (note that wave number is to wavelength as circular frequency is to period) and $\bar{f} = 1/\bar{T}$. Note that at a given frequency, the wavelength increases with increasing wave propagation velocity. Equation (5.12) indicates that the displacement varies harmonically with respect to both time and position as illustrated in Figure 5.4. Equation 5.13 and Figure 5.4 show that the wave number is to the wavelength as the circular frequency is to the period of vibration. For a wave propagating in the positive x -direction only ($B = 0$), differentiating $u(x, t)$ twice with respect to x and twice with respect to t and substituting into the wave equation [equation (5.10)] gives

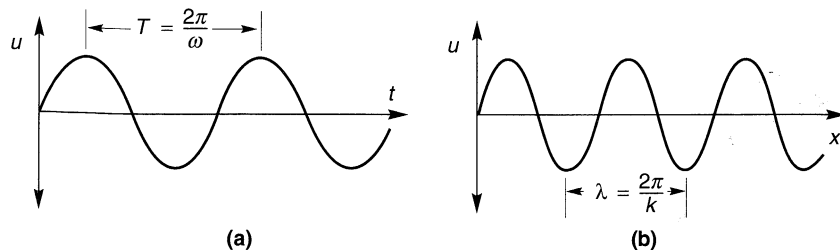


Figure 5.4 Particle displacement (a) as function of time, and (b) as function of position along the rod.

$$-\bar{\omega}^2 A \cos(\bar{\omega}t - kx) = -v^2 k^2 A \cos(\bar{\omega}t - kx) \quad (5.14)$$

which reduces to the identity $\bar{\omega} = kv$, thereby verifying equation (5.12) as a solution to the wave equation.

Using complex notation (Appendix A), the equivalent form of the solution can be written as

$$u(x, t) = Ce^{i(\bar{\omega}t - kx)} + De^{i(\bar{\omega}t + kx)} \quad (5.15)$$

This form of the solution can be verified in the same way as the trigonometric form.

Example 5.3

Calculate the wavelengths of harmonic longitudinal and torsional waves traveling along constrained steel and vulcanized rubber rods. Assume that the waves are harmonic at a frequency of 10 Hz.

Solution Using equation 5.13 and the wave propagation velocities computed in Examples 5.1 and 5.2,

Longitudinal waves

$$\text{Steel: } \lambda = \frac{v_p}{f} = \frac{19556 \text{ ft/sec}}{10 \text{ sec}^{-1}} = 1956 \text{ ft}$$

$$\text{Vulcanized rubber: } \lambda = \frac{v_p}{f} = \frac{101691 \text{ ft/sec}}{10 \text{ sec}^{-1}} = 10169 \text{ ft}$$

Torsional waves

$$\text{Steel: } \lambda = \frac{v_s}{f} = \frac{10434 \text{ ft/sec}}{10 \text{ sec}^{-1}} = 1043 \text{ ft}$$

$$\text{Vulcanized rubber: } \lambda = \frac{v_s}{f} = \frac{3216 \text{ ft/sec}}{10 \text{ sec}^{-1}} = 322 \text{ ft}$$

5.2.2 Three-Dimensional Wave Propagation

The preceding discussion of wave propagation in rods illustrates some of the basic principles of wave propagation, but an infinite rod is hardly an adequate model for describing the propagation of seismic waves through the earth. Since the earth is three-dimensional and sources of seismic energy are three-dimensional, seismic waves must be described in terms of three-dimensional wave propagation.

Derivations of three-dimensional equations of motion follow the same steps as those used for one-dimensional propagation; the equations of motion are formulated from equilibrium considerations, stress-strain relationships, and strain-displacement relationships. In the three-dimensional case, however, the various relationships are more complex and the derivation more cumbersome. Brief reviews of three-dimensional stress and strain notation and three-dimensional stress-strain behavior will precede derivation of the equations of motion.

5.2.2.1 Review of Stress Notation

The stress at a point on some plane passing through a solid does not usually act normal to that plane but has both normal and shear components. Considering a small element with one corner at the center of an x - y - z Cartesian coordinate system (Figure 5.5), a total of nine components of stress will act on its faces. These stresses are denoted by σ_{xx} , σ_{xy} , σ_{xz} , and

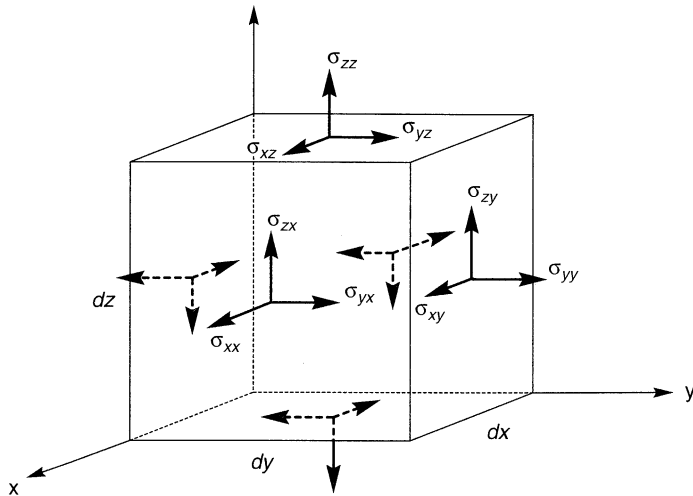


Figure 5.5 Stress notation for element of dimensions dx by dy by dz .

so on, where the first and second letters in the subscript describe the direction of the stress itself and the axis perpendicular to the plane in which it acts. Thus σ_{xx} , σ_{yy} , and σ_{zz} , are *normal stresses*, while the other six components represent *shear stresses*. Moment equilibrium of the element requires that

$$\sigma_{xy} = \sigma_{yx} \quad \sigma_{xz} = \sigma_{zx} \quad \sigma_{yz} = \sigma_{zy} \quad (5.16)$$

which means that only six independent components of stress are required to define the state of stress of the element completely. In some references, the notation σ_x , σ_y , σ_z , τ_{xy} , τ_{yz} , and τ_{xz} is used to describe σ_{xx} , σ_{yy} , σ_{zz} , σ_{xy} , σ_{yz} , and σ_{xz} , respectively.

5.2.2.2 Review of Strain Notation

Components of strain are easily visualized by considering the two-dimensional strain in the x - y plane shown in Figure 5.6. The point P , at coordinates (x_0, y_0) , is at one corner of the infinitesimal element $PQRS$ which has a square shape before deformation. After deformation, the infinitesimal element has been displaced, distorted, and rotated into the shape $P'Q'R'S'$. From Figure 5.6, $\tan \alpha_1 = dv/dx$ and $\tan \alpha_2 = du/dy$, where u and v represent displacements in the x - and y -directions, respectively. The shear strain in the x - y plane is given by $\epsilon_{xy} = \alpha_1 + \alpha_2$. For small deformations, the angles may be taken equal to their tangents so that the relationship between the shear strain and the displacements is $\epsilon_{xy} = dv/dx + du/dy$. The *rotation* of the element about the z -axis is given by $\Omega_z = (\alpha_1 - \alpha_2)/2$. Analogous definitions can be developed for the x - z and y - z planes. For the three-dimensional case, the *strain-displacement relationships* are defined by

$$\begin{aligned} \epsilon_{xx} &= \frac{du}{dx} & \epsilon_{yy} &= \frac{dv}{dy} & \epsilon_{zz} &= \frac{dw}{dz} \\ \epsilon_{xy} &= \frac{dv}{dx} + \frac{du}{dy} & \epsilon_{yz} &= \frac{dw}{dy} + \frac{dv}{dz} & \epsilon_{zx} &= \frac{du}{dz} + \frac{dw}{dx} \end{aligned} \quad (5.17)$$

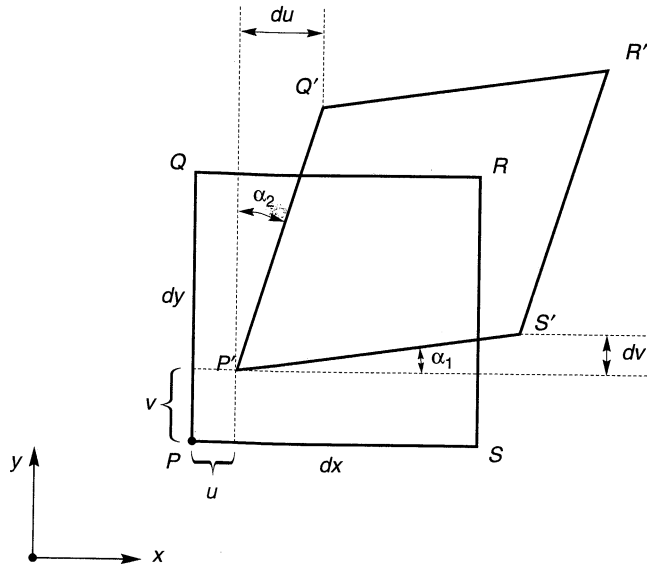


Figure 5.6 Square element subjected to plane strain deformation.

Rigid-body rotation about the x -, y -, and z -axes are given by the *rotation-displacement relationships*

$$\Omega_x = \frac{1}{2} \left(\frac{dw}{dy} - \frac{dv}{dz} \right) \quad \Omega_y = \frac{1}{2} \left(\frac{du}{dz} - \frac{dw}{dx} \right) \quad \Omega_z = \frac{1}{2} \left(\frac{dv}{dx} - \frac{du}{dy} \right) \quad (5.18)$$

The first three quantities, ε_{xx} , ε_{yy} , and ε_{zz} , represent the extensional and compressional strain parallel to the x -, y -, and z -axes, and are called *normal strains*. The second three quantities, ε_{xy} , ε_{yz} , and ε_{zx} , represent the components of shear strain in the planes corresponding to their suffixes. These six quantities are the components of strain that correspond to the deformation at P . In some references, the notation ε_x , ε_y , ε_z , γ_{xy} , γ_{yz} , and γ_{xz} is used to describe ε_{xx} , ε_{yy} , ε_{zz} , ε_{xy} , ε_{yz} , and ε_{xz} , respectively.

5.2.2.3 Review of Stress–Strain Relationships

Stresses and strains are proportional in a linear elastic body. The stress–strain relationship can be described by *Hooke's law*, which can be written in generalized form as

$$\begin{aligned} \sigma_{xx} &= c_{11}\varepsilon_{xx} + c_{12}\varepsilon_{yy} + c_{13}\varepsilon_{zz} + c_{14}\varepsilon_{xy} + c_{15}\varepsilon_{yz} + c_{16}\varepsilon_{zx} \\ \sigma_{yy} &= c_{21}\varepsilon_{xx} + c_{22}\varepsilon_{yy} + c_{23}\varepsilon_{zz} + c_{24}\varepsilon_{xy} + c_{25}\varepsilon_{yz} + c_{26}\varepsilon_{zx} \\ \sigma_{zz} &= c_{31}\varepsilon_{xx} + c_{32}\varepsilon_{yy} + c_{33}\varepsilon_{zz} + c_{34}\varepsilon_{xy} + c_{35}\varepsilon_{yz} + c_{36}\varepsilon_{zx} \\ \sigma_{xy} &= c_{41}\varepsilon_{xx} + c_{42}\varepsilon_{yy} + c_{43}\varepsilon_{zz} + c_{44}\varepsilon_{xy} + c_{45}\varepsilon_{yz} + c_{46}\varepsilon_{zx} \\ \sigma_{yz} &= c_{51}\varepsilon_{xx} + c_{52}\varepsilon_{yy} + c_{53}\varepsilon_{zz} + c_{54}\varepsilon_{xy} + c_{55}\varepsilon_{yz} + c_{56}\varepsilon_{zx} \\ \sigma_{zx} &= c_{61}\varepsilon_{xx} + c_{62}\varepsilon_{yy} + c_{63}\varepsilon_{zz} + c_{64}\varepsilon_{xy} + c_{65}\varepsilon_{yz} + c_{66}\varepsilon_{zx} \end{aligned} \quad (5.19)$$

where the 36 coefficients represent the elastic constants of the material. The requirement that the elastic strain energy must be a unique function of the strain (which requires that $c_{ij} = c_{ji}$ for all i and j) reduces the number of independent coefficients to 21. If the material is isotropic, the coefficients must be independent of direction, so that

$$\begin{aligned} c_{12} &= c_{21} = c_{13} = c_{31} = c_{23} = c_{32} = \lambda \\ c_{44} &= c_{55} = c_{66} = \mu \\ c_{11} &= c_{22} = c_{33} = \lambda + 2\mu \end{aligned} \quad (5.20)$$

and all other constants are zero. Therefore, Hooke's law for an isotropic, linear, elastic material allows all components of stress and strain to be expressed in terms of the two *Lamé constants*, λ and μ :

$$\begin{aligned} \sigma_{xx} &= \lambda\bar{\epsilon} + 2\mu\epsilon_{xx} & \sigma_{xy} &= \mu\epsilon_{xy} \\ \sigma_{yy} &= \lambda\bar{\epsilon} + 2\mu\epsilon_{yy} & \sigma_{yz} &= \mu\epsilon_{yz} \\ \sigma_{zz} &= \lambda\bar{\epsilon} + 2\mu\epsilon_{zz} & \sigma_{zx} &= \mu\epsilon_{zx} \end{aligned} \quad (5.21)$$

where the *volumetric strain* $\bar{\epsilon} = \epsilon_{xx} + \epsilon_{yy} + \epsilon_{zz}$. Note that the symbol λ is used universally for both Lamé's constant and for wavelength; the context in which it is used should make its meaning obvious.

For convenience, several other parameters are often used to describe the stress-strain behavior of isotropic, linear, elastic materials, each of which can be expressed in terms of Lamé's constants. Some of the more common of these are

$$\text{Young's modulus: } E = \frac{\mu(3\lambda + 2\mu)}{\lambda + \mu} \quad (5.22a)$$

$$\text{Bulk modulus: } K = \lambda + \frac{2\mu}{3} \quad (5.22b)$$

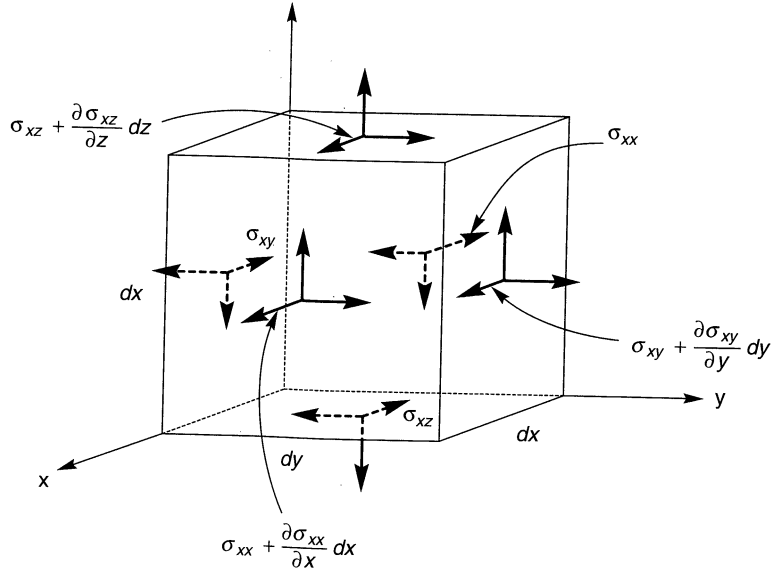
$$\text{Shear modulus: } G = \mu \quad (5.22c)$$

$$\text{Poisson's ratio: } \nu = \frac{\lambda}{2(\lambda + \mu)} \quad (5.22d)$$

Hooke's law for an isotropic, linear, elastic material can be expressed using any combination of two of these parameters and/or Lamé's constants.

5.2.2.4 Equations of Motion for a Three-Dimensional Elastic Solid

The three-dimensional equations of motion for an elastic solid are obtained from equilibrium requirements in much the same way as for the one-dimensional rod, except that equilibrium must be ensured in three perpendicular directions. Consider the variation in stress across an infinitesimal cube aligned with its sides parallel to the x - y - z axes shown in Figure 5.7. Assuming that the average stress on each face of the cube is represented by the stress shown at the center of the face, the resultant forces acting in the x -, y -, and z -directions can be evaluated. In the x -direction, the unbalanced external forces must be balanced by an inertial force in that direction, so that

Figure 5.7 Stresses in x -direction on infinitesimal cube.

$$\begin{aligned} \rho dx dy dz \frac{\partial^2 u}{\partial t^2} = & \left(\sigma_{xx} + \frac{\partial \sigma_{xx}}{\partial x} dx \right) dy dz - \sigma_{xx} dy dz \\ & + \left(\sigma_{xy} + \frac{\partial \sigma_{xy}}{\partial y} dy \right) dx dz - \sigma_{xy} dx dz \\ & + \left(\sigma_{xz} + \frac{\partial \sigma_{xz}}{\partial z} dz \right) dx dy - \sigma_{xz} dx dy \end{aligned} \quad (5.23)$$

which simplifies to

$$\rho \frac{\partial^2 u}{\partial t^2} = \frac{\partial \sigma_{xx}}{\partial x} + \frac{\partial \sigma_{xy}}{\partial y} + \frac{\partial \sigma_{xz}}{\partial z} \quad (5.24)$$

Repeating this operation in the y - and z -directions gives

$$\rho \frac{\partial^2 v}{\partial t^2} = \frac{\partial \sigma_{yx}}{\partial x} + \frac{\partial \sigma_{yy}}{\partial y} + \frac{\partial \sigma_{yz}}{\partial z} \quad (5.24b)$$

$$\rho \frac{\partial^2 w}{\partial t^2} = \frac{\partial \sigma_{zx}}{\partial x} + \frac{\partial \sigma_{zy}}{\partial y} + \frac{\partial \sigma_{zz}}{\partial z} \quad (5.24c)$$

Equations (5.24) represent the *three-dimensional equations of motion* of an elastic solid. Note that these equations of motion were derived solely on the basis of equilibrium considerations and thus apply to solids of any stress-strain behavior. To express these equations of motion in terms of displacements, it is again necessary to use a stress-strain relationship and a strain-displacement relationship. Using Hooke's law as developed in Section 5.2.2.3, the first of the equations of motion [equation (5.24a)] can be written in terms of strains as.

$$\rho \frac{\partial^2 u}{\partial t^2} = \frac{\partial}{\partial x} (\lambda \bar{\varepsilon} + 2\mu \varepsilon_{xx}) + \frac{\partial}{\partial y} (\mu \varepsilon_{xy}) + \frac{\partial}{\partial z} (\mu \varepsilon_{xz}) \quad (5.25)$$

Substituting the strain-displacement relationships

$$\varepsilon_{xx} = \frac{\partial u}{\partial x} \quad \varepsilon_{xy} = \frac{\partial v}{\partial x} + \frac{\partial u}{\partial y} \quad \varepsilon_{xz} = \frac{\partial w}{\partial x} + \frac{\partial u}{\partial z}$$

into equation (5.25) produces the desired equation of motion in terms of displacements:

$$\rho \frac{\partial^2 u}{\partial t^2} = (\lambda + \mu) \frac{\partial \bar{\varepsilon}}{\partial x} + \mu \nabla^2 u \quad (5.26a)$$

where the *Laplacian operator* ∇^2 represents

$$\nabla^2 = \frac{\partial^2}{\partial x^2} + \frac{\partial^2}{\partial y^2} + \frac{\partial^2}{\partial z^2}$$

Repeating this process in the y and z directions gives

$$\rho \frac{\partial^2 v}{\partial t^2} = (\lambda + \mu) \frac{\partial \bar{\varepsilon}}{\partial y} + \mu \nabla^2 v \quad (5.26b)$$

$$\rho \frac{\partial^2 w}{\partial t^2} = (\lambda + \mu) \frac{\partial \bar{\varepsilon}}{\partial z} + \mu \nabla^2 w \quad (5.26c)$$

5.2.2.5 Solutions of the Three-Dimensional Equations of Motion

Together, equations (5.26) represent the three-dimensional equations of motion for an isotropic, linear, elastic solid. It turns out that these equations can be manipulated to produce two wave equations. Consequently, only two types of waves can travel through such an unbounded solid. The characteristics of each type of wave will be revealed by their respective wave equations.

The solution for the first type of wave can be obtained by differentiating each of equations (5.26) with respect to x , y , and z and adding the results together to give

$$\begin{aligned} \rho \left(\frac{\partial^2 \varepsilon_{xx}}{\partial t^2} + \frac{\partial^2 \varepsilon_{yy}}{\partial t^2} + \frac{\partial^2 \varepsilon_{zz}}{\partial t^2} \right) &= (\lambda + \mu) \left(\frac{\partial^2 \bar{\varepsilon}}{\partial x^2} + \frac{\partial^2 \bar{\varepsilon}}{\partial y^2} + \frac{\partial^2 \bar{\varepsilon}}{\partial z^2} \right) \\ &\quad + \mu \left(\frac{\partial^2 \varepsilon_{xx}}{\partial x^2} + \frac{\partial^2 \varepsilon_{yy}}{\partial y^2} + \frac{\partial^2 \varepsilon_{zz}}{\partial z^2} \right) \end{aligned}$$

or

$$\rho \frac{\partial^2 \bar{\varepsilon}}{\partial t^2} = (\lambda + \mu) \nabla^2 \bar{\varepsilon} + \mu \nabla^2 \bar{\varepsilon} \quad (5.27)$$

Rearranging yields the wave equation

$$\frac{\partial^2 \bar{\varepsilon}}{\partial t^2} = \frac{\lambda + 2\mu}{\rho} \nabla^2 \bar{\varepsilon} \quad (5.28)$$

Recalling that $\bar{\epsilon}$ is the volumetric strain (which describes deformations that involve no shearing or rotation), this wave equation describes an *irrotational*, or *dilatational*, wave. It indicates that a dilatational wave will propagate through the body at a velocity

$$v_p = \sqrt{\frac{\lambda + 2\mu}{\rho}} \quad (5.29)$$

This type of wave is commonly known as a *p-wave* (or primary wave) and v_p is referred to as the *p-wave velocity* of the material. The general nature of p-wave motion was illustrated in Figure 2.1a. Note that particle displacements are parallel to the direction of wave propagation, just as they were in the constrained rod of Section 5.2.1.1. The longitudinal wave in the constrained rod is actually a p-wave. Using equations (5.22c) and (5.22d), v_p can be written in terms of the shear modulus and Poisson's ratio as

$$v_p = \sqrt{\frac{G(2 - 2\nu)}{\rho(1 - 2\nu)}} \quad (5.30)$$

As ν approaches 0.5 (at which point the body becomes incompressible, i.e., infinitely stiff with respect to dilatational deformations), v_p approaches infinity.

To obtain the solution for the second type of wave, $\bar{\epsilon}$ is eliminated by differentiating equation (5.26b) with respect to z and equation (5.26c) with respect to y , and subtracting one from the other:

$$\rho \frac{\partial}{\partial t^2} \left(\frac{\partial w}{\partial y} - \frac{\partial v}{\partial z} \right) = \mu \nabla^2 \left(\frac{\partial w}{\partial y} - \frac{\partial v}{\partial z} \right) \quad (5.31)$$

Recalling the definition of rotation [equation (5.19)], equation (5.31) can be written in the form of the wave equation

$$\frac{\partial^2 \Omega_x}{\partial t^2} = \frac{\mu}{\rho} \nabla^2 \Omega_x \quad (5.32)$$

which describes an *equivoluminal*, or *distortional* wave, of rotation about the x -axis. Similar expressions can be obtained by the same process for rotation about the y - and z -axes. Equation (5.32) shows that a distortional wave will propagate through the solid at a velocity

$$v_s = \sqrt{\frac{\mu}{\rho}} = \sqrt{\frac{G}{\rho}} \quad (5.33)$$

This type of wave is commonly known as a *s-wave* (or *shear wave*) and v_s is referred to as the *shear wave velocity* of the material. Note that the particle motion is constrained to a plane perpendicular to the direction of wave propagation, just as it was in the case of the torsional wave of Section 5.2.1.2. Consequently, the torsional wave represented a form of an s-wave. The close relationship between s-wave velocity and shear modulus is used to advantage in many of the field and laboratory tests discussed in Chapter 6. The general nature of s-wave motion was illustrated in Figure 2.1b.

S-waves are often divided into two types, or resolved into two perpendicular components. SH-waves are s-waves in which particle motion occurs only in a horizontal plane. SV-waves are s-waves whose particle motion lies in a vertical plane. A given s-wave with arbitrary particle motion can be represented as the vector sum of its SH and SV components.

In summary, only two types of waves, known as *body waves*, can exist in an unbounded (infinite) elastic solid. P-waves involve no rotation of the material they pass through and travel at velocity, v_p . S-waves involve no volume change and travel at velocity, v_s . The velocities of p- and s-waves depend on the stiffnesses of the solid with respect to the types of deformation induced by each wave. Comparing the velocities [equations (5.30) and (5.33)]

$$\frac{v_p}{v_s} = \sqrt{\frac{2 - 2\nu}{1 - 2\nu}} \quad (5.34)$$

the p-wave velocity can be seen to exceed the s-wave velocity by an amount that depends on the compressibility (as reflected in Poisson's ratio) of the body. For a typical Poisson's ratio of 0.3 for geologic materials, the ratio $v_p/v_s = 1.87$.

5.3 WAVES IN A SEMI-INFINITE BODY

The earth is obviously not an infinite body—it is a very large sphere with an outer surface on which stresses cannot exist. For near-surface earthquake engineering problems, the earth is often idealized as a semi-infinite body with a planar free surface (the effects of the earth's curvature are neglected). The boundary conditions associated with the free surface allow additional solutions to the equations of motion to be obtained. These solutions describe waves whose motion is concentrated in a shallow zone near the free surface (i.e., *surface waves*). Since earthquake engineering is concerned with the effects of earthquakes on humans and their environment, which are located on or very near the earth's surface, and since they attenuate with distance more slowly than body waves, surface waves are very important.

Two types of surface waves are of primary importance in earthquake engineering. One, the *Rayleigh wave*, can be shown to exist in a homogeneous, elastic half-space. The other surface wave, the *Love wave*, requires a surficial layer of lower s-wave velocity than the underlying half-space. Other types of surface waves exist but are much less significant from an earthquake engineering standpoint.

5.3.1 Rayleigh Waves

Waves that exist near the surface of a homogeneous elastic half-space were first investigated by Rayleigh (1885) and are known to this date as *Rayleigh waves*. To describe Rayleigh waves, consider a *plane wave* (Figure 5.8) that travels in the x -direction with zero particle displacement in the y -direction ($v = 0$). The z -direction is taken as positive downward, so all particle motion occurs in the $x-z$ plane. Two *potential functions*, Φ and Ψ , can be defined to describe the displacements in the x - and z -directions:

$$u = \frac{\partial\Phi}{\partial x} + \frac{\partial\Psi}{\partial z} \quad (5.35a)$$

$$w = \frac{\partial\Phi}{\partial z} - \frac{\partial\Psi}{\partial x} \quad (5.35b)$$

The volumetric strain, or *dilatation*, $\bar{\epsilon}$, of the wave is given by $\bar{\epsilon} = \epsilon_{xx} + \epsilon_{zz}$, or

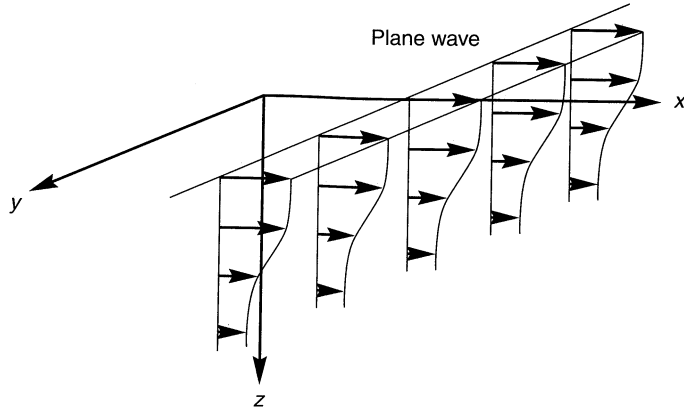


Figure 5.8 Motion induced by a typical plane wave that propagates in the x -direction. Wave motion does not vary in the y -direction.

$$\bar{\varepsilon} = \frac{\partial u}{\partial x} + \frac{\partial w}{\partial z} = \frac{\partial}{\partial x} \left(\frac{\partial \Phi}{\partial x} + \frac{\partial \Psi}{\partial z} \right) + \frac{\partial}{\partial z} \left(\frac{\partial \Phi}{\partial z} - \frac{\partial \Psi}{\partial x} \right) = \frac{\partial^2 \Phi}{\partial x^2} + \frac{\partial^2 \Phi}{\partial z^2} = \nabla^2 \Phi \quad (5.36)$$

The rotation in the $x-z$ plane is given [equation (5.19)] by

$$2\Omega_y = \frac{\partial u}{\partial z} - \frac{\partial w}{\partial x} = \frac{\partial}{\partial z} \left(\frac{\partial \Phi}{\partial x} + \frac{\partial \Psi}{\partial z} \right) - \frac{\partial}{\partial z} \left(\frac{\partial \Phi}{\partial z} - \frac{\partial \Psi}{\partial x} \right) = \frac{\partial^2 \Psi}{\partial z^2} + \frac{\partial^2 \Psi}{\partial x^2} = \nabla^2 \Psi \quad (5.37)$$

Use of the potential functions allows separation of the effects of dilatation and rotation [i.e., equations (5.36) and (5.37) indicate that Φ and Ψ are associated with dilatation and rotation, respectively]. Therefore, Rayleigh waves can be thought of as combinations of p- and s-waves (SV waves for this case, since the $x-z$ plane is vertical) that satisfy certain boundary conditions. Substitution of the expressions for u and w into the equations of motion as written in equations (5.26a) and (5.26c) gives

$$\rho \frac{\partial}{\partial x} \left(\frac{\partial^2 \Phi}{\partial t^2} \right) + \rho \frac{\partial}{\partial z} \left(\frac{\partial^2 \Psi}{\partial t^2} \right) = (\lambda + 2\mu) \frac{\partial}{\partial x} (\nabla^2 \Phi) + \mu \frac{\partial}{\partial z} (\nabla^2 \Psi) \quad (5.38a)$$

$$\rho \frac{\partial}{\partial z} \left(\frac{\partial^2 \Phi}{\partial t^2} \right) - \rho \frac{\partial}{\partial x} \left(\frac{\partial^2 \Psi}{\partial t^2} \right) = (\lambda + 2\mu) \frac{\partial}{\partial z} (\nabla^2 \Phi) - \mu \frac{\partial}{\partial x} (\nabla^2 \Psi) \quad (5.38b)$$

Solving equations (5.38) simultaneously for $\partial^2 \Phi / \partial t^2$ and $\partial^2 \Psi / \partial t^2$ shows

$$\frac{\partial^2 \Phi}{\partial t^2} = \frac{\lambda + 2\mu}{\rho} \nabla^2 \Phi = v_p^2 \nabla^2 \Phi \quad (5.39a)$$

$$\frac{\partial^2 \Psi}{\partial t^2} = \frac{\mu}{\rho} \nabla^2 \Psi = v_s^2 \nabla^2 \Psi \quad (5.39b)$$

If the wave is harmonic with frequency ω and wave number k_R , so that it propagates with *Rayleigh wave velocity* $v_R = \omega/k_R$, the potential functions can be expressed as

$$\Phi = F(z) e^{i(\omega t - k_R x)} \quad (5.40a)$$

$$\Psi = G(z) e^{i(\omega t - k_R z)} \quad (5.40b)$$

where F and G are functions that describe the manner in which the amplitude of the dilatational and rotational components of the Rayleigh wave vary with depth. Substituting these expressions for Φ and Ψ into equations (5.39) gives

$$-\frac{\omega^2}{v_p^2} F(z) = -k_R^2 F(z) + \frac{d^2 F(z)}{dz^2} \quad (5.41a)$$

$$-\frac{\omega^2}{v_s^2} G(z) = -k_R^2 G(z) + \frac{d^2 G(z)}{dz^2} \quad (5.41b)$$

which can be rearranged to give the second-order differential equations

$$\frac{d^2 F}{dz^2} - \left(k_R^2 - \frac{\omega^2}{v_p^2} \right) F = 0 \quad (5.42a)$$

$$\frac{d^2 G}{dz^2} - \left(k_R^2 - \frac{\omega^2}{v_s^2} \right) G = 0 \quad (5.42b)$$

The general solution to these equations can be written in the form

$$F(z) = A_1 e^{-qz} + B_1 e^{qz} \quad (5.43a)$$

$$G(z) = A_2 e^{-sz} + B_2 e^{sz} \quad (5.43b)$$

where

$$q^2 = k_R^2 - \frac{\omega^2}{v_p^2}$$

$$s^2 = k_R^2 - \frac{\omega^2}{v_s^2}$$

The second term of equations (5.43) corresponds to a disturbance whose displacement amplitude approaches infinity with increasing depth. Since this type of behavior is not realistic, B_1 and B_2 must be zero, and the potential functions can finally be written as

$$\Phi = A_1 e^{-qz + i(\omega t - k_R z)} \quad (5.44a)$$

$$\Psi = A_2 e^{-sz + i(\omega t - k_R z)} \quad (5.44b)$$

Since neither shear nor normal stresses can exist at the free surface of the half-space, $\sigma_{xz} = 0$ and $\sigma_{zz} = 0$ when $z = 0$. Therefore,

$$\sigma_{zz} = \lambda \bar{\epsilon} + 2\mu \epsilon_{zz} = \lambda \bar{\epsilon} + 2\mu \frac{dw}{dz} = 0 \quad (5.45a)$$

$$\sigma_{xz} = \mu \epsilon_{xz} = \mu \left(\frac{dw}{dx} + \frac{du}{dz} \right) = 0 \quad (5.45b)$$

Using the potential function definitions of u and w [equations (5.35)] and the solution for the potential functions [equation (5.44)], the free surface boundary conditions can be rewritten as

$$\sigma_{zz}(z = 0) = A_1[(\lambda + 2\mu)q^2 - \lambda k_R^2] - 2iA_2\mu k_R s = 0 \quad (5.46a)$$

$$\sigma_{xz}(z = 0) = 2iA_1k_R q + A_2(s^2 + k_R^2) = 0 \quad (5.46b)$$

which can be rearranged to yield

$$\frac{A_1(\lambda + 2\mu)q^2 - \lambda k_R^2}{A_2} - 1 = 0 \quad (5.47a)$$

$$\frac{A_1}{A_2} \frac{2iqk_R}{s^2 + k_R^2} + 1 = 0 \quad (5.47b)$$

With these results, the velocities and displacement patterns of Rayleigh waves can be determined.

5.3.1.1 Rayleigh Wave Velocity

The velocity at which Rayleigh waves travel is of interest in geotechnical earthquake engineering. As discussed in Chapter 6, Rayleigh waves are often mechanically generated and their velocities measured in the field to investigate the stiffness of surficial soils. Adding equations (5.47) and cross-multiplying gives

$$4q\mu sk_R^2 = (s^2 + k_R^2)[(\lambda + 2\mu)q^2 - \lambda k_R^2] \quad (5.48)$$

which, upon introducing the definitions of q and s and factoring out a $G^2 k_R^8$ term, yields

$$16 \left(1 - \frac{\omega^2}{v_p^2 k_R^2}\right) \left(1 - \frac{\omega^2}{v_s^2 k_R^2}\right) = \left(2 - \frac{\lambda + 2\mu}{\mu} \frac{\omega^2}{v_p^2 k_R^2}\right)^2 \left(2 - \frac{\omega^2}{v_s^2 k_R^2}\right)^2 \quad (5.49)$$

Defining K_{Rs} as the ratio of the Rayleigh wave velocity to the s-wave velocity

$$K_{Rs} = \frac{v_R}{v_s} = \frac{\omega}{v_s k_R}$$

then

$$\frac{v_R}{v_p} = \frac{\omega}{v_p k_R} = \frac{\omega}{v_s k_R \sqrt{(\lambda + 2\mu)/\mu}} = \alpha K_{Rs}$$

where $\alpha = \sqrt{\mu/(\lambda + 2\mu)} = \sqrt{(1 - 2\nu)/(2 - 2\nu)}$. Then equation (5.49) can be rewritten as

$$16(1 - \alpha^2 K_{Rs}^2)(1 - K_{Rs}^2) = \left(2 - \frac{1}{\alpha^2} \alpha^2 K_{Rs}^2\right)^2 (2 - K_{Rs}^2)^2 \quad (5.50)$$

which can be expanded and rearranged into the equation

$$K_{Rs}^6 - 8K_{Rs}^4 + (24 - 16\alpha^2)K_{Rs}^2 + 16(\alpha^2 - 1) = 0 \quad (5.51)$$

This equation is cubic in K_{Rs}^2 , and real solutions for K_{Rs} can be found for various values of Poisson's ratio. These allow evaluation of the ratios of the Rayleigh wave velocity to both s- and p-wave velocities as functions of ν . The solution shown in Figure 5.9 shows that Rayleigh waves travel slightly slower than s-waves for all values of Poisson's ratio except 0.5.

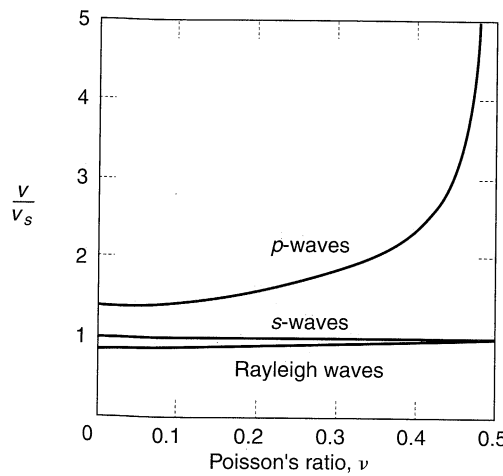


Figure 5.9 Variation of Rayleigh wave and body wave propagation velocities with Poisson's ratio.

5.3.1.2 Rayleigh Wave Displacement Amplitude

Section 5.3.1.1 showed how the velocity of a Rayleigh wave compares with that of p- and s-waves. Some of the intermediate results of that section can be used to illustrate the nature of particle motion during the passage of Rayleigh waves. Substituting the solutions for the potential functions Φ and Ψ [equations (5.44)] into the expressions for u and w [equation 5.35] and carrying out the necessary partial differentiations yields

$$u = -A_1 ik_R e^{-qz + i(\omega t - k_R x)} - A_2 se^{-sz + i(\omega t - k_R x)} \quad (5.52a)$$

$$w = (-A_1 ik_R e^{-qz + i(\omega t - k_R x)}) + A_2 ik_R e^{-sz + i(\omega t - k_R x)} \quad (5.52b)$$

From equation (5.47b),

$$A_2 = -\frac{2qik_R}{s^2 + k_R^2} A_1$$

which, substituting into equations (5.52), gives

$$u = A_1 \left(-ik_R e^{-qz} + \frac{2iqsk_R}{s^2 + k_R^2} e^{-sz} \right) e^{i(\omega t - k_R x)} \quad (5.53a)$$

$$w = A_1 \left(\frac{2qk_R^2}{s^2 + k_R^2} e^{-sz} - qe^{-qz} \right) e^{i(\omega t - k_R x)} \quad (5.53b)$$

where the terms in parentheses describe the variation of the amplitudes of u and w with depth. These horizontal and vertical displacement amplitudes are illustrated for several values of

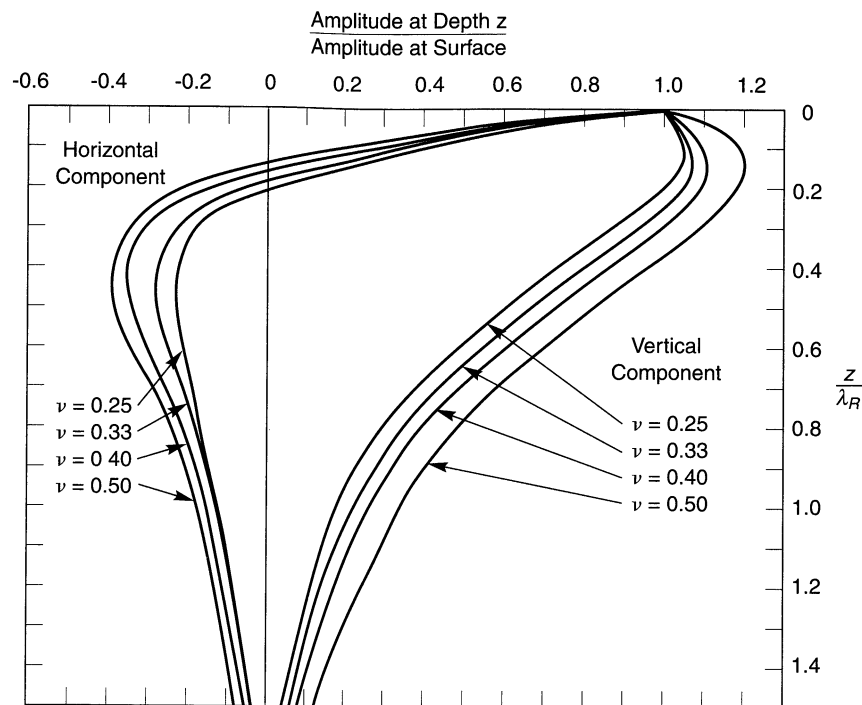


Figure 5.10 Horizontal and vertical motion of Rayleigh waves. A negative amplitude ratio indicates that the displacement is in the opposite direction of the surface displacement. (After Richart et al., 1970.)

Poisson's ratio in Figure 5.10. Examination of equations (5.53) indicates that the horizontal and vertical displacements are out of phase by 90° . Hence the horizontal displacement will be zero when the vertical displacement reaches its maximum (or minimum), and vice versa. The motion of a particle near the surface of the half-space is in the form of a retrograde ellipse (as opposed to the prograde ellipse particle motion observed at the surface of water waves). The general nature of Rayleigh wave motion was illustrated in Figure 2.2a.

The Rayleigh waves produced by earthquakes were once thought to appear only at very large epicentral distances (several hundred km). It is now recognized, however, that they can be significant at much shorter distances (a few tens of kilometers). The ratio of minimum epicentral distance, R , to focal depth, h , at which Rayleigh waves first appear in a homogeneous medium is given by

$$\frac{R}{h} = \frac{1}{\sqrt{(\nu_P/\nu_R)^2 - 1}} \quad (5.54)$$

where ν_P and ν_R are the wave propagation velocities of p-waves and Rayleigh waves, respectively (Ewing et al., 1957).

5.3.2 Love Waves

In a homogeneous elastic half-space, only p-waves, s-waves, and Rayleigh waves can exist. If the half-space is overlain by a layer of material with lower body wave velocity, however, *Love waves* can develop (Love, 1927). Love waves essentially consist of SH-waves that are trapped by multiple reflections within the surficial layer. Consider the case of a homogeneous surficial layer of thickness H overlying a homogeneous half-space as shown in Figure 5.11. A Love wave traveling in the $+x$ -direction would involve particle displacements only in the y -direction (SH-wave motion), and could be described by the equation

$$v(x, z, t) = V(z) e^{i(k_L x - \omega t)} \quad (5.55)$$

where v is the particle displacement in the y -direction, $V(z)$ describes the variation of v with depth, and k_L is the wave number of the Love wave. The Love wave must satisfy the wave equations for s-waves in both the surficial layer and the half-space

$$\frac{\partial^2 v}{\partial t^2} = \begin{cases} \frac{G_1}{\rho_1} \left(\frac{\partial^2 v}{\partial x^2} + \frac{\partial^2 v}{\partial z^2} \right) & \text{for } 0 \leq z \leq H \\ \frac{G_2}{\rho_2} \left(\frac{\partial^2 v}{\partial x^2} + \frac{\partial^2 v}{\partial z^2} \right) & \text{for } z \geq H \end{cases} \quad (5.56a)$$

$$(5.56b)$$

The amplitude can be shown (Aki and Richards, 1980) to vary with depth according to

$$V(z) = \begin{cases} A_1 e^{-v_1 z} + B_1 e^{v_1 z} & \text{for } 0 \leq z \leq H \\ A_2 e^{-v_2 z} + B_2 e^{v_2 z} & \text{for } z \geq H \end{cases} \quad (5.57a)$$

$$(5.57b)$$

where the A and B coefficients describe the amplitudes of downgoing and upgoing waves, respectively, and

$$v_1 = \sqrt{\frac{k_L^2 - \omega^2}{G_1/\rho_1}} \quad v_2 = \sqrt{\frac{k_L^2 - \omega^2}{G_2/\rho_2}} \quad (5.58)$$

Since the half-space extends to infinite depth, B_2 must be zero (no energy can be supplied or reflected at infinite depth to produce an upgoing wave). The requirement that all stresses vanish at the ground surface is satisfied if

$$\frac{\partial v}{\partial z} = \frac{\partial V(z)}{\partial z} e^{i(k_L x - \omega t)} = -A_1 v_1 e^{-v_1 z} + v_1 B_1 e^{v_1 z} = (A_1 - B_1) v_1 (e^{-v_1 z} + e^{v_1 z}) = 0$$

in other words, if $A_1 = B_1$. The amplitudes can now be rewritten in terms of the two remaining unknown amplitudes as

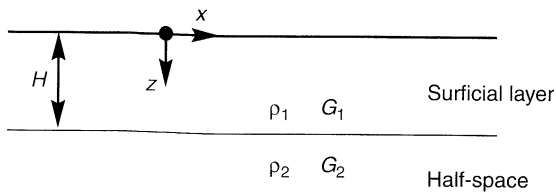


Figure 5.11 Schematic illustration of softer surficial layer ($G_1/\rho_1 < G_2/\rho_2$) overlying elastic half-space, the simplest conditions for which Love waves can exist.

$$V(z) = \begin{cases} A_1(e^{-v_1 z} + e^{v_1 z}) & \text{for } 0 \leq z \leq H \\ A_2 e^{-v_2 z} & \text{for } z \geq H \end{cases} \quad (5.59a)$$

At the $z = H$ interface, continuity of stresses requires that

$$2iG_1 v_1 A_1 \sin(iv_1 H) = G_2 v_2 A_2 e^{-v_2 H} \quad (5.60)$$

and compatibility of displacements requires that

$$2A_1 \cos(iv_1 H) = A_2 e^{-v_2 H} \quad (5.61)$$

Using equations (5.60) and (5.61), A_2 can be expressed in terms of A_1 by

$$A_2 = \frac{2 \cos(iv_1 H)}{e^{-v_2 H}} A_1 \quad (5.62)$$

Substituting equations (5.59) and (5.60) into (5.55) gives

$$v(x, z, t) = \begin{cases} 2A_1 \cos\left[\omega\left(\frac{1}{v_{s1}^2} - \frac{1}{v_L^2}\right)^{1/2} z\right] e^{i(k_L x - \omega t)} & \text{for } 0 \leq z \leq H \end{cases} \quad (5.63a)$$

$$\begin{cases} 2A_1 \cos\left[\omega\left(\frac{1}{v_{s1}^2} - \frac{1}{v_L^2}\right)^{1/2} H\right] \exp\left[-\omega\left(\frac{1}{v_L^2} - \frac{1}{v_{s2}^2}\right)^{1/2}(z - H)\right] e^{i(k_L x - \omega t)} & \text{for } z \geq H \end{cases} \quad (5.63b)$$

where v_{s1} and v_{s2} are the shear wave velocities of materials 1 and 2, respectively, and v_L is the velocity of the Love wave. Equation (5.63) shows, as illustrated in Figure 5.12, that the Love wave displacement amplitude varies sinusoidally with depth in the surficial layer and decays exponentially with depth in the underlying half-space. Because of this, Love waves are often described as SH-waves that are trapped in the surficial layer. The general nature of Love wave displacement was shown in Figure 2.2a.

The Love wave velocity is given by the solution of

$$\tan \omega H \left(\frac{1}{v_{s1}^2} - \frac{1}{v_L^2} \right)^{1/2} = \frac{G_2 \sqrt{1/v_L^2 - 1/v_{s2}^2}}{G_1 \sqrt{1/v_{s1}^2 - 1/v_L^2}} \quad (5.64)$$

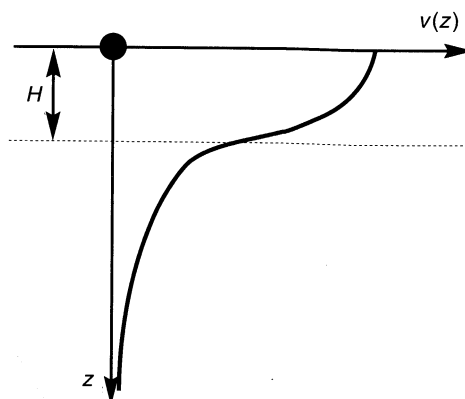


Figure 5.12 Variation of particle displacement amplitude with depth for Love waves.

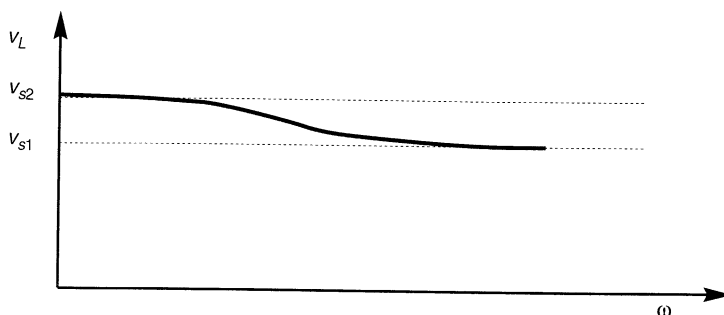


Figure 5.13 Variation of Love wave velocity with frequency.

which indicates, as illustrated in Figure 5.13 that Love wave velocities range from the s-wave velocity of the half-space (at very low frequencies) to the s-wave velocity of the surficial layer (at very high frequencies). This frequency dependence indicates that Love waves are dispersive (Section 5.3.4).

5.3.3 Higher-Mode Surface Waves

Any surface wave must (1) satisfy the equation of motion, (2) produce zero stress at the ground surface, and (3) produce zero displacement at infinite depth. Nontrivial solutions do not exist for arbitrary combinations of frequency and wave number; rather, a set of discrete and unique wave numbers exist for a given frequency. Each wave number describes a different displacement pattern, or *mode*, of the surface wave. The preceding derivations have been limited to the *fundamental modes* of Rayleigh and Love waves, which are the most important for earthquake engineering applications. Detailed treatment of higher-mode surface waves can be found in most advanced seismology texts.

5.3.4 Dispersion of Surface Waves

For a homogeneous half-space, the Rayleigh wave velocity was shown to be related to the body wave velocities by Poisson's ratio. Since the body wave velocities are constant with depth, the Rayleigh wave velocity in a homogeneous half-space is independent of frequency. The velocity of the Love wave, on the other hand, varies with frequency between an upper and a lower limit.

Dispersion is a phenomenon in which waves of different frequency (and different wavelength) propagate at different velocities. Hence Love waves are clearly *dispersive*, and Rayleigh waves in a homogeneous half-space are *nondispersive*. Near the earth's surface, however, soil and rock stiffnesses usually increase with depth. Since the depth to which a Rayleigh wave causes significant displacement increases with increasing wavelength (Figure 5.10), Rayleigh waves of long wavelength (low frequency) can propagate faster than Rayleigh waves of short wavelength (high frequency). Therefore, in the real world of heterogeneous materials, Rayleigh waves are also dispersive. The dispersion of Rayleigh waves can be used to evaluate subsurface stiffness profiles by field testing techniques described in Chapter 6.

Since the velocities of both Rayleigh waves and Love waves decrease with increasing frequency, the low-frequency components of surface waves produced by earthquakes can

be expected to arrive at a particular site before their high-frequency counterparts. This tendency to spread the seismic energy over time is an important effect of dispersion.

5.3.5 Phase and Group Velocities

The solutions for Rayleigh wave velocity, v_R , and Love wave velocity, v_L , were based on the assumption of harmonic loading which produces an infinite wave train. These velocities describe the rate at which points of constant phase (e.g., peaks, troughs, or zero points) travel through the medium and are called *phase velocities*. A transient disturbance may produce a packet of waves with similar frequencies. This packet of waves travels at the *group velocity*, c_g , given by

$$c_g = c + k \frac{dc}{dk} \quad (5.65)$$

where c is the phase velocity (equal to v_R or v_L , depending on which type of wave is being considered) and k is the wave number (equal to ω/v_R or ω/v_L). In a nondispersive material, $dc/dk = 0$, so the group velocity is equal to the phase velocity. Since both v_R and v_L generally decrease with increasing frequency in geologic materials, dc/dk is less than zero and the group velocity is lower than the phase velocity. Consequently, a wave packet would appear to consist of a series of individual peaks that appear at the back end of the packet, move through the packet to the front, and then disappear. The opposite behavior can be observed by (for $c < c_g$) dropping a rock into a calm pond of water and watching the resulting ripples carefully.

5.4 WAVES IN A LAYERED BODY

The model of a homogeneous elastic half-space is useful for explaining the existence of body waves and Rayleigh waves, and the addition of a softer surficial layer allows Love waves to be described. In the earth, however, conditions are much more complicated with many different materials of variable thickness occurring in many areas. To analyze wave propagation under such conditions, and to understand the justification for idealizations of actual conditions when all features cannot be explicitly analyzed, the general problem of wave behavior at interfaces must be investigated.

5.4.1 One-Dimensional Case: Material Boundary in an Infinite Rod

Consider a harmonic stress wave traveling along a constrained rod in the $+x$ direction and approaching an interface between two different materials, as shown in Figure 5.14. Since the wave is traveling toward the interface, it will be referred to as the *incident wave*. Since it is traveling in material 1, its wavelength will be $\lambda_1 = 2\pi/k_1$, and it can therefore be described by

$$\sigma_I(x, t) = \sigma_I e^{i(\omega t - k_1 x)} \quad (5.66a)$$

When the incident wave reaches the interface, part of its energy will be transmitted through the interface to continue traveling in the positive x -direction through material 2. This *transmitted wave* will have a wavelength $\lambda_2 = 2\pi/k_2$. The remainder will be reflected at the interface and will travel back through material 1 in the negative x -direction as a *reflected wave*. The transmitted and reflected waves can be described by

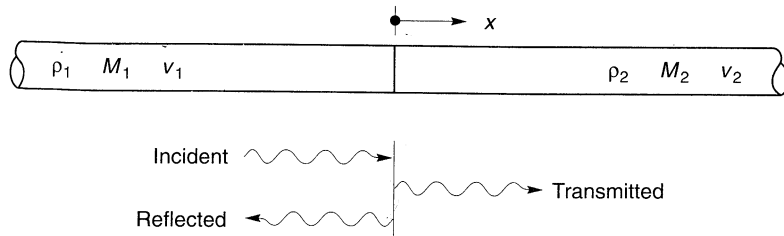


Figure 5.14 One-dimensional wave propagation at material interface. Incident and reflected waves travel in opposite directions in material 1. The transmitted wave travels through material 2 in the same direction as the incident wave.

$$\sigma_T(x, t) = \sigma_t e^{i(\omega t - k_2 x)} \quad (5.66b)$$

$$\sigma_R(x, t) = \sigma_r e^{i(\omega t + k_1 x)} \quad (5.66c)$$

Assuming that the displacements associated with each of these waves are of the same harmonic form as the stresses that cause them; that is,

$$u_I(x, t) = A_i e^{i(\omega t - k_1 x)} \quad (5.67a)$$

$$u_R(x, t) = A_r e^{i(\omega t + k_1 x)} \quad (5.67b)$$

$$u_T(x, t) = A_t e^{i(\omega t - k_2 x)} \quad (5.67c)$$

Stress-strain and strain-displacement relationships can be used to relate the stress amplitudes to the displacement amplitudes:

$$\sigma_I(x, t) = M_1 \frac{\partial u_I(x, t)}{\partial x} = -ik_1 M_1 A_i e^{i(\omega t - k_1 x)} \quad (5.68a)$$

$$\sigma_R(x, t) = M_1 \frac{\partial u_R(x, t)}{\partial x} = +ik_1 M_1 A_r e^{i(\omega t + k_1 x)} \quad (5.68b)$$

$$\sigma_T(x, t) = M_2 \frac{\partial u_T(x, t)}{\partial x} = -ik_2 M_2 A_t e^{i(\omega t - k_2 x)} \quad (5.68c)$$

From these, the stress amplitudes are related to the displacement amplitudes by

$$\sigma_i = -ik_1 M_1 A_i \quad (5.69a)$$

$$\sigma_r = +ik_1 M_1 A_r \quad (5.69b)$$

$$\sigma_t = -ik_2 M_2 A_t \quad (5.69c)$$

At the interface, both compatibility of displacements and continuity of stresses must be satisfied. The former requires that

$$u_I(0, t) + u_R(0, t) = u_T(0, t) \quad (5.70)$$

and the latter that

$$\sigma_I(0, t) + \sigma_R(0, t) = \sigma_T(0, t) \quad (5.71)$$

Substituting equations (5.67) and (5.66) into equations (5.70) and (5.71), respectively, indicates that

$$A_i + A_r = A_t \quad (5.72)$$

$$\sigma_i + \sigma_r = \sigma_t \quad (5.73)$$

at the interface. Substituting equations (5.69) into equation (5.73) and using the relationship $kM = \omega\rho v$, gives

$$-\rho_1 v_1 A_i + \rho_1 v_1 A_r = -\rho_2 v_2 A_t = -\rho_2 v_2 (A_i + A_r) \quad (5.74)$$

Equation (5.74) can be rearranged to relate the displacement amplitude of the reflected wave to that of the incident wave:

$$A_r = \frac{\rho_1 v_1 - \rho_2 v_2}{\rho_1 v_1 + \rho_2 v_2} A_i = \frac{1 - \rho_2 v_2 / \rho_1 v_1}{1 + \rho_2 v_2 / \rho_1 v_1} A_i \quad (5.75)$$

and knowing A_i and A_r , equation (5.72) can be used to determine A_t as

$$A_t = \frac{2\rho_1 v_1}{\rho_1 v_1 + \rho_2 v_2} A_i = \frac{2}{1 + \rho_2 v_2 / \rho_1 v_1} A_i \quad (5.76)$$

Remember that the product of the density and the wave propagation velocity is the specific impedance of the material. Equations (5.75) and (5.76) indicate that the partitioning of energy at the interface depends only on the ratio of the specific impedances of the materials on either side of the interface. Defining the *impedance ratio* as $\alpha_z = \rho_2 v_2 / \rho_1 v_1$, the displacement amplitudes of the reflected and transmitted waves are

$$A_r = \frac{1 - \alpha_z}{1 + \alpha_z} A_i \quad (5.77)$$

$$A_t = \frac{2}{1 + \alpha_z} A_i \quad (5.78)$$

After evaluating the effect of the interface on the displacement amplitudes of the reflected and transmitted waves, its effect on stress amplitudes can be investigated. From equations (5.69)

$$A_i = -\frac{\sigma_i}{ik_1 M_1} \quad (5.79a)$$

$$A_r = \frac{\sigma_r}{ik_1 M_1} \quad (5.79b)$$

$$A_t = -\frac{\sigma_t}{ik_2 M_2} \quad (5.79c)$$

Substituting equations (5.79) into equations (5.77) and (5.78) and rearranging gives

$$\sigma_r = \frac{\alpha_z - 1}{1 + \alpha_z} \sigma_i \quad (5.80)$$

$$\sigma_t = \frac{2\alpha_z}{1 + \alpha_z} \sigma_i \quad (5.81)$$

The importance of the impedance ratio in determining the nature of reflection and transmission at interfaces can clearly be seen. Equations (5.77), (5.78), (5.80), and (5.81) indicate that fundamentally different types of behavior occur when the impedance ratio is less than or greater than 1. When the impedance ratio is less than 1, an incident wave can be thought of as approaching a "softer" material. For this case, the reflected wave will have a smaller stress amplitude than the incident wave and its sign will be reversed (an incident compression pulse will be reflected as a tensile pulse, and vice versa). If the impedance ratio is greater than 1, the incident wave is approaching a "stiffer" material in which the stress amplitude of the transmitted wave will be greater than that of the incident wave and the stress amplitude of the reflected wave will be less than, but of the same sign, as that of the incident wave. The displacement amplitudes are also affected by the impedance ratio. The relative stress and displacement amplitudes of reflected and transmitted waves at boundaries with several different impedance ratios are illustrated in Table 5-1.

The cases of $\alpha_z = 0$ and $\alpha_z = \infty$ are of particular interest. An impedance ratio of zero implies that the incident wave is approaching a "free end" across which no stress can be transmitted ($\sigma_t = 0$). To satisfy this zero stress boundary condition, the displacement of the boundary (the transmitted displacement) must be twice the displacement amplitude of the incident wave ($A_t = 2A_i$). The reflected wave has the same amplitude as the incident wave but is of the opposite polarity ($\sigma_r = -\sigma_i$). In other words, a free end will reflect a compression wave as a tension wave of identical amplitude and shape and a tension wave as an identical compression wave. An infinite impedance ratio implies that the incident wave is approaching a "fixed end" at which no displacement can occur ($u_t = 0$). In that case the stress at the boundary is twice that of the incident wave ($\sigma_t = 2\sigma_i$) and the reflected wave has the same amplitude and polarity as the incident wave ($A_r = -A_i$).

The case of $\alpha_z = 1$, in which the impedances on each side of the boundary are equal, is also of interest. Equations (5.77), (5.78), (5.80), and (5.81) indicate that no reflected wave

Table 5-1 Influence of Impedance Ratio on Displacement and Stress Amplitudes of Reflected and Transmitted Waves

Impedance Ratio, α_z	Displacement Amplitudes			Stress Amplitudes		
	Incident	Reflected	Transmitted	Incident	Reflected	Transmitted
0	A_i	A_i	$2A_i$	σ_i	$-\sigma_i$	0
$\frac{1}{4}$	A_i	$3A_i/5$	$8A_i/5$	σ_i	$-3\sigma_i/5$	$2\sigma_i/5$
$\frac{1}{2}$	A_i	$A_i/3$	$4A_i/3$	σ_i	$-\sigma_i/3$	$2\sigma_i/3$
1	A_i	0	A_i	σ_i	0	σ_i
2	A_i	$-A_i/3$	$2A_i/3$	σ_i	$\sigma_i/3$	$4\sigma_i/3$
4	A_i	$-3A_i/5$	$2A_i/5$	σ_i	$3\sigma_i/5$	$8\sigma_i/5$
∞	A_i	$-A_i$	0	σ_i	σ_i	$2\sigma_i$

is produced and that the transmitted wave has, as expected, the same amplitude and polarity as the incident wave. In other words, all of the elastic energy of the wave crosses the boundary unchanged and travels away, never to return. Another way of looking at a boundary with an impedance ratio of unity is as a boundary between two identical, semi-infinite rods. A harmonic wave traveling in the positive x -direction (Figure 5.15a) would impose an axial force [see equation (5.5)] on the boundary:

$$F = \sigma_x A = \rho v_m A i$$

This axial force is identical to that which would exist if the semi-infinite rod on the right side of the boundary were replaced by a dashpot (Figure 5.15b) of coefficient $c = \rho v_m A$. In other words, the dashpot would absorb all the elastic energy of the incident wave, so the response of the rod on the left would be identical for both cases illustrated in Figure 5.15. This result has important implications for ground response and soil-structure interaction analyses (Chapter 7), where the replacement of a semi-infinite domain by discrete elements such as dashpots can provide tremendous computational efficiencies.

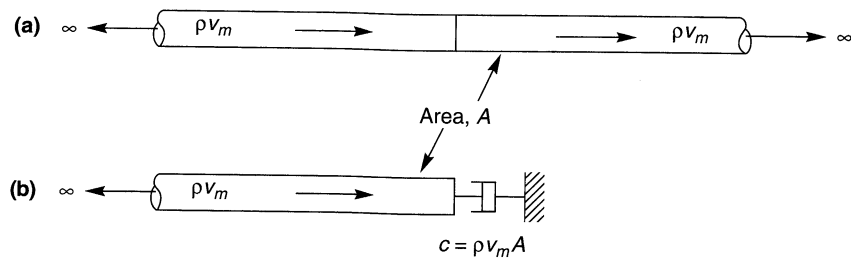


Figure 5.15 (a) Harmonic wave traveling along two connected semi-infinite rods; (b) semi-infinite rod attached to dashpot. With proper selection of dashpot coefficient, response in semi-infinite rod on left will be identical for both cases.

Example 5.4

A vertically propagating shear wave travels upward through a layered soil deposit. Compute the amplitudes of the reflected and transmitted waves that develop when the shear wave reaches the boundary shown in Figure E5.4.

Solution Although the transmission-reflection behavior in the preceding section was derived for constrained longitudinal waves, extension to the case of shear waves is straightforward. The (shear wave) impedance ratio for an upward-traveling wave is

$$\alpha_z = \frac{(1.76 \text{ Mg/m}^3)(400 \text{ m/sec})}{(2.24 \text{ Mg/m}^3)(750 \text{ m/sec})} = 0.419$$

The stress amplitude of the reflected wave is given by equation (5.79)

$$\sigma_r = \frac{\alpha_z - 1}{1 + \alpha_z} \sigma_i = \frac{0.419 - 1}{1 + 0.419} (100 \text{ kPa}) = -40.9 \text{ kPa}$$

From equation (5.80), the stress amplitude of the transmitted wave is

$$\sigma_t = \frac{2\alpha_z}{1 + \alpha_z} \sigma_i = \frac{2(0.419)}{1 + 0.419} (100 \text{ kPa}) = 59.1 \text{ kPa}$$

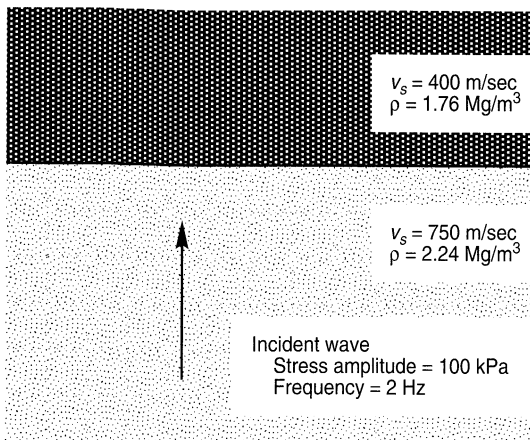


Figure E5.4

The displacement amplitude of the incident wave can be computed from the shear wave equivalent of equation 5.78a

$$\begin{aligned} A_i &= -\frac{\alpha_i}{ik_1 G_1} = \frac{i\alpha_i}{\rho_1 \omega v_{s1}} \\ &= \frac{i(100 \text{ kN/m}^2)(1 \text{ Mg}/9.807 \text{ kN})(9.807 \text{ m/sec}^2)}{(2.24 \text{ Mg/m}^3)2\pi(2 \text{ Hz})(750 \text{ m/sec})} = 0.00477 \text{ m} = 4.77 \text{ mm} \end{aligned}$$

The i term simply describes the 90° phase angle between stresses and displacements. Then, using equations (5.76) and (5.77), the displacement amplitudes of the reflected and transmitted waves are

$$\begin{aligned} A_r &= \frac{1-\alpha_z}{1+\alpha_z} A_i = \frac{1-0.419}{1+0.419}(4.77 \text{ mm}) = 1.95 \text{ mm} \\ A_t &= \frac{2}{1+\alpha_z} A_i = \frac{2}{1+0.419}(4.77 \text{ mm}) = 6.72 \text{ mm} \end{aligned}$$

In this example, the incident wave travels from a material of higher impedance to a material of lower impedance. As a result, the displacement amplitude of the transmitted wave is greater than that of the incident wave, but the stress amplitude is smaller.

5.4.2 Three-Dimensional Case: Inclined Waves

In general, waves will not approach interfaces at 90° angles as they did in Section 5.4.1. The orientation of an *inclined body wave* can strongly influence the manner in which energy is reflected and transmitted across an interface. Fermat's principle defines the propagation time of a seismic pulse between two arbitrary points A and B as the minimum travel time along any continuous path that connects A and B . The path that produces the minimum travel time is called a *ray path*, and its direction is often represented by a vector called a *ray*. A *wavefront* is defined as a surface of equal travel time, consequently, a ray path must (in an isotropic material) be perpendicular to the wavefront as illustrated in Figure 5.16. Snell considered the change of direction of ray paths at interfaces between materials with different wave propagation velocities. Using Fermat's principle, Snell showed that

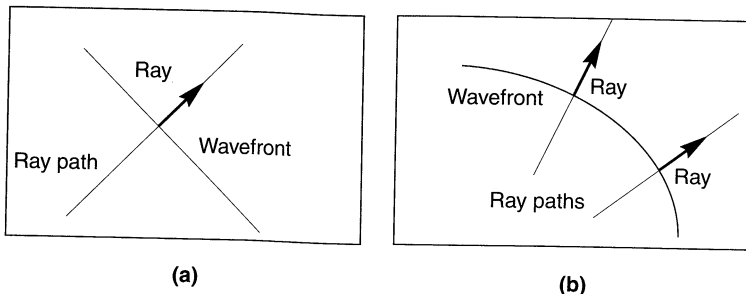


Figure 5.16 Ray path, ray, and wavefront for (a) plane wave and (b) curved wavefront.

$$\frac{\sin i}{v} = \text{constant} \quad (5.82)$$

where i is the angle between the ray path and the normal to the interface and v is the velocity of the wave (p- or s-wave) of interest. This relationship holds for both reflected and transmitted waves. It indicates that the transmitted wave will be *refracted* (except when $i = 0$) when the wave propagation velocities are different on each side of the interface.

Consider the case of two half-spaces of different elastic materials in contact with each other. As for the previous case, the requirements of equilibrium and compatibility and the theory of elasticity can be used to determine the nature of and distribution of energy among the reflected and transmitted waves for the cases of an incident p-wave, an incident SV-wave, and an incident SH-wave.

The types of waves produced by incident p-, SV-, and SH-waves are shown in Figure 5.17. Since incident p- and SV-waves involve particle motion perpendicular to the plane of the interface; they will each produce both reflected and refracted p- and SV-waves. An incident SH-wave does not involve particle motion perpendicular to the interface; consequently, only SH-waves are reflected and refracted. The directions and relative amplitudes of the waves produced at the interface depend on both the direction and amplitude of the

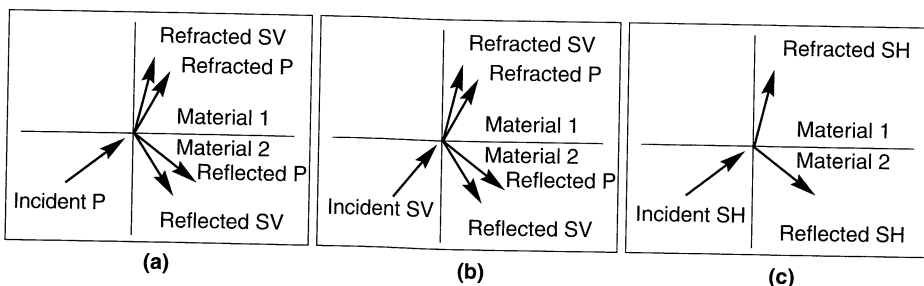


Figure 5.17 Reflected and refracted rays resulting from incident (a) p-wave, (b) SV-wave, and (c) SH-wave.

incident wave. Using Snell's law and the requirements of equilibrium and compatibility, these directions and amplitudes can be determined. Using the notation of Richter (1958):

Wave Type	Velocity	Amplitude	Angle with Normal
Incident p	U	A	a
Incident s	V	B	b
Reflected p	U	C	c
Reflected s	V	D	d
Refracted p	Y	E	e
Refracted s	Z	F	f

the directions of all waves are easily related to the direction of the incident wave using Snell's law:

$$\frac{\sin a}{U} = \frac{\sin b}{V} = \frac{\sin c}{U} = \frac{\sin d}{V} = \frac{\sin e}{Y} = \frac{\sin f}{Z} \quad (5.83)$$

Since incident and reflected waves travel through the same material, $a = c$ and $b = d$, which shows that the *angle of incidence* is equal to the *angle of reflection* for both p- and s-waves.

The *angle of refraction* is uniquely related to the angle of incidence by the ratio of the wave velocities of the materials on each side of the interface. Snell's law indicates that waves traveling from higher-velocity materials into lower-velocity materials will be refracted closer to the normal to the interfaces. In other words, waves propagating upward through horizontal layers of successively lower velocity (as is common near the earth's surface) will be refracted closer and closer to a vertical path (Figure 5.18). This phenomenon is relied upon heavily by many of the methods of ground response analysis presented in Chapter 7.

The *critical angle of incidence*, i_c , is defined as that which produces a refracted wave that travels parallel to the interface (e or $f = 90^\circ$). Therefore,

$$i_c = \sin^{-1} \frac{U}{Y} = \sin^{-1} \frac{V}{Z} \quad (5.84)$$

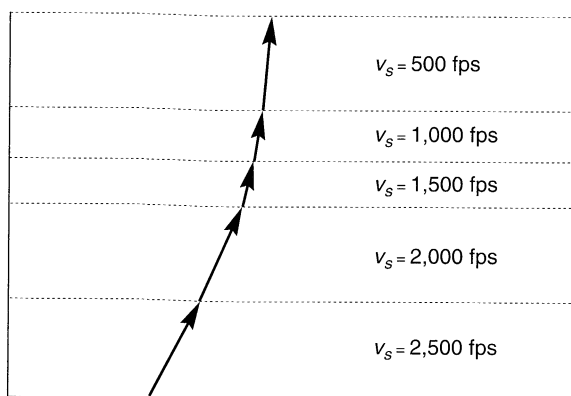


Figure 5.18 Refraction of an SH-wave ray path through series of successively softer (lower v_s) layers. Note that orientation of ray path becomes closer to vertical as ground surface is approached. Reflected rays are not shown.

The concept of critical refraction is used in the interpretation of seismic refraction tests (Section 6.3.1.1).

Assuming that the incident wave is simple harmonic, satisfaction of the requirements of equilibrium and compatibility at the interface give rise to the following systems of simultaneous equations (Richter, 1958), which allows the amplitudes of the reflected and refracted waves (C, D, E , and F) to be expressed in terms of the amplitude of the incident p-wave (A).

$$\begin{aligned} (A - C) \sin a + D \cos b - E \sin e + F \cos f &= 0 \\ (A + C) \cos a + D \sin b - E \cos e - F \sin f &= 0 \\ -(A + C) \sin 2a + D \frac{U}{V} \cos 2b + EK \left(\frac{Z}{V} \right)^2 \frac{U}{Y} \sin 2e - FK \left(\frac{Z}{V} \right)^2 \frac{U}{Z} \cos 2f &= 0 \quad (5.85) \\ -(A - C) \cos 2b + D \frac{V}{U} \sin 2b + EK \frac{Y}{U} \cos 2f - FK \frac{Z}{U} \sin (2f) &= 0 \end{aligned}$$

where $K = \rho_1/\rho_2$ (the subscripts 1 and 2 refer to materials 1 and 2, respectively). Note that the amplitudes are functions of the angle of incidence, the velocity ratio, and the density ratio. Figure 5.19 shows the variation of amplitude with angle of p-wave incidence for the following conditions: $U = 8.000$, $Y = 2.003$, $K = 0.606$, and $v = 0.25$. The sensitivity of the reflected and refracted wave amplitudes to the angle of incidence is apparent. SV-waves are neither reflected nor refracted at angles of incidence of 0° and 90° , but can carry the majority of the wave energy away from the interface at intermediate angles.

For an incident SV-wave, both SV- and p-waves are reflected and refracted. The equilibrium/compatibility equations relating the relative amplitudes are

$$\begin{aligned} (B + D) \sin b + C \cos a - E \cos e - F \sin f &= 0 \\ (B - D) \cos b + C \sin a + E \sin e - F \cos f &= 0 \\ (B + D) \cos 2b - C \frac{V}{U} \sin 2a + EK \frac{Z^2}{VY} \sin 2e - FK \frac{Z}{V} \cos 2f &= 0 \quad (5.86) \\ -(B - D) \sin 2b + C \frac{U}{V} \cos 2b + EK \frac{Y}{V} \cos 2f + FK \frac{Z}{V} \sin 2f &= 0 \end{aligned}$$

which produce the amplitude behavior shown in Figure 5.20. For angles of incidence greater than $\sin^{-1}(V/U)$, about 36° in Figure 5.20(a), no p-wave can be reflected, so the incident wave energy must be carried away by the remaining waves. A more detailed discussion of this phenomenon can be found in McCamy et al. (1962).

An incident SH-wave involves no particle motion perpendicular to the interface; consequently, it cannot produce p-waves ($C = E = 0$) or SV-waves. The equilibrium/compatibility equations are considerably simplified and easily solved as

$$\begin{aligned} D &= \frac{1 - K \frac{Z \cos f}{V \cos b}}{1 + K \frac{Z \cos f}{V \cos b}} B \\ F &= B \left(1 + \frac{1 - K \frac{Z \cos f}{V \cos b}}{1 + K \frac{Z \cos f}{V \cos b}} \right) \quad (5.87) \end{aligned}$$

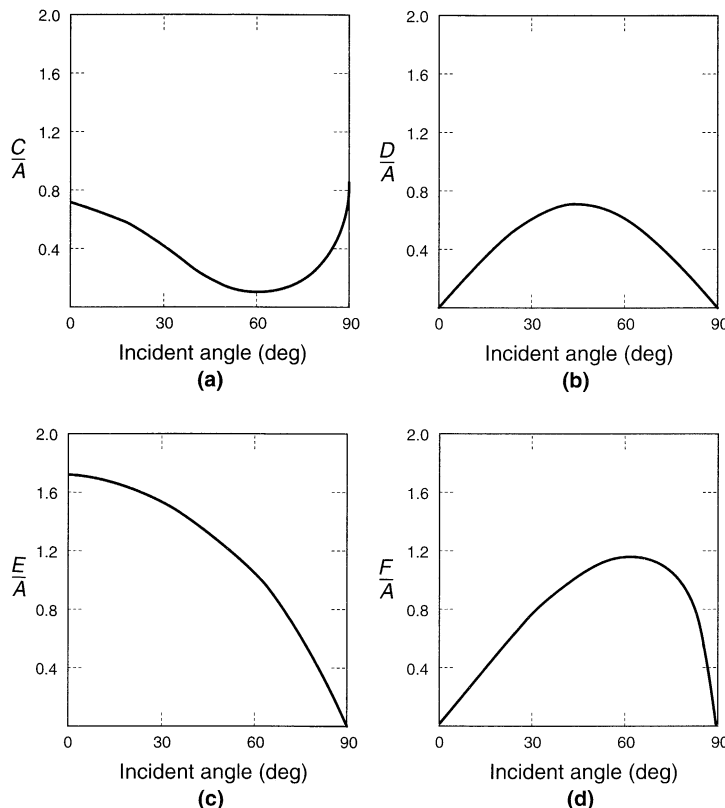


Figure 5.19 Ratio of amplitudes of (a) reflected p-wave, (b) reflected SV-wave, (c) refracted p-wave, and (d) refracted SV-wave to amplitude of incident p-wave versus angle of incidence.

The preceding results show that the interaction of stress waves with boundaries can be quite complicated. As seismic waves travel away from the source of an earthquake, they invariably encounter heterogeneities and discontinuities in the earth's crust. The creation of new waves and the reflection and refraction of ray paths by these heterogeneities cause seismic waves to reach a site by many different paths. Since the paths have different lengths, the motion at the site is spread out in time by this *scattering* effect.

5.5 ATTENUATION OF STRESS WAVES

The preceding sections have considered only the propagation of waves in linear elastic materials. In a homogeneous linear elastic material, stress waves travel indefinitely without change in amplitude. This type of behavior cannot occur, however, in real materials. The amplitudes of stress waves in real materials, such as those that comprise the earth, attenuate with distance. This attenuation can be attributed to two sources, one of which involves the

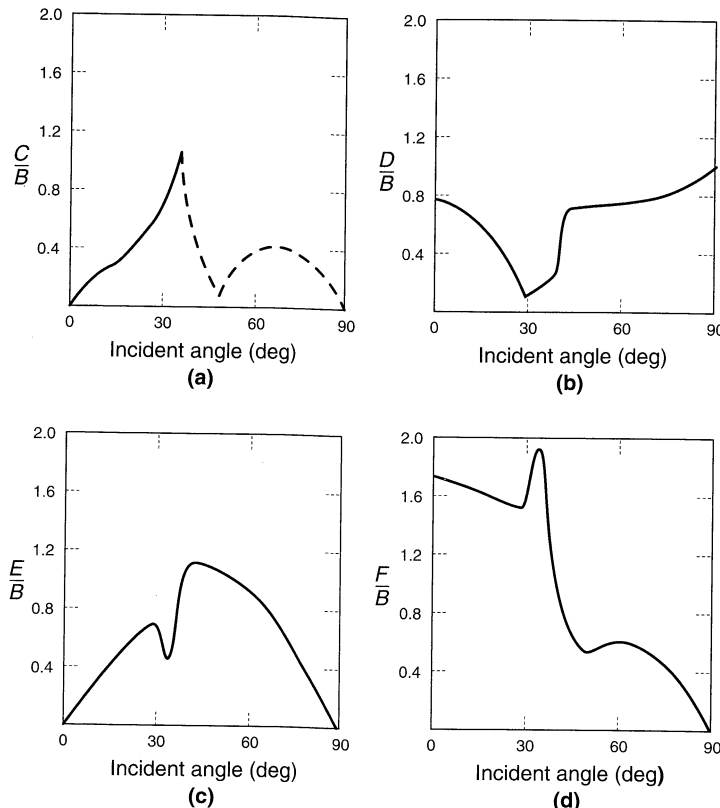


Figure 5.20 Ratio of amplitudes of (a) reflected p-wave, (b) reflected SV-wave, (c) refracted p-wave, and (d) refracted SV-wave to amplitude of incident SV-wave versus angle of incidence.

materials through which the waves travel and the other the geometry of the wave propagation problem.

5.5.1 Material Damping

In real materials, part of the elastic energy of a traveling wave is always converted to heat. The conversion is accompanied by a decrease in the amplitude of the wave. Viscous damping, by virtue of its mathematical convenience, is often used to represent this dissipation of elastic energy. For the purposes of viscoelastic wave propagation, soils are usually modelled as Kelvin–Voigt solids (i.e., materials whose resistance to shearing deformation is the sum of an elastic part and a viscous part). A thin element of a Kelvin–Voigt solid can be illustrated as in Figure 5.21.

The stress–strain relationship for a Kelvin–Voigt solid in shear can be expressed as

$$\tau = G\gamma + \eta \frac{\partial \gamma}{\partial t} \quad (5.88)$$

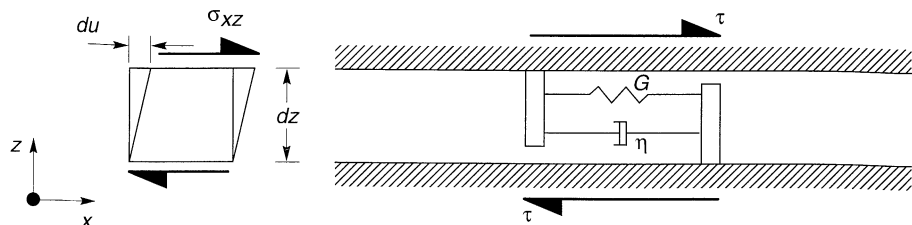


Figure 5.21 Thin element of a Kelvin–Voigt solid subjected to horizontal shearing. Total resistance to shearing deformation is given by the sum of an elastic (spring) component and a viscous (dashpot) component.

where τ ($= \sigma_{xz}$) is the shear stress, γ ($= \partial u / \partial z$) is the shear strain, and η is the viscosity of the material. Thus the shear stress is the sum of an elastic part (proportional to strain) and a viscous part (proportional to strain rate). For a harmonic shear strain of the form

$$\gamma = \gamma_0 \sin \omega t \quad (5.89)$$

the shear stress will be

$$\tau = G\gamma_0 \sin \omega t + \omega \eta \gamma_0 \cos \omega t \quad (5.90)$$

Together, equations (5.89) and (5.90) show that the stress–strain loop of a Kelvin–Voigt solid is elliptical. The elastic energy dissipated in a single cycle is given by the area of the ellipse, or

$$\Delta W = \int_{t_0}^{t_0 + 2\pi/\omega} \tau \frac{\partial \gamma}{\partial t} dt = \pi \eta \omega \gamma_0^2$$

which indicates that the dissipated energy is proportional to the frequency of loading. Real soils, however, dissipate elastic energy hysteretically, by the slippage of grains with respect to each other. As a result, their energy dissipation characteristics are insensitive to frequency. For discrete Kelvin–Voigt systems (Appendix B), the damping ratio, ξ , was shown to be related to the force–displacement (or, equivalently, the stress–strain) loop as shown in Figure 5.22. Since the peak energy stored in the cycle is

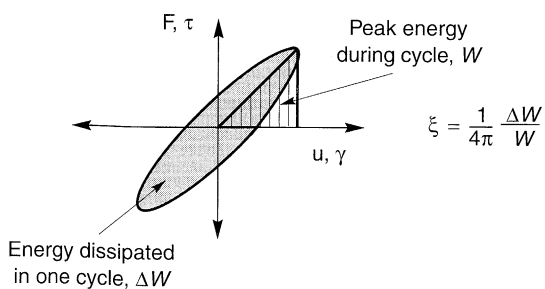


Figure 5.22 Relationship between hysteresis loop and damping ratio.

$$W = \frac{1}{2}G\gamma_0^2$$

then

$$\xi = \frac{1}{4\pi} \frac{\pi\eta\omega\gamma_0^2}{\frac{1}{2}G\gamma_0^2} = \frac{\eta\omega}{2G} \quad (5.91)$$

To eliminate frequency dependence while maintaining the convenience of the viscoelastic formulation, equation (5.91) is often rearranged to produce an equivalent viscosity that is inversely proportional to frequency. The use of this equivalent viscosity ensures that the damping ratio is independent of frequency:

$$\eta = \frac{2G\xi}{\omega} \quad (5.92)$$

A Kelvin–Voigt solid for vertically propagating SH-waves may be represented by a stack of infinitesimal elements of the type shown schematically in Figure 5.21. The one-dimensional equation of motion for vertically propagating SH-waves can be written as

$$\rho \frac{\partial^2 u}{dt^2} = \frac{\partial \sigma_{xz}}{\partial z} \quad (5.93)$$

Substituting equation (5.88) into (5.93) with $\tau = \sigma_{xz}$ and $\gamma = \partial u / \partial z$, and differentiating the right side allows the wave equation to be expressed as

$$\rho \frac{\partial^2 u}{dt^2} = G \frac{\partial^2 u}{dz^2} + \eta \frac{\partial^3 u}{\partial z^2 \partial t} \quad (5.94)$$

For harmonic waves, the displacements can be written as

$$u(z, t) = U(z) e^{i\omega t} \quad (5.95)$$

which, when substituted into the wave equation (5.94) yields the ordinary differential equation

$$(G + i\omega\eta) \frac{d^2 U}{dz^2} = -\rho\omega^2 U \quad (5.96)$$

or

$$G^* \frac{d^2 U}{dz^2} = -\rho\omega^2 U \quad (5.97)$$

where $G^* = G + i\omega\eta$ is the *complex shear modulus*. The complex shear modulus is analogous to the complex stiffness described in Section B.6.3 of Appendix B. Using equation (5.92) to eliminate frequency dependence, the complex shear modulus can also be expressed as $G^* = G(1 + 2i\xi)$. This equation of motion has the solution

$$u(z, t) = A e^{i(\omega t - k^* z)} + B e^{i(\omega t + k^* z)} \quad (5.98)$$

where A and B depend on the boundary conditions and $k^* = \omega \sqrt{\rho/G^*}$ is the *complex wave number*. It can be shown (after Kolsky, 1963) that k^* is given by

$$k^* = k_1 + ik_2 \quad (5.99)$$

where

$$\begin{aligned} k_1^2 &= \frac{\rho\omega^2}{2G(1+4\xi^2)}(\sqrt{1+4\xi^2}+1) \\ k_2^2 &= \frac{\rho\omega^2}{2G(1+4\xi^2)}(\sqrt{1+4\xi^2}-1) \end{aligned} \quad (5.100)$$

and only the positive root of k_1 and the negative root of k_2 have physical significance. Note that for the inviscid case ($\eta = \xi = 0$), $k_2 = 0$ and $k_1 = k$. For a wave propagating in the positive z -direction, the solution can be written as

$$u(z, t) = Ae^{k_2 z} e^{i(\omega t - k_1 z)} \quad (5.101)$$

which shows (since k_2 is negative) that material damping produces exponential attenuation of wave amplitude with distance.

Although the Kelvin–Voigt model is by far the most commonly used model for soils, it represents only one of an infinite number of rheological models. By rearranging and adding more springs and dashpots, many different types of behavior can be modeled, although the complexity of the wave equation solution increases dramatically as the number of springs and dashpots increases.

Example 5.5

A harmonic plane wave with a period of 0.3 sec travels through a viscoelastic material ($G = 1.6 \times 10^6$ psf, $\eta = 9000$ lb-sec/ft², $\gamma = 140$ pcf). Determine the distance over which the displacement amplitude of the plane wave would be halved.

Solution From equation (5.101), the displacement amplitude at $z = z_1$ is

$$u(z_1) = A \exp(k_2 z_1)$$

If $z = z_2$ represents the location at which the displacement amplitude is halved, then

$$u(z_2) = A \exp(k_2 z_2) = \frac{1}{2} A \exp(k_2 z_1)$$

which leads to

$$\exp[k_2(z_2 - z_1)] = \frac{1}{2}$$

or

$$z_2 - z_1 = \frac{\ln(1/2)}{k_2}$$

For this case

$$\xi = \frac{\eta\omega}{2G} = \frac{2\pi\eta}{2GT} = \frac{2\pi(9000 \text{ lb-sec/ft}^2)}{2(1.6 \times 10^6 \text{ lb/ft}^2)(0.3 \text{ sec})} = 0.059$$

Then, from equation (5.100)

$$k_2 = \sqrt{\frac{\frac{140 \text{ lb/ft}^2}{32.2 \text{ ft/sec}^2}(2\pi/0.3 \text{ sec})^2}{2(1.6 \times 10^6 \text{ lb/ft}^2)(1 + 4(0.059)^2)}}(\sqrt{1 + 4(0.059)^2} - 1) = -0.002$$

so

$$z_2 - z_1 = \frac{\ln(0.5)}{-0.002} = 347 \text{ ft}$$

5.5.2 Radiation Damping

Since material damping absorbs some of the elastic energy of a stress wave, the *specific energy* (elastic energy per unit volume) decreases as the wave travels through a material. The reduction of specific energy causes the amplitude of the stress wave to decrease with distance. The specific energy can also decrease by another common mechanism, which can be illustrated by the propagation of stress waves along an undamped conical rod.

Consider the unconstrained conical rod of small apex angle shown in Figure 5.23 and assume that it is subjected to stress waves of wavelength considerably larger than the diameter of the rod in the area of interest. If the apex angle is sufficiently small, the normal stress will be uniform across each of two spherical surfaces that bound an element of width dr , and will act in a direction virtually parallel to the axis of the rod. Letting u represent the displacement parallel to the axis of the rod, the equation of motion in that direction can be written, using exactly the same approach used in Section 5.2.1.1, as

$$\rho r^2 \alpha dr \frac{\partial^2 u}{\partial t^2} = \left(\sigma + \frac{\partial \sigma}{\partial r} dr \right) (r + dr)^2 \alpha - \sigma r^2 \alpha \quad (5.102)$$

which simplifies to

$$\rho r \frac{\partial^2 u}{\partial t^2} = r \frac{\partial \sigma}{\partial r} + 2\sigma \quad (5.103)$$

Substituting the stress-strain and strain-displacement relationships (assuming now that the ends of the element are planar) gives

$$\rho r \frac{\partial^2 u}{\partial t^2} = Er \frac{\partial^2 u}{\partial r^2} + 2E \frac{\partial u}{\partial r} \quad (5.104)$$

or

$$\frac{\partial^2 (ur)}{\partial t^2} = \frac{E \partial^2 (ur)}{\rho \partial r^2} \quad (5.105)$$

which is the now-familiar wave equation. Its solution will be of the form

$$u(r, t) = \frac{1}{r} [f(vt - r) + g(vt + r)] \quad (5.106)$$

where $v = \sqrt{E/\rho}$. Equation (5.106) indicates that the amplitude of the wave will decrease with distance (even though the total elastic energy remains the same). The reduction is of

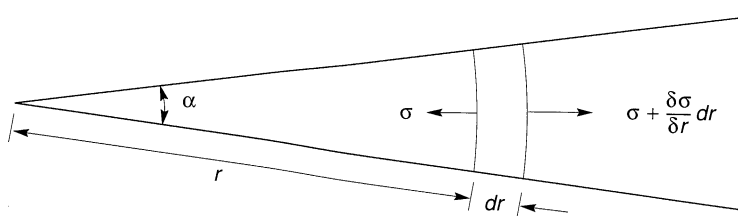


Figure 5.23 Conical rod of apex angle α .

purely geometric origin, resulting from the decrease in specific energy that occurs as the area of the rod increases.

Even though elastic energy is conserved (no conversion to other forms of energy takes place), this reduction in amplitude due to spreading of the energy over a greater volume of material is often referred to as *radiation damping* (also as *geometric damping* and *geometric attenuation*). It should be distinguished from material damping in which elastic energy is actually dissipated by viscous, hysteretic, or other mechanisms.

When earthquake energy is released from a fault below the ground surface, body waves travel away from the source in all directions. If the rupture zone can be represented as a point source, the wavefronts will be spherical and the preceding analysis can easily be extended to show that geometric attenuation causes the amplitude to decrease at a rate of $1/r$. It can also be shown (Bullen, 1953) that geometric attenuation of surface waves causes their amplitudes to decrease at a rate of essentially $1/(\sqrt{r})$; in other words, surface waves attenuate (geometrically) much more slowly than body waves. This explains the greater proportion of surface wave motion (relative to body wave motion) that is commonly observed at large epicentral distances. This explains the advantages of the surface wave magnitude, relative to body wave magnitude, for characterization of distant earthquakes.

For problems in which energy is released from a finite source, ranging from the large-scale case of rupture along an earthquake fault to the smaller-scale case of a vibrating foundation, radiation damping can be extremely important. In such cases the effects of radiation damping often dominate those of material damping.

5.6 SUMMARY

1. Only body waves can travel through an unbounded, homogeneous solid. There are two types of body waves: p- and s-waves. P-waves are irrotational, or dilatational, waves—they induce volumetric but not shearing deformations in the materials they travel through. The direction of particle movement caused by p-waves is parallel to the direction in which the wave is traveling. S-waves, also known as shear waves, involve shearing but not volumetric deformations. The passage of an s-wave causes particle movement perpendicular to the direction of wave travel.
2. Body waves travel at velocities that depend on the stiffness and density of the material they travel through. Because geologic materials are stiffer in volumetric compression than in shear, p-waves travel faster through them than do s-waves.
3. The interaction of inclined body waves with the stress-free surface of the earth produces surface waves. The motions produced by surface waves are concentrated in a shallow zone near the surface.
4. Rayleigh waves are the most important type of surface wave for earthquake engineering applications. In a homogeneous elastic half-space, Rayleigh waves would travel slightly more slowly than s-waves and would produce both vertical and horizontal particle motions that follow a retrograde elliptical pattern.
5. The depth to which Rayleigh waves induce significant motion is inversely proportional to the frequency of the wave. Low-frequency Rayleigh waves can produce particle motion at large depths, but the motions produced by high-frequency Rayleigh waves are confined to shallow depths.

6. When body wave velocities increase with depth, as they generally do in the earth's crust, Rayleigh wave velocities are frequency dependent. Low-frequency Rayleigh waves, which induce motion in deeper, stiffer materials, travel faster than high-frequency Rayleigh waves. Waves with frequency-dependent velocities are said to be dispersive.
7. Love waves are surface waves that can develop in the presence of a soft surficial layer. Love waves are dispersive—their velocities vary with frequency between the shear wave velocity of the surficial layer (at high frequencies) and the shear wave velocity of the underlying material (at low frequencies).
8. When a body wave strikes a rigid boundary oriented perpendicular to its direction of travel, the wave is perfectly reflected as an identical wave traveling back in the opposite direction. The zero-displacement boundary condition requires that the stress at the boundary be twice that of the wave away from the boundary. When a body wave strikes a stress-free boundary oriented perpendicular to its direction of travel, the wave is reflected as an identical wave of opposite polarity travelling back in the same direction. The zero-stress boundary condition requires that the particle motion at the boundary be twice as large as the particle motion away from the boundary.
9. When a body wave strikes a normal boundary between two different materials, part of the wave energy is reflected and part is transmitted across the boundary. The behavior of the wave at the boundary is governed by the ratio of the specific impedances of the materials on either side of the boundary. This impedance ratio determines the amplitudes and polarities of the reflected and transmitted waves.
10. When body waves strike boundaries between different materials at angles other than 90° , part of the wave energy is reflected and part is refracted as it crosses the boundary. If the direction of particle motion is parallel to the boundary, the reflected and refracted waves will be of the same form as the incident wave. If not, new types of waves can be created; for example, an inclined p-wave that strikes a horizontal boundary will produce reflected p- and SV-waves, and also refracted p- and SV-waves.
11. When an inclined wave travels upward through horizontal layers that become successively softer, the portion of the wave that crosses each layer boundary will be refracted closer and closer to a vertical direction.
12. The amplitude of a stress wave decreases as the wave travels through the earth's crust. There are two primary mechanisms that cause this attenuation of wave amplitude. The first, material damping, is due to absorption of energy by the materials the wave is traveling through. The second, radiation damping, results from the spreading of wave energy over a greater volume of material as it travels away from its source.

HOMWORK PROBLEMS

- 5.1 Determine the wave propagation velocity of a longitudinal wave in a constrained rod of: (a) steel, (b) cast iron, (c) concrete with $f'_c = 4,000$ psi.
- 5.2 Determine the wave propagation velocity of a torsional wave in a constrained rod of: (a) steel, (b) cast iron, (c) concrete with $f'_c = 4,000$ psi.
- 5.3 Derive an expression for the wave propagation velocity of a longitudinal wave in an unconstrained elastic rod with Young's modulus, E, Poisson's ratio, v, and density, ρ . Neglect the

effects of radial displacements in your derivation. How does this velocity compare with that of a longitudinal wave in a constrained rod?

- 5.4** A constrained steel rod is subjected to a harmonic axial stress at a frequency of 1 Hz.
- Determine the wavelength of the axial displacements along the rod.
 - Determine the phase angle between displacements measured at points on the rod located 1 ft, 10 ft, 100 ft, 1000 ft, and 10000 ft apart.
 - Repeat Part (a) for loading frequencies of 10 Hz, 100 Hz, 1 kHz, and 1 MHz.
- 5.5** A constrained steel rod is subjected to a harmonic torsional stress at a frequency of 1 Hz.
- Determine the wavelength of the angular rotations along the rod.
 - Determine the phase angle between rotations measured at points on the rod located 1 ft, 10 ft, 100 ft, 1000 ft, and 10000 ft apart.
 - Repeat Part (a) for loading frequencies of 10 Hz, 100 Hz, 1 kHz, and 1 MHz.
- 5.6** Determine the depth at which the vertical displacement amplitude of a Rayleigh wave is equal to one-half of the vertical displacement amplitude at the ground surface. For Rayleigh waves traveling through crystalline bedrock with a constant shear modulus of 57 ksi and specific gravity of 2.7, plot the variation of this depth with frequency for $f = 0.1$ Hz to $f = 20$ Hz.

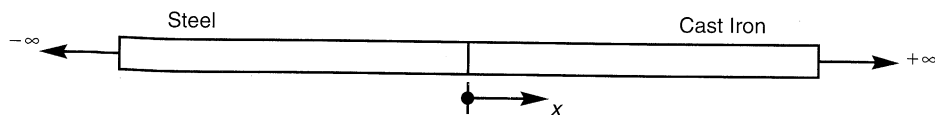


Figure P5.7

- 5.7** The infinite rod shown above is half steel and half cast iron. If a stress pulse of amplitude 100 psi (compression positive) and frequency 1000 Hz travels through the steel in the +x-direction, determine the displacement amplitude of the transmitted wave that travels through the cast iron.

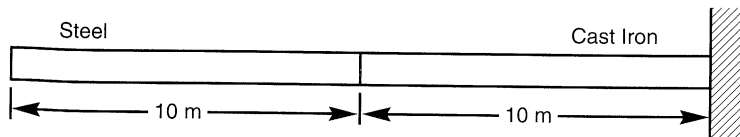


Figure P5.8

- 5.8** The finite rod shown above is subjected to an impact load that produces a rectangular axial stress pulse of amplitude 100 psi and duration 0.1 msec at its left end. The left end of the rod is free and the right end is fixed. Assuming that the impact began at $t = 0$, determine and plot the axial stress at the mid-point of the cast iron section from $t = 0$ to $t = 15$ msec.

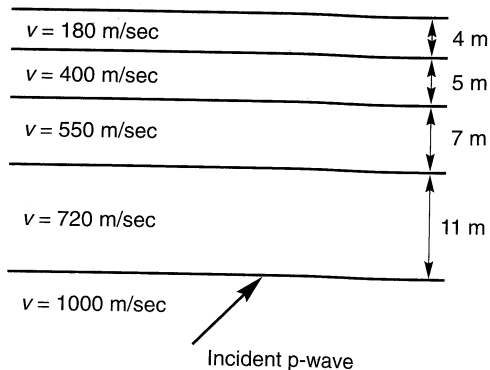


Figure P5.9

- 5.9** Consider the layered soil deposit shown above. Determine and plot the paths of the refracted and reflected rays if an incident raypath strikes the lowest boundary at a 45° angle. Show only the first reflection and refraction at each layer boundary.
- 5.10** Seismologists usually describe the effects of material damping by the quality factor. Quality factor values on the order of 300 and 500 are typically used for waves travelling through the earth's crust in western North America (WNA) and eastern North America (ENA), respectively. Why are higher quality factors used for ENA? What damping ratios do these quality factors correspond to?

6

Dynamic Soil Properties

6.1 INTRODUCTION

The nature and distribution of earthquake damage is strongly influenced by the response of soils to cyclic loading. This response is controlled in large part by the mechanical properties of the soil. Geotechnical earthquake engineering encompasses a wide range of problems involving many types of loading and many potential mechanisms of failure, and different soil properties influence the behavior of the soil for different problems. For many important problems, particularly those dominated by wave propagation effects, only low levels of strain are induced in the soil. For other important problems, such as those involving the stability of masses of soil, large strains are induced in the soil. The behavior of soils subjected to dynamic loading is governed by what have come to be popularly known as *dynamic soil properties*. While recognizing that the properties themselves are not dynamic (indeed, they apply to a host of nondynamic problems), that term will be used in this book because of its conciseness and familiarity.

Detailed treatment of every aspect of the behavior of cyclically loaded soils is beyond the scope of a book such as this. This chapter addresses the most important aspects of their behavior in the context of the various geotechnical earthquake engineering problems addressed in the following chapters. It presents a variety of methods by which low- and high-strain soil behavior can be measured in the field and in the laboratory. The behavior of cyclically loaded soils, and different approaches to its characterization, are also described.

6.2 REPRESENTATION OF STRESS CONDITIONS BY THE MOHR CIRCLE

The cyclic properties of soils depend on the state of stress in the soil prior to loading and on the stresses imposed by the loading. To discuss soil properties and their relationship to the various types of cyclic loading encountered in geotechnical earthquake engineering problems, the concepts and terminology used to describe stresses must be specified. Although such concepts are ordinarily presented early in a first course on soil mechanics, their importance in the understanding and solution of geotechnical earthquake engineering problems (particularly the liquefaction problems discussed in Chapter 9) is sufficient to warrant their repetition here.

The stress conditions at any point in a mass of soil can be described by the normal and shear stresses acting on a particular plane passing through that point. Because most normal stresses in soils are compressive (soils cannot, in general, resist tensile stresses), it is customary in geotechnical engineering to describe compressive stresses as positive. Consequently, positive shear stresses are those that tend to cause counterclockwise rotation of the body they act upon, and clockwise angles are positive. Figure 6.1 illustrates the sign conventions for normal and shear stresses; σ_x and σ_y are the normal stresses acting on planes normal to the x - and y -axes, respectively, τ_{xy} (and τ_{yx}) is the shear stress in the y -direction (x -direction) on the plane normal to the x -axis (y -axis), and σ_α and τ_α are the normal and shear stresses on the plane inclined at angle α . In structural mechanics, the opposite conventions are generally used.

The notation used to describe the foregoing stresses is different than that used to develop the equations of motion for three-dimensional wave propagation in Chapter 5. For that problem of solid mechanics, the standard notation of solid mechanics was used. For this chapter and the remainder of the book, the notation above, which is most commonly used in geotechnical engineering, is used. The equivalence of the two notations was discussed in Section 5.2.2.1.

It is often necessary to consider the stresses on several different planes that pass through a particular point. Equilibrium requirements can be used (e.g., Holtz and Kovacs, 1981) to express the normal and shear stresses on a plane inclined at an angle, α , to the x -axis as

$$\sigma_\alpha = \frac{\sigma_x + \sigma_y}{2} + \frac{\sigma_y - \sigma_x}{2} \cos 2\alpha - \tau_{xy} \sin 2\alpha \quad (6.1a)$$

$$\tau_\alpha = \frac{\sigma_x - \sigma_y}{2} \sin 2\alpha - \tau_{xy} \cos 2\alpha \quad (6.1b)$$

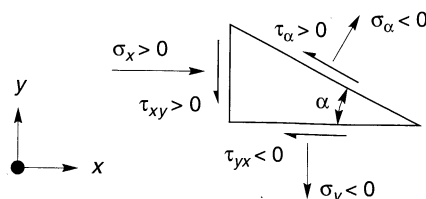


Figure 6.1 Sign conventions for normal and shear stresses.

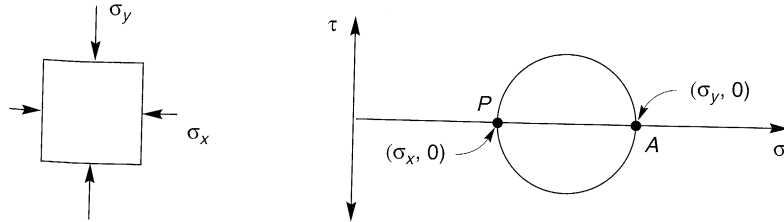


Figure 6.2 Mohr circle of stress for element subjected to major principal stress, σ_y , and minor principal stress, σ_x . Location of pole denoted by P .

Equations (6.1) describe a circle whose center is at $[\sigma = (\sigma_x + \sigma_y)/2, \tau = 0]$ and whose radius is $\sqrt{[(\sigma_y - \sigma_x)/2]^2 + \tau_{xy}^2}$. This circle, shown in Figure 6.2, is the well-known *Mohr circle of stress*. The Mohr circle simply illustrates the stress conditions acting on an element graphically and, as such, is very useful for understanding states of stress and stresses induced by external loading. It will be used often in the remainder of this book.

Equations (6.1) allow the stresses on planes of different inclination to be determined analytically, but they can also be determined graphically using the *pole* of the Mohr circle. The pole has a useful property: any line drawn through the pole will intersect the Mohr circle at a point that describes the shear and normal stresses on a plane parallel to that line. Consider the element shown in Figure 6.2 subjected to a vertical normal stress, σ_y , and a horizontal normal stress, σ_x . The shear stresses on the boundaries are zero. The stress conditions on the horizontal plane are known: $\sigma = \sigma_y$ and $\tau = 0$. Since the property of the pole states that a horizontal line drawn through it must intersect the Mohr circle at a point describing those stress conditions, a horizontal line drawn through the point describing those stress conditions will intersect the Mohr circle at the pole. For the case of Figure 6.2, the point of known stress conditions is point A and the plane for which the stress conditions are known is horizontal. Consequently, a horizontal line drawn through point A must intersect the Mohr circle at the pole, labeled as point P .

Example 6.1

Compute the normal and shear stresses on a plane passing through the element shown in Figure E6.1a and inclined at 45° clockwise from horizontal.

Solution The stresses on the horizontal plane are $\sigma = 4$ and $\tau = +1$. Drawing a horizontal line through this point reveals the location of the pole at point P . Note that the known stresses on the

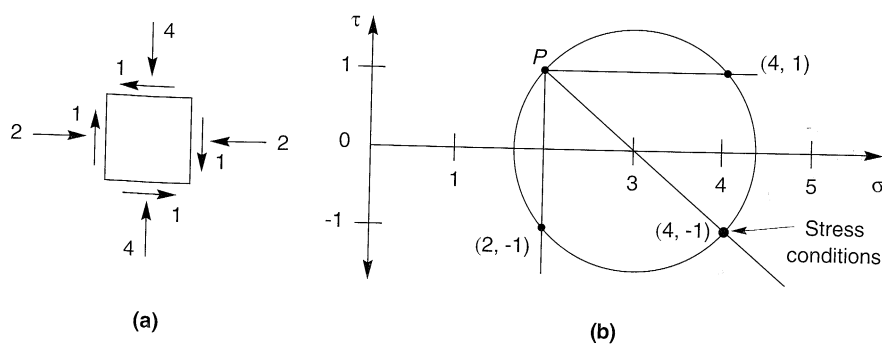


Figure E6.1

vertical plane, $\sigma = 2$ and $\tau = -1$, could just as easily have been used with a vertical line to determine the location of the pole. Once the pole has been identified, the stress conditions on any plane can be determined. Drawing a line through the pole parallel to the plane of interest (Figure E6.1b) shows that the stresses on that plane are $\sigma = 4$ and $\tau = -1$.

6.2.1 Principal Stresses

Two points on the Mohr circle are of particular interest. The points where the circle intersects the normal stress axis describe the normal stresses on planes where no shear stresses exist. Those planes are called *principal stress planes* and the normal stresses that act on them are called *principal stresses*. The *principal stress axes* are aligned in the directions of the principal stresses; therefore, they are perpendicular to the principal stress planes. The largest principal stress is the *major principal stress*, σ_1 , and the smallest is the *minor principal stress*, σ_3 . There is also an *intermediate principal stress*, σ_2 , that can take on any value between σ_1 and σ_3 ; a complete Mohr diagram would include σ_2 , as shown in Figure 6.3. Since the mechanical behavior of soils is much more sensitive to the relationship between σ_1 and σ_3 than to the value of σ_2 , and since σ_2 and σ_3 are often nearly equal, the value of σ_2 is usually not shown.

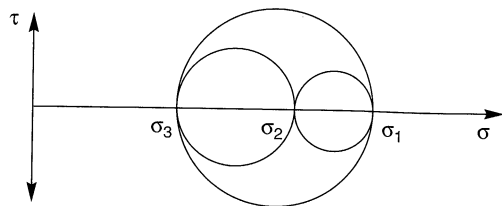


Figure 6.3 Mohr circles of stress including intermediate principal stress, σ_2 .

The pole can be used to determine the orientation of the principal stress planes. The fact that the angle between two lines passing through any point on a semicircle and the “corners” of the semicircle is 90° confirms that the major and minor principal stresses act perpendicular to each other (the intermediate principal stress acts mutually perpendicular to the major and minor principal stresses). Figure 6.4a shows the orientation of the principal stress axes on the element shown previously in Figure E6.1b. If the shear stress, τ_{xy} , is increased from 1 to 2

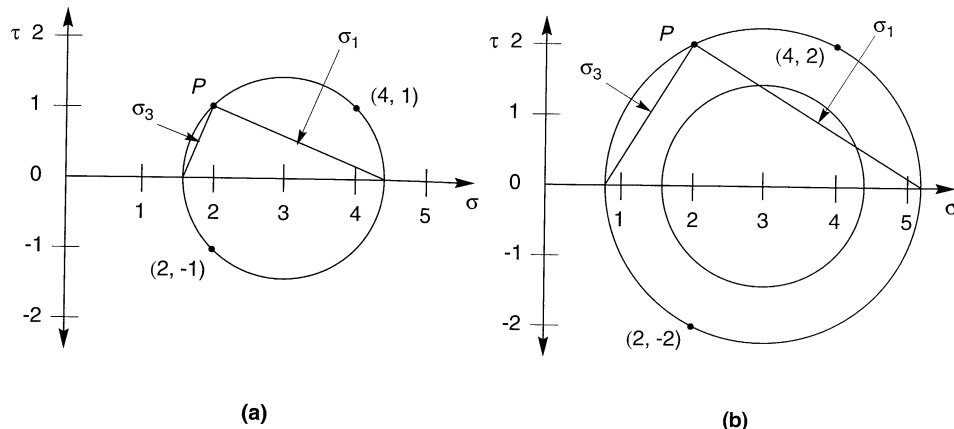


Figure 6.4 Orientation of principal stress axes for (a) $\tau_{xy} = 1$ and (b) $\tau_{xy} = 2$. Note the rotation of principal stress axes that accompanies the change in τ_{xy} .

with σ_x and σ_y held constant, the Mohr circle grows to the size shown in Figure 6.4b. Note that the increase in shear stress is accompanied by rotation of the principal stress axes.

6.2.2 Stress Paths

The variation in stress conditions acting on an element of soil can be tracked by plotting the Mohr circle at various stages in the loading sequence, but such a plot can quickly become difficult to decipher for many loading sequences. It is much simpler to observe the stress conditions by plotting the variation of the position of a single point on the Mohr circle. The *stress point* usually selected is the very top of the Mohr circle, as shown in Figure 6.5. The path taken by the stress point during loading is called the *stress path*. Since many properties of soil are dependent on the stress path induced by the applied loading, the stress path is a very useful tool in geotechnical engineering. [In a considerable body of geotechnical engineering literature, particularly that relating to the constitutive modelling of soils, the stress point is defined according to $p = (\sigma_1 + \sigma_2 + \sigma_3)/3$ and $q = \sigma_1 - \sigma_3$. Although each form has its own merits, they essentially present the same information; the form of Figure 6.5 is more commonly used in geotechnical earthquake engineering and will be used hereafter.]

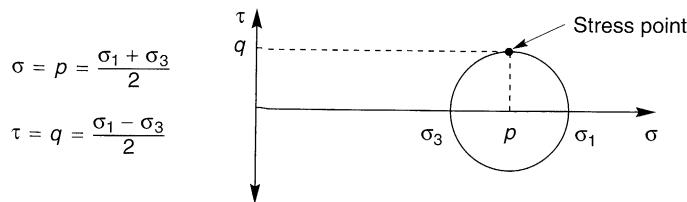


Figure 6.5 Location and definition of stress point on which stress path is based.

Stress paths can be expressed in terms of total or effective stresses. Since the effective stress is equal to the difference between the total stress and the pore pressure, the effective stress path is described by

$$p' = \frac{\sigma'_1 + \sigma'_3}{2} = \frac{(\sigma_1 - u) + (\sigma_3 - u)}{2} = \frac{\sigma_1 + \sigma_3}{2} - \frac{2u}{2} = p - u \quad (6.2a)$$

$$q' = \frac{\sigma'_1 - \sigma'_3}{2} = \frac{(\sigma_1 - u) - (\sigma_3 - u)}{2} = \frac{\sigma_1 - \sigma_3}{2} = q \quad (6.2b)$$

Total and effective stress paths are often plotted together; the horizontal distance between the two is equal to the pore pressure.

Many soil deposits are formed by sedimentation of soil particles through water. As more and more soil is deposited, consolidation causes the volume to decrease and the effective stresses to increase. If the process is one-dimensional (i.e., if the soil particles move only in the vertical direction), the minor principal stress will be proportional to the major principal stress and the effective stress path of an element of soil below the ground surface will move from A to B in Figure 6.6. The slope of the stress path in this range is given by

$$m_0 = \frac{dq}{dp'} = \frac{d\left(\frac{\sigma'_1 - \sigma'_3}{2}\right)}{d\left(\frac{\sigma'_1 + \sigma'_3}{2}\right)} = \frac{\sigma'_1 - \sigma'_3}{\sigma'_1 + \sigma'_3} = \frac{\sigma'_1(1 - K_0)}{\sigma'_1(1 + K_0)} = \frac{1 - K_0}{1 + K_0} \quad (6.3)$$

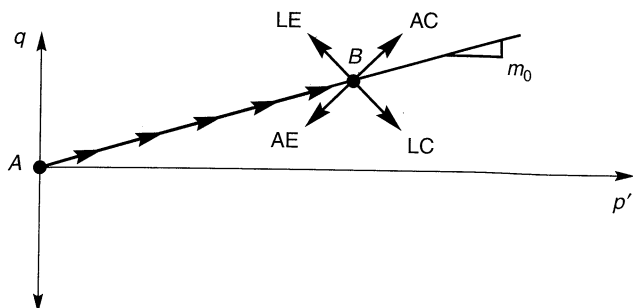


Figure 6.6 Effective stress paths for K_0 consolidation (A to B) and subsequent drained loading along axial compression (AC), axial extension (AE), lateral compression (LC), and lateral extension (LE) stress paths.

where $K_0 = \sigma'_3 / \sigma'_1$ is the *coefficient of lateral earth pressure at rest*. If the ground surface is level, the principal stress axes will be vertical and horizontal.

After the soil has consolidated, slow (drained) external loading can cause the stress path to move in a variety of directions. If the vertical stress increases while the horizontal stress remains constant (a condition often approximated by foundation loading), the stress path will move in the direction labeled AC in Figure 6.6. If the horizontal stress decreases with constant vertical stress (as in the development of *active earth pressure* conditions), the stress path moves in the direction LE. If the vertical stress is decreased with constant horizontal stress (as beneath an excavation), the stress path moves in the AE direction, and if the horizontal stress increases with constant vertical stress (*passive earth pressure* conditions), the stress path moves in the direction labeled LC. For each of these idealized conditions, no shear stresses are induced on vertical or horizontal planes; consequently, the principal stress axes remain vertical and horizontal (although they will instantaneously exchange positions if the p' -axis is crossed).

Most realistic loading conditions involve simultaneous changes in horizontal and vertical stresses and/or the development of shear stresses on horizontal and vertical planes. Consider an element of soil beneath a level ground surface (Figure 6.7a) subjected to vertically propagating s-waves. At stage A, the element is under at-rest conditions with the Mohr circle as indicated in Figure 6.7b and the stress path at point A in Figure 6.7c. Since the major principal stress is vertical, the pole of the Mohr circle is at the point $(\sigma'_h, 0)$ in Figure 6.7b. A vertically propagating shear wave will produce shear stresses on horizontal and vertical planes and distort the element as shown in stage B of Figure 6.7a. Since the shear stresses increase while the vertical and horizontal stresses remain constant, the radius of the Mohr circle increases but the center does not move (Figure 6.7b). The stress path (Figure 6.7c) moves vertically, as does the position of the pole (Figure 6.7b), which indicates that the principal stress axes are rotated from their initial vertical and horizontal positions. Since the horizontal shear stresses are cyclic in nature, their direction will reverse after going back through the $\tau_{hv} = \tau_{vh} = 0$ position in stage C. Note that the stress conditions at stage C are identical to those of stage A, and that the principal stress axes have rotated back to the vertical and horizontal positions. At stage D, the shear stresses act in the opposite direction and the principal stress axes rotate in the opposite direction as in stage B. Thus the loading induced by vertically propagating shear waves can be described by the stress path of Figure 6.7c and a principal stress axis rotation. Note that the stress path never indicates isotropic stress conditions (it never reaches the p' -axis) and that the principal stress axes rotate continuously.

The nature of principal stress axis rotation is significant. Research (e.g., Wong and Arthur, 1986; Symes et al., 1988; Sayao and Vaid, 1989) has shown that principal stress

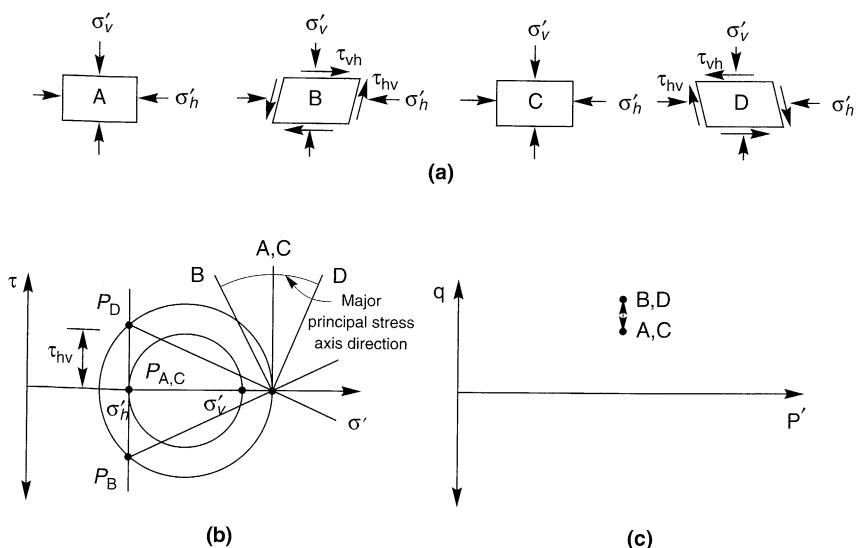


Figure 6.7 (a) Stress and strain conditions imposed on element of soil below level ground surface by vertically propagating shear waves at four different times; (b) Mohr circles, locations of poles, and orientations of major principal stress axis; (c) stress path.

rotation can cause shear and volumetric strain by itself (i.e., even if the stress point does not move). Hence some of the strain induced by vertically propagating shear waves results from principal stress rotation; this effect is not present in many field and laboratory tests.

Example 6.2

A reconstituted triaxial specimen of dry sand is consolidated isotropically to an effective confining pressure of 200 kPa, and then loaded in drained triaxial compression to a deviator stress ($\sigma_1 - \sigma_3$) of 200 kPa. At that point the specimen is subjected to a harmonic deviator stress that oscillates between 100 and 300 kPa. Plot the total and estimated effective stress paths.

Solution Because the sand is dry, no pore pressures exist, so the total and effective stresses are equal. During preparation, the stresses acting on the specimen are very small, so the stress path is at point A in Figure E6.2. Isotropic consolidation takes the stress path to point B, and drained triaxial compression takes it to point C. Harmonic loading then causes the stress path to oscillate between points D and E.

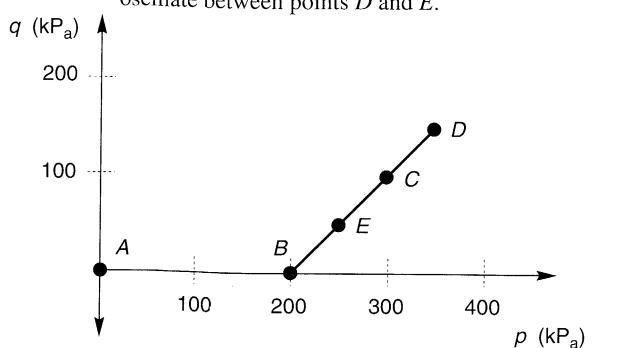


Figure E6.2

6.3 MEASUREMENT OF DYNAMIC SOIL PROPERTIES

The measurement of dynamic soil properties is a critical task in the solution of geotechnical earthquake engineering problems. A wide variety of field and laboratory techniques are available, each with different advantages and limitations with respect to different problems. Many are oriented toward measurement of low-strain properties and many others toward properties mobilized at larger strains. The selection of testing techniques for measurement of dynamic soil properties requires careful consideration and understanding of the specific problem at hand. Efforts should always be made to use tests or test procedures that replicate the initial stress conditions and the anticipated cyclic loading conditions as closely as possible.

Soil properties that influence wave propagation and other low-strain phenomena include stiffness, damping, Poisson's ratio, and density. Of these, stiffness and damping are the most important; the others have less influence and tend to fall within relatively narrow ranges. The stiffness and damping characteristics of cyclically loaded soils are critical to the evaluation of many geotechnical earthquake engineering problems—not only at low strains but because soils are nonlinear materials, also at intermediate and high strains. At high levels of strain, the influence of the rate and number of cycles of loading on shear strength may also be important. Volume change characteristics are also important at high strain levels.

The measurement of these important soil properties in field and laboratory tests is presented in the following sections. Many of the tests have been developed specifically to measure dynamic soil properties; others are modified versions of tests commonly used to measure soil behavior under monotonic loading conditions. The applicability of the various tests to dynamic soil properties is emphasized here—descriptions of their applications to static properties may be found in standard geotechnical engineering texts (e.g., Lambe and Whitman, 1969; Holtz and Kovacs, 1981).

Any investigation of dynamic soil properties should be performed with due recognition of the inevitable uncertainty in measured properties. Sources of uncertainty include the inherent variability of soils (a result of the geologic environment in which they were deposited), inherent anisotropy (a function of the soil structure or “fabric”), induced anisotropy (caused by anisotropic stress conditions), drilling and sampling disturbance, limitations of field and/or laboratory testing equipment, testing errors, and interpretation errors. Some of these sources of uncertainty can be minimized by careful attention to test details, but others cannot.

6.3.1 Field Tests

Field tests allow the properties of the soil to be measured *in situ* (i.e., in their existing state where the complex effects of existing stress, chemical, thermal, and structural conditions are reflected in the measured properties). The measurement of dynamic soil properties by field tests has a number of advantages. Field tests do not require sampling, which can alter the stress, chemical, thermal, and structural conditions in soil specimens. Many field tests measure the response of relatively large volumes of soil, thereby minimizing the potential for basing property evaluation upon small, unrepresentative specimens. Many field tests induce soil deformations that are similar to those of the problem of interest, particularly for wave propagation and foundation design problems. On the other hand, field tests do not allow the effects of conditions other than the *in situ* conditions to be investigated easily, nor do they

allow porewater drainage to be controlled. In many field tests, the specific soil property of interest is not measured but must be determined indirectly, by theoretical analysis or empirical correlation.

Some field tests can be performed from the ground surface, while others require the drilling of boreholes or the advancement of a probe into the soil. Surface tests are often less expensive and can be performed relatively quickly. They are particularly useful for materials in which drilling and sampling or penetration is difficult. Borehole tests, on the other hand, have the advantage of the information gained directly from the boring: visual and laboratory-determined soil characteristics, water table location, and so on. Also, the interpretation of borehole tests is usually more direct than that of surface tests.

6.3.1.1 Low-Strain Tests

Low-strain tests generally operate at strain levels that are not large enough to induce significant nonlinear stress-strain behavior in the soil, typically at shear strains below about 0.001%. As such, most are based on the theory of wave propagation in linear materials. Many involve the measurement of body wave velocities which can easily be related to low-strain soil moduli. Others involve the development of standing waves, whose measured frequencies and/or wavelengths can be used to compute low-strain moduli.

Seismic geophysical tests represent an important class of field tests for determination of dynamic soil properties. Seismic tests involve the creation of transient and/or steady-state stress waves and the interpretation of their behavior from measurements made at one or more different locations. In many seismic tests, a source produces a “pulse” of waves whose times of arrival are measured at distant receivers. The source, which may range from a sledgehammer blow to the ground surface to a buried explosive charge, will generally produce p-waves, s-waves, and surface waves. The relative amplitudes of each depend on how the impulse is generated. Explosive sources and vertical impact sources (Figure 6.8a and b) are rich in p-wave content. SH-waves are produced most efficiently by striking the end of a beam pressed tightly against the ground surface (Figure 6.8c).

Since p-waves travel fastest, their arrivals at distant receivers are most easily detected and their arrival times most easily measured. S-wave resolution can be improved markedly by reversing the polarity of the impulse, as is easily accomplished for SH-waves by striking the other end of the beam of Figure 6.8c. Since the polarity of the train of p-waves is not reversed, subtracting the reversed record from the original record will diminish the p-wave amplitudes while enhancing the s-wave amplitudes. Wave arrivals can also be enhanced by adding, or “stacking,” records from multiple impulses; the random noise portions of the records tend to cancel each other while the actual waves are reinforced.

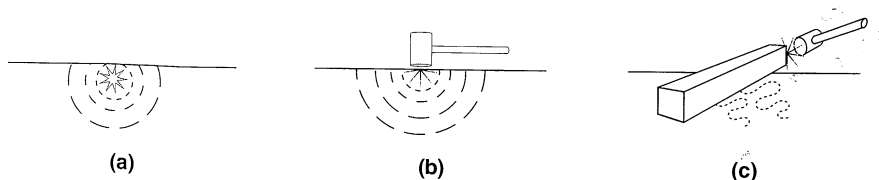


Figure 6.8 Different methods for creation of impulsive disturbances for seismic geophysical tests: (a) shallow explosives; (b) vertical impact; (c) horizontal impact.

Careful consideration of groundwater conditions is essential for proper interpretation of seismic geophysical test measurements. P-waves travel through groundwater at about 5000 ft/sec, depending on temperature and salinity. Soft, saturated soils may propagate p-waves at these high velocities even though the velocity is not indicative of the stiffness of the soil skeleton. Failure to consider groundwater effects can result in significant overestimation of soil stiffness. The groundwater problem can largely be avoided by using s-waves which are propagated by the soil skeleton and not the groundwater.

Seismic Reflection Test. The seismic reflection test allows the wave propagation velocity and thickness of surficial layers to be determined from the ground surface or in offshore environments. The test and its interpretation are conceptually very simple. The reflection test is most useful for investigation of large-scale and/or very deep stratigraphy. It is rarely used for delineation of shallow soil layers.

For the simple profile shown in Figure 6.9a, the test is performed by producing an impulse (usually rich in p-waves) at the source, S , and measuring the arrival time at the receiver, R . The impulse produces stress waves that radiate away from the source in all directions with a hemispherical wavefront. Some of the wave energy follows a direct path from S to R and arrives at R at

$$t_d = \frac{\text{distance of travel}}{\text{wave velocity}} = \frac{x}{v_{p1}} \quad (6.4)$$

By measuring x and t_d , the p-wave velocity of the upper layer, v_{p1} , can easily be determined. Another portion of the impulse energy travels downward and strikes the horizontal layer boundary at an angle of incidence

$$i = \tan^{-1} \frac{x}{2H} \quad (6.5)$$

The part of that wave that is reflected back toward the ground surface arrives at the receiver at

$$t_r = \frac{\text{distance of travel}}{\text{wave velocity}} = \frac{2\sqrt{H^2 + (x/2)^2}}{v_{p1}} = \frac{\sqrt{4H^2 + x^2}}{v_{p1}} \quad (6.6)$$

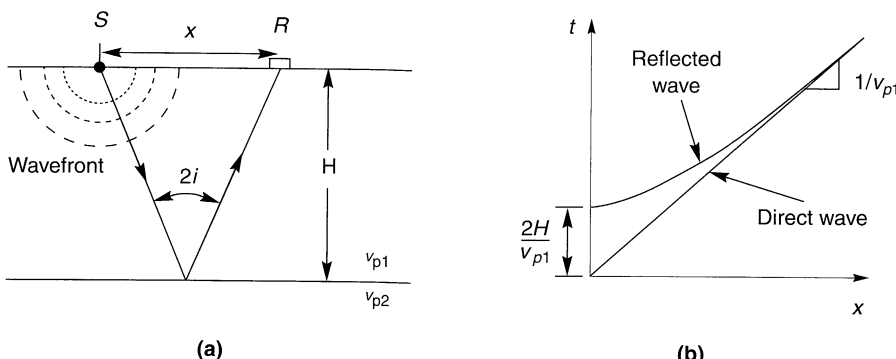


Figure 6.9 (a) Ray path for incident and reflected p-wave from horizontal layer boundary; (b) variation of travel time for direct and reflected waves. Difficulty in resolution increases with increasing source-receiver separation.

By measuring t_r and knowing x and v_{p1} from the direct wave calculation, the thickness of the upper layer can be calculated as

$$H = \frac{1}{2} \sqrt{t_r^2 v_{p1}^2 - x^2} \quad (6.7)$$

Figure 6.9b shows how the arrival times for the direct and reflected waves are related; the difference in arrival times decreases with increasing distance. When, as is usually the case, actual conditions differ from the simple assumptions of horizontal layering above, multiple measurements must be made. In the case of the inclined layer boundary shown in Figure 6.10, for example, travel-time measurements at receivers A and B can be used to determine the angle of inclination as

$$\sin \alpha = \frac{v_{p1}^2 (t_{RA} + t_{RB})(t_{RB} - t_{RA})}{4z_\alpha(x_B - x_A)} - \frac{x_A + x_B}{4z_\alpha} \quad (6.8)$$

where $v_{p1} = x_A/t_{dA} = x_B/t_{dB}$ and t_{dA} and t_{dB} are the direct wave arrival times at receivers A and B, respectively. If receiver A is placed at the source ($x_A = 0$), then

$$z_\alpha = \frac{t_{RA} v_{p1}}{2} \quad (6.9)$$

$$\sin \alpha = \frac{v_{p1}^2 (t_{RA} + t_{RB})(t_{RB} - t_{RA}) - x_B^2}{2t_{RA} v_{p1} x_B} \quad (6.10)$$

The characteristics of deeper layers may be evaluated using reflections from deeper interfaces (Griffiths and King, 1965; Ewing et al., 1957; Kleyn, 1983). The method is limited, however, by the difficulty associated with determining the arrival time of the reflected waves, particularly for cases in which reflected waves arrive while the receivers are still responding to direct waves. Interpretation of results for profiles with low-velocity layers may also be difficult.

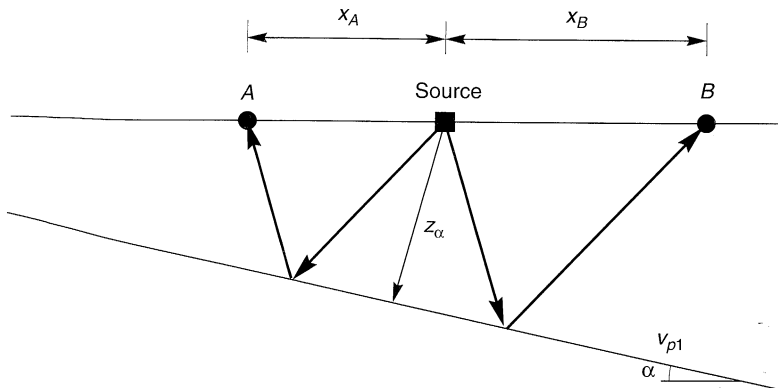


Figure 6.10 Source and receiver layout for reflection test with inclined layer boundary.

Example 6.3

A loose deposit of overconsolidated clay is underlain by bedrock. Previous subsurface investigations in the area suggest that the bedrock surface is nearly horizontal. A seismic reflection

survey shows the arrival of distinct p-waves at a geophone 38 msec and 200 msec after an impulsive load is applied at a point 20 m from the geophone. Determine the thickness and the p-wave velocity of the clay deposit.

Solution Assuming that the first p-wave arrival is caused by the direct p-wave, the p-wave velocity is given by

$$v_{p1} = \frac{x}{t_d} = \frac{20 \text{ m}}{0.038 \text{ sec}} = 526 \text{ m/sec}$$

If the second p-wave is due to the reflected wave, the thickness of the deposit is given by

$$H = \frac{1}{2} \sqrt{t_R^2 v_{p1}^2 - x^2} = \frac{1}{2} \sqrt{(0.200 \text{ sec})^2 (526 \text{ m/sec})^2 - (20 \text{ m})^2} = 51.6 \text{ m}$$

Seismic Refraction Test. The seismic refraction test eliminates the most important limitation of the seismic reflection test by using the arrival times of the first waves, regardless of path, to reach a given receiver. The test involves measurement of the travel times of p- and/or s-waves from an impulse source to a linear array of points along the ground surface at different distances from the source. Although the seismic refraction test is more commonly used than the seismic reflection test, its greatest earthquake engineering application is also for delineation of major stratigraphic units.

A typical test setup is shown in Figure 6.11. An impulsive energy source, which can be mechanical or explosive, is located at or near the ground surface. A series of receivers, usually geophones, are placed in a linear array. One receiver is located at the source. The output of all of the receivers is recorded when the impulse load is triggered. From these recordings the arrival times of the first waves to reach each receiver can be determined and

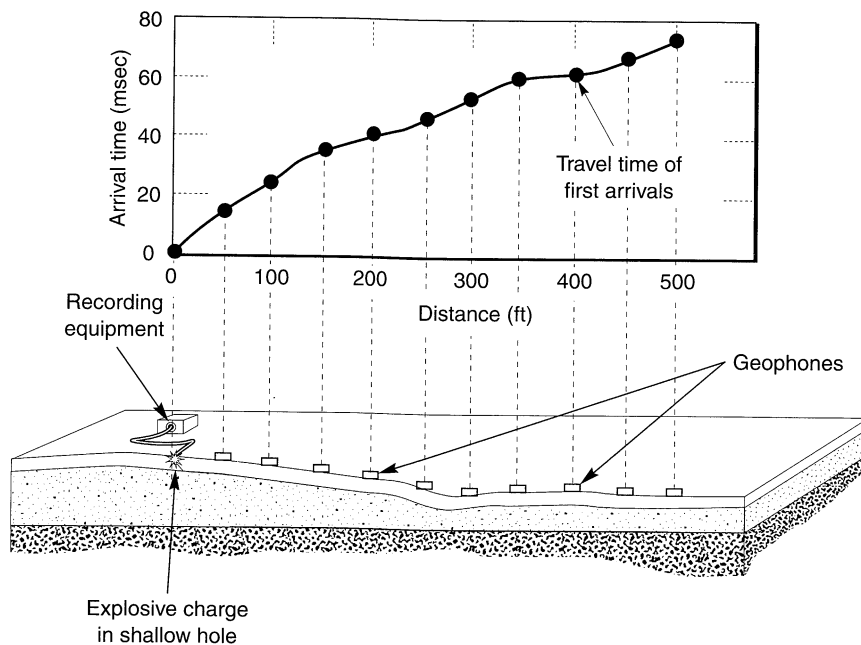


Figure 6.11 Seismic refraction test setup. (After Redpath, 1973.)

plotted as a function of source-receiver distance, as shown in Figure 6.11. If the receivers were all excited by a single stress wave traveling along the ground surface at constant velocity, v (the test can be performed and interpreted with p- or s-waves, so v could be v_p or v_s), the arrival time-distance plot would be a straight line of slope $1/v$ that passed through the origin. Figure 6.11 shows that this is clearly not the case—a different, more complicated mechanism is at work.

Horizontal Layering. Assume that the seismic refraction test is being conducted on the surface of a two-layered elastic half-space as shown in Figure 6.13. The impulse produces stress waves that travel away from the source in all directions with a hemispherical wavefront. Some of the energy travels directly from the source to the receivers in the form of a *direct wave*, arriving at the n th receiver at a travel time

$$t_{dn} = \frac{x_n}{v_1} \quad (6.11)$$

where v_1 is the wave propagation velocity of material 1. Other rays travel downward toward the boundary between materials 1 and 2. At that boundary, these rays are reflected and refracted, with the directions of the refracted rays determined by Snell's law (Section 5.4.2). At the critical angle of incidence, i_c , the refracted ray will travel parallel to the boundary. According to Huygens' principle (which says that any point on a wavefront acts as the source of a new disturbance) and Snell's law, this critically refracted wave will produce a *head wave* in material 1 that will travel at v_1 in a direction inclined at $(90^\circ - i_c)$ to the boundary. The resulting wavefront can have a portion controlled by the direct wave and a portion controlled by the head wave, as illustrated in Figure 6.12. Note that the direct wave produces the first wave arrival at short source-receiver distances, but the head wave arrives before the direct wave at distances greater than the *critical distance*, x_c .

At distances greater than x_c , a ray that travels downward at velocity v_1 through material 1, is critically refracted to travel in material 2 at velocity v_2 and is then critically refracted back up through material 1 at velocity, v_1 will reach a receiver faster than a ray that travels along the shorter direct path at velocity v_1 . The travel time required for the head wave to reach the n th receiver (Figure 6.13) can be written as

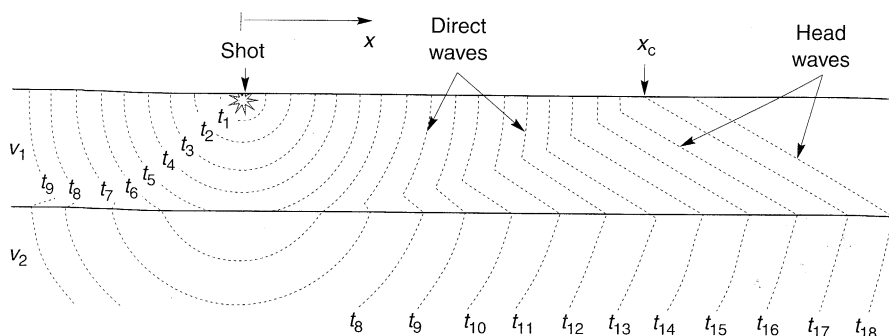


Figure 6.12 Wavefronts for first-arriving waves in a seismic refraction survey. Note that first arrivals near the source are from direct waves but, at distances greater than the critical distance, x_c , the first arrivals are from head waves. (After Corps of Engineers, 1979.)

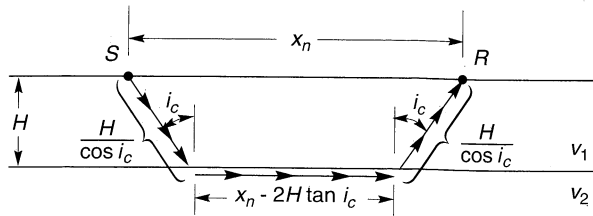


Figure 6.13 Travel path for first arrival when $x_n > x_c$.

$$t_{hn} = \frac{H}{v_1 \cos i_c} + \frac{x_n - 2H \tan i_c}{v_2} + \frac{H}{v_1 \cos i_c} \quad (6.12)$$

Substituting the result of Snell's law for critical incidence, $\sin i_c = v_1/v_2$, and the trigonometric identity $\cos^2 i_c = 1 - \sin^2 i_c$, and rearranging yields

$$t_{hn} = \frac{x_n}{v_2} + 2H \sqrt{\frac{1}{v_1^2} - \frac{1}{v_2^2}} \quad (6.13)$$

If a receiver was placed exactly at the critical distance, x_c , the direct wave and the head wave would reach it at exactly the same time (i.e., $t_{dn} = t_{hn}$). Consequently, from equations (6.11) and (6.13),

$$\frac{x_c}{v_1} = \frac{x_c}{v_2} + 2H \sqrt{\frac{1}{v_1^2} - \frac{1}{v_2^2}} \quad (6.14)$$

from which

$$H = \frac{x_c}{2} \sqrt{\frac{v_2 - v_1}{v_2 + v_1}} \quad (6.15)$$

Therefore, the travel time-distance diagram allows three important characteristics of the subsurface conditions, namely v_1 , v_2 , and H , to be obtained.

For the case of multiple horizontal layers, the travel time-distance diagram will exhibit more than one break in slope, as illustrated in Figure 6.14. The distances corresponding to these slope breaks can be used, along with the slopes themselves, to determine the thicknesses of deeper layers. The thickness of the k th layer, for example, would be given by (Corps of Engineers, 1979)

$$H_k = \frac{x_{ck}}{2} \sqrt{\frac{v_{k+1} - v_k}{v_{k+1} + v_k}} + \sum_{j=1}^{k-1} \frac{H_j}{v_j} \frac{v_{k+1} \sqrt{v_k^2 - v_j^2} - v_k \sqrt{v_{k+1}^2 - v_j^2}}{\sqrt{v_{k+1}^2 - v_k^2}} \quad (k \geq 2) \quad (6.16)$$

In the preceding paragraphs, it has been explicitly assumed that the velocity of each layer is smaller than the layer immediately below it. For many geologic conditions this is a good assumption, but when it is not, the results of a seismic refraction test can be misleading. A low-velocity layer underlying a higher-velocity layer (i.e., a *velocity reversal*) will not appear as an individual segment on the travel time-distance diagram. Instead, it will cause the computed depths of the layer boundaries to be greater than the actual depths (Redpath, 1973). Also, *blind zones*, where a subsurface layer exists but is not indicated by the travel time-distance diagram, can be caused by insufficient layer thickness or insufficient velocity

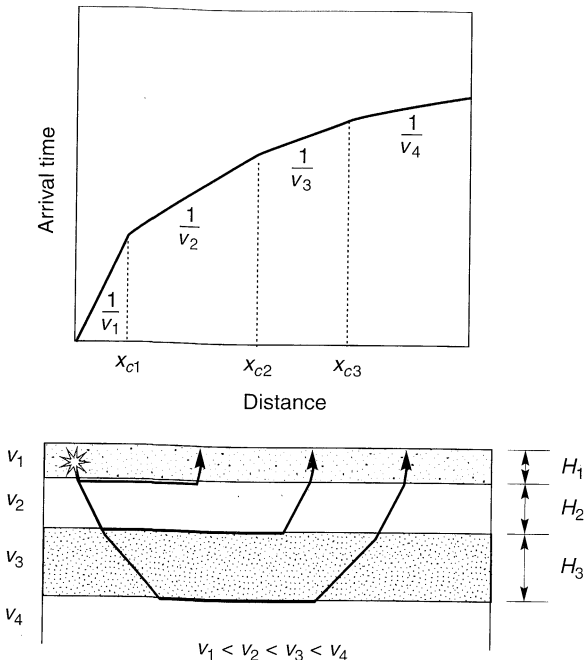


Figure 6.14 Travel time–distance diagram for multiple horizontal layers.
(After Redpath, 1973.)

contrast (Soske, 1959). In such cases the head wave from a deeper layer can overtake the head wave of an intermediate layer before it reaches the ground surface. The undetected existence of a blind zone will cause the computed depth of the deeper layer to be less than the actual depth (Redpath, 1973). In cases where the velocity increases continuously with depth (e.g., sands, gravels, normally consolidated clays), ray paths will be curved rather than straight, as previously assumed. For the case where velocity is proportional to depth (Figure 6.15), the ray paths will become circular arcs. The resulting time–distance curves can be transformed into curves of velocity versus depth (Redpath, 1973; Corps of Engineers, 1979).

Inclined or Irregular Layering. When the boundaries between layers are not parallel, the travel time–distance diagram will not yield the true velocities of all layers directly since the apparent velocity (the distance between adjacent receivers divided by the difference in their arrival times) is influenced by the slope of the layer boundaries and the critical angles of incidence. Referring to Figure 6.16, the apparent velocity from a seismic refraction test in the down-dip direction, v_{2D} , is lower than the apparent velocity, v_{2U} , from an identical test in the up-dip direction. From Snell's law,

$$\sin(i_c + \alpha) = \frac{v_1}{v_{2D}} \quad (6.17a)$$

$$\sin(i_c - \alpha) = \frac{v_1}{v_{2U}} \quad (6.17b)$$

which can be rearranged to produce the *apparent dip angle* (the dip angle in the vertical plane of the array of receivers)

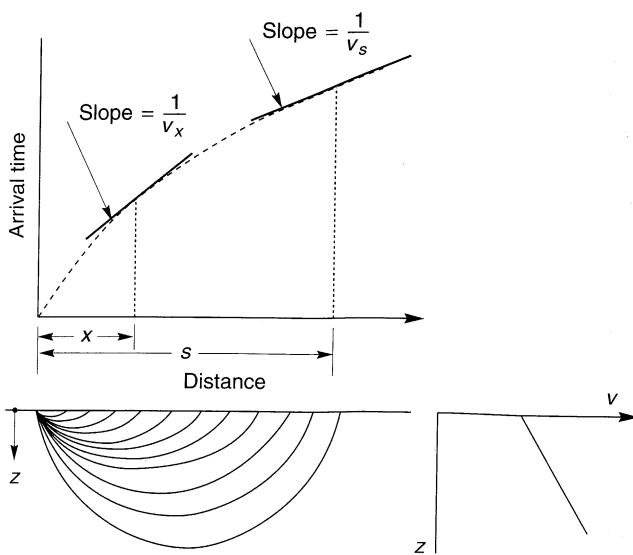


Figure 6.15 Ray paths and travel time-distance diagram for a single layer with linearly increasing velocity. (After Redpath, 1973.)

$$\alpha = \frac{1}{2} \left(\sin^{-1} \frac{v_1}{v_{2U}} - \sin^{-1} \frac{v_1}{v_{2D}} \right) \quad (6.18)$$

The apparent dip angle is equal to the true dip angle only when the dip vector lies within the plane of the receiver array. In other cases, another survey utilizing a nonparallel array of receivers is required to determine the true dip (Richart et al., 1970). The thickness of the upper layer, measured perpendicular to the layer boundary at each shot point, can be computed as

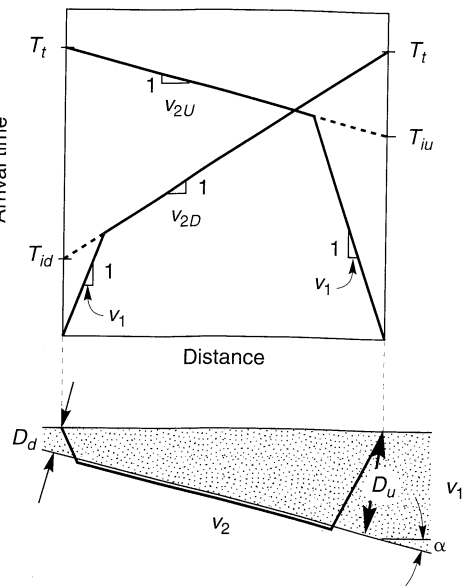


Figure 6.16 Reverse profiling used to identify irregular or sloping interfaces. Concept of apparent velocity in underlying layer is also illustrated. (After Redpath, 1973.)

$$D_d = \frac{v_1 T_{id}}{2 \cos \alpha} \quad (6.19a)$$

$$D_u = \frac{v_1 T_{iu}}{2 \cos \alpha} \quad (6.19b)$$

The true value of v_2 is given by

$$v_2 = \frac{2v_2 D v_2 U}{v_2 D + v_2 U} \cos \alpha \quad (6.20)$$

The preceding discussion illustrates the importance of reverse profiling for cases of inclined layering. Since the nature of the layering is not often known in advance, as well as to provide additional data, reverse profiling is routinely performed.

Example 6.4

A seismic refraction survey with reverse profiling between two shot points located 120 m apart shows the p-wave arrival times listed below. Determine the thickness of the surficial layer of soil.

Geophone	Distance from Shot Point A (m)	p-Wave Arrival Time (msec)	Distance from Shot Point B (m)	p-Wave Arrival Time (msec)
A	0	0	120	88
B	5	11	100	78
C	10	26	80	67
D	20	49	60	58
E	40	65	40	47
F	60	71	20	37
G	80	76	10	26
H	100	83	5	12
I	120	88	0	0

Solution The arrival time-distance diagrams for the forward and reverse profiles are plotted in Figure E6.4.

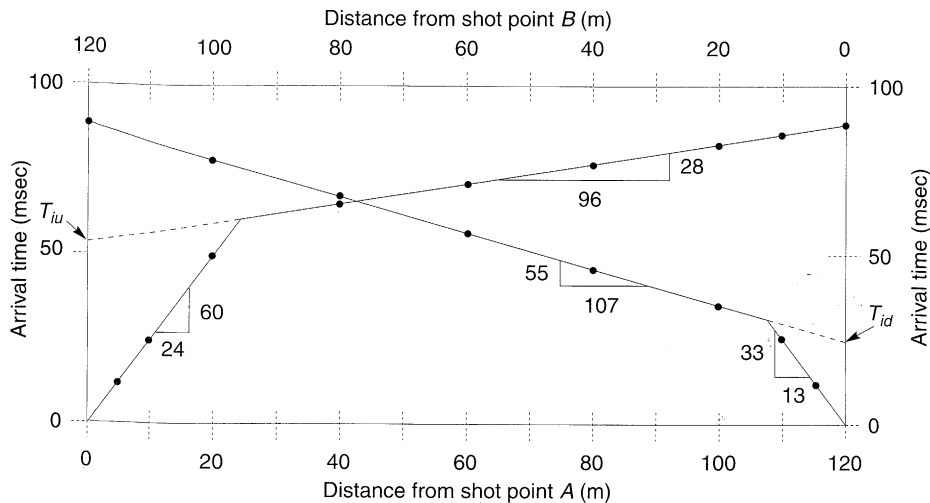


Figure E6.4

From the initial slopes of the travel-time diagrams, the average p-wave velocity of the surficial layer is given by

$$v_1 = \frac{1}{2} \left(\frac{24 \text{ m}}{0.060 \text{ sec}} + \frac{13 \text{ m}}{0.033 \text{ sec}} \right) = 397 \text{ m/sec}$$

The apparent velocities in the down-dip and up-dip directions are

$$v_{2D} = \frac{107 \text{ m}}{0.055 \text{ sec}} = 1945 \text{ m/sec}$$

$$v_{2U} = \frac{96 \text{ m}}{0.028 \text{ sec}} = 3429 \text{ m/sec}$$

The apparent dip angle can then be computed as

$$\alpha = \frac{1}{2} \left(\sin^{-1} \frac{v_1}{v_{2D}} - \sin^{-1} \frac{v_1}{v_{2U}} \right) = \frac{1}{2} \left(\sin^{-1} \frac{397}{1945} - \sin^{-1} \frac{397}{3429} \right) = 2.56^\circ$$

Then the depths of the layer boundary, measured perpendicular to the boundary, at shot points A and B are

$$D_A = \frac{v_1 T_{id}}{2 \cos \alpha} = \frac{(397 \text{ m/sec})(0.029 \text{ sec})}{2 \cos 2.56^\circ} = 5.8 \text{ m}$$

$$D_B = \frac{v_1 T_{iu}}{2 \cos \alpha} = \frac{(397 \text{ m/sec})(0.053 \text{ sec})}{2 \cos 2.56^\circ} = 10.5 \text{ m}$$

A more general procedure can be developed to interpret the results of tests on soil profiles with layers of variable thickness. Consider the site of Figure 6.17, where waves from the two sources SP₁ and SP₂ reach a receiver at point D at arrival times T_{D1} and T_{D2} , respectively. The total time [i.e., the total travel time from the location of SP₁ to that of SP₂ (and vice versa)], is given by

$$T_t = \frac{AB}{v_1} + \frac{BCEF}{v_2} + \frac{FG}{v_1} = \frac{z_1}{v_1 \cos i_c} + \frac{s - z_1 \tan i_c - z_2 \tan i_c}{v_2} + \frac{z_2}{v_1 \cos i_c} \quad (6.21)$$

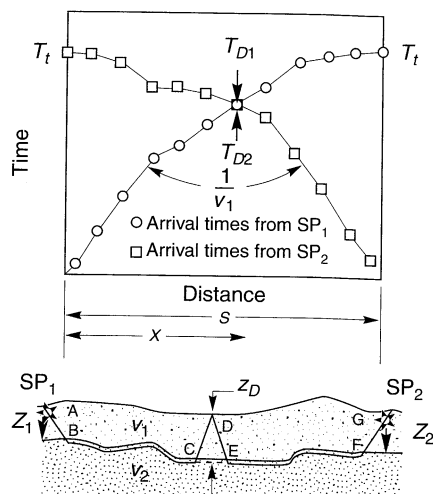


Figure 6.17 Forward and reverse profiles for layer of irregular thickness. (After Corps of Engineers, 1979.)

where z_1 and z_2 are the vertical thicknesses of the surficial layer at SP₁ and SP₂, respectively. The arrival times at point D are given by

$$T_{D1} = \frac{AB}{v_1} + \frac{BC}{v_2} + \frac{CD}{v_1} = \frac{z_1}{v_1 \cos i_c} + \frac{x_D - z_1 \tan i_c - z_D \tan i_c}{v_2} + \frac{z_D}{v_1 \cos i_c} \quad (6.22)$$

$$T_{D2} = \frac{FG}{v_1} + \frac{EF}{v_2} + \frac{DE}{v_1} = \frac{z_2}{v_1 \cos i_c} + \frac{(s - x_D) - z_2 \tan i_c - z_D \tan i_c}{v_2} + \frac{z_D}{v_1 \cos i_c} \quad (6.23)$$

The velocity of the lower layer, v_2 , is inversely proportional to the difference between the arrival times from the forward and reverse profiles (i.e., a plot of arrival time difference versus distance has a slope of $2/v_2$). Combining equations (6.21) through (6.23) and substituting $v_2 = v_1/\sin i_c$ yields

$$T_{D1} + T_{D2} - T_t = \frac{2z_D}{v_1} \frac{1 - \sin^2 i_c}{\cos i_c} \quad (6.24)$$

Therefore

$$z_D = \frac{1}{2} \frac{(T_{D1} + T_{D2} - T_t)v_1}{\cos i_c} \quad (6.25)$$

By moving the receiver (point D) to different locations (or using multiple geophones), the variation of surficial layer thickness between SP₁ and SP₂ can be determined. Implicit in the preceding derivation is the assumption that the first arrivals at D are from head waves from the same layer rather than from direct waves. Long arrays may be required to ensure the validity of this assumption over distances of interest.

Suspension Logging Test. Suspension logging, although commonly used in petroleum exploration, has only recently been applied to geotechnical earthquake engineering problems. A probe 5 to 6 m (15 to 20 ft) long is lowered into an uncased borehole filled with water or drilling fluid. A horizontal reversible-polarity solenoid located near the base of the probe produces a sharp, impulsive pressure wave in the drilling fluid. Upon reaching the borehole wall, the pressure wave produces both p- and s-waves in the surrounding soil. These waves travel through the soil and eventually transmit energy back through the drilling fluid to two biaxial geophones located about 1 m (3 ft) apart near the top of the probe. To enhance identification of p- and s-wave arrivals, the procedure is repeated with an impulse of opposite polarity. Differences in arrival times are used to compute the average p- and s-wave velocities of the soil between the geophones. The suspension test allows measurement of wave propagation velocities in a single, uncased borehole, but the frequencies of the waves (500 to 2,000 Hz for s-waves and 1000 to 3000 Hz for p-waves) are much higher than those of interest in geotechnical earthquake engineering.

Because the solenoid travels with the geophones down the borehole, the amplitude of the signals is relatively constant at all depths. As a result, the suspension logging test is effective at great depths—up to 2 km (Nigbor and Imai, 1994). By overlapping measurement points, resolutions of less than 1 m (3.1 ft) can be obtained. This capability is particularly useful at sites that may have thin layers of soft or weak soil. The presence of tube waves may limit the effectiveness of the suspension logging test in cased boreholes.

Steady-State Vibration (Rayleigh Wave) Test. The problem of detecting wave arrivals and measuring arrival times is eliminated in tests that interpret properties from the characteristics of steady-state vibrations. The displacements along the ground surface adjacent to a vertically vibrating circular footing are caused primarily by Rayleigh waves (Miller and Pursey, 1955). Since Rayleigh waves produce both vertical and horizontal displacements, the ground surface will, for a constant loading frequency, be distorted as shown in exaggerated form in Figure 6.18. By placing a receiver at the center of the footing and moving another receiver to points at different distances from the receiver, the locations of points vibrating in-phase can be determined. The horizontal distances between such points are equal to the wavelength of the Rayleigh wave. By measuring the Rayleigh wavelength, the Rayleigh wave phase velocity, v_R , can be calculated as

$$v_R = \omega \lambda_R / 2\pi = f \lambda_R \quad (6.26)$$

From the phase velocity, Poisson's ratio, and Figure 5.10, the shear wave velocity can be estimated. For many soils, $v_s \approx 1.09 v_R$.

For soils whose stiffness varies with depth, dispersion will cause the Rayleigh wave phase velocity to vary with frequency. The shape of the Rayleigh wave displacement profile (Figure 5.10) suggests that the measured phase velocity corresponds to the soil properties at a depth of about $\lambda_R/3$ (Gazetas, 1991) to $\lambda_R/2$ (Heukelom and Foster, 1960; Richart et al., 1970). By varying the loading frequency in the field, the variation of shear wave velocity with depth can be estimated. The steady-state vibration test is useful for determining the near-surface shear wave velocity but cannot easily provide detailed resolution of highly variable velocity profiles. For geotechnical earthquake engineering applications, the steady-state vibration test has largely been supplanted by the spectral analysis of surface waves test.

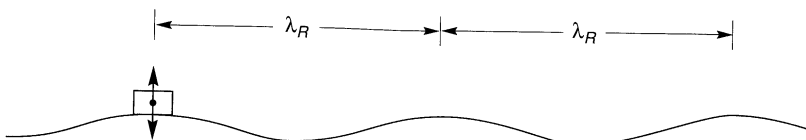


Figure 6.18 Rayleigh wave-induced deformation of ground surface adjacent to vertically vibrating footing. (After Richart et al., 1970.)

Spectral Analysis of Surface Waves Test. The shape of a *dispersion curve* [i.e., a plot of Rayleigh wave velocity versus frequency (or wavelength)], at a particular site is related to the variation of body wave velocities with depth. The preceding steady-state test can be used to generate a dispersion curve by repeating the test at different loading frequencies. This process, however, tends to be quite time consuming in the field. With the use of digital data acquisition and signal-processing equipment, a dispersion curve can be obtained from an impulsive or random noise load. The measurement and interpretation of dispersion curves obtained in this way, known as *spectral analysis of surface waves* (SASW) (Heisey et al., 1982; Nazarian and Stokoe, 1983; Stokoe et al., 1994), is one of the most significant recent advances in shallow seismic exploration.

The SASW test is performed by placing two vertical receivers on the ground surface in line with an impulsive or random noise source, as illustrated in Figure 6.19. The output of both

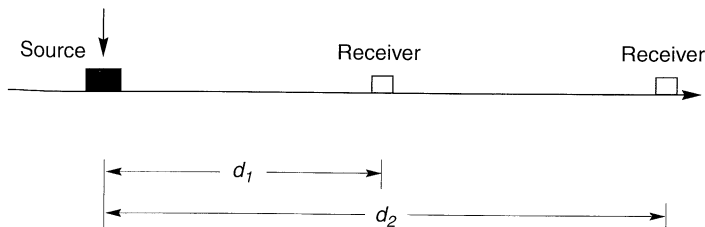


Figure 6.19 Typical configuration of source and receivers in a SASW test. Receiver spacing is changed in such a way that $d_1 + d_2$ remains constant.

receivers is recorded and transformed to the frequency domain using the fast Fourier transform. After transformation, the phase difference, $\phi(f)$, can be computed for each frequency. The corresponding travel time between receivers can be calculated for each frequency from

$$\Delta t(f) = \frac{\phi(f)}{2\pi f} \quad (6.27)$$

Since the distance between receivers, $\Delta d = d_2 - d_1$, is known, the Rayleigh wave phase velocity and wavelength can be calculated as functions of frequency:

$$v_R(f) = \frac{\Delta d}{\Delta t(f)} \quad (6.28)$$

$$\lambda_R(f) = \frac{v_R(f)}{f} \quad (6.29)$$

With modern electronic instrumentation, these calculations can be performed in the field virtually in real time. The results can be used to plot the experimental dispersion curve (Figure 6.20). While the test should, in theory, yield good results for a single receiver spacing, practical considerations dictate that several different receiver spacings be used. At each spacing, the midpoint between the two receivers is kept at the same distance from the source.

Identification of the thickness and shear wave velocity of subsurface layers involves the iterative matching of a theoretical dispersion curve to the experimental dispersion curve. The Haskell–Thomson solution (Thomson, 1950; Haskell, 1953) for a series of uniform elastic layers of infinite horizontal extent is used to predict the theoretical dispersion curve. Initial estimates of the thickness and shear wave velocity of each layer are then adjusted until the values that produce the best fit to the experimental dispersion curve are identified. This identification procedure is usually referred to as *inversion* (Nazarian, 1984). For profiles in which the shear wave velocity varies irregularly with depth, the dispersion curve may be influenced by higher-mode Rayleigh waves (Gucunski and Woods, 1991; Tokimatsu et al., 1992).

SASW tests have a number of important advantages over other field tests. They can be performed quickly, they require no borehole, they can detect low-velocity layers, and they can be used to considerable depth (>100 m). Comparison of shear wave velocity profiles obtained from SASW testing and cross-hole testing (see the next section) have shown good agreement (Hiltunen and Woods, 1988). SASW testing is particularly useful at sites where drilling and sampling are difficult; it has been used successfully in such materials as

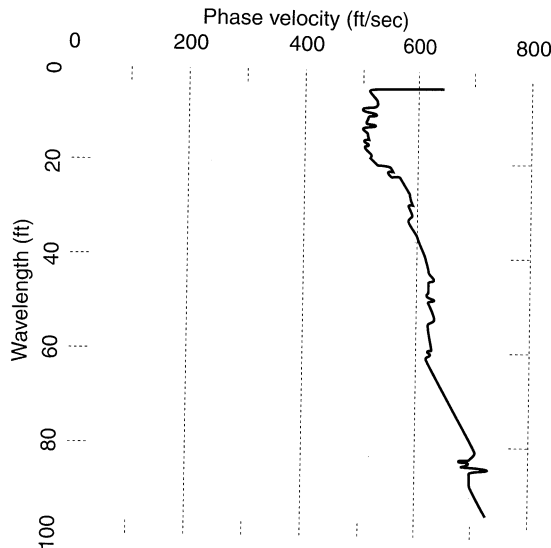


Figure 6.20 Experimental dispersion curve from SASW test. (After Gucunski and Woods, 1991; used by permission of the University of Missouri-Rolla.)

gravels and debris flow deposits (Stokoe et al., 1988) and landfills (Kavazanjian et al., 1994). The procedure does, however require specialized equipment and experienced operators. Its applicability is also limited to sites at which the assumptions of the Haskell–Thomson solution (e.g., horizontal layering) are at least approximately satisfied.

Seismic Cross-Hole Test. Seismic cross-hole tests use two or more boreholes to measure wave propagation velocities along horizontal paths. The simplest cross-hole test configuration (Figure 6.21a) consists of two boreholes, one of which contains an impulse energy source and the other a receiver. By fixing both the source and the receiver at the same depth in each borehole, the wave propagation velocity of the material between the boreholes at that depth is measured. By testing at various depths, a velocity profile can be obtained. When possible, use of more than two boreholes is desirable (Figure 6.21b) to minimize possible inaccuracies resulting from trigger time measurement, casing and backfill (material placed between the casing and the borehole wall) effects, and site anisotropy. Wave propagation velocities can then be calculated from differences in arrival times at adjacent pairs of boreholes. Arrival times can be determined by eye using points of common phase (first arrival, first peak, first trough, etc.) or by the type of cross-correlation techniques commonly used in petroleum exploration (Roesler, 1977).

Since the impulse sources must be located in the borehole, variation of the p-wave/s-wave content is more difficult than for methods in which it is at the surface. When explosive sources are used, the wave content is shifted toward higher p-wave content when larger charges are used, particularly when detonated above the ground surface (Woods, 1978). A number of mechanical impulse sources have been used, including the driving of a standard penetration test (Section 6.3.1.2) sampler, vertical impact loading of rods connected to borehole packers or jacks, torsional impact loading of a torque foot at the bottom of the borehole (Stokoe and Hoar, 1978), and other techniques (Applegate, 1974; Stokoe and Abdel-razzak, 1975; Auld, 1977). The best results are generally obtained when the polarity of the impulse

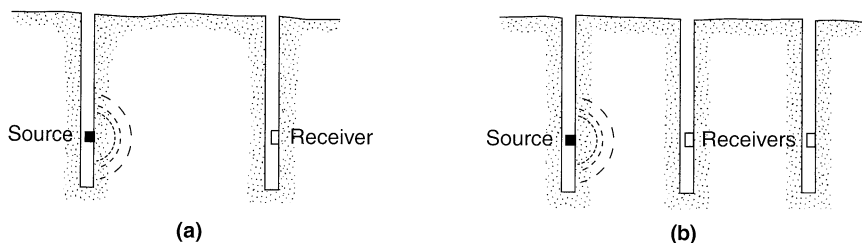


Figure 6.21 Seismic cross-hole test: (a) direct measurement using two-hole configuration; (b) interval measurement using three-hole configuration.

source is reversible, hence the frequent preference for mechanical sources over explosive sources.

The cross-hole test often allows individual soil layers to be tested since layer boundaries are frequently nearly horizontal. It can also detect hidden layers that can be missed by seismic refraction surveys. Cross-hole tests can yield reliable velocity data to depths of 30 to 60 m (100 to 200 ft) using mechanical impulse sources, and to greater depths with explosive sources. On the other hand, the sensitivity of the measured velocities to source-receiver distance often requires borehole deviation surveys, particularly for boreholes more than 15 to 20 m (50 to 65 ft) deep. The measured velocities may not be equal to the actual velocities when higher-velocity layers exist nearby. In such cases, more advanced methods of interpretation that can account for refraction (e.g., Butler et al., 1978) are required. Hryciw (1989) presented methods for correction of ray-path curvature in materials of continuously varying velocity.

Amplitude attenuation measurements from cross-hole tests involving three or more boreholes has been used to compute the material damping ratio of soils (Hoar and Stokoe, 1984; Mok et al., 1988; EPRI, 1993). The procedure requires accurately calibrated and oriented receivers that are well coupled to the borehole wall. By assuming a radiation pattern, the effects of geometric attenuation (radiation damping) can be separated from the measured attenuation to leave the attenuation due to material damping. The required assumptions render such approaches best suited to sites of simple geometry and homogeneous soil conditions.

Example 6.5

Determine the SV-wave velocity from the cross-hole test trigger and geophone records shown in Figure E6.5. The trigger and geophone are located 5 m apart. The solid line represents the response from a downward impact on a mechanical source and the dotted line represents the response from an upward impact.

Solution There is an obvious wave arrival at the geophone at about 2 msec after impact at the source. However, close examination of the geophone record shows that the polarity of this early arrival was not influenced by the polarity of the impact; consequently, the early arrival can be identified as a p-wave. At a later point, the arrival of waves whose polarity is reversed by the reversal of impact polarity is observed. These represent SV-waves—the arrival time of 23 msec after impact (determined graphically) indicates an SV-wave velocity of

$$v_s = \frac{x}{\Delta t} = \frac{5 \text{ m}}{0.023 \text{ sec}} = 217 \text{ m/sec}$$

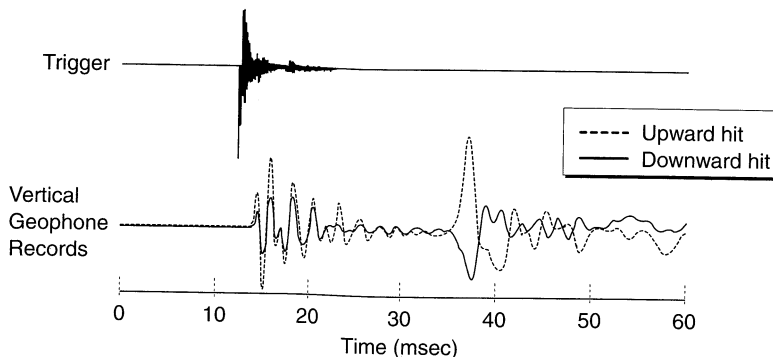


Figure E6.5

Seismic Down-Hole (Up-Hole) Test. Seismic down-hole (or up-hole) tests can be performed in a single borehole. In the down-hole test, an impulse source is located on the ground surface adjacent to the borehole. A single receiver that can be moved to different depths, or a string of multiple receivers at predetermined depths, is fixed against the walls of the borehole, and a single triggering receiver is located at the energy source (Figure 6.22). All receivers are connected to a high-speed recording system so that their output can be measured as a function of time. In the up-hole test, a movable energy source is located in the borehole with a single receiver on the ground surface adjacent to the borehole.

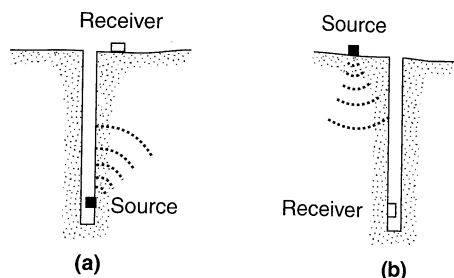


Figure 6.22 (a) Seismic up-hole test, and (b) seismic down-hole test.

The objective of the down-hole (or up-hole) test is to measure the travel times of p- and/or s-waves from the energy source to the receiver(s). By properly locating the receiver positions, a plot of travel time versus depth can be generated (Figure 6.23). The slope of the travel-time curve at any depth represents the wave propagation velocity at that depth.

S-waves can be generated much more easily in the down-hole test than the up-hole test; consequently, the down-hole test is more commonly used. With an SH-wave source, the down-hole test measures the velocity of waves similar to those that carry most seismic energy to the ground surface. Because the waves must travel through all materials between the impulse source and the receivers, the down-hole test allows detection of layers that can be hidden in seismic refraction surveys. Potential difficulties with down-hole (and up-hole) tests and their interpretation can result from disturbance of the soil during drilling of the borehole, casing and borehole fluid effects, insufficient or excessively large impulse sources, background

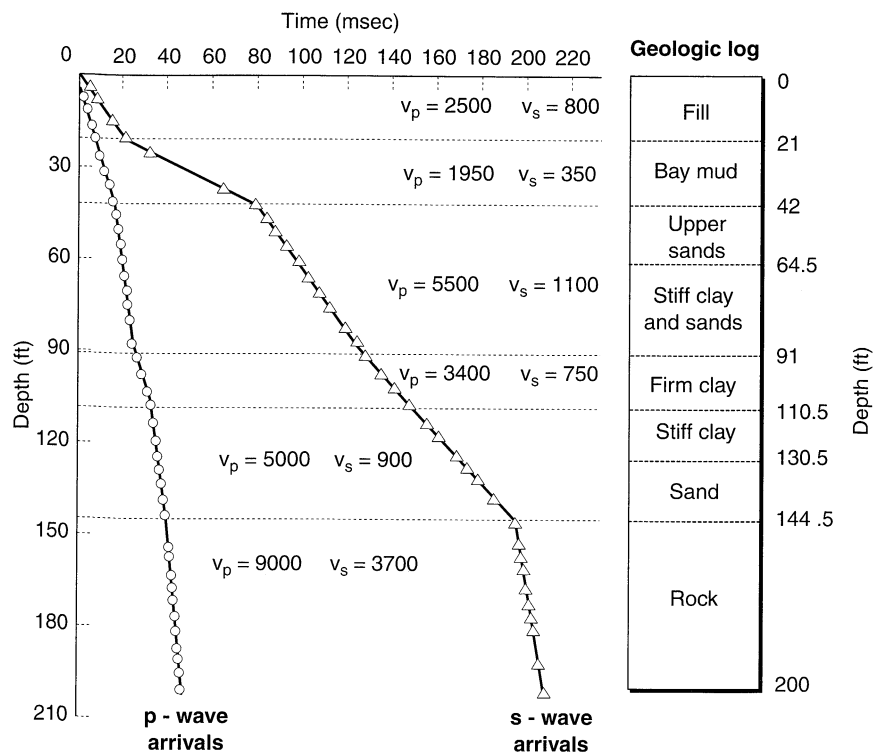


Figure 6.23 Travel-time curve from down-hole test in San Francisco Bay area. (After Schwarz and Musser, 1972.)

noise effects, and groundwater table effects. The effects of material and radiation damping on waveforms can make identification of s-wave arrivals difficult at depths greater than 30 to 60 m (100 to 200 ft). Efforts toward measurement of damping ratios in the down-hole test have also been made (Redpath et al., 1982; Redpath and Lee, 1986; EPRI, 1993).

Seismic Cone Test. The seismic cone test (Robertson et al., 1985) is very similar to the down-hole test, except that no borehole is required. A seismic cone penetrometer consists of a conventional cone penetrometer (Section 6.3.1.2) outfitted with a geophone or accelerometer mounted just above the friction sleeve. At different stages in the cone penetration sounding, penetration is stopped long enough to generate impulses at the ground surface, often by striking each end of a beam pressed against the ground by the outriggers of the cone rig, with an instrumented hammer. Travel time-depth curves can be generated and interpreted in the same way as for down-hole tests. Although down-hole (and up-hole) tests have usually been performed to complement other tests or to provide redundancy, the efficiency of the seismic cone test may lead to its more common use. Cross-hole seismic tests using two seismic cones have also been performed (e.g., Baldi et al., 1988).

6.3.1.2 High-Strain Tests

The field of in situ testing of soils has expanded tremendously in the past 25 years as a number of new devices and procedures have been developed and implemented. While

these tests are most commonly used to measure high-strain characteristics such as soil strength, their results have also been correlated to low-strain soil properties. For geotechnical earthquake engineering problems, the standard penetration test, cone penetration test, dilatometer test, and pressuremeter test are of particular interest.

Standard Penetration Test. The *standard penetration test* (SPT) is by far the oldest and most commonly used *in situ* test in geotechnical engineering. It is also commonly used in a number of geotechnical earthquake engineering applications. In the SPT, a standard split-barrel sampler (Figure 6.24) is driven into the soil at the bottom of a borehole by repeated blows (30 to 40 blows per minute) of a 140-lb (63.6 kg) hammer released from a height of 30 in (76 cm). The standard SPT sampler should have a constant inside diameter; the use of samplers designed to accommodate internal sample liners can underestimate penetration resistance by 10 to 20% when the liners are not in place. The sampler is usually driven 18 in. (46 cm); the number of blows required to achieve the last 12 in. (30 cm) of penetration is taken as the *standard penetration resistance*, N . The N value is a function of the soil type, confining pressure, and soil density, but is also influenced by the test equipment and procedures. In fact, studies have shown that different equipment and procedures are quite common both within the United States and other countries, and that they strongly influence the energy delivered to the soil by each blow of the hammer (Kovacs et al., 1977; Schmertmann et al., 1978; Kovacs and Salomone, 1982). Seed et al. (1985) recommended that the test be performed in 4- to 5-in.-diameter (10 to 13 cm) rotary boreholes with upward deflection of bentonite drilling mud using a tricone or baffled drag bit. The recommended sampler should have a constant inside diameter and be connected to A or AW [for depths less than 15 m (50 ft)] or N or NW (for greater depths) drill rods. Driving at a rate of 30 to 40 blows per minute with 60% of the theoretical free-fall energy delivered to the sampler was also recommended. It has become common to normalize the N value to an overburden pressure of 1 ton/ft² (100 kPa) and to correct it to an energy ratio of 60% (the average ratio of the actual energy delivered by safety hammers to the theoretical free-fall energy) according to

$$(N_1)_{60} = N_m C_N \frac{E_m}{0.60 E_{ff}} \quad (6.30)$$

where N_m is the measured penetration resistance, C_N an overburden correction factor (Figure 6.25), E_m the actual hammer energy, and E_{ff} the theoretical free-fall hammer energy. The corrected standard penetration resistance, $(N_1)_{60}$, has been correlated to many important properties of coarse-grained soils. Correlations for the properties of fine-grained soils are much less reliable.

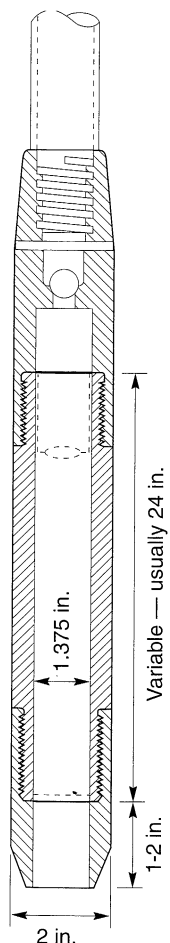
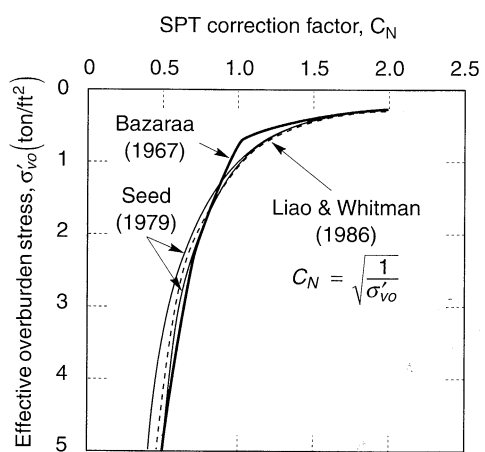
Example 6.6

A site in Japan had the measured SPT resistances indicated in table E6.6. Ishihara (1993) indicated that the SPT procedures used in Japan deliver about 72% of the theoretical free-fall energy to the sampler. Assuming that the sands have an average void ratio of 0.44 and that the water table is at a depth of 1.5 m, compute the corresponding $(N_1)_{60}$ values.

Solution Given the void ratio of 0.44, and assuming that $G_s = 2.7$, the average dry and submerged densities of the sand are 1.874 Mg/m^3 and 1.180 Mg/m^3 , respectively. These densities can be used to compute the vertical effective stress values that correspond to each depth at which the SPT resistance was measured (column 3 below). For example, the vertical effective stress at a depth of 6.2 m is given by

Table E6-6

Depth (m)	N_m	Depth (m)	N_m
1.2	7	11.2	23
2.2	4	12.2	13
3.2	3	13.2	11
4.2	3	14.2	11
5.2	5	15.2	24
6.2	9	16.2	27
7.2	12	17.2	5
8.2	12	18.2	6
9.2	14	19.2	4
10.2	9	20.2	38

**Figure 6.24**
SPT sampler.**Figure 6.25** SPT overburden correction factor. (After Liao and Whitman, 1986.)

$$\sigma'_{v0} = \left[(1.5 \text{ m}) \left(1.874 \frac{\text{Mg}}{\text{m}^3} \right) + (4.7 \text{ m}) \left(1.180 \frac{\text{Mg}}{\text{m}^3} \right) \right] \left(9.81 \frac{\text{m}}{\text{sec}^2} \right) = 82.0 \text{ kPa}$$

By converting the vertical effective stresses from units of kPa to units of tons/ft², the value of the correction factor at each depth can be computed by the relationship of Liao and Whitman (1986) (column 4 below). For example, the correction factor at a depth of 6.2 m is given by

$$C_N = \sqrt{\frac{1}{(82.0 \text{ kPa})[(0.01044 \text{ tons/ft}^2)/\text{kPa}]}} = 1.08$$

Then the corrected SPT resistances can be computed using equation (6.30) (column 6 below). For a depth of 6.2 m,

$$(N_1)_{60} = N_m C_N \frac{E_m}{0.60 E_{ff}} = (9)(1.08) \frac{0.72 E_{ff}}{0.60 E_{ff}} = 11.7$$

The appropriate values for all depths are tabulated below.

(1) Depth (m)	(2) N_m	(3) σ'_{v0} (kPa)	(4) C_N	(5) E_m/E_{ff}	(6) $(N_1)_{60}$
1.2	7	22.1	2.08	0.72	17.3
2.2	4	35.7	1.64	0.72	7.9
3.2	3	47.3	1.42	0.72	5.1
4.2	3	58.8	1.28	0.72	4.6
5.2	5	70.4	1.16	0.72	7.0
6.2	9	82.0	1.08	0.72	11.7
7.2	12	93.6	1.01	0.72	14.6
8.2	12	105.3	0.95	0.72	13.7
9.2	14	116.8	0.91	0.72	15.2
10.2	9	128.4	0.86	0.72	9.3
11.2	23	140.0	0.83	0.72	22.8
12.2	13	151.5	0.79	0.72	12.4
13.2	11	163.1	0.77	0.72	10.1
14.2	11	174.7	0.74	0.72	9.8
15.2	24	186.3	0.72	0.72	20.7
16.2	27	197.9	0.70	0.72	22.5
17.2	5	209.4	0.68	0.72	4.1
18.2	6	221.1	0.66	0.72	4.7
19.2	4	232.7	0.64	0.72	3.1
20.2	38	244.3	0.63	0.72	28.5

For gravelly soils, the *Becker hammer penetration test* (BPT) can be used in the same way as the SPT is for sands. In a recommended BPT procedure (Harder and Seed, 1986), a closed 6.6.in.-OD drill bit at the end of a 6.6.in. (16.8 cm) OD steel casing is driven into the soil by an ICE 180 diesel pile-driving hammer (8100 ft-lb/blow (110 N-m/blow) rated energy). The BPT resistance is taken as the number of blows per foot of penetration, corrected for variations in the diesel hammer bounce chamber pressure (which reflect the effects of soil resistance and combustion conditions on hammer energy). By comparing the results from the BPT and SPT at the same sandy sites, Harder and Seed (1986) found that the BPT and SPT resistances were related as shown in Table 6-1.

Rather than relying on bounce chamber pressures, Sy and Campanella (1994) used a pile driving analyzer to measure the maximum transferred energy, ENTHRU. With energy

Table 6.1 Equivalence of Corrected BPT and SPT Resistances

Corrected BPT Blowcount, N_{BC}	Corrected SPT Blowcount, N_{60}
0	0
20	~20
40	~34
60	~46
80	~58
100	~70

measurements, the BPT resistance can be corrected to a reference ENTHRU level of 30% of the rated energy of an ICE 180 diesel hammer

$$N_{b30} = N_b \frac{\text{ENTHRU}}{30}$$

where ENTHRU is expressed as a percentage. Considering the effects of skin resistance along the sides of the BPT casing, the graphical correlation with SPT resistance shown in Figure 6.26 was developed.

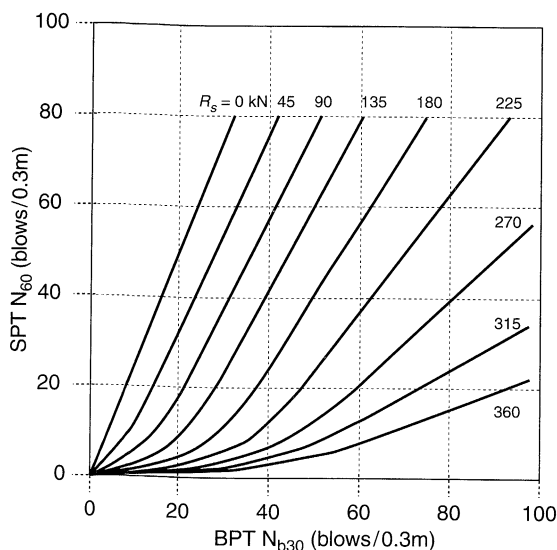


Figure 6.26 BPT-SPT correlations for different BPT shaft resistances. (After Sy and Campanella, 1984; used with permission.)

Cone Penetration Test. In recent years, use of the cone penetration test (CPT) in geotechnical engineering practice has increased sharply. The CPT involves the steady penetration of a standard cone penetrometer (Figure 6.27a) into the ground. The standard cone penetrometer has a conical tip of 10 cm^2 (1.55 in^2) area and 60° apex angle immediately below a cylindrical friction sleeve of 150 cm^2 (23.3 in^2) surface area. The penetrometer is pushed into the ground at a constant rate of 2 cm/sec (0.8 in/sec). The tip and friction sleeve are each connected to load cells that measure the tip resistance, q_c , and sleeve resistance, f_s , during penetration (Figure 6.27b). The friction ratio, $\text{FR} = f_s/q_c$, is also

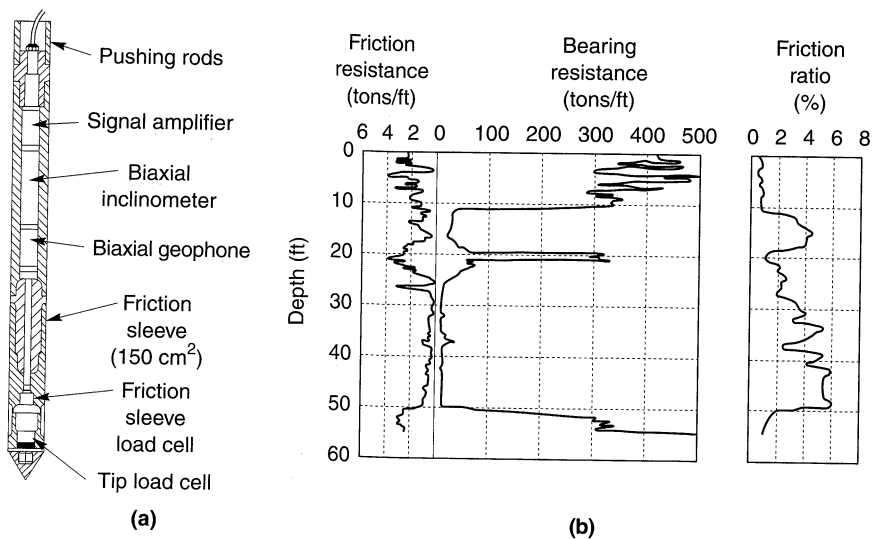


Figure 6.27 (a) Typical cone penetrometer with seismic cone capabilities (after Baldi et al., 1988); (b) results of cone penetration sounding (after Ward, 1986).

a useful parameter—it is high in cohesive soils and low in cohesionless soils. The absolute and relative magnitudes of the penetration resistances can be correlated to many of the same properties as the SPT, and also to soil type.

The CPT can be performed rapidly (usually about four times faster than drilling and sampling) and relatively inexpensively. It provides a continuous profile of penetration resistance that can detect the presence of thin layers or seams that are easily missed in SPT testing. The capabilities of cone penetrometers can be enhanced by adding additional transducers to measure additional variables such as porewater pressure (in the *piezocene*) or wave propagation velocity [in the *seismic CPT* (Section 6.3.1.1)]. However, the CPT cannot be used at sites with very stiff and/or very dense soils without damaging the probe or rods. The presence of gravel-size particles can also limit the use of the CPT.

Dilatometer Test. The *dilatometer test* (DMT) uses a flat dilatometer (Figure 6.28), a stainless steel blade with a thin flat circular expandable steel membrane on one side (Marchetti, 1980). The dilatometer is jacked into the ground with the membrane surface flush with the surrounding blade surface. At intervals of 10 to 20 cm (4 to 8 in.), penetration is stopped and the membrane inflated by pressurized gas. The pressure at which the membrane moves by 0.05 mm (0.002 in.) (the lift-off pressure, p_0) and the pressure at which its center moves 1.1 mm (0.043 in.) (p_1) are recorded, corrected, and used with the hydrostatic pressure, u_0 , and the effective overburden pressure, σ'_{vo} , to compute various indices to which soil properties can be correlated. The most commonly used of these indices are the material index, I_D , the horizontal stress index, K_D , and the dilatometer modulus, E_D , given by

$$I_D = \frac{p_1 - p_0}{p_1 - u_0} \quad (6.31)$$

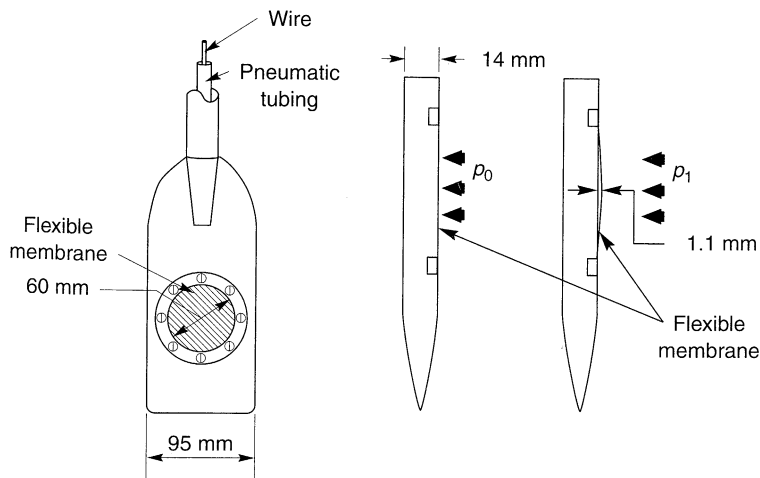


Figure 6.28 Front and side views of the Marchetti flat dilatometer. (After Baldi et al., 1986.)

$$K_D = \frac{p_0 - u_0}{\sigma'_{v0}} \quad (6.32)$$

$$E_D = \alpha(p_1 - p_0) \quad (6.33)$$

where α is equal to 34.7 for a 60-mm (2.4 in.) membrane diameter and a membrane deflection of 1.1 mm (0.043 in.). Dilatometer parameters have been correlated to low-strain soil stiffness (Section 6.4.2.1) and liquefaction resistance (Section 9.5.3.1).

Pressuremeter Test. The *pressuremeter test* (PMT) is the only in situ test capable of measuring stress-strain, as well as strength, behavior (Mair and Wood, 1987). The pressuremeter (Figure 6.29a) is a cylindrical device that uses a flexible membrane to

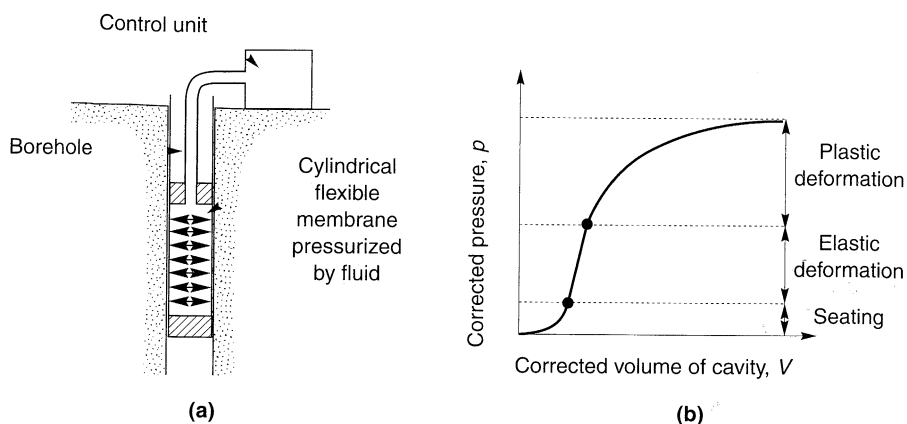


Figure 6.29 Pressuremeter test: (a) test setup; (b) typical pressuremeter curve. (After Mair and Wood, 1987.)

apply a uniform pressure to the walls of a borehole. Deformation of the soil can be measured by the volume of fluid injected into the flexible membrane or by feeler arms for pressuremeters that use compressed gas. After correcting the measured pressures and volume changes for system compliance, elevation differences, and membrane effects, a pressure–volume curve (Figure 6.29b) can be developed. Using cavity expansion theory, the pressure–volume curve can be used to compute the stress–strain behavior. Self-boring pressuremeters, which minimize soil disturbance, and push-in pressuremeters, which can penetrate soft soils very quickly, have also been developed.

Other Field Tests. A number of variations of the preceding tests have been used to measure dynamic soil properties, and new tests are also being developed. The concept of *geotomography* follows from advances in the medical imaging field (Johnson et al., 1978; Lytle, 1978). Using multiple sources and receivers, a large matrix of source–receiver travel times can be measured and compared with predictions of a ray-tracing model that can account for refraction and reflection at possible material boundaries between the sources and receivers. The number, position, and inclination of material boundaries are adjusted until the computed travel-time matrix matches the observed matrix. Although geotomography is still in its infancy, it offers the potential for rapid, detailed resolution of two- and three-dimensional subsurface structures. An apparatus that measures electrical conductivity of soil–porewater systems (Arulmoli et al., 1985) has been used to estimate in situ density and low-strain stiffness and to evaluate liquefaction potential. An *in situ borehole torsional test system* (Henke and Henke, 1991) advances two thin, concentric tubes into the soil at the bottom of a borehole. Records of rotation versus cyclic torque applied to the inner tube have shown behavior similar to that of stress–strain curves in controlled laboratory tests.

6.3.2 Laboratory Tests

Laboratory tests are usually performed on relatively small specimens that are assumed to be representative of a larger body of soil. The specimens are tested as *elements* (i.e., they are subjected to uniform initial stresses and uniform changes in stress or strain conditions). In other laboratory tests, specimens are tested as *models* and the results must be interpreted in terms of the nonuniform boundary conditions acting on the model.

The ability of laboratory tests to provide accurate measurements of soil properties depends on their ability to replicate the initial conditions and loading conditions of the problem of interest. No laboratory test can represent all possible stress and strain paths with general rotation of principal stress axes; consequently, different tests will be most suitable for different problems.

6.3.2.1 Sampling

Element tests are performed on soil specimens. For problems involving the response of soils to be placed as fills, specimens can be constructed from bulk or disturbed samples by simulating the compaction process as closely as possible in the laboratory. When the properties of an existing soil are needed, however, the problem becomes more difficult. Tests on existing soils can be performed on undisturbed or reconstituted specimens. However, in many instances the results will be different between these tests because of differences in soil fabric between natural and reconstituted soil specimens, even when densities and applied stresses are similar.

Dynamic soil properties are influenced by many factors, including density and stress conditions, and other factors, such as soil fabric or structure, age, stress and strain history, and cementation. While the void ratio and stress conditions can be recreated in a reconstituted specimen, the effects of the other factors cannot. Since the effects of these other factors are manifested primarily at low strain levels, they are easily destroyed by sample disturbance. For the results of laboratory tests to reflect the actual behavior of the in situ soil as closely as possible, high-quality undisturbed samples must be obtained.

For cohesive soils, procedures for the preparation of test specimens by carefully trimming thin-walled tube or block samples are fairly well established. Undisturbed sampling of cohesionless soils such as clean sands and gravels is more difficult. Even thin-walled sampling tubes can cause significant disturbance of clean sands, causing densification of loose sands and dilation of dense sands (Marcuson et al., 1977). The use of block sampling (Horn, 1978) has proven effective, but the process is laborious and may not be practical below certain depths. The use of freezing and coring was first described by Hvorslev (1949). This approach has been shown to be effective when the confining pressure is maintained and when free drainage is maintained continuously at the freezing front (Singh et al., 1979). Konno et al. (1993), for example, described the successful retrieval of undisturbed samples by coring through a 140-cm-diameter column of sandy gravel frozen by liquid nitrogen circulating through a central 73-mm steel tube for a period of about 160 hrs.

6.3.2.2 Low-Strain Element Tests

Only a limited number of laboratory tests are able to determine the properties of soils at low strain levels. These include the resonant column test, the ultrasonic pulse test, and the piezoelectric bender element test.

Resonant Column Test. The resonant column test is the most commonly used laboratory test for measuring the low-strain properties of soils. It subjects solid or hollow cylindrical specimens to harmonic torsional or axial loading by an electromagnetic loading system (Figure 6.30a). The loading systems usually apply harmonic loads for which the frequency and amplitude can be controlled, but random noise loading (Al-Sanad and Aggour, 1984) and impulse loading (Tawfig et al., 1988) have also been used.

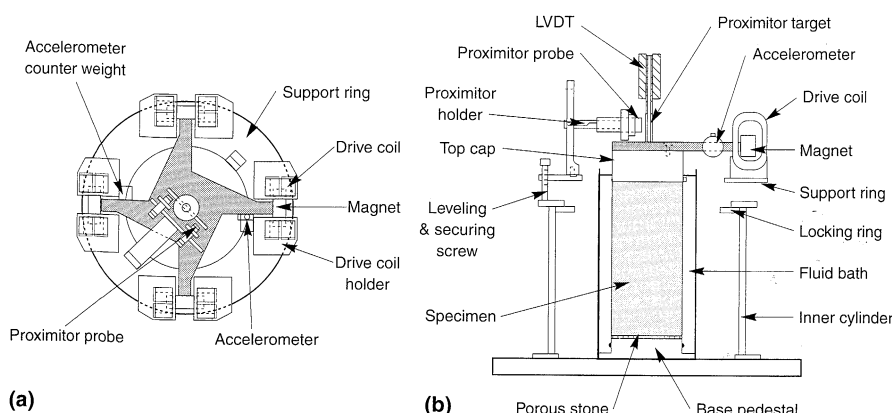


Figure 6.30 Typical resonant column test apparatus: (a) top view of loading system, and (b) profile view of loading system and soil specimen. (After EPRI, 1993.)

After the resonant column specimen has been prepared and consolidated, cyclic loading is begun. The loading frequency is initially set at a low value and is then gradually increased until the response (strain amplitude) reaches a maximum. The lowest frequency at which the response is locally maximized is the fundamental frequency of the specimen. The fundamental frequency is a function of the low-strain stiffness of the soil, the geometry of the specimen, and certain characteristics of the resonant column apparatus.

The shear modulus can be related to the fundamental frequency by the following procedure. Consider a resonant column specimen of height, h , fixed against rotation of its base, with polar moment of inertia, J , subjected to harmonic torsional loading (Figure 6.30b). From equation (5.8), the elastic resistance of the specimen produces a torque at its top,

$$T = GJ \frac{\partial\theta}{\partial z} = G \frac{I}{\rho} \frac{\partial\theta}{\partial z} \quad (6.34)$$

where I is the mass polar moment of inertia of the specimen. This torque must be equal to the inertial torque of the loading system. If the elements of the torsional loading system connected to the top of the specimen have a mass polar moment of inertia, I_0 , the inertial torque is

$$T = -I_0 h \frac{\partial^2\theta}{\partial t^2} \quad (6.35)$$

Assuming that the rotations of the specimen are also harmonic, they can be described by

$$\theta(z, t) = \Theta(z)(C_1 \cos \omega t + C_2 \sin \omega t) \quad (6.36)$$

where $\Theta(z) = C_3 \cos kz + C_4 \sin kz$. The zero rotation boundary condition at the base ($z = 0$) requires $C_3 = 0$, and the equality of equations (6.34) and (6.35) requires, at the fundamental frequency, $\omega_n = k_n v_s$, so that

$$\begin{aligned} & G \frac{I}{\rho} C_4 k_n \cos k_n h (C_1 \cos \omega_n t + C_2 \sin \omega_n t) \\ &= -I_0 h (-\omega_n^2 C_4 \sin k_n h) (C_1 \cos \omega_n t + C_2 \sin \omega_n t) \end{aligned}$$

which can be expressed as

$$\frac{I}{I_0} = \frac{\omega_n h}{v_s} \tan \frac{\omega_n h}{v_s} \quad (6.37)$$

For a given specimen, I , I_0 , and h are generally known at the time that cyclic loading begins. The fundamental frequency is then obtained experimentally, and equation (6.37) is used to calculate v_s . The shear modulus is then obtained from $G = \rho v_s^2$. Damping can be determined from the frequency response curve using the half-power bandwidth method (Section B.6.1 of Appendix B) or from the logarithmic decrement by placing the specimen in free vibration.

For longitudinal loading, the analogous equation is

$$\frac{W}{W_0} = \frac{\omega_n h}{v_l} \tan \frac{\omega_n h}{v_l} \quad (6.38)$$

where W is the weight of the specimen, W_0 the weight of the loading system, and $v_l = \sqrt{E/\rho}$ the longitudinal wave propagation velocity.

If the loading system was massless ($I_0 = 0$), equation (6.37) would degrade to

$$v_s = \frac{2\omega_n h}{\pi} = 4f_n h \quad (6.39)$$

where f_n is the fundamental frequency in hertz. In this case the rotations would follow a quarter-sine-wave pattern over the height of the specimen at the fundamental frequency. Adding the mass of the loading system results in a more linear variation of rotation and, consequently, more uniform strain conditions over the height of the specimen.

The shear strain in a solid cylindrical resonant column specimen loaded in torsion varies from zero at the centerline of the specimen to a maximum value at its outer edge. In situations in which the shear modulus varies with shear strain amplitude, the effects of nonuniform strain can be significant (Drnevich, 1967, 1972). The use of hollow specimens minimizes the variation of shear strain amplitude across the specimen.

Large-diameter resonant column devices have been used for gravelly soils (Woods, 1991) and rock (Prange, 1981). Konno et al. (1993) performed what could be described as in situ resonant column tests of gravelly soils at a potential nuclear power plant site in Japan. In these tests the material in two 10-m-ID (32.8 ft) circular trenches was excavated and replaced with water-filled bags to depths of 5 m (16 ft) and 9 m (30 ft). Concrete cap blocks 3 (10 ft) and 5 m (16 ft) thick were cast on top of each of the resulting soil columns. Vibratory shakers were placed on top of the blocks near the edges; cyclic torsional loading was applied to the soil column by operating the jacks 180° out of phase. By performing frequency sweeps, the response of the soil columns could be measured at shear strain amplitudes up to 0.01%.

Example 6.7

A 6-in.-high specimen of soft silty clay with a unit weight of 105 lb/ft³ is tested in a resonant column device with $I/I_0 = 0.4$. From the frequency response curve shown in Figure E6.7, determine the shear modulus of the specimen.

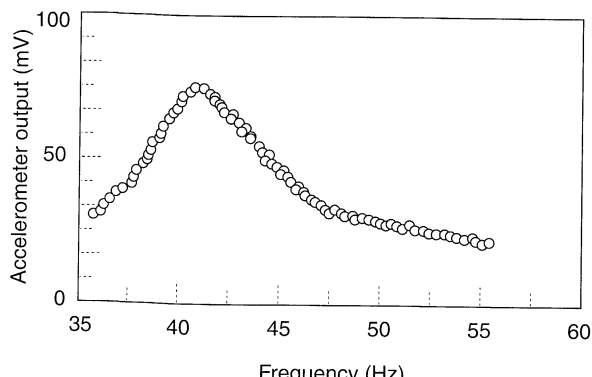


Figure E6.7

Solution The maximum amplitude of the accelerometer output occurs at the fundamental frequency of the specimen, determined graphically to be

$$f_n = 41 \text{ Hz}$$

Then equation (6.37) can be written as

$$\frac{I}{I_0} = \frac{\omega_n h}{v_s} \tan \frac{\omega_n h}{v_s} = 0.4$$

which is satisfied when $\omega_n h/v_s = 0.593$. Then

$$v_s = \frac{\omega_n h}{0.593} = \frac{2\pi f_n h}{0.593} = \frac{2\pi(41)(0.5)}{0.593} = 212 \text{ ft/sec}$$

$$G = \rho v_s^2 = \frac{105 \text{ lb}/\text{ft}^3}{32.2 \text{ ft/sec}^2} (212 \text{ ft/sec})^2 = 146,557 \text{ lb}/\text{ft}^2$$

The resonant column test allows stiffness and damping characteristics to be measured under controlled conditions. The effects of effective confining pressure, strain amplitude, and time can readily be investigated. However, measurement of porewater pressure is difficult, and the material properties are usually measured at frequencies above those of most earthquake motions.

Ultrasonic Pulse Test. Wave propagation velocities can be measured in the laboratory by means of the ultrasonic pulse test (Lawrence, 1963; Nacci and Taylor, 1967). Ultrasonic transmitters and receivers are attached to platens that can be placed at each end of a specimen with the distance separating them carefully measured. The transmitters and receivers are made of piezoelectric materials which exhibit changes in dimensions when subjected to a voltage across their faces, and which produce a voltage across their faces when distorted. A high-frequency electrical pulse applied to the transmitter causes it to deform rapidly and produce a stress wave that travels through the specimen toward the receiver. When the stress wave reaches the receiver, it generates a voltage pulse that is measured. The distance between the transmitter and receiver is divided by the time difference between the voltage pulses to obtain the wave propagation velocity. The ultrasonic pulse test is particularly useful for very soft materials, such as seafloor sediments, since it can be performed while the soil is still in the sampling tube (Woods, 1978).

Piezoelectric Bender Element Test. Another type of test that allows measurement of shear wave velocity on laboratory specimens makes use of piezoelectric bender elements (Shirley and Anderson, 1975; De Alba et al., 1984; Dyvik and Madshus, 1985). Bender elements are constructed by bonding two piezoelectric materials together in such a way that a voltage applied to their faces causes one to expand while the other contracts, causing the entire element to bend as shown in Figure 6.31. Similarly, a lateral disturbance of the bender element will produce a voltage, so the bender elements can be used as both s-wave transmitters and receivers.

In most setups, the bender elements protrude into opposite ends of a soil specimen. A voltage pulse is applied to the transmitter element, which causes it to produce an s-wave.

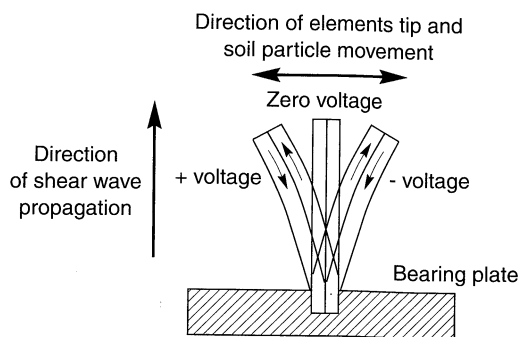


Figure 6.31 Piezoelectric bender element. Positive voltage causes element to bend one way, negative voltage causes it to bend the other.

When the s-wave reaches the other end of the specimen, distortion of the receiver element produces another voltage pulse. The time difference between the two voltage pulses is measured with an oscilloscope and divided into the distance between the tips of the bender elements to give the s-wave velocity of the specimen.

Piezoelectric bender elements have been incorporated into conventional and cubical triaxial devices, direct simple shear devices, oedometers, and model tests. Since the specimen is not disturbed during the bender element test, it can be subsequently tested for other soil characteristics.

6.3.2.3 High-Strain-Element Tests

At high shear strain amplitudes, soils generally exhibit volume change tendencies. Under drained loading conditions, these tendencies are allowed to manifest themselves in the form of volumetric strain, but under undrained conditions they result in changes in pore pressure (and effective stress). Since soil behavior is governed by effective stresses, all methods of testing soils at high strain levels must be capable of controlling porewater drainage from the specimen and measuring volume changes and/or pore pressures accurately. The problem of *system compliance* (volume changes due to the testing apparatus rather than the soil), which can lead to errors in volume change/pore pressure measurement, is important in the interpretation of high-strain test results. *Membrane penetration* in coarse-grained soil is an important contributor to system compliance.

Cyclic Triaxial Test. Just as the triaxial compression test is the most commonly used laboratory test for measurement of soil properties under static loading conditions, the cyclic triaxial test has been the most commonly used test for measurement of dynamic soil properties at high strain levels. In the triaxial test, a cylindrical specimen is placed between top and bottom loading platens and surrounded by a thin rubber membrane (Figure 6.32). The specimen is subjected to a radial stress, usually applied pneumatically, and an axial stress. By virtue of these boundary conditions, the principal stresses in the specimen are always vertical and horizontal.

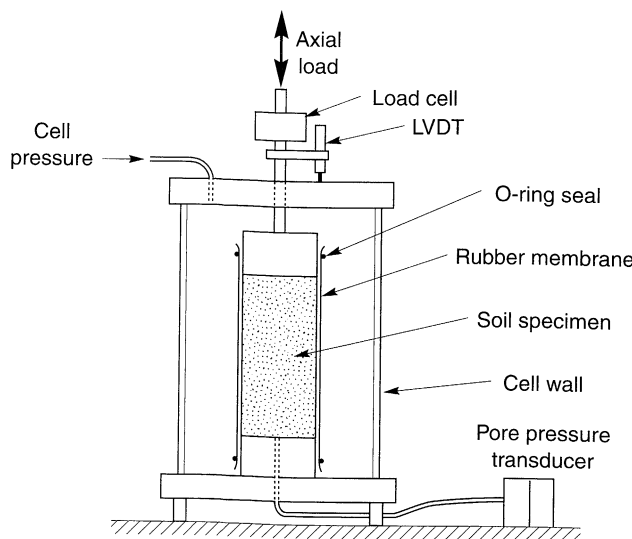


Figure 6.32 Typical triaxial apparatus.

The difference between the axial stress and the radial stress is called the *deviator stress*. In the cyclic triaxial test, the deviator stress is applied cyclically, either under stress-controlled conditions (typically by pneumatic or hydraulic loaders), or under strain-controlled conditions (by servohydraulic or mechanical loaders). Cyclic triaxial tests are most commonly performed with the radial stress held constant and the axial stress cycled at a frequency of about 1 Hz.

As with the static triaxial test, the cyclic triaxial test can be performed under isotropically consolidated or anisotropically consolidated conditions, thereby producing the stress paths shown in Figure 6.33. Figure 6.33a shows the cyclic deviator stress and total stress path for an isotropically consolidated specimen. Isotropically consolidated tests are commonly used to represent level-ground sites where no initial shear stresses exist on horizontal planes. The test begins with zero shear stress (point A) and the deviator stress is initially increased. Since the axial stress is then greater than the radial stress, the major and minor principal stress axes are vertical and horizontal, respectively. After the deviator stress reaches its maximum value (point B), it decreases and approaches a value of zero (point C). Just before it reaches point C, the major principal stress axis is still vertical, but it rotates instantaneously to horizontal as point C is passed and the deviator stress becomes negative. At point C, no shear stress exists on the specimen. This process of stress reversal repeats itself throughout the test, with instantaneous 90° rotations of the principal stress axes occurring every time the deviator stress passes through zero.

To model conditions in and beneath slopes where initial shear stresses exist, anisotropically consolidated triaxial tests are performed. Figure 6.33b refers to an anisotropically consolidated specimen for which the cyclic deviator stress amplitude is greater than the deviator stress during consolidation. Stress reversals also exist in this situation, even though the cyclic deviator stress is no longer symmetric about the p -axis. If the cyclic deviator stress

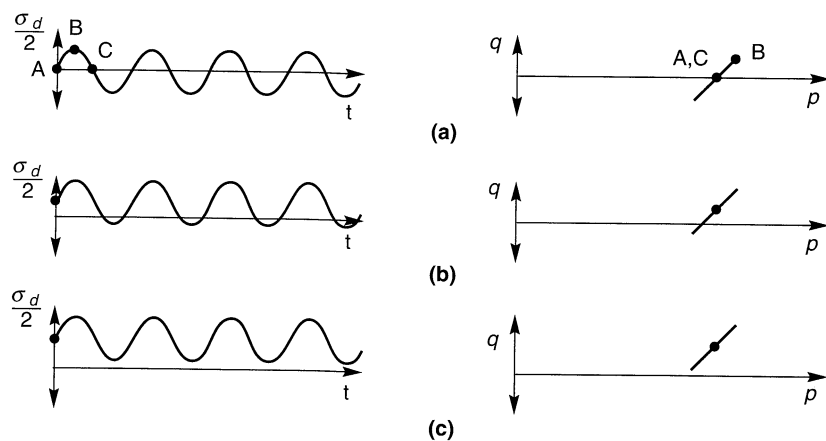


Figure 6.33 Time histories of deviator stress and stress paths for (a) isotropically consolidated conditions, (b) anisotropically consolidated conditions with cyclic deviator stress amplitude greater than deviator stress during consolidation (producing stress reversals), and (c) anisotropically consolidated conditions with cyclic deviator stress amplitude less than deviator stress during consolidation (no stress reversals).

amplitude is smaller than the deviator stress during consolidation (Figure 6.33c), no stress reversals will occur. For this case, the principal stress axes will not rotate and the specimen will never reach the zero shear stress condition. The stress paths in Figure 6.33 are obviously different with respect to initial stress conditions, stress path, and principal stress axis rotation than those imposed on the element of soil subjected to vertically propagating s-waves shown in Figure 6.7. These differences illustrate the fundamental difficulty in the direct application of properties obtained from the cyclic triaxial test to actual wave propagation problems.

In some cases, the cell pressure is also applied cyclically. By decreasing (or increasing) the cell pressure by the same amount that the deviator stress is increased (or decreased) by, the Mohr circle can be made to expand and contract about a constant center point. The resulting stress path will then oscillate vertically, much like that shown for the case of vertically propagating s-waves (Figure 6.7). Although the stress path of such a triaxial test can be made to match that induced by a vertically propagating s-wave, the principal stresses in the triaxial test remain constrained to the vertical and horizontal direction rather than rotating continuously as caused by the s-wave.

The stresses and strains measured in the cyclic triaxial test can be used to compute the shear modulus and damping ratio (Section 6.4.2). The cyclic triaxial test allows stresses to be applied uniformly, although stress concentrations can exist at the cap and base, and allows drainage conditions to be accurately controlled (when the effects of membrane penetration are mitigated). It requires only minor modification of standard triaxial testing equipment. On the other hand, the cyclic triaxial test cannot model stress conditions that exist in most actual seismic wave propagation problems. Bedding errors and system compliance effects generally limit measurements to shear strains greater than about 0.01%, although local strain measurement (e.g., Burland and Symes, 1982; Ladd and Dutko, 1985; Goto et al., 1991) can produce accurate measurements at strain levels as small as 0.0001%.

Membrane penetration effects can be important in cyclic triaxial tests of coarse sands and gravels. After consolidation, the thin triaxial membrane will penetrate the perimeter voids of coarse sand and gravel specimens. As excess pore pressures develop during cyclic loading, the net pressure on the membrane decreases and its penetration increases. When this happens, the effective volume of the voids increases and the excess pore pressure drops below the level it would have had if true constant-volume conditions had been maintained. Because they allow the effective stresses to be higher than they would be under constant-volume conditions, membrane penetration effects can lead to inaccurate stiffness and damping measurements and unconservative estimation of liquefaction resistance (Chapter 9). Procedures have been developed for measurement (Vaid and Negussey, 1984; Kramer and Sivaneswaran, 1989a), minimization (Lade and Hernandez, 1977; Raju and Venkataramana, 1980), compensation (Seed and Anwar, 1986; Tokimatsu and Nakamura, 1986), and posttest correction (Martin et al., 1978; Kramer and Sivaneswaran, 1989b) of membrane penetration effects.

Example 6.8

A cyclic triaxial test on a saturated clay specimen produces the stress-strain loop shown in Figure E6.8. Determine the secant shear modulus and damping ratio.

Solution Graphically, the slope of a straight line between the ends of the stress-strain curve shows that

$$E_{\text{sec}} = \frac{236 \text{ kPa}}{0.014} = 16,857 \text{ kPa}$$

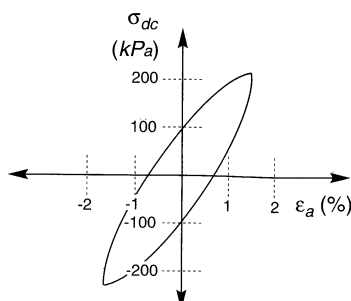


Figure E6.8

Then, assuming that the saturated clay is loaded under undrained conditions, $\nu = 0.5$, so

$$G_{sec} = \frac{E}{2(1+\nu)} = \frac{16,857 \text{ kPa}}{2(1+0.5)} = 5619 \text{ kPa}$$

The area of the hysteresis loop is 4.52 kPa and the area of the triangle denoting the maximum strain energy is 1.65 kPa. Then

$$\xi = \frac{1}{4\pi} \frac{\text{area of hysteresis loop}}{\text{area of triangle}} = \frac{4.52 \text{ kPa}}{1.65 \text{ kPa}} = 0.218$$

Cyclic Direct Simple Shear Test. The cyclic direct simple shear test is capable of reproducing earthquake stress conditions much more accurately than is the cyclic triaxial test. It is most commonly used for liquefaction testing. In the cyclic direct simple shear test, a short, cylindrical specimen is restrained against lateral expansion by rigid boundary platens (Cambridge-type device), a wire-reinforced membrane (NGI-type device), or a series of stacked rings (SGI-type device). By applying cyclic horizontal shear stresses to the top or bottom of the specimen, the test specimen is deformed (Figure 6.34) in much the same way as an element of soil subjected to vertically propagating s-waves (Figure 6.7).

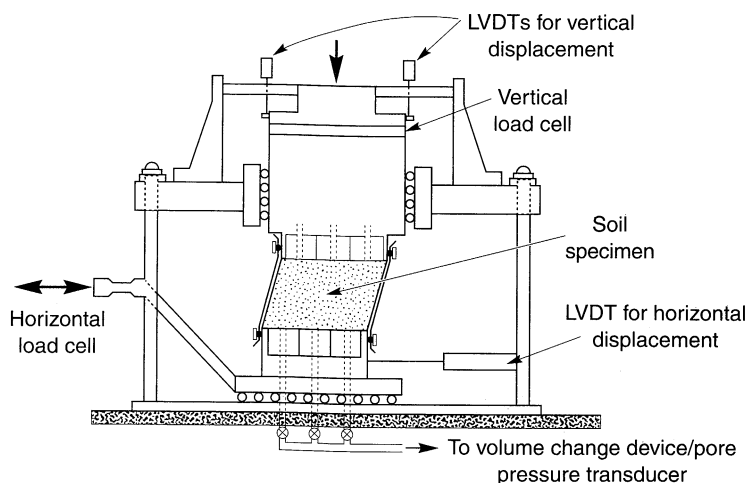


Figure 6.34 NGI cyclic simple shear apparatus. Soil specimen is contained within wire-reinforced rubber membrane. (After Airey and Wood, 1987.)

The simple shear apparatus, however, applies shear stresses only on the top and bottom surfaces of the specimen. Since no complementary shear stresses are imposed on the vertical sides, the moment caused by the horizontal shear stresses must be balanced by non-uniformly distributed shear and normal stresses. The effects of nonuniformity of stresses can be reduced by increasing the diameter/height ratio of the specimen; such effects are small at diameter/height ratios greater than about 8:1 (Kovacs and Leo, 1981). Conventional simple shear apparatuses are limited by their inability to impose initial stresses other than those corresponding to K_0 conditions. In recent years, simple shear devices that allow independent control of vertical and horizontal stresses have been developed. To better simulate actual earthquake conditions, Pyke (1973) used a large shaking table to produce a two-directional large-scale simple shear apparatus with a diameter/height ratio of about 9 in one direction and 20 in the other. Small-scale, bidirectional, cyclic simple shear apparatuses have also been developed (Boulanger et al., 1993).

Cyclic Torsional Shear Test. Many of the difficulties associated with the cyclic triaxial and cyclic direct simple shear tests can be avoided by loading cylindrical soil specimens in torsion. Cyclic torsional shear tests allow isotropic or anisotropic initial stress conditions and can impose cyclic shear stresses on horizontal planes with continuous rotation of principal stress axes. They are most commonly used to measure stiffness and damping characteristics over a wide range of strain levels.

Ishihara and Li (1972) developed a torsional triaxial test that used solid specimens. Dobry et al. (1985) used strain-controlled cyclic torsional loading along with stress-controlled axial loading of solid specimens to develop a CyT-CAU test that has proven effective for measurement of liquefaction behavior. Torsional testing of solid specimens, however, produces shear strains that range from zero along the axis of the specimen to a maximum value at the outer edge. To increase the radial uniformity of shear strains, others (e.g., Drnevich, 1967, 1972) developed hollow cylinder cyclic torsional shear apparatuses (Figure 6.35). While hollow cylinder tests offer perhaps the best uniformity and control

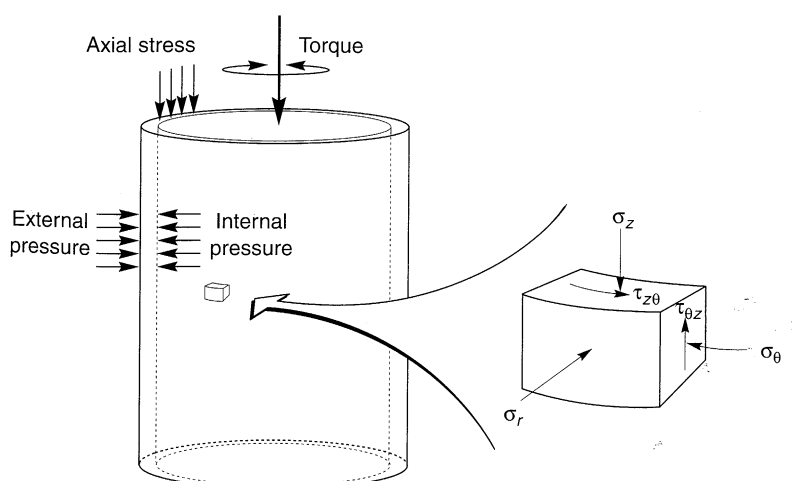


Figure 6.35 Hollow cylinder apparatus. The specimen is enclosed within internal and external membranes on which internal and external pressures can be applied independently. Application of cyclic torque induces cyclic shear stresses on horizontal planes.

over stresses and drainage, specimen preparation can be difficult and the equipment is not widely available.

6.3.2.4 Model Tests

In contrast to element tests, model tests usually attempt to reproduce the boundary conditions of a particular problem by subjecting a small-scale physical model of a full-scale *prototype structure* to cyclic loading. Model tests may be used to evaluate the performance of a particular prototype or to study the effects of different parameters on a general problem. While model testing is very useful for identification of important phenomena and verification of predictive theories, it has not yet developed to the point of being used directly for design of significant structures or facilities.

The behavior of soils is sensitive to stress level; soils that exhibit contractive behavior under high normal stresses may exhibit dilative behavior at lower stress levels. One of the most significant challenges in model testing, therefore, is the problem of testing models whose stress dependency matches that of the full-scale prototype. Because this is very difficult under the gravitational field of the earth, one common approach involves testing under increased gravitational fields. Model tests can therefore be divided into those performed under the gravitational field of the earth ($1g$ model tests) and those performed under higher gravitational accelerations. The $1g$ tests are most commonly performed with the use of shaking tables; tests under increased gravitational fields are usually performed in a geotechnical centrifuge.

Both shaking table and centrifuge model tests share certain drawbacks, among the most important of which are similitude and boundary effects. Because different aspects of the response of a $1/N$ -scale model are governed by different scale factors, similitude cannot be assured for all parameters simultaneously. Boundary effects are usually associated with the metallic bins or boxes in which shaking table and centrifuge models are usually constructed. The sidewalls can restrain soil movement and reflect energy that would radiate away in the prototype problem. The industrial filler material Duxseal has been used as an absorbent wall lining with some success (Steedman, 1991).

Shaking Table Tests. In the early years of geotechnical earthquake engineering, virtually all physical model testing was performed on shaking tables. Shaking table research has provided valuable insight into liquefaction, postearthquake settlement, foundation response, and lateral earth pressure problems. Most shaking tables utilize a single horizontal translation degree of freedom, but shaking tables with multiple degrees of freedom have also been developed. Shaking tables are usually driven by servohydraulic actuators (Figure 6.36); their dynamic loading capacities are controlled by the capacity of the hydraulic pumps that serve the actuators. Large pumps and large actuators are required to produce large displacements of heavy models at moderate or high frequencies.

Shaking tables of many sizes have been used for geotechnical earthquake engineering research. Some are quite large, allowing models with dimensions of several meters to be tested. Thus shaking tables can often utilize actual, prototype soils rather than resorting to the smaller particle sizes often required for smaller scale model tests. For these large models, soils can be placed, compacted relatively easily, and instrumented relatively easily. Shaking table models can be easily viewed from different perspectives during testing.

On the other hand, high gravitational stresses cannot be produced in a shaking table test. Though the contractive behavior associated with high normal stresses at significant

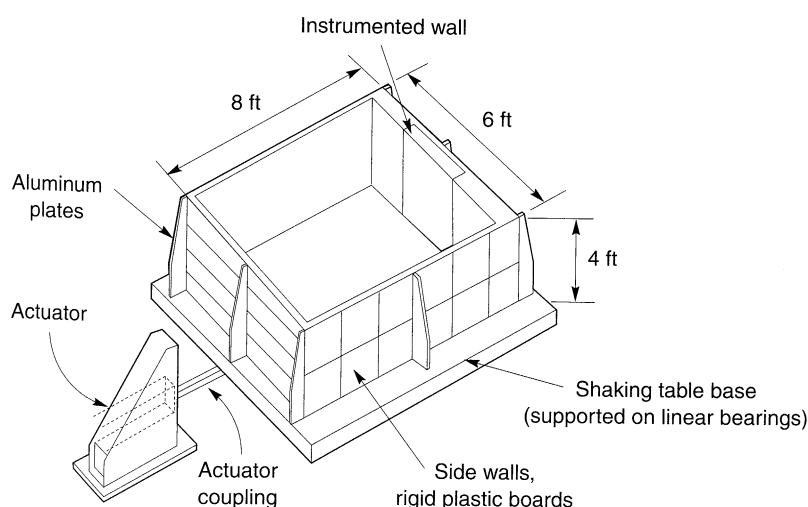


Figure 6.36 Shaking table with soil bin used for dynamic earth pressure research.
(After Sherif et al., 1982.)

depths can be simulated by placing soil very loosely during model preparation, the process of preparing such models is quite difficult. Because of the low normal stress levels, the contribution of factors that produce a cohesive component of strength will be greater in the model than in the prototype. Correction procedures (e.g., Hettler and Gudehus, 1985; Iai, 1989) have been developed to aid in the interpretation of shaking table test results.

Centrifuge Tests. In a centrifuge test, a $1/N$ -scale model located at a distance, r , from the axis of a centrifuge (Figure 6.37) is rotated at a rotational speed, $\Omega = \sqrt{N/r}$, which is sufficient to raise the acceleration field at the location of the model to N times the acceleration of gravity. In principle, the stress conditions at any point in the model should then be identical to those at the corresponding point in the full-scale prototype. The overall behavior (e.g., displacements, failure mechanisms, etc.) should also be identical.

Centrifuge tests are restricted to much smaller models than even moderate-sized shaking tables. Since the gravitational field increases with radial distance, the gravitational

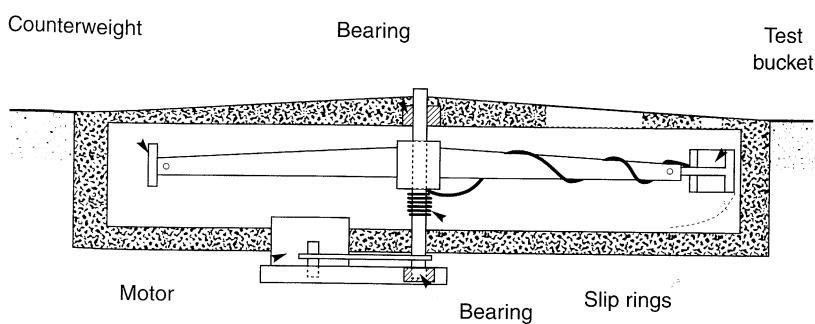


Figure 6.37 Cross section through a geotechnical centrifuge. (After O'Reilly, 1991.)

acceleration at the top of the model is lower than that at the bottom of the model. Since the gravitational field acts in the radial direction, the horizontal plane is curved (O'Reilly, 1991) by an amount that decreases with increasing centrifuge radius.

Similitude considerations are very important in the planning and interpretation of centrifuge tests. Scaling factors for a number of parameters are shown in Table 6-2. The scaling factors show how dynamic events are speeded up in the centrifuge. For example, the stresses and strains in a 30-m (100-ft)-high prototype earth dam could be modeled with a 30-cm (1-ft)-high centrifuge model accelerated to 100g (of course, the particle size of the model soil will correspond to a prototype particle size that is 100 times larger, too). A harmonic 1-Hz base motion lasting 10 sec at the prototype scale would be modeled by a 100-Hz motion lasting 0.1 sec in the model. The dissipation of any generated pore pressures, however, would occur 10,000 times as fast in the model as in the field. For this reason, viscous fluids such as glycerin or silicon oil are often used as pore fluids in centrifuge models. Improved estimates of prototype behavior can be obtained using the modeling of models technique (Schofield, 1980), which involves comparing the response of models of different size at the same prototype scale.

Obviously, high-speed transducers and data acquisition systems are required to obtain useful results in dynamic centrifuge tests. Because the scaling laws apply to all parts of the model, miniaturized transducers and cables are required to minimize their influence on the response of the model.

Table 6-2 Scaling Factors for Centrifuge Modeling^a.

Type of Event	Quantity	Model Dimension	
		Prototype Dimension	
All events	Stress	1	
	Strain	1	
	Length	$1/N$	
	Mass	$1/N^3$	
	Density	1	
	Force	$1/N^2$	
	Gravity	N	
	Time	$1/N$	
Dynamic events	Frequency	N	
	Acceleration	N	
	Strain rate	N	
	Time	$1/N^2$	
Diffusion events	Strain rate	N^2	

Source: After Kutter and James (1989).

^aValues are based on the assumption that the same soils and fluid are used in the model and the prototype and that the soil properties are not rate dependent.

Other Model Tests. In recent years the hydraulic gradient similitude test, originally developed by Zelikson (1969), has been used to measure dynamic soil properties (e.g., Yan and Byrne, 1990, 1991). The hydraulic gradient similitude test achieves high body forces by subjecting a model to a controlled, downward-acting hydraulic gradient. Since the body forces are aligned with flow lines, the presence of flow obstructions or nonuniform soil

conditions can cause "gravity" to act in different directions at different locations. Such effects complicate interpretation of the test results and restrict the use of the test to a relatively narrow range of problems.

6.3.3 Interpretation of Observed Ground Response

Interpretation of the response of instrumented, full-scale structures subjected to dynamic loading or earthquakes can provide invaluable information on dynamic soil properties and other geotechnical earthquake engineering parameters. This approach requires well-instrumented sites, either with vertical arrays or closely spaced instruments at soil and rock sites. At such sites the actual motions at the base and surface of a soil deposit can be used with a suitable ground response model (Chapter 7) to identify the dynamic soil properties (specifically, shear modulus and damping) that produce the best agreement between predicted and actual motions (e.g., Abdel-Ghaffar and Scott, 1979; Tokimatsu and Midorikawa, 1981; Chang et al., 1991; Glaser, 1995). Obviously, this approach requires an earthquake to produce ground motions, and the strain levels to which the dynamic soil properties can be measured are controlled by the strains produced by the earthquake. Examples of observed ground response from which dynamic soil properties can be identified are presented in Sections 8.2.2 and 8.2.3. As instrumentation and remote data acquisition systems continue to improve, more full-scale response data are likely to become available.

6.4 STRESS-STRAIN BEHAVIOR OF CYCLICALLY LOADED SOILS

The mechanical behavior of soils can be quite complex under static, let alone seismic loading conditions. Geotechnical engineers are constantly challenged by the need to characterize the most important aspects of cyclic soil behavior as accurately as possible with simple, rational models. The point at which the conflicting requirements of simplicity and accuracy are balanced depends on many factors, and many combinations have been proposed.

For the purposes of this book, three broad classes of soil models will be discussed: *equivalent linear models*, *cyclic nonlinear models*, and *advanced constitutive models*. Of these, equivalent linear models are the simplest and most commonly used but have limited ability to represent many aspects of soil behavior under cyclic loading conditions. At the other end of the spectrum, advanced constitutive models can represent many details of dynamic soil behavior, but their complexity and difficulty of calibration currently renders them impractical for many common geotechnical earthquake engineering problems. Nevertheless, each class of soil model reveals important information about the cyclic behavior of soils.

6.4.1 Some Basic Aspects of Particulate Matter Behavior

Before considering specific stress-strain models, it is useful to examine some basic aspects of the mechanical behavior of particulate media. Several important aspects of low-strain soil behavior can be illustrated by considering the soil as an assemblage of discrete elastic particles. Hertz (1881) studied the behavior of identical spheres of radius, R , compressed against each other by a normal force, N (Timoshenko and Goodier, 1951), and showed that

$$N = \frac{2\sqrt{2}GR^{3/2}}{3(1-\nu)}\delta_N^{3/2} \quad (6.40)$$

where G and v are the elastic constants of the spheres and δ_N is the change in distance between the centers of the spheres. For a cubically packed array of spheres loaded along one of the packing axes (Figure 6.38), the average normal stress is obtained by dividing the normal force by its tributary area, that is,

$$\sigma = \frac{N}{(2R)^2} = \frac{N}{4R^2} \quad (6.41)$$

Then the tangent modulus for uniaxial loading is given by

$$E_{\tan} = \frac{d\sigma}{d\varepsilon} = \frac{dN/4R^2}{d\delta_N/2R} = \frac{1}{2R} \frac{dN}{d\delta_N} = \frac{3}{2} \left[\frac{2G}{3(1-v)} \right]^{2/3} \sigma^{1/3} \quad (6.42)$$

which suggests that the stiffness should, theoretically, vary with the cube root of the axial stress. When a tangential force, T , is applied, elastic distortion causes the centers of the spheres to be displaced perpendicular to their original axis (Mindlin and Deresiewicz, 1953; Dobry et al., 1982) by an amount

$$\delta_T = \left[1 - \left(1 - \frac{T}{fN} \right)^{2/3} \right] \left\{ \frac{3fN}{4E} (2-v) (1+v) \left[\frac{3(1-v^2)NR}{4E} \right]^{-1/3} \right\} \quad T \leq fN \quad (6.43)$$

where f is the coefficient of friction between the spheres (note that δ_T is a nonlinear function of T). When T becomes equal to fN , gross sliding of the particle contacts occurs (though slippage of part of the contact can occur before this point). This gross sliding is required for permanent particle reorientation; consequently, volume changes (drained conditions) cannot occur and excess pore pressures (undrained conditions) cannot be generated when gross sliding does not occur. The shear strain corresponding to the initiation of gross sliding

$$\gamma_{tv} = \frac{\delta_T(T=fN)}{2R} = 2.08 \frac{(2-v)(1+v)f}{(1-v^2)^{1/2} E^{2/3}} \sigma^{2/3} \quad (6.44)$$

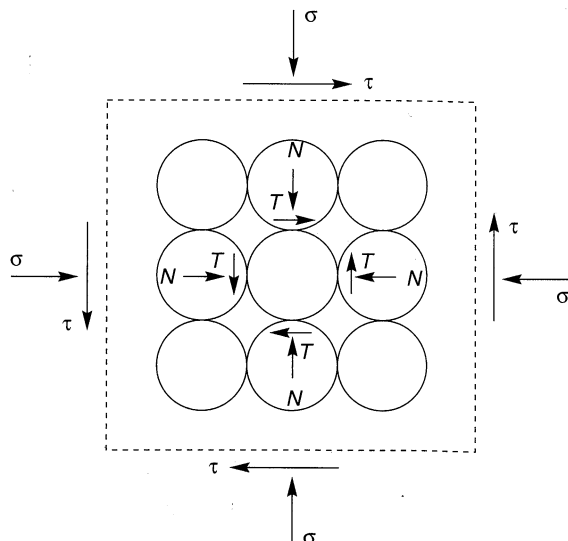


Figure 6.38 Cubically packed assemblage of spheres subjected to normal stress, σ , and shear stress, τ , that produce interparticle contact forces N and T . (After Dobry et al., 1982.)

is called the *volumetric threshold shear strain*. When the properties of quartz ($E = 11 \times 10^6$ psi (7.6×10^7 kPa), $\nu = 0.31$, $f = 0.50$) are substituted into equation (6.44), the threshold shear strain is given by

$$\gamma_{tv}(\%) = 0.000175 \sigma^{2/3} \quad (6.45)$$

where σ is in psf. For confining pressures of practical interest (500 to 4000 psf (25 to 200 kPa)), equation (6.44) would predict a threshold shear strain between 0.01 and 0.04%. Real soils, of course, do not consist of regular arrays of spherical particles, but the existence of a threshold shear strain very close to that predicted by equation (6.44) has been observed experimentally for sands under both drained (Drnevich and Richart, 1970; Youd, 1972; Pyke, 1973) and undrained (Park and Silver, 1975; Dobry and Ladd, 1980; Dobry et al., 1982) loading conditions. The simple idealized analysis of a regular array of spheres helps illustrate the reason for its existence. Experimental evidence suggests that the volumetric threshold shear strain increases with plasticity index (PI); the volumetric threshold shear strain of a clay with PI = 50 is approximately one order of magnitude greater than that of a sand, with PI = 0 (Vucetic, 1994). Experimental evidence also indicates (Vucetic, 1994) that soils exhibit linear elastic behavior below a linear cyclic threshold shear strain, γ_{tl} , that is approximately 30 times smaller than γ_{tv} .

Such analyses of the interaction of individual soil particles can provide insight into the mechanical behavior of soils. In recent years, tremendous advances have been made in *micromechanical modeling* of soils. Micromechanical models account for the kinematics and contact interactions of individual soil particles, thereby eliminating the need for a global constitutive model. A number of computational models have been developed with various restrictions on dimensionality, particle shape and size distribution, particle kinematics, and contact behavior (e.g., Cundall and Strack, 1979; Ting et al., 1989; Ng and Dobry, 1994). Although the computational effort involved in tracking the motion of each individual particle is currently too large to allow their use for practical problems with complicated boundary conditions, they have provided useful insight into several aspects of soil behavior.

6.4.2 Equivalent Linear Model

A typical soil subjected to symmetric cyclic loading as would be expected beneath a level ground surface far from adjacent structures, might exhibit a hysteresis loop of the type shown in Figure 6.39. This hysteresis loop can be described in two ways: first, by the actual path of the loop itself, and second, by parameters that describe its general shape. In general terms, two important characteristics of the shape of a hysteresis loop are its inclination and its breadth. The inclination of the loop depends on the stiffness of the soil, which can be described at any point during the loading process by the *tangent shear modulus*, G_{tan} . Obviously, G_{tan} varies throughout a cycle of loading, but its average value over the entire loop can be approximated by the secant shear modulus

$$G_{sec} = \frac{\tau_c}{\gamma_c} \quad (6.46)$$

where τ_c and γ_c are the shear stress and shear strain amplitudes, respectively. Thus G_{sec} describes the general inclination of the hysteresis loop. The breadth of the hysteresis loop is

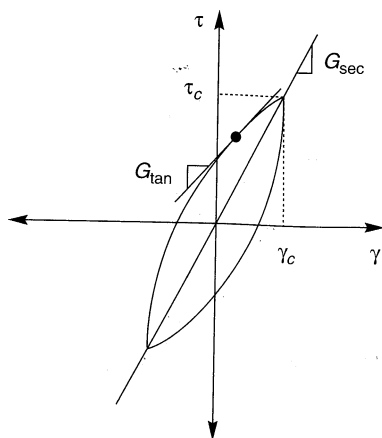


Figure 6.39 Secant shear modulus, G_{sec} , and tangent shear modulus, G_{\tan} .

related to the area, which as a measure of energy dissipation, can conveniently be described (Section B.6.1) by the damping ratio

$$\xi = \frac{W_D}{4\pi W_S} = \frac{1}{2\pi} \frac{A_{\text{loop}}}{G_{\text{sec}} \gamma_c^2} \quad (6.47)$$

where W_D is the dissipated energy, W_S the maximum strain energy, and A_{loop} the area of the hysteresis loop. The parameters G_{sec} and ξ are often referred to as *equivalent linear* material parameters. For certain types of ground response analyses, they are used directly to describe the soil behavior; other types of analyses require the actual path of the hysteresis loop as described by a cyclic nonlinear or advanced constitutive model. Both types of ground response analysis are described in Chapter 7.

Because some of the most commonly used methods of ground response analysis are based on the use of equivalent linear properties, considerable attention has been given to the characterization of G_{sec} and ξ for different soils. It is important to recognize, however, that the equivalent linear model is only an approximation of the actual nonlinear behavior of the soil. The assumption of linearity embedded in its use has important implications when it is used for ground response analysis, as discussed in Chapter 7. It also means that it cannot be used directly for problems involving permanent deformation or failure; equivalent linear models imply that the strain will always return to zero after cyclic loading, and since a linear material has no limiting strength, failure cannot occur. Nevertheless, the assumption of linearity allows a very efficient class of computational models to be used for ground response analyses, and it is commonly employed for that reason.

6.4.2.1 Shear Modulus

Laboratory tests have shown that soil stiffness is influenced by cyclic strain amplitude, void ratio, mean principal effective stress, plasticity index, overconsolidation ratio, and number of loading cycles. The secant shear modulus of an element of soil varies with cyclic shear strain amplitude. At low strain amplitudes, the secant shear modulus is high, but it decreases as the strain amplitude increases. The locus of points corresponding to the tips of hysteresis loops of various cyclic strain amplitudes is called a *backbone* (or *skeleton*)

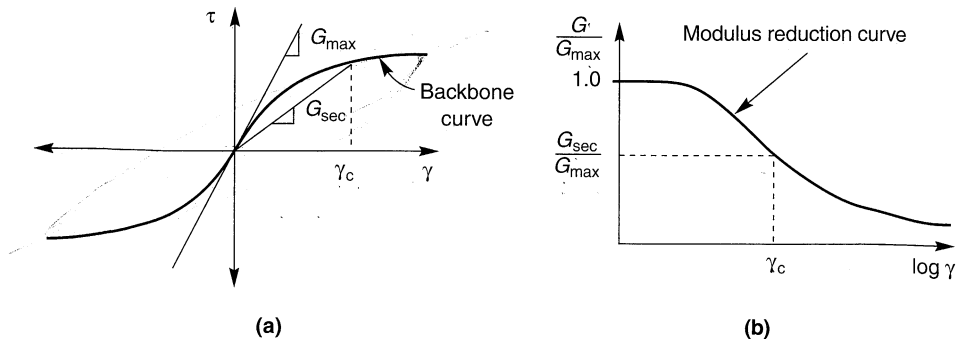


Figure 6.40 Backbone curve showing typical variation of G_{\sec} with shear strain.

curve (Figure 6.40a); its slope at the origin (zero cyclic strain amplitude) represents the largest value of the shear modulus, G_{\max} . At greater cyclic strain amplitudes, the *modulus ratio* G_{\sec}/G_{\max} (the “sec” subscript will hereafter be dropped for convenience and consistency with the notation commonly used in the geotechnical earthquake engineering literature) drops to values of less than 1. Characterization of the stiffness of an element of soil therefore requires consideration of both G_{\max} and the manner in which the modulus ratio G/G_{\max} varies with cyclic strain amplitude and other parameters. The variation of the modulus ratio with shear strain is described graphically by a *modulus reduction curve* (Figure 6.40b). The modulus reduction curve presents the same information as the backbone curve; either one can be determined from the other.

Maximum Shear Modulus, G_{\max} . Since most seismic geophysical tests induce shear strains lower than about $3 \times 10^{-4}\%$, the measured shear wave velocities can be used to compute G_{\max} as

$$G_{\max} = \rho v_s^2 \quad (6.48)$$

The use of measured shear wave velocities is generally the most reliable means of evaluating the in situ value of G_{\max} for a particular soil deposit, and the seismic geophysical tests described in Section 6.3.1.1 are commonly used for that purpose. Care must be taken in the interpretation of shear wave velocity, particularly at sites with anisotropic stress conditions, which can cause measured shear wave velocities to vary with the direction of wave propagation and particle movement (Roesler, 1979; Stokoe et al., 1985; Yan and Byrne, 1991).

When shear wave velocity measurements are not available, G_{\max} can be estimated in several different ways. Laboratory test data suggest that the maximum shear modulus can be expressed as

$$G_{\max} = 625F(e)(OCR)^k p_a^{1-n} (\sigma'_m)^n \quad (6.49)$$

where $F(e)$ is a function of the void ratio, OCR the overconsolidation ratio, k an overconsolidation ratio exponent (Table 6-3), σ'_m the mean principal effective stress [$\sigma'_m = (\sigma'_1 + \sigma'_2 + \sigma'_3)/3$], n a stress exponent, and p_a is atmospheric pressure in the same units as σ'_m and G_{\max} . Hardin (1978) proposed that $F(e) = 1/(0.3 + 0.7e^2)$, while Jamiolkowski et al. (1991) suggested that $F(e) = 1/e^{1.3}$. The stress exponent is often taken as $n = 0.5$ but can be computed

Table 6-3 Overconsolidation Ratio Exponent, K

Plasticity Index	k
0	0.00
20	0.18
40	0.30
60	0.41
80	0.48
≥ 100	0.50

Source: After Hardin and Drnevich (1972b).

for individual soils from the results of laboratory tests at different effective confining pressures. It should be apparent that G_{\max} , p_a , and σ'_m must be expressed in the same units. Equation (6.49) can also be used to adjust measured G_{\max} values to represent conditions that are different (e.g., increased effective stresses) from those at which the measurements were made.

Other empirical relationships have been proposed for specific soil types. The maximum shear modulus of sand, for example, is often estimated as

$$G_{\max} = 1000 K_{2,\max} (\sigma'_m)^{0.5} \quad (6.50)$$

where $K_{2,\max}$ is determined from the void ratio or relative density (Table 6-4) and σ'_m is in lb/ft² (Seed and Idriss, 1970). Field tests have consistently shown that shear wave velocities of gravels are significantly higher than those of sands, indicating that G_{\max} of gravel is higher than that of sand. $K_{2,\max}$ values for gravels are typically in the range 80 to 180 (Seed et al., 1984). For fine-grained soils, preliminary estimates of the maximum shear modulus can be obtained from plasticity index, overconsolidation ratio, and undrained strength (Table 6-5). Because undrained strengths are highly variable and because shear moduli and undrained strengths vary differently with effective confining pressure, these results must be used carefully.

Table 6-4 Estimation of $K_{2,\max}$

e	$K_{2,\max}$	D_r (%)	$K_{2,\max}$
0.4	70	30	34
0.5	60	40	40
0.6	51	45	43
0.7	44	60	52
0.8	39	75	59
0.9	34	90	70

Source: Adapted from Seed and Idriss (1970).

The maximum shear modulus can also be estimated from in situ test parameters. A number of empirical relationships between G_{\max} and various in situ test parameters have been developed; some of the more widely published are presented in Table 6-6. The inherent difficulty of correlating a small strain parameter such as G_{\max} with penetration parameters that relate to much larger strains is evident from the scatter in the data on which they are based and from the variability of the results obtained by different investigators. As such, the usefulness of such correlations is currently limited to preliminary estimates of G_{\max} .

Table 6-5 Values of G_{\max}/s_u^a

Plasticity Index	Overconsolidation Ratio, OCR		
	1	2	5
15–20	1100	900	600
20–25	700	600	500
35–45	450	380	300

Source: After Weiler (1988).

^a Undrained strength measured in CU triaxial compression.

However, the application of in situ testing to geotechnical earthquake engineering problems is only in its early stages, and significant advances can be expected as additional data become available.

Evaluation of shear modulus can be complicated by rate and time effects (Anderson and Woods, 1975, 1976; Anderson and Stokoe, 1978; Isenhower and Stokoe, 1981). Rate effects can cause G_{\max} to increase with increasing strain rate. The influence of strain rate on G_{\max} increases with increasing soil plasticity; for San Francisco Bay mud ($PI \approx 40$), G_{\max} increases about 4% per tenfold increase in strain rate. Rate effects can be significant when comparing G_{\max} values obtained from field shear wave velocity measurements (usually made with the use of impulsive disturbances which produce relatively high frequencies) with values obtained from laboratory tests. The shear wave velocity, and hence G_{\max} , increases approximately linearly with the logarithm of time past the end of primary consolidation to an extent that cannot be attributed solely to the effects of secondary compression. The change of stiffness with time can be described by

$$\Delta G_{\max} = N_G (G_{\max})_{1000} \quad (6.51)$$

where ΔG_{\max} is the increase in G_{\max} over one log cycle of time and $(G_{\max})_{1000}$ is the value of G_{\max} at a time of 1000 min past the end of primary consolidation. N_G increases with increasing plasticity index, PI, and decreases with increasing OCR (Kokushu et al., 1982). For normally consolidated clays, N_G can be estimated from the relationship

$$N_G \approx 0.027 \sqrt{PI}$$

Anderson and Woods (1975) showed that some of the discrepancy between G_{\max} values from field and laboratory tests could be explained by time effects, and that N_G could be used to correct the G_{\max} values from laboratory tests to better represent actual in situ conditions.

A brief summary of the effects of environmental and loading conditions on the maximum shear modulus of normally and moderately overconsolidated soils is presented in Table 6-7.

Modulus Reduction, G/G_{\max} . In the early years of geotechnical earthquake engineering, the modulus reduction behaviors of coarse- and fine-grained soils were treated separately (e.g., Seed and Idriss, 1970). Recent research, however, has revealed a gradual transition between the modulus reduction behavior of nonplastic coarse-grained soil and plastic fine-grained soil.

Zen et al. (1978) and Kokushu et al. (1982) first noted the influence of soil plasticity on the shape of the modulus reduction curve; the shear modulus of highly plastic soils was

Table 6-6 Empirical Relationships between G_{\max} and In Situ Test Parameters

In Situ Test	Relationship	Soil Type	References	Comments
SPT	$G_{\max} = 20,000(N_1)_{60}^{0.333}(\sigma'_m)^{0.5}$	Sand	Ohta and Goto (1976), Seed et al. (1986)	G_{\max} and σ'_m in lb/ft ²
	$G_{\max} = 325N_{60}^{0.68}$	Sand	Imai and Tonouchi (1982)	G_{\max} in kips/ft ²
	$G_{\max} = 1634(q_c)^{0.250}(\sigma'_v)^{0.375}$	Quartz sand	Rix and Stokoe (1991)	G_{\max}, q_c and σ'_v in kPa; Based on field tests in Italy and on calibration chamber tests
CPT _i	(Figure 6.41)	Silica sand	Baldi et al. (1986)	G_{\max}, q_c and σ'_v in kPa; Based on field tests in Italy
	$G_{\max} = 406(q_c)^{0.695}e^{-1.130}$	Clay	Mayne and Rix (1993)	G_{\max}, q_c and σ'_v in kPa; Based on field tests at worldwide sites
DMT	$G_{\max} / E_d = 2.72 \pm 0.59$	Sand	Baldi et al. (1986)	Based on calibration chamber tests
	$G_{\max} / E_d = 2.2 \pm 0.7$	Sand	Bellotti et al. (1986)	Based on field tests
	$G_{\max} = \frac{530}{(\sigma'_v/p_a)^{0.25}} \frac{\gamma_D/\gamma_w - 1}{2.7 - \gamma_D/\gamma_w} K_o^{0.25} (p_a \sigma'_v)^{0.5}$	Sand, silt, clay	Hryciw (1990)	G_{\max}, p_a, σ'_v in same units; γ_D is dilatometer-based unit weight of soil; based on field tests
PMT	$3.6 \leq \frac{G_{\max}}{G_{ur,c}} \leq 4.8$	Sand	Bellotti et al. (1986)	$G_{ur,c}$ is corrected unloading-reloading modulus from cyclic PMT
	$G_{\max} = \alpha_p \frac{1.68}{G_{ur}}$	Sand	Byrne et al. (1991)	G_{ur} is secant modulus of unloading-reloading portion of PMG; α_p is factor that depends on unloading-reloading stress conditions; based on theory and field test data

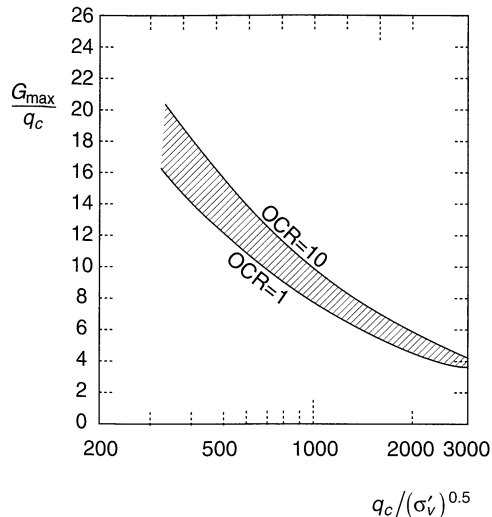


Figure 6.41 Estimation of G_{\max} from CPT tip resistance for uncemented silica sands.
(After Baldi et al., 1989.)

Table 6-7 Effect of Environmental and Loading Conditions on Maximum Shear Modulus of Normally Consolidated and Moderately Overconsolidated Soils

Increasing Factor	G_{\max}
Effective confining pressure, σ'_m	Increases with σ'_m
Void ratio, e	Decreases with e
Geologic age, t_g	Increases with t_g
Cementation, c	Increases with c
Overconsolidation ratio, OCR	Increases with OCR
Plasticity index, PI	Increases with PI if OCR > 1; stays about constant if OCR = 1
Strain rate, $\dot{\gamma}$	No effect for non-plastic soils; increases with $\dot{\gamma}$ for plastic soils (up to ~10% increase per log cycle increase in $\dot{\gamma}$)
Number of loading cycles, N	Decreases after N cycles of large γ_c , but recovers later with time in clays; increases with N for sand

Source: Modified from Dobry and Vucetic (1987).

observed to degrade more slowly with shear strain than did low-plasticity soils. After reviewing experimental results from a broad range of materials, Dobry and Vucetic (1987) and Sun et al. (1988) concluded that the shape of the modulus reduction curve is influenced more by the plasticity index than by the void ratio and presented curves of the type shown in Figure 6.42. These curves show that the linear cyclic threshold shear strain, γ_{lt} , is greater for highly plastic soils than for soils of low plasticity. This characteristic is extremely important; it can strongly influence the manner in which a soil deposit will amplify or attenuate earthquake motions. The PI = 0 modulus reduction curve from Figure 6.42 is very similar to the

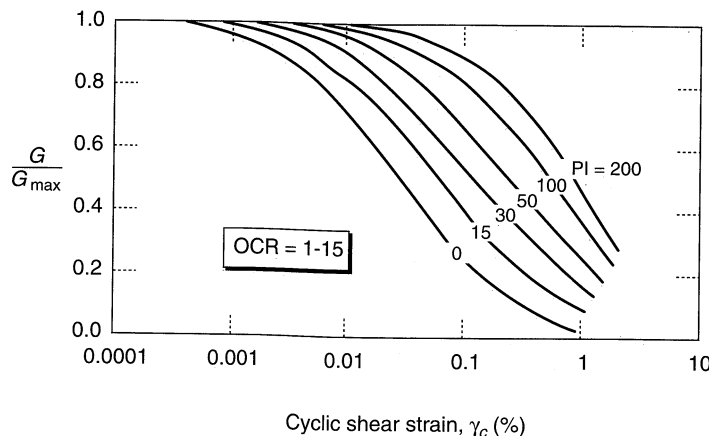


Figure 6.42 Modulus reduction curves for fine-grained soils of different plasticity.
(After Vučetić and Dobry (1991). Effect of soil plasticity on cyclic response. *Journal of Geotechnical Engineering*, Vol. 117, No. 1. Reprinted by permission of ASCE.)

average modulus reduction curve that was commonly used for sands (Seed and Idriss, 1970) when coarse- and fine-grained soils were treated separately. This similarity suggests that the modulus reduction curves of Figure 6.42 may be applicable to both fine- and coarse-grained soils (this conclusion should be confirmed for individual coarse-grained soils, particularly those that could exhibit aging or cementation effects). The difficulty of testing very large specimens has precluded the widespread testing of gravelly soils in the laboratory, but available test data indicate that the average modulus reduction curve for gravel is similar to, though slightly flatter than, that of sand (Seed et al., 1986; Yasuda and Matsumoto, 1993).

Modulus reduction behavior is also influenced by effective confining pressure, particularly for soils of low plasticity (Iwasaki et al., 1978; Kokoshu, 1980). The linear cyclic threshold shear strain, γ_{lt} , is greater at high effective confining pressures than at low effective confining pressures. The effects of effective confining pressure and plasticity index on modulus reduction behavior were combined by Ishibashi and Zhang (1993) in the form

$$\frac{G}{G_{\max}} = K(\gamma, \text{PI}) (\sigma'_m)^{m(\gamma, \text{PI}) - m_o} \quad (6.52)$$

where

$$K(\gamma, \text{PI}) = 0.5 \left\{ 1 + \tanh \left[\ln \left(\frac{0.000102 + n(\text{PI})}{\gamma} \right)^{0.492} \right] \right\}$$

$$m(\gamma, \text{PI}) - m_o = 0.272 \left\{ 1 - \tanh \left[\ln \left(\frac{0.000556}{\gamma} \right)^{0.4} \right] \right\} \exp(-0.0145\text{PI}^{1.3})$$

$$n(\text{PI}) = \begin{cases} 0.0 & \text{for PI} = 0 \\ 3.37 \times 10^{-6} \text{ PI}^{1.404} & \text{for } 0 < \text{PI} \leq 15 \\ 7.0 \times 10^{-7} \text{ PI}^{1.976} & \text{for } 15 < \text{PI} \leq 70 \\ 2.7 \times 10^{-5} \text{ PI}^{1.115} & \text{for PI} > 70 \end{cases}$$

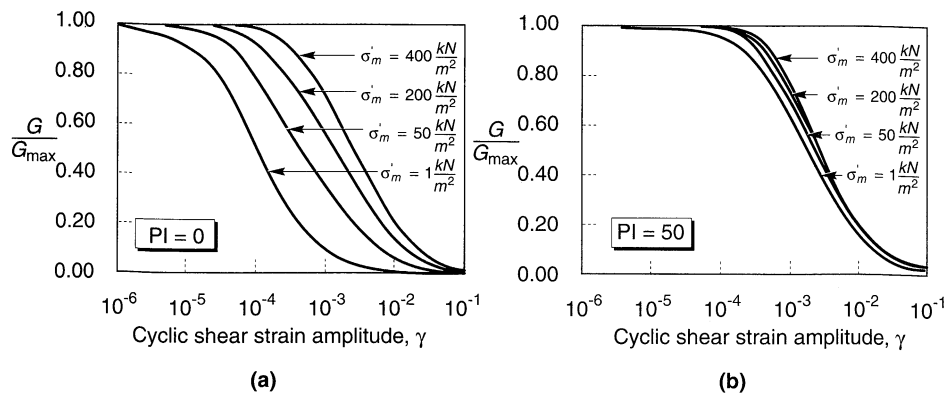


Figure 6.43 Influence of mean effective confining pressure on modulus reduction curves for (a) nonplastic ($PI = 0$) soil, and (b) plastic ($PI = 50$) soil. (After Ishibashi (1992). Discussion, *Journal of Geotechnical Engineering*, Vol. 118, No. 5. Reprinted by permission of ASCE.)

The effect of confining pressure on modulus reduction behavior of low- and high-plasticity soils is illustrated in Figure 6.43.

Under stress-controlled harmonic loading conditions, pore pressure generation and structural changes can cause the shear strain amplitude of a soil specimen to increase with increasing number of cycles. If clay or saturated sand specimens are loaded harmonically under strain-controlled undrained conditions, the shear stress amplitude would be observed to decrease with increasing number of cycles. Both conditions illustrate the tendency for repeated cyclic loads to degrade the stiffness of the specimen. For cohesive soils, the value of the shear modulus after N cycles, G_N , can be related to its value in the first cycle, G_1 , by

$$G_N = \delta G_1 \quad (6.53)$$

where the *degradation index*, δ , is given by $\delta = N^{-t}$ and t is the *degradation parameter* (Idriss et al., 1978). The degradation parameter has been shown to decrease with increasing PI and increasing overconsolidation ratio, and to increase with increasing cyclic strain amplitude (Idriss et al., 1980; Vucetic and Dobry, 1989; Tan and Vucetic, 1989). The effects of stiffness degradation on modulus reduction behavior is shown in Figure 6.44.

The influence of various environmental and loading conditions on the modulus ratio of normally consolidated and moderately overconsolidated clays is described in Table 6-8.

6.4.2.2 Damping Ratio

Theoretically, no hysteretic dissipation of energy takes place at strains below the linear cyclic threshold shear strain. Experimental evidence, however, shows that some energy is dissipated even at very low strain levels (the mechanism is not well understood), so the damping ratio is never zero. Above the threshold strain, the breadth of the hysteresis loops exhibited by a cyclically loaded soil increase with increasing cyclic strain amplitude, which indicates that the damping ratio increases with increasing strain amplitude.

Just as modulus reduction behavior is influenced by plasticity characteristics, so is damping behavior (Kokushu et al., 1982; Dobry and Vucetic, 1987; Sun et al., 1988). Damping ratios of highly plastic soils are lower than those of low plasticity soils at the same

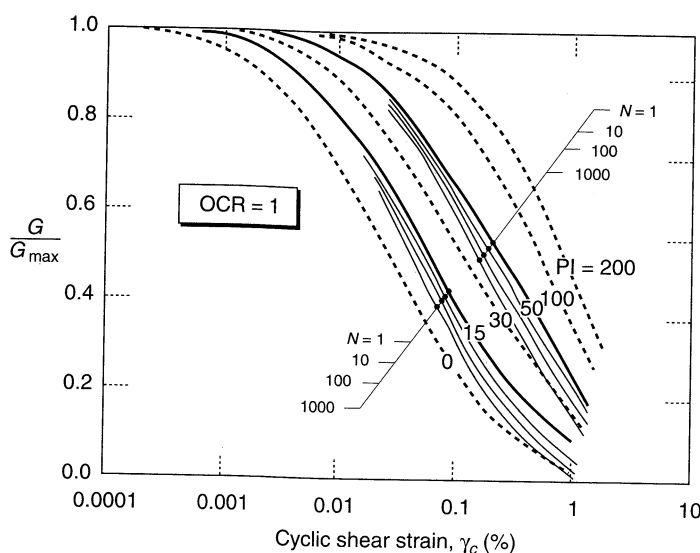


Figure 6.44 Effect of cyclic degradation on shear modulus. (After Vucetic and Dobry (1991). Effect of soil plasticity on cyclic response, *Journal of Geotechnical Engineering*, Vol 117, No. 1. Reprinted by permission of ASCE.)

Table 6-8. Effect of Environmental and Loading Conditions on Modulus Ratio (at a Given Strain Level) of Normally Consolidated and Moderately Overconsolidated Soils

Increasing Factor	G/G_{\max}
Confining pressure, σ'_m	Increases with σ'_m ; effect decreases with increasing PI
Void ratio, e	Increases with e
Geologic age, t_g	May increase with t_g
Cementation, c	May increase with c
Overconsolidation ratio, OCR	Not affected
Plasticity index, PI	Increases with PI
Cyclic strain, γ_c	Decreases with γ_c
Strain rate, $\dot{\gamma}$	G increases with $\dot{\gamma}$ but G/G_{\max} probably not affected if G and G_{\max} are measured at same $\dot{\gamma}$
Number of loading cycles, N	Decreases after N cycles of large γ_c (G_{\max} measured before N cycles) for clays; for sands, can increase (under drained conditions) or decrease (under undrained conditions)

Source: Modified from Dobry and Vucetic (1987).

cyclic strain amplitude (Figure 6.45). The PI = 0 damping curve from Figure 6.45 is nearly identical to the average damping curve that was used for coarse-grained soils when they

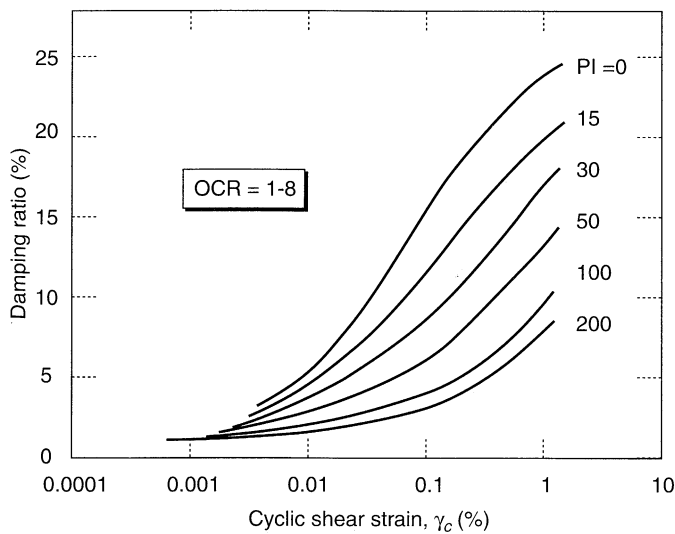


Figure 6.45 Variation of damping ratio of fine-grained soil with cyclic shear strain amplitude and plasticity index. (After Vucetic and Dobry (1991). Effect of soil plasticity on cyclic response, *Journal of Geotechnical Engineering*, Vol. 117, No. 1. Reprinted by permission of ASCE.)

were treated separately from fine-grained soils. This similarity suggests that the damping curves of Figure 6.45 can be applied to both fine- and coarse-grained soils. The damping behavior of gravel is very similar to that of sand (Seed et al., 1984).

Damping behavior is also influenced by effective confining pressure, particularly for soils of low plasticity. Ishibashi and Zhang (1993) developed an empirical expression for the damping ratio of plastic and nonplastic soils. Using equation (6.52) to compute the modulus reduction factor, G/G_{\max} , the damping ratio is given by

$$\xi = 0.333 \frac{1 + \exp(-0.0145\text{PI}^{1.3})}{2} \left[0.586 \left(\frac{G}{G_{\max}} \right)^2 - 1.547 \frac{G}{G_{\max}} + 1 \right] \quad (6.54)$$

The influence of various environmental and loading conditions on the damping ratio of normally consolidated and moderately overconsolidated soils is described in Table 6-9.

6.4.3 Cyclic Nonlinear Models

The nonlinear stress-strain behavior of soils can be represented more accurately by cyclic nonlinear models that follow the actual stress-strain path during cyclic loading. Such models are able to represent the shear strength of the soil, and with an appropriate pore pressure generation model, changes in effective stress during undrained cyclic loading. A variety of cyclic nonlinear models have been developed; all are characterized by (1) a backbone curve and (2) a series of “rules” that govern unloading-reloading behavior, stiffness degradation, and other effects. The simplest of these models have relatively simple backbone curves and only a few basic rules. More complex models may incorporate many additional rules that allow the model to better represent the effects of irregular loading, densification, pore pressure generation, or

Table 6-9. Effect of Environmental and Loading Conditions on Damping Ratio of Normally Consolidated and Moderately Overconsolidated Soils

Increasing Factor	Damping ratio, ξ
Confining pressure, σ'_m	Decreases with σ'_m ; effect decreases with increasing PI
Void ratio, e	Decreases with e
Geologic age, t_g	Decreases with t_g
Cementation, c	May decrease with c
Overconsolidation ratio, OCR	Not affected
Plasticity index, PI	Decreases with PI
Cyclic strain, γ_c	Increases with γ_c
Strain rate, $\dot{\gamma}$	Stays constant or may increase with $\dot{\gamma}$
Number of loading cycles, N	Not significant for moderate γ_c and N

Source: Modified from Dobry and Vucetic (1987).

other effects. The applicability of cyclic nonlinear models, however, is generally restricted to a fairly narrow, albeit important range of initial conditions and stress paths.

The performance of cyclic nonlinear models can be illustrated by a very simple example in which the shape of the backbone curve is described by $\tau = F_{bb}(\gamma)$. The shape of any backbone curve is tied to two parameters, the initial (low-strain) stiffness and the (high-strain) shear strength of the soil. For the simple example, the backbone function, $F_{bb}(\gamma)$, can be described by a hyperbola

$$F_{bb}(\gamma) = \frac{G_{\max}\gamma}{1 + (G_{\max}/\tau_{\max})|\gamma|} \quad (6.55)$$

The shape of the hyperbolic backbone curve is illustrated in Figure 6.46. Other expressions [e.g., the Ramberg–Osgood model (Ramberg and Osgood, 1943)] can also be used to describe the backbone curve. Alternatively, backbone curves can be constructed from modulus reduction curves.

The quantities G_{\max} and τ_{\max} may be measured directly, computed, or obtained by empirical correlation. For the example model, the response of the soil to cyclic loading is governed by the following four rules:

1. For initial loading, the stress–strain curve follows the backbone curve.

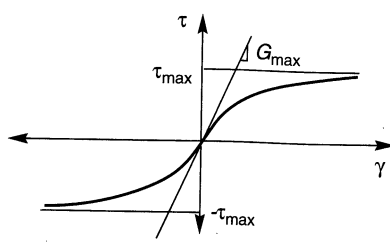


Figure 6.46 Hyperbolic backbone curve asymptotic to $\tau = G_{\max} \gamma$ and to $\tau = \tau_{\max}$ (and $\tau = -\tau_{\max}$).

2. If a stress reversal occurs at a point defined by (γ_r, τ_r) , the stress-strain curve follows a path given by

$$\frac{\tau - \tau_r}{2} = F_{bb} \left(\frac{\gamma - \gamma_r}{2} \right)$$

In other words, the unloading and reloading curves have the same shape as the backbone curve (with the origin shifted to the loading reversal point) but is enlarged by a factor of 2. These first two rules, which describe *Masing behavior* (Masing, 1926), are not sufficient to describe soil response under general cyclic loading. As a result, additional rules are needed.

3. If the unloading or reloading curve exceeds the maximum past strain and intersects the backbone curve, it follows the backbone curve until the next stress reversal.
 4. If an unloading or reloading curve crosses an unloading or reloading curve from the previous cycle, the stress-strain curve follows that of the previous cycle.

Models that follow these four rules are often called *extended Masing models*. An example of the extended Masing model is shown in Figure 6.47. Cyclic loading begins at point A, and the stress-strain curve during initial loading (from A to B) follows the backbone curve as required by rule 1. At point B, the loading is reversed and the unloading portion of the stress-strain curve moves away from B along the path required by rule 2. Note that the initial unloading modulus is equal to G_{max} . The unloading path intersects the backbone curve at point C and, according to rule 3, continues along the backbone curve until the next loading reversal at point D. The reloading curve then moves away from D as required by rule 2, and the process is repeated for the remainder of the applied loading. Although this model is very simple and is expressed only in terms of effective stresses, it inherently incorporates the hysteretic nature of damping and the strain-dependence of the shear modulus and damping ratio. Other unloading-reloading models are available (e.g., Iwan, 1967; Finn et al., 1977; Vucetic, 1990); the Cundall-Pyke model (Pyke, 1979) is particularly straightforward and easily implemented into ground response analyses. To avoid spurious response at very low strain levels, some cyclic nonlinear models require the addition of a small

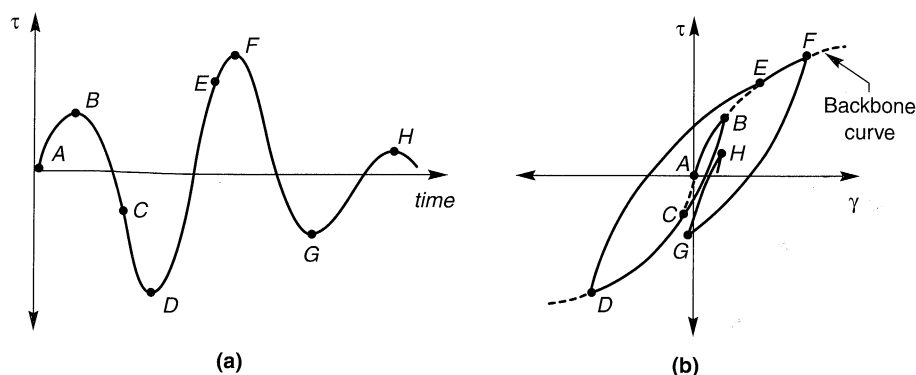


Figure 6.47 Extended Masing rules: (a) variation of shear stress with time; (b) resulting stress-strain behavior (backbone curve indicated by dashed line).

amount of low strain damping. Note that the cyclic nonlinear model does not require the shear strain to be zero when the shear stress is zero. The ability to represent the development of permanent strains is one of the most important advantages of cyclic nonlinear models over equivalent linear models.

This simple example model does not, however, allow for the determination of shear-induced volumetric strains that can lead to hardening under drained conditions or to pore pressure development with attendant stiffness degradation under undrained conditions. Such factors are accounted for in the majority of the cyclic nonlinear models commonly used in geotechnical earthquake engineering practice (e.g., Finn et al., 1977; Pyke, 1979, 1985).

The ability to compute changes in pore pressure, hence also changes in effective stress, represents another significant advantage of cyclic nonlinear models over equivalent linear models. As pore pressures increase, effective stresses decrease, and consequently the values of G_{\max} and τ_{\max} decrease. Since the shape and position of the backbone curve depends on G_{\max} and τ_{\max} , the backbone curve “degrades” with increasing pore pressure. As with actual soils, the stiffness in a stress–strain model depends not only on the cyclic strain amplitude, as implied by the equivalent linear model, but also on the stress history of the soil. When incorporated into computational models for ground response analysis, cyclic nonlinear models allow prediction of the generation, redistribution, and eventual dissipation of pore pressures during and after earthquake shaking. These capabilities are very useful for evaluation of liquefaction hazards (Chapter 9).

6.4.4 Advanced Constitutive Models

The most accurate and general methods for representation of soil behavior are based on advanced constitutive models that use basic principles of mechanics to describe observed soil behavior for (a) general initial stress conditions, (b) a wide variety of stress paths, (c) rotating principal stress axes, (d) cyclic or monotonic loading, (e) high or low strain rates, and (f) drained or undrained conditions.

Such models generally require a *yield surface* that describes the limiting stress conditions for which elastic behavior is observed, a *hardening law* that describes changes in the size and shape of the yield surface as plastic deformation occurs, and a *flow rule* that relates increments of plastic strain to increments of stress. The Cam–Clay (Roscoe and Schofield, 1963) and modified Cam–Clay (Roscoe and Burland, 1968) models were among the first of this type. Improvements in the prediction of shear strains have resulted from the use of multiple nested yield loci within the yield surface (Mroz, 1967; Prevost, 1977) and the development of bounding surface models (Dafalias and Popov, 1979) which incorporate a smooth transition from elastic to plastic behavior. Detailed treatment of such advanced constitutive models is beyond the scope of this book. The interested reader can refer to a number of sources, including Desai and Siriwardane (1984), Dafalias and Herrmann (1982), Wroth and Housley (1985), Lade (1988), and Wood (1991).

Although advanced constitutive models allow considerable flexibility and generality in modeling the response of soils to cyclic loading, their description usually requires many more parameters than equivalent linear models or cyclic nonlinear models. Evaluation of these parameters can be difficult, and the parameters obtained from one type of test can be different from those obtained from another. Although the use of advanced constitutive models will undoubtedly increase, these practical problems have, to date, limited their use in geotechnical earthquake engineering practice.

6.4.5 Discussion

A hierarchy of models are available for characterization of the stress-strain behavior of cyclically loaded soils. The models range considerably in complexity and accuracy; a model that is appropriate for one type of problem may not be appropriate for another. No single stress-strain model is appropriate for all problems. Selection of a stress-strain model requires careful consideration of the problem to which it is to be applied, recognition of the assumptions and limitations of the available models, and a good understanding of how the model is used in all required analyses.

6.5 STRENGTH OF CYCLICALLY LOADED SOILS

The effect of cyclic loading on the limiting strength of soils is of considerable importance in geotechnical earthquake engineering. Problems of slope stability, foundation performance, and retaining wall behavior, among others, are strongly influenced by the strength that the soil can mobilize at large strains.

Soil strength behavior is most conveniently discussed in terms of coarse-grained cohesionless soils and fine-grained cohesive soils under drained and undrained conditions. Earthquake loading is generally applied so rapidly that all but the most permeable of soils are loaded under undrained conditions. The strength of cohesionless soils is inextricably tied to the phenomenon of liquefaction, a problem so important in geotechnical earthquake engineering that it is treated in a separate chapter (Chapter 9). The following discussion is directed toward the effect of cyclic loading on the undrained shear strength of cohesive soils.

6.5.1 Definitions of Failure

The shear strength of an element of soil is typically defined as the shear stress mobilized at the point of “failure,” but failure can be defined in many different ways. In the field, failure is usually associated with deformations that exceed some serviceability limit. Since deformation results from the integration of strains over some volume of soil, the point of failure of an element of soil is often defined in terms of a limiting strain.

Consider an element of soil in drained equilibrium under anisotropic stress conditions in a cyclic direct simple shear test (point A in Figure 6.48). The application of a cyclic shear stress, τ_{cyc} , produces (under stress-controlled conditions) a cyclic shear strain, γ_{cyc} , but also an increase in the average strain, γ_{ave} . The average shear strain increases with increasing numbers of loading cycles. Clearly, the strength of the soil during cyclic loading could be defined in terms of limiting values of γ_{cyc} or γ_{ave} or of some combination of the two. The available strength of the soil under monotonic loading (after the cyclic loading has ended) may also be of interest.

The following sections discuss two measures of the strength of a cyclically loaded soil. The “cyclic” strength is based on a limiting value of cyclic and/or average strain *during cyclic loading* (although the soil may not actually be in a state of failure as defined by effective stress conditions). The “monotonic” strength is the ultimate static strength that can be mobilized *after cyclic loading has ended*.

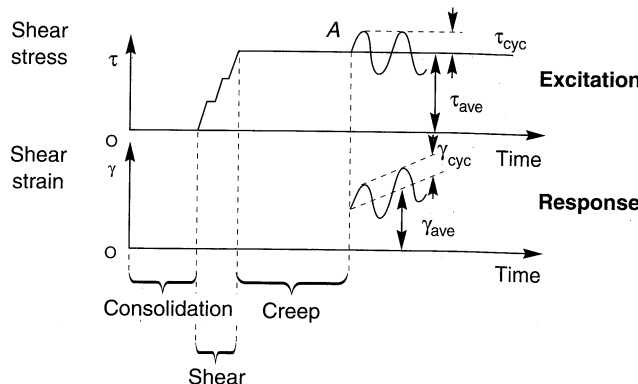


Figure 6.48 Definitions of average and cyclic shear stress and shear strain. (After Goulois et al., 1985. Used by permission of ASTM.)

6.5.2 Cyclic Strength

The levels of both cyclic and permanent deformations are of interest in a number of geotechnical earthquake engineering problems. They are also important in the design of foundations for marine structures subjected to wave loading, and much of the current state of knowledge of cyclic strength has come from research in that area. The cyclic strength of an element of soil depends on the relationship between the average shear stress, τ_{ave} , and the cyclic shear stress, τ_{cyc} . When the average shear stress is low, unidirectional strains will accumulate slowly, so the average shear strain will also be low. The amplitude of the cyclic strain, however, may become large if the cyclic shear stress is large. If, on the other hand, the average shear stress is high (relative to the static shear strength, s_u), substantial unidirectional strains can develop even when the cyclic shear stress is small.

For the case of $\tau_{ave} = 0$, no unidirectional strain will develop, so failure must be defined in terms of the cyclic shear strain, γ_{cyc} . When failure is defined in terms of a specific level of cyclic shear strain (often 3 percent), the *cyclic strength ratio*, defined as τ_{cyc}/s_u , decreases with increasing numbers of cycles, as shown in Figure 6.49. At cyclic stress ratios below some limiting value, however, the failure strain will never be reached (i.e., stable response will be achieved). This limiting cyclic stress ratio, referred to as the *critical level of repeated loading* (CLRL) by Sangrey et al. (1969), increases with increasing soil plasticity. Hermann and Houston (1980) found CLRL values ranging from 0.05 for a nonplastic silt to 0.55 for San Francisco Bay mud.

For cases in which τ_{ave} is greater than zero, both γ_{cyc} and γ_{ave} will depend on τ_{cyc} and τ_{ave} (Seed and Chan, 1966). Investigations of the cyclic response of marine clays (e.g., Meimon and Hicher, 1980; Goulois et al., 1985; Andersen et al., 1988) have shown that γ_{cyc} depends predominantly on τ_{cyc} and the number of cycles, and γ_{ave} depends predominantly on τ_{ave} and the number of cycles (Figure 6.50).

In the development of a procedure for estimating earthquake-induced permanent deformations in dams and embankments, Makdisi and Seed (1978) defined the dynamic yield strength of soils that exhibit small changes in pore pressure under undrained loading as 80% of the undrained strength of the soil. Substantial permanent deformations can develop when the total (static plus cyclic) shear stress exceeds the dynamic yield strength.

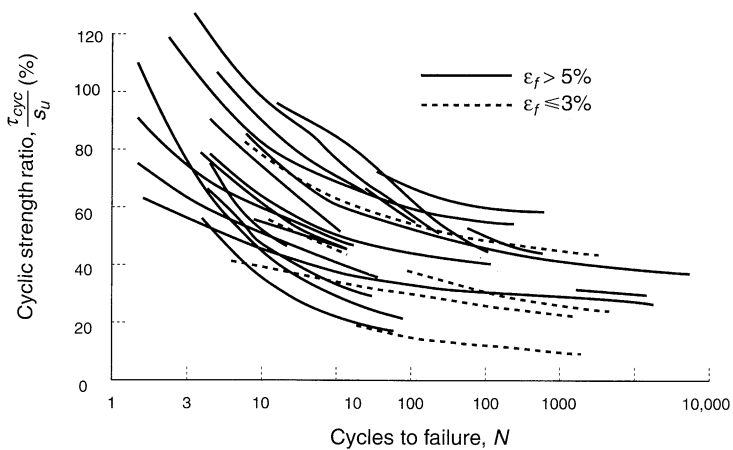


Figure 6.49 Variation of cyclic strength ratio with number of cycles for different soils.
(After Lee and Focht, 1976.)

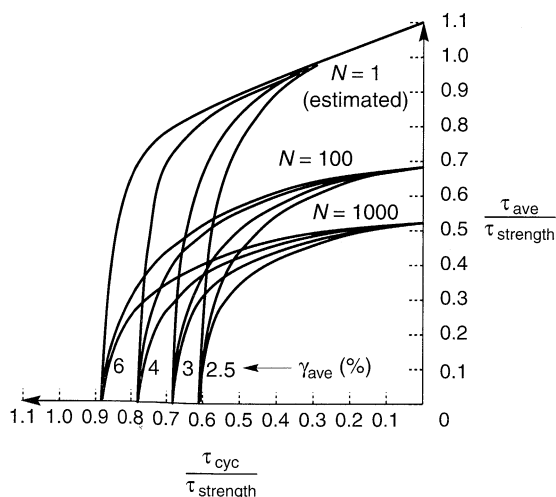


Figure 6.50 Variation of average shear strain with average shear stress, cyclic shear stress, and number of cycles in cyclic direct simple shear tests on plastic Drammen clay. τ_{strength} is a reference strength measured under slow loading conditions with $\tau_{\text{ave}} = 0$. Cyclic loading applied at a period of 10 sec.
(After Goulois et al., 1985. Used by permission of ASTM.)

6.5.3 Monotonic Strength

Evaluation of the static stability of slopes and retaining walls and the capacity of foundations after earthquake shaking has ended is another important problem in geotechnical earthquake engineering. Such problems require evaluation of the available shear strength of the soil after the earthquake has ended. This postearthquake strength must reflect any effects of cyclic loading imposed by the earthquake.

As pointed out by Castro and Christian (1976), the ultimate (residual, high-strain) undrained shear strength of a saturated soil is controlled by its void ratio and structure. Barring any change in soil structure, a saturated soil at a particular void ratio will mobilize a

specific undrained strength, with little influence of the history of stresses and strains by which that strength is arrived at. For such soil conditions, the undrained strength after cyclic loading will be equal to the undrained strength before undrained loading (at the same strain rate). Since cyclic loading induces positive excess pore pressures, the effective stress in an element of soil sheared monotonically after being subjected to cyclic loading will be lower than that in an identical element that is sheared monotonically without prior cyclic loading. Consequently, the element that had been cycled would be expected to exhibit more dilative behavior but to have a lower stiffness in the early stages of monotonic undrained loading than the element that had not been cycled.

Changes in monotonic strength can be caused by disturbance of the soil structure during cyclic loading. The extent to which the structure of the soil is disturbed is influenced by the relationship between the cyclic strain amplitude and the strain at which failure occurs under monotonic loading conditions (Thiers and Seed, 1969). Substantial structural disturbance can modify the stress-strain behavior and reduce the monotonic shear strength. The six triaxial specimens shown in Figure 6.51 had similar void ratios (except specimen 6, which had a somewhat higher void ratio than the rest) at the end of consolidation. Specimen 1 was sheared monotonically immediately after consolidation, but specimens 2 to 6 were first subjected to varying levels of cyclic loading. Since the void ratios were nearly the same, the specimens would therefore be expected to have similar monotonic strengths. As shown by the stress-strain curves and stress paths, they behaved largely as would be expected. After being subjected to different levels of cyclic strain, their ultimate (large strain) strengths were similar (except specimen 6, which was lower than the others). Differences in the ultimate strength can be explained by small differences in the void ratios and also by differences in the extent of structural disturbance induced by the cyclic loading.

Thiers and Seed (1969) found that the ultimate strength of three clays decreased by less than 10% when the cyclic strain amplitude was less than one-half of the failure strain from monotonic tests. At higher cyclic strain amplitudes, the reduction in strength was more

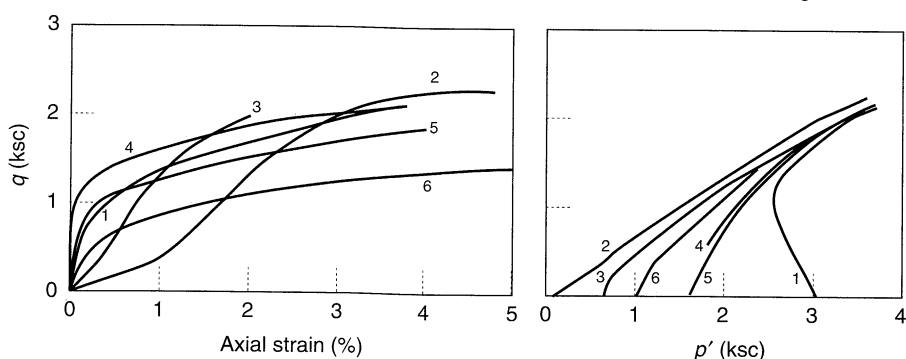


Figure 6.51 Effect of cyclic loading on subsequent monotonic undrained loading behavior of triaxial specimens of a slightly plastic silt: (a) stress-strain behavior; (b) effective stress path behavior. Specimen 1 was tested in conventional CU test with no prior cyclic loading. Specimens 2 to 6 were subjected to different levels of cyclic loading prior to monotonic loading. Note the dilative nature of the stress paths of specimens 2 to 6 compared to specimen 1. (After Castro and Christian, 1976.)

dramatic, as illustrated in Figure 6.52. Similar results have been obtained by others (e.g., Koutsoftas, 1978; Byrne et al., 1984).

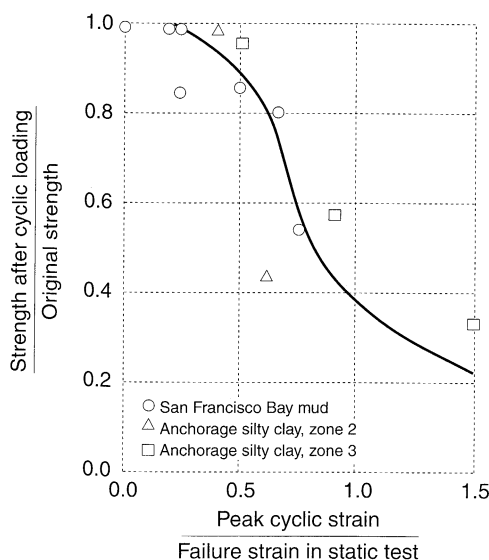


Figure 6.52 Effect of peak cyclic strain on monotonic strength after cyclic loading. (After Thiers and Seed, 1969. Used by permission of ASTM.)

6.6 SUMMARY

1. Earthquake damage is strongly influenced by the dynamic response of soil deposits. The cyclic nonlinear and strength characteristics of soils govern their dynamic response during earthquakes.
2. The measurement of dynamic soil properties is an important aspect of geotechnical earthquake engineering. A variety of field and laboratory techniques are available; some are oriented toward measurement of low-strain behavior and others toward measurement of soil behavior at high strain levels.
3. Field tests allow measurement of soil properties in situ; the complex effects of existing stress, chemical, thermal, and structural conditions are therefore reflected in the measured soil properties. Many field tests measure the response of large volumes of soil and induce soil deformation similar to those induced by earthquakes. Because in situ conditions cannot be easily controlled or varied, field tests do not allow measurement of the behavior of the soil under other stress states or soil conditions.
4. A number of field tests measure low-strain soil properties, particularly wave propagation velocities. These tests include seismic reflection, seismic refraction, steady-state vibration, spectral analysis of surface waves, seismic crosshole, seismic downhole (and uphole), and seismic cone tests. Other field tests, such as the standard penetration, cone penetration, dilatometer, and pressuremeter tests, measure the properties of the soil at higher strain levels.

5. Laboratory tests allow the control and measurement of stresses, strains, and porewater pressures. As a result, they can often simulate anticipated initial and dynamic stress conditions better than field tests. The results of laboratory tests, however, may be influenced by sample disturbance. Sample disturbance has a particularly strong effect on low-strain properties.
6. Several laboratory tests measure low-strain soil properties. Among these are the resonant column test, the ultrasonic pulse test, and the piezoelectric bender element test. The cyclic triaxial test, cyclic direct shear test, and cyclic torsional shear test can be used to measure dynamic soil properties at higher strain levels.
7. Dynamic soil properties may also be inferred from the results of model tests. Shaking table tests can accommodate relatively large models, but their inability to produce high gravitational stresses can make extrapolation to prototype conditions difficult. Centrifuge tests can satisfy similitude requirements much better than shaking table tests but must be performed on relatively small models.
8. Soils exhibit nonlinear, inelastic, stress-strain behavior under cyclic loading conditions. At low strain levels, the stiffness of a soil is greatest and the damping is smallest. At higher strain levels, the effects of nonlinearity and inelasticity increase, producing lower stiffness and greater damping. Complete characterization of such behavior is very complicated. For the great majority of geotechnical earthquake engineering analyses, however, approximate characterization is sufficient. Three broad classes of stress-strain models are used for geotechnical earthquake engineering analyses: equivalent linear models, cyclic nonlinear models, and advanced constitutive models.
9. Equivalent linear models treat soils as a linear viscoelastic materials. Nonlinear behavior is accounted for by the use of strain-dependent stiffness and damping parameters. The stiffness of the soil is usually characterized by the maximum shear modulus, which is mobilized at low strains, and a modulus reduction curve, which shows how the shear modulus decreases at larger strains. Damping behavior is characterized by the damping ratio, which increases with increasing strain amplitude. The shapes of the modulus reduction and damping curves are influenced by soil plasticity and, for soils of very low plasticity, by effective confining pressure.
10. Cyclic nonlinear models represent the nonlinear, inelastic behavior of soils using a nonlinear backbone curve and a series of rules that govern unloading-reloading behavior. Backbone curves are usually described by simple functions that reflect the transition from the initial stiffness (at low strain levels) to the ultimate strength (at high strain levels). The unloading-reloading rules control the behavior of the model during stress reversals and ensure that it behaves in a manner similar to that exhibited by actual soils subjected to irregular cyclic loading. In contrast to equivalent linear models, cyclic nonlinear models allow permanent strains to develop. Cyclic nonlinear models can also be coupled with pore pressure generation models to predict changes in effective stress during cyclic loading. Modeling such behavior requires that the original backbone curve be degraded (softened) as pore pressures increase.

11. Advanced constitutive models use basic principles of mechanics to describe soil behavior for general initial stress conditions, a wide variety of stress paths with rotating principal stresses, cyclic or monotonic loading, high or low strain rates, and drained or undrained conditions. As such, they are much more general than equivalent linear or cyclic nonlinear models. The penalty for this increased generality comes in the form of increased complexity, an increased number of model parameters (some of which can be difficult to determine), and increased computational effort when incorporated into ground response or soil-structure interaction analyses.
12. The shear strength of soil can be influenced by cyclic loading. The level of permanent strain that develops in a cyclically loaded element of soil depends on the relationship between the average (static) shear stress and the cyclic shear stress. If the average shear stress is zero, only cyclic strains will develop and failure is defined in terms of a limiting cyclic strain level. If the average shear stress is greater than zero, cyclic stresses can produce unidirectional as well as cyclic shear strains. The rate at which unidirectional strain develops is influenced by the relative magnitudes of the average and cyclic shear stresses. The ultimate strength of a soil loaded monotonically after an episode of cyclic loading is also important. Because the undrained of a saturated soil is controlled by its density and structure, the postearthquake undrained strength will (barring structural changes) be essentially the same as the static undrained strength, even if excess pore pressures have developed during cyclic loading.

HOMEWORK PROBLEMS

- 6.1** At a level site, bedrock is overlain by a layer of overconsolidated clay of variable thickness. A seismic refraction survey is conducted with 13 receivers placed on a straight line between two shot points located 1,000 ft apart. From the p-wave arrival times listed below, determine and plot the subsurface profile in the central 800 ft portion of the survey. Determine the p-wave velocities of the overconsolidated clay and the underlying bedrock.

Receiver	Distance from SP 1	Arrival time from SP 1 (msec)	Distance from SP 2	Arrival time from SP 2 (msec)
A	0	0	1000	124
B	50	15	950	119
C	100	30	900	114
D	200	48	800	105
E	300	58	700	96
F	400	67	600	85
G	500	78	500	75
H	600	91	400	73
I	700	108	300	68
J	800	113	200	47
K	900	115	100	30
L	950	119	50	15
M	1000	124	0	0

- 6.2** The figure below shows the vertical response of geophones located at the same depths in vertical boreholes spaced 5 m apart. The waves recorded at the geophones resulted from downward (solid lines) and upward (dashed lines) impacts on a mechanical source at the same depth in a third borehole that was colinear with the other two boreholes. Determine the average SV-wave velocity of the soil between the geophones.

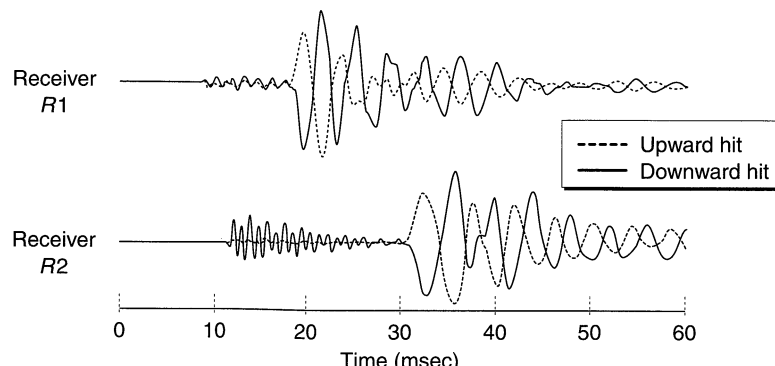


Figure P6.2

- 6.3** Estimate the damping ratio of the resonant column specimen from which the frequency response curve of Figure E6.7 was obtained.
- 6.4** Portions of the time histories of deviator stress and axial strain from a stress-controlled cyclic triaxial test are shown below. Compute the secant shear modulus and damping ratio of the test specimen. Assuming that the soil is saturated and its response is consistent with the Masing criteria, estimate the maximum shear modulus of the soil.

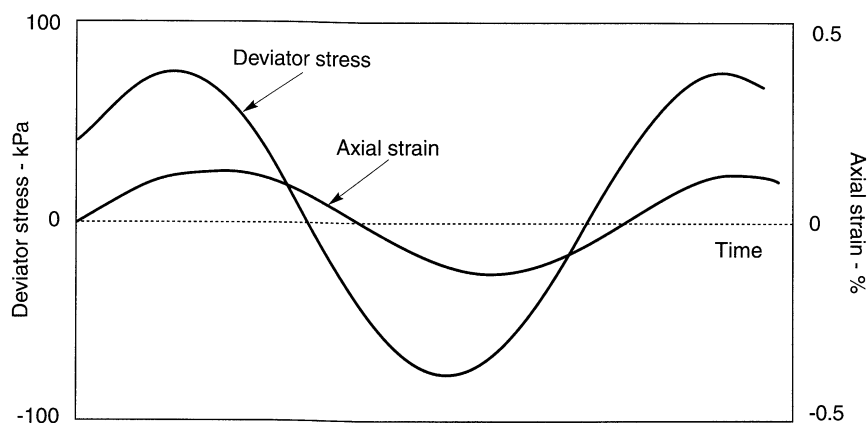


Figure P6.4

- 6.5** A site is underlain by about 14 m of hydraulic fill sand with the following properties.

Grain size characteristics: $D_{10} < 0.074 \text{ mm}$

$$D_{30} = 0.14 \text{ mm}$$

$$D_{50} = 0.17 \text{ mm}$$

$$D_{60} = 0.20 \text{ mm}$$

Saturated unit weight = 18.8 kN/m^3

Average uncorrected SPT resistance = 6 blows/ft

Average cone tip resistance = 3 MPa

The groundwater table is located at a depth of 2m.

- (a) Estimate the shear wave velocity of the hydraulic fill at a depth of 5 m by as many procedures as the available data will support.

- (b) Shear wave velocity measurements at this site have indicated hydraulic fill shear wave velocities ranging from about 120 m/sec - 200 m/sec at 5 m depth with an average value of about 170 m/sec. Comment on the level of agreement between the estimated shear wave velocities from Part (a) and the measured shear wave velocities.

- 6.6** At the site described in Problem 6.5, the hydraulic fill is underlain by a 15 m thick deposit of medium stiff, normally consolidated silty clay with the following properties:

Water content = 40%

Liquid limit = 46

Plastic limit = 23

Saturated unit weight = 15.9 kN/m^3

Cone tip resistance = 8 to 14 kg/cm^2

Undrained shear strength = 27 to 61 kPa

- (a) Estimate the shear wave velocity of the silty clay at a depth of 20 m by as many procedures as the available data will support.

- (b) Shear wave velocity measurements at this site have indicated silty clay shear wave velocities ranging from about 120 m/sec - 180 m/sec at 20 m depth with an average value of about 155 m/sec. Comment on the level of agreement between the estimated shear wave velocities from Part (a) and the measured shear wave velocities.

- 6.7** Determine and plot the backbone curve that would correspond to the Vucetic-Dobry modulus reduction curve for a clay with PI = 15.

- 6.8** Compute and plot the modulus reduction curve for a silty clay (PI = 30) at a mean effective confining pressure of 40 kPa using the relationship of Ishibashi and Zhang (1993). How does this curve compare with that shown in Figure 6.42?

- 6.9** Compute and plot the damping ratio curves that correspond to the modulus reduction curves shown in Figure 6.43. Comment on the influence of effective confining pressure on damping characteristics of low and high plasticity soils.
- 6.10** An element of soil with a maximum shear modulus of 700,000 psf and an undrained strength of 1000 psf is subjected to the time history of shear stress shown below. Assuming that the backbone curve is hyperbolic, and that the soil follows the extended Masing criteria, plot the resulting stress-strain behavior. Mark all points at which the unloading-reloading rules governing the stress-strain behavior change (i.e. mark as 1-2 at the point where control over the stress-strain response shifts from Rule 1 to Rule 2).

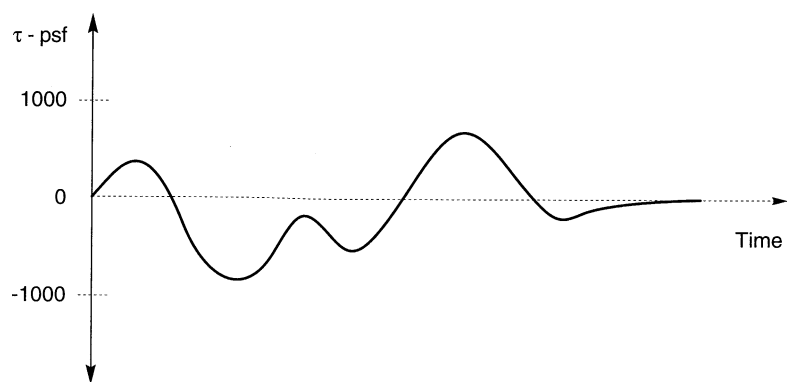
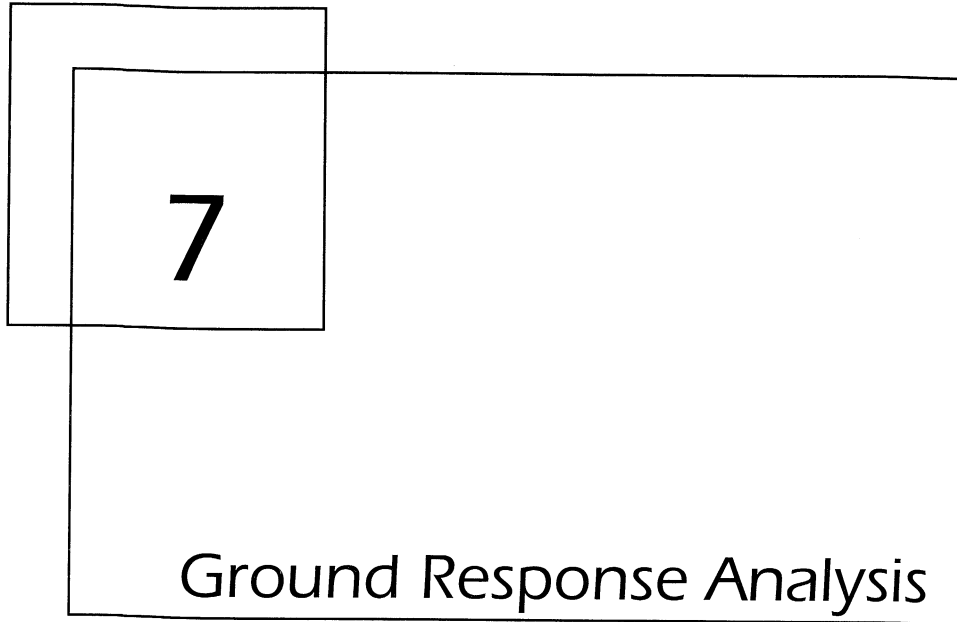


Figure P6.10



7

Ground Response Analysis

7.1 INTRODUCTION

One of the most important and most commonly encountered problems in geotechnical earthquake engineering is the evaluation of ground response. *Ground response analyses* are used to predict ground surface motions for development of design response spectra, to evaluate dynamic stresses and strains for evaluation of liquefaction hazards, and to determine the earthquake-induced forces that can lead to instability of earth and earth-retaining structures.

Under ideal conditions, a complete ground response analysis would model the rupture mechanism at the source of an earthquake, the propagation of stress waves through the earth to the top of bedrock beneath a particular site, and would then determine how the ground surface motion is influenced by the soils that lie above the bedrock. In reality, the mechanism of fault rupture is so complicated and the nature of energy transmission between the source and the site so uncertain that this approach is not practical for common engineering applications. In practice, empirical methods based on the characteristics of recorded earthquakes are used to develop predictive relationships of the types discussed in Chapter 3. These predictive relationships are often used in conjunction with a seismic hazard analysis to predict bedrock motion characteristics at the site. The problem of ground response analysis then becomes one of determining the response of the soil deposit to the motion of the bedrock immediately beneath it. Despite the fact that seismic waves may travel through tens

of kilometers of rock and often less than 100 m of soil, the soil plays a very important role in determining the characteristics of the ground surface motion.

The influence of local soil conditions on the nature of earthquake damage has been recognized for many years. Since the 1920s, seismologists and, more recently, geotechnical earthquake engineers have worked toward the development of quantitative methods for predicting the influence of local soil conditions on strong ground motion. Over the years, a number of techniques have been developed for ground response analysis. The techniques are often grouped according to the dimensionality of the problems they can address, although many of the two- and three-dimensional techniques are relatively straightforward extensions of corresponding one-dimensional techniques. This chapter describes the most commonly used methods for one-, two-, and three-dimensional ground response, and introduces the problem of soil–structure interaction.

7.2 ONE-DIMENSIONAL GROUND RESPONSE ANALYSIS

When a fault ruptures below the earth's surface, body waves travel away from the source in all directions. As they reach boundaries between different geologic materials, they are reflected and refracted. Since the wave propagation velocities of shallower materials are generally lower than the materials beneath them, inclined rays that strike horizontal layer boundaries are usually reflected to a more vertical direction. By the time the rays reach the ground surface, multiple refractions have often bent them to a nearly vertical direction (Figure 7.1). One-dimensional ground response analyses are based on the assumption that all boundaries are horizontal and that the response of a soil deposit is predominantly caused by SH-waves propagating vertically from the underlying bedrock. For one-dimensional ground response analysis, the soil and bedrock surface are assumed to extend infinitely in the horizontal direction. Procedures based on this assumption have been shown to predict ground response that is in reasonable agreement with measured response in many cases.

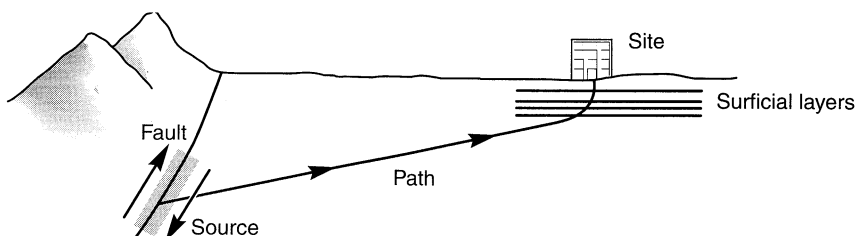


Figure 7.1 Refraction process that produces nearly vertical wave propagation near the ground surface.

Before describing any of the ground response models, it is necessary to define several terms that are commonly used to describe ground motions. With reference to Figure 7.2a, the motion at the surface of a soil deposit is the *free surface motion*. The motion at the base of the soil deposit (also the top of bedrock) is called a *bedrock motion*. The motion at a location where bedrock is exposed at the ground surface is called a *rock outcropping motion*. If the soil deposit was not present (Figure 7.2b), the motion at the top of bedrock would be the *bedrock outcropping motion*.

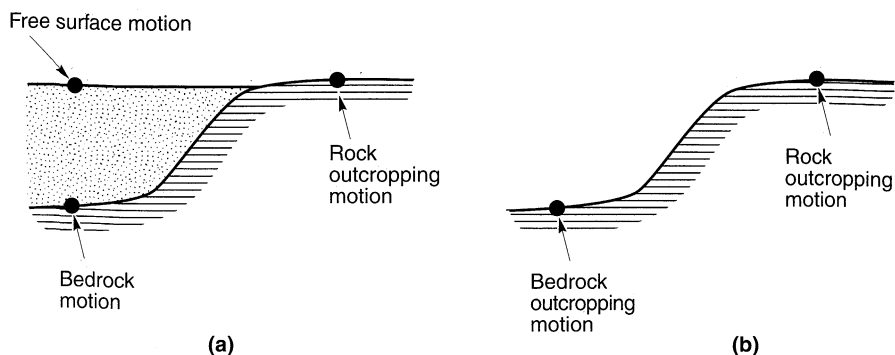


Figure 7.2 Ground response nomenclature: (a) soil overlying bedrock; (b) no soil overlying bedrock. Vertical scale is exaggerated.

7.2.1 Linear Approach

The manner in which transfer functions can be used to compute the response of single-degree-of-freedom systems is illustrated in Appendix B (Section B.5.4.2). An important class of techniques for ground response analysis is also based on the use of transfer functions. For the ground response problem, transfer functions can be used to express various response parameters, such as displacement, velocity, acceleration, shear stress, and shear strain, to an input motion parameter such as bedrock acceleration. Because it relies on the principle of superposition, this approach is limited to the analysis of linear systems. Non-linear behavior can be approximated, however, using an iterative procedure with equivalent linear soil properties.

The mathematical aspects of the transfer function approach were described in Section B.5.4.2 of Appendix B. Although the calculation involve manipulation of complex numbers, the approach itself is quite simple. A known time history of bedrock (input) motion is represented as a Fourier series, usually using the FFT (Section A.3.4). Each term in the Fourier series of the bedrock (input) motion is then multiplied by the transfer function to produce the Fourier series of the ground surface (output) motion. The ground surface (output) motion can then be expressed in the time domain using the inverse FFT. Thus the transfer function determines how each frequency in the bedrock (input) motion is amplified, or deamplified, by the soil deposit.

7.2.1.1 Evaluation of Transfer Functions

The key to the linear approach is the evaluation of transfer functions. In the following sections, transfer functions are derived for a series of successively more complicated geotechnical conditions. Although the simplest of these may only rarely be applicable to actual problems, they illustrate some of the important effects of soil deposits on ground motion characteristics without undue mathematical complexity. The more complex are capable of describing the most important aspects of ground response and are very commonly used in geotechnical earthquake engineering practice.

Uniform Undamped Soil on Rigid Rock. First, consider a uniform layer of isotropic, linear elastic soil overlying rigid bedrock as shown in Figure 7.3. Harmonic horizontal motion of the bedrock will produce vertically propagating shear waves in the overlying soil. The resulting horizontal displacement can be expressed, using the results of Section 5.2.1.3, as

$$u(z, t) = Ae^{i(\omega t + kz)} + Be^{i(\omega t - kz)} \quad (7.1)$$

where ω is the circular frequency of ground shaking, k the wave number ($= \omega/v_s$) and A and B the amplitudes of waves traveling in the $-z$ (upward) and $+z$ (downward) directions, respectively. At the free surface ($z = 0$), the shear stress, and consequently the shear strain, must vanish; that is,

$$\tau(0, t) = G\gamma(0, t) = G \frac{\partial u(0, t)}{\partial z} = 0 \quad (7.2)$$

Substituting (7.1) into (7.2) and differentiating yields

$$Gik(Ae^{ik(0)} - Be^{-ik(0)})e^{i\omega t} = Gik(A - B)e^{i\omega t} = 0 \quad (7.3)$$

which is satisfied (nontrivially) when $A = B$. The displacement can then be expressed as

$$u(z, t) = 2A \frac{e^{ikz} + e^{-ikz}}{2} e^{i\omega t} = 2A \cos kz e^{i\omega t} \quad (7.4)$$

which describes a *standing wave* of amplitude $2A \cos kz$. The standing wave is produced by the constructive interference of the upward and downward traveling waves and has a fixed shape with respect to depth. Equation (7.4) can be used to define a transfer function that describes the ratio of displacement amplitudes at any two points in the soil layer. Choosing these two points to be the top and bottom of the soil layer gives the transfer function

$$F_1(\omega) = \frac{u_{\max}(0, t)}{u_{\max}(H, t)} = \frac{2Ae^{i\omega t}}{2A \cos kz e^{i\omega t}} = \frac{1}{\cos kz} = \frac{1}{\cos (\omega H/v_s)} \quad (7.5)$$

The modulus of the transfer function is the amplification function

$$|F_1(\omega)| = \sqrt{\{\text{Re}[F_1(\omega)]\}^2 + \{\text{Im}[F_1(\omega)]\}^2} = \frac{1}{|\cos (\omega H/v_s)|} \quad (7.6)$$

which indicates that the surface displacement is always at least as large as the bedrock displacement (since the denominator can never be greater than 1) and, at certain frequencies, is

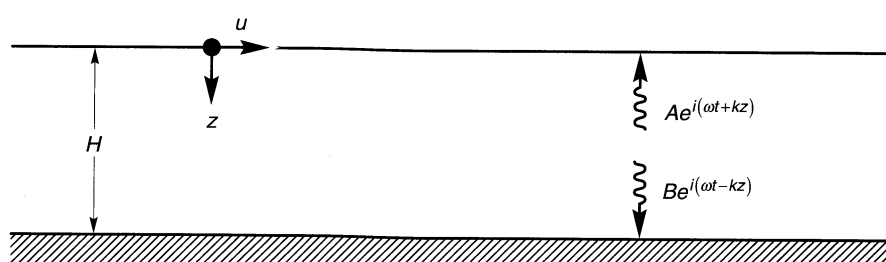


Figure 7.3 Linear elastic soil deposit of thickness H underlain by rigid bedrock.

much larger. Thus $|F_1(\omega)|$ is the ratio of the free surface motion amplitude to the bedrock motion amplitude (or, since the bedrock is rigid in this case, the bedrock outcropping motion). As $\omega H/v_s$ approaches $\pi/2 + n\pi$, the denominator of equation (7.6) approaches zero, which implies that infinite amplification, or *resonance*, will occur (Figure 7.4). Even this very simple model illustrates that the response of a soil deposit is highly dependent upon the frequency of the base motion, and that the frequencies at which strong amplification occurs depend on the geometry (thickness) and material properties (s-wave velocity) of the soil layer.

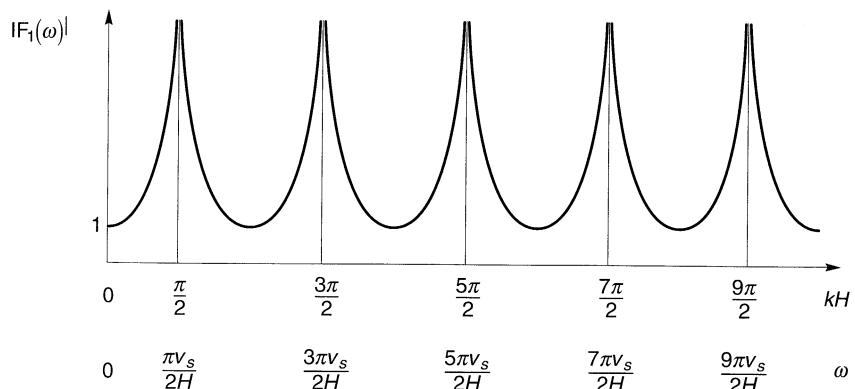


Figure 7.4 Influence of frequency on steady-state response of undamped linear elastic layer.

Example 7.1

Compute the time history of acceleration at the surface of the linear elastic soil deposit shown in Figure E7.1a in response to the E-W component of the Gilroy No. 1 (rock) motion (Figure 3.1).

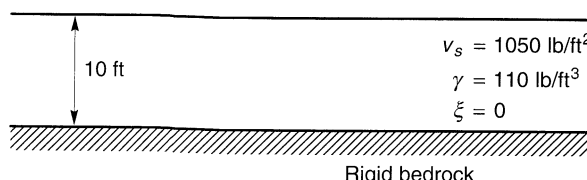


Figure E7.1a

Solution Computation of the ground surface motion from the bedrock motion can be accomplished in the following series of steps:

1. Obtain the time history of acceleration of the input motion. In this case the input motion is the E-W component of the Gilroy No. 1 (rock) motion shown in Figure E7.1b. The Gilroy No. 1 record consists of 2000 acceleration values at 0.02-sec intervals.
2. Compute the Fourier series of the bedrock (input) motion. The Fourier series is complex valued; its one-sided Fourier amplitude spectrum (Section A.3 of Appendix A) is shown in Figure E7.1c. The Fourier amplitude spectrum is defined for frequencies up to $1/2\Delta t = 25 \text{ Hz}$, but most of the energy in the bedrock motion is at frequencies less than 5 to 10 Hz.
3. Compute the transfer function that relates the ground surface (output) motion to the bedrock (input) motion. From equation (7.5), the transfer function (Figure E7.1d) for the case of undamped soil is real valued. The transfer function has values of 1 below frequencies

of about 10 Hz. However, at frequencies that approach the fundamental frequency of the soil deposit ($f_0 = v_s/4H = 26.25$ Hz), the transfer function begins to take on large values.

4. Compute the Fourier series of the ground surface (output) motion as the product of the transfer function and the Fourier series of the bedrock (input) motion. At frequencies less than 5 to 10 Hz, the Fourier spectrum of the ground surface motion is virtually the same as that of the bedrock motion. Although the transfer function indicates that frequencies above 20 Hz or so will be amplified strongly, the input motion is weak in that frequency range. The one-sided amplitude spectrum is shown in Figure E7.1e. Examination of this Fourier amplitude spectrum indicates that the ground surface motion has somewhat more high-frequency motion, but is generally similar to that of the bedrock motion.
5. Obtain the time history of the ground surface motion by inverting its Fourier series. As illustrated in Figure E7.1f, the time history of ground surface motion has a somewhat greater content of high-frequency components, but is generally similar to the time history of bedrock motion.

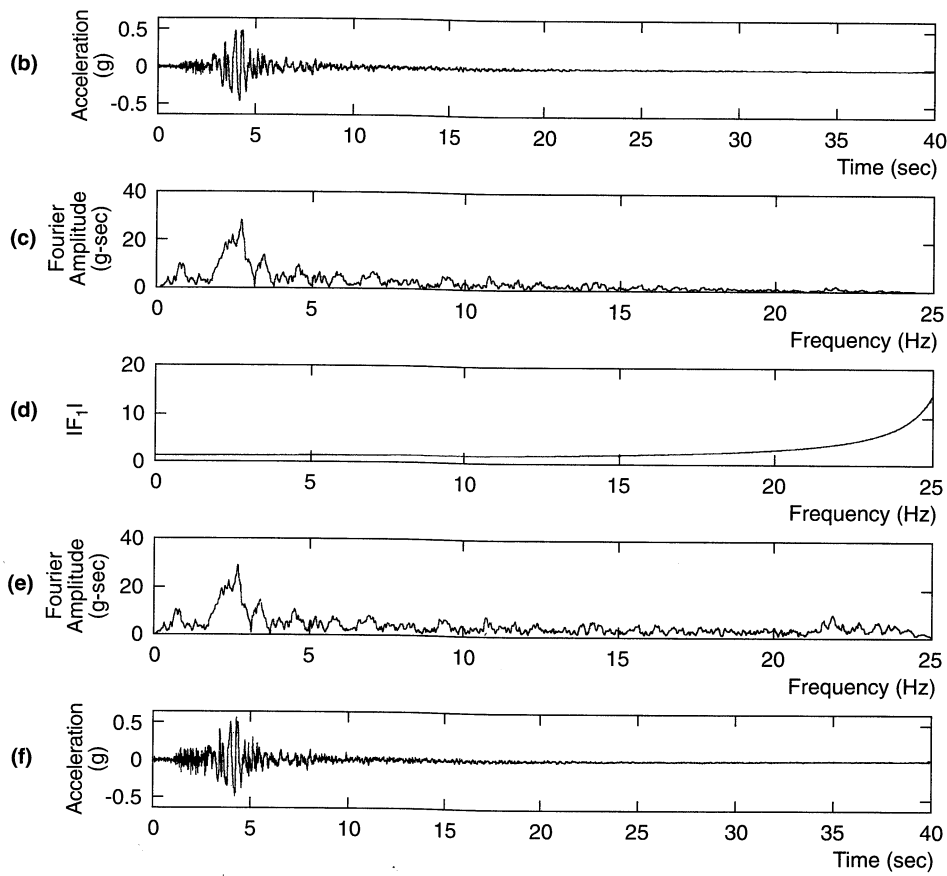


Figure E7.1b-f

Because the soil layer had a high natural frequency (intentionally selected to avoid the extremely large transfer function values that exist near the natural frequency of an undamped layer), its effect on the ground surface motion was relatively small.

Uniform, Damped Soil on Rigid Rock. Obviously, the type of unbounded amplification predicted by the previous analysis cannot physically occur. The previous analysis assumed no dissipation of energy, or damping, in the soil. Since damping is present in all materials, more realistic results can be obtained by repeating the analysis with damping. Assuming the soil to have the shearing characteristics of a Kelvin–Voigt solid, the wave equation can be written [equation (5.94)] as

$$\rho \frac{\partial^2 u}{\partial t^2} = G \frac{\partial^2 u}{\partial z^2} + \eta \frac{\partial^3 u}{\partial z^2 \partial t} \quad (7.7)$$

As shown in equation (5.94), the solution to this wave equation is of the form

$$u(z, t) = A e^{i(\omega t + k^* z)} + B e^{i(\omega t - k^* z)}$$

where k^* is a complex wave number with real part k_1 and imaginary part k_2 . Repeating the previous algebraic manipulations with the complex wave number, the transfer function for the case of damped soil over rigid rock can be expressed as

$$F_2(\omega) = \frac{1}{\cos k^* H} = \frac{1}{\cos(\omega H/v_s^*)} \quad (7.8)$$

Since the frequency-independent complex shear modulus (Section 5.5.1) is given by $G^* = G(1 + i2\xi)$, the complex shear wave velocity can be expressed as

$$v_s^* = \sqrt{\frac{G^*}{\rho}} = \sqrt{\frac{G(1 + i2\xi)}{\rho}} \approx \sqrt{\frac{G}{\rho}}(1 + i\xi) = v_s(1 + i\xi) \quad (7.9)$$

for small ξ . Then the complex wave number can be written, again for small ξ , as

$$k^* = \frac{\omega}{v_s^*} = \frac{\omega}{v_s(1 + i\xi)} \approx \frac{\omega}{v_s}(1 - i\xi) = k(1 - i\xi) \quad (7.10)$$

and finally, the transfer function, as

$$F_2(\omega) = \frac{1}{\cos k(1 - i\xi)H} = \frac{1}{\cos [\omega H/v_s(1 + i\xi)]} \quad (7.11)$$

Using the identity $|\cos(x + iy)| = \sqrt{\cos^2 x + \sinh^2 y}$, the amplification function can be expressed as

$$|F_2(\omega)| = \frac{1}{\sqrt{\cos^2 kH + \sinh^2 \xi kH}} \quad (7.12)$$

Since $\sinh^2 y \approx y^2$ for small y , the amplification function can be simplified to

$$|F_2(\omega)| \approx \frac{1}{\sqrt{\cos^2 kH + (\xi kH)^2}} = \frac{1}{\sqrt{\cos^2 (\omega H/v_s) + [\xi(\omega H/v_s)]^2}} \quad (7.13)$$

For small damping ratios, equation (7.13) indicates that amplification by a damped soil layer also varies with frequency. The amplification will reach a local maximum whenever $kH \approx \pi/2 + n\pi$ but will never reach a value of infinity since (for $\xi > 0$) the denominator will

always be greater than zero. The frequencies that correspond to the local maxima are the *natural frequencies* of the soil deposit. The variation of amplification factor with frequency is shown for different levels of damping in Figure 7.5. This amplification factor is also equal to the ratio of the free surface motion amplitude to the bedrock (or bedrock outcropping) motion amplitude. Comparing Figures 7.4 and 7.5 shows that damping affects the response at high frequencies more than at lower frequencies.

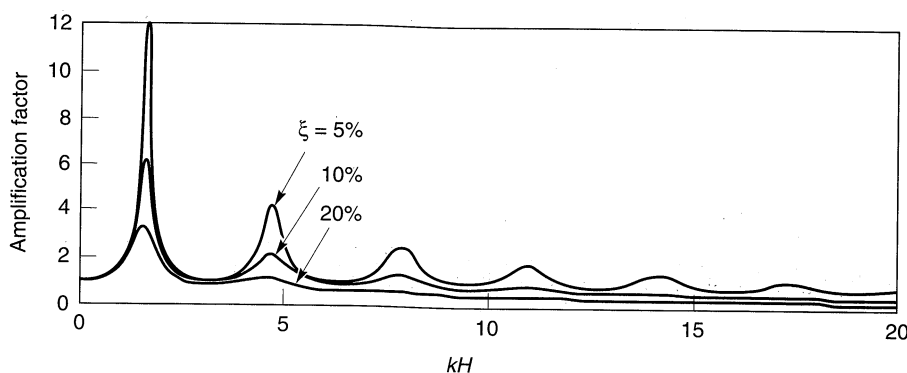


Figure 7.5 Influence of frequency on steady-state response of damped, linear elastic layer.

The *n*th natural frequency of the soil deposit is given by

$$\omega_n \approx \frac{v_s}{H} \left(\frac{\pi}{2} + n\pi \right) \quad n = 0, 1, 2, \dots, \infty \quad (7.14)$$

Since the peak amplification factor decreases with increasing natural frequency, the greatest amplification factor will occur approximately at the lowest natural frequency, also known as the *fundamental frequency*.

$$\omega_0 = \frac{\pi v_s}{2H} \quad (7.15)$$

The period of vibration corresponding to the fundamental frequency is called the *characteristic site period*,

$$T_s = \frac{2\pi}{\omega_0} = \frac{4H}{v_s} \quad (7.16)$$

The characteristic site period, which depends only on the thickness and shear wave velocity of the soil, provides a very useful indication of the period of vibration at which the most significant amplification can be expected.

At each natural frequency, a standing wave develops in the soil. Normalized deformed shapes, or *mode shapes*, for the first three natural frequencies are shown in Figure 7.6. Note that the soil displacements are in phase at all depths in the fundamental mode, but not in the higher modes. At frequencies above the fundamental frequency, part of the soil deposit may be moving in one direction while another part is moving in the opposite direction. This phenomenon must be considered in the evaluation of inertial forces in soil masses required for seismic stability analyses (Chapter 10).

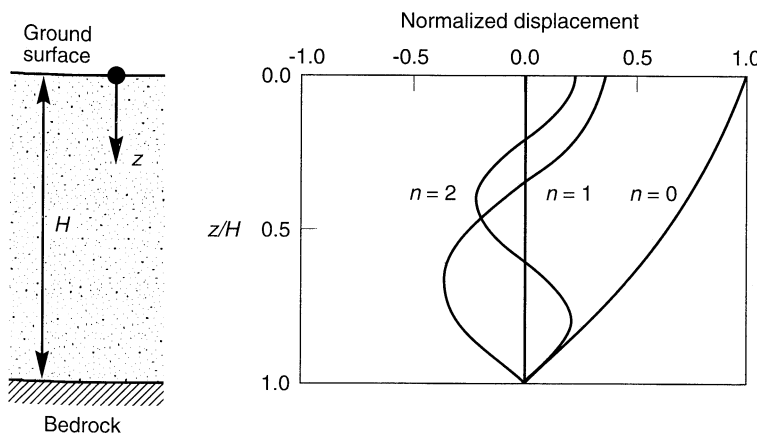


Figure 7.6 Displacement patterns for standing waves at fundamental ($n = 0$), second ($n = 1$) and third ($n = 2$) natural frequencies for a soil layer with $\xi = 5\%$. Displacements are normalized by maximum displacement at the fundamental frequency.

Example 7.2

The site at which the Gilroy No. 2 (soil) earthquake motion shown in Figure 3.1 was recorded is underlain by some 540 ft of soil underlain by shale and serpentinite bedrock. The shear wave velocity of the soil varies from about 1000 ft/sec at depths less than about 130 ft to about 2000 ft/sec at greater depths. Assuming an average shear wave velocity of 1500 ft/sec², an average unit weight of 125 lb/ft³, a damping ratio of 5%, and rigid bedrock (Figure E7.2a), compute the ground surface motion that would occur if the bedrock was subjected to the E-W component of the Gilroy No. 1 (rock) motion.

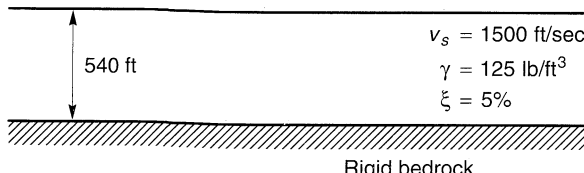


Figure E7.2a

Solution Computation of the ground surface motion from the bedrock motion can be accomplished in the same five steps as described in Example 7.1:

1. Obtain the time history of acceleration of the input motion. This step is identical to step 1 in Example 7.1; the motion is shown in Figure E7.2b.
2. Compute the Fourier series of the bedrock (input) motion. This step is also identical to step 2 in Example 7.1; the result is shown in Figure E7.2c.
3. Compute the transfer function that relates the ground surface (output) motion to the bedrock (input) motion. From equation (7.11), the transfer function for the case of damped soil is complex valued. The modulus of the transfer function is shown in Figure E7.2d. The shape of the transfer function indicates that significant amplification will occur at several natural frequencies, and that higher frequencies (greater than about 10 Hz) will be suppressed.

4. Compute the Fourier series of the ground surface (output) motion as the product of the transfer function and the Fourier series of the bedrock (input) motion. The Fourier spectrum of the ground surface motion (Figure E7.2e) shows amplification at the natural frequencies of the soil deposit and little high-frequency motion.
5. Obtain the time history of the ground surface motion by inverting the Fourier series. The time history of ground surface motion (Figure E7.2f) indicates that peak accelerations at the ground surface and bedrock levels are similar, but the frequency contents are different. Because the ground surface motion is weighted toward lower frequencies, the peak velocity and displacement at the ground surface are likely to be considerably greater than at bedrock.

The rigid bedrock analysis predicts a peak ground surface acceleration of $0.452 g$, which is considerably greater than the peak acceleration of $0.322g$ actually recorded at the Gilroy No. 2 (soil) station.

Uniform, Damped Soil on Elastic Rock. The preceding two sections developed expressions for amplification factors for soils overlying rigid bedrock. If the bedrock is rigid, its motion will be unaffected by motions in, or even the presence of, the overlying

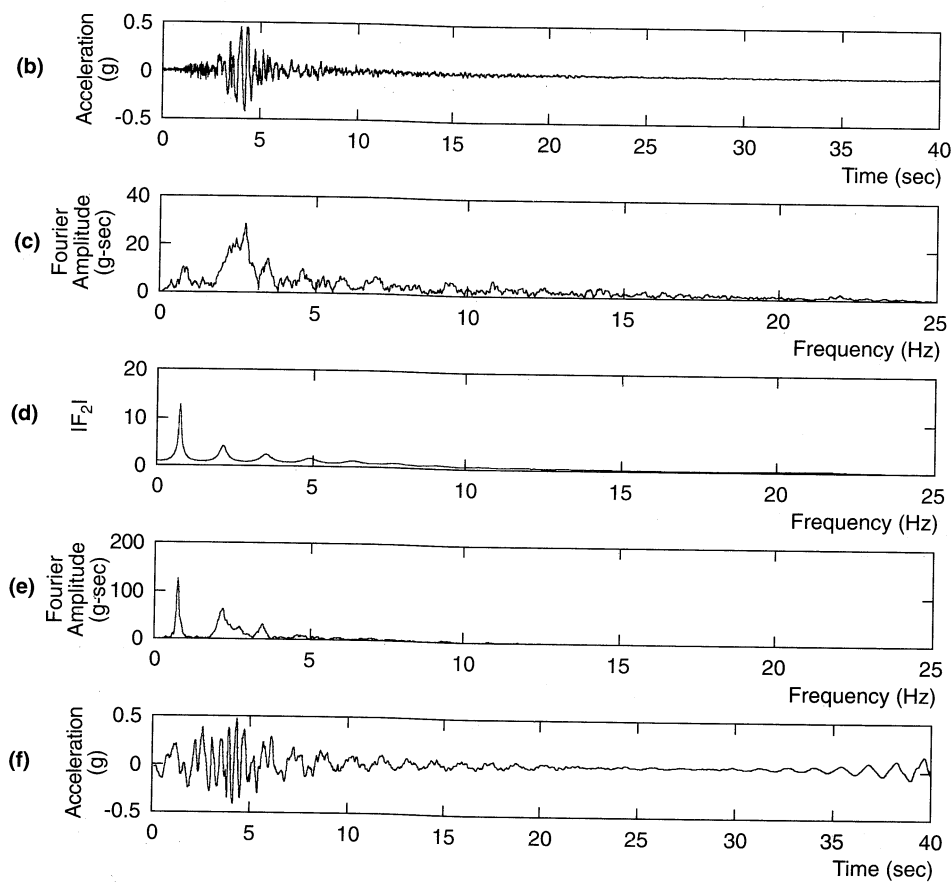


Figure E7.2b-f

soil. It acts as a fixed end (Section 5.4.1) boundary. Any downward-traveling waves in the soil will be completely reflected back toward the ground surface by the rigid layer, thereby trapping all of the elastic wave energy within the soil layer.

If the rock is elastic, however, downward-traveling stress waves that reach the soil–rock boundary will be reflected only partially; part of their energy will be transmitted through the boundary to continue traveling downward through the rock. If the rock extends to great depth (large enough that waves reflected from any deeper material boundaries do not return to the soil–rock boundary soon enough, or with sufficient amplitude, to influence the response of the soil deposit), the elastic energy of these waves will effectively be removed from the soil layer. This is a form of radiation damping, and it causes the free surface motion amplitudes to be smaller than those for the case of rigid bedrock.

Consider the case of a soil layer overlying a halfspace of elastic rock (Figure 7.7). If the subscripts s and r refer to soil and rock, respectively, the displacements due to vertically propagating s -waves in each material can be written as

$$u_s(z_s, t) = A_s e^{i(\omega t + k_s^* z_s)} + B_s e^{i(\omega t - k_s^* z_s)} \quad (7.17a)$$

$$u_r(z_r, t) = A_r e^{i(\omega t + k_r^* z_r)} + B_r e^{i(\omega t - k_r^* z_r)} \quad (7.17b)$$

The free surface effect, as before, requires that $A_s = B_s$, and compatibility of displacements and continuity of stresses at the soil–rock boundary require that

$$u_s(z_s = H) = u_r(z_r = 0) \quad (7.18)$$

$$\tau_s(z_s = H) = \tau_r(z_r = 0) \quad (7.19)$$

Substituting equations (7.17) into equation (7.18) yields

$$A_s(e^{ik_s^* H} + e^{-ik_s^* H}) = A_r + B_r \quad (7.20)$$

From equation (7.19) and the definition of shear stress ($\tau = G \partial u / \partial z$)

$$A_s i G_s k_s^* (e^{ik_s^* H} - e^{-ik_s^* H}) = i G_r k_r^* (A_r - B_r) \quad (7.21)$$

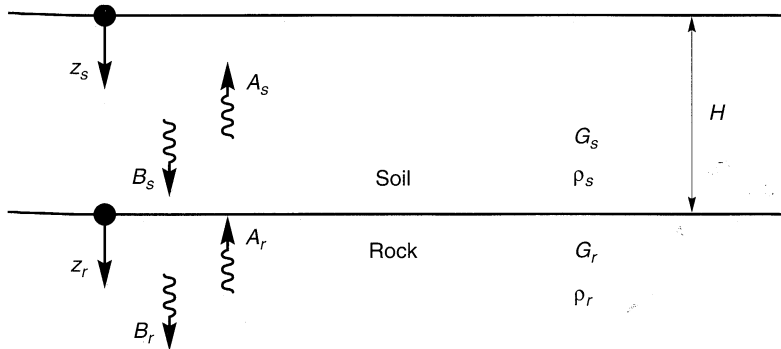


Figure 7.7 Nomenclature for the case of a soil layer overlying a half-space of elastic rock.

or

$$\frac{G_s k_s^*}{G_r k_r^*} A_s (e^{ik_s^* H} - e^{-ik_s^* H}) = A_r - B_r \quad (7.22)$$

The ratio

$$\frac{G_s k_s^*}{G_r k_r^*} = \frac{\rho_s v_{ss}^*}{\rho_r v_{sr}^*} = \alpha_z^* \quad (7.23)$$

where v_{ss}^* and v_{sr}^* are the complex shear wave velocities of the soil and rock, respectively, and α_z^* is the *complex impedance ratio* (see Section 5.4.1). Solving equations (7.20) and (7.22) simultaneously gives

$$A_r = \frac{1}{2} A_s [(1 + \alpha_z^*) e^{ik_s^* H} + (1 - \alpha_z^*) e^{-ik_s^* H}] \quad (7.24a)$$

$$B_r = \frac{1}{2} A_s [(1 - \alpha_z^*) e^{ik_s^* H} + (1 + \alpha_z^*) e^{-ik_s^* H}] \quad (7.24b)$$

Suppose that a vertically propagating shear wave of amplitude, A , traveled upward through the rock. If the soil was not present, the free surface effect at the rock outcrop would produce a bedrock outcropping motion of amplitude $2A$. With the soil present, the free surface motion amplitude would be

$$2A_s = \frac{4A}{(1 + \alpha_z^*) e^{ik_s^* H} + (1 - \alpha_z^*) e^{-ik_s^* H}}$$

Defining the transfer function, F_3 , as the ratio of the soil surface amplitude to the rock outcrop amplitude,

$$F_3(\omega) = \frac{2}{(1 + \alpha_z^*) e^{ik_s^* H} + (1 - \alpha_z^*) e^{-ik_s^* H}} \quad (7.25)$$

which, using Euler's law, can be rewritten as

$$F_3(\omega) = \frac{1}{\cos k_s^* H + i \alpha_z^* \sin k_s^* H} = \frac{1}{\cos(\omega H/v_{ss}^*) + i \alpha_z^* \sin(\omega H/v_{ss}^*)} \quad (7.26)$$

The modulus of $F_3(\omega)$ cannot be expressed in a very compact form when soil damping exists. To illustrate the important effect of bedrock elasticity, however, the amplification factor for undamped soil can be expressed as

$$|F_3(\omega, \xi = 0)| = \frac{1}{\sqrt{\cos^2 k_s^* H + \alpha_z^2 \sin^2 k_s^* H}} \quad (7.27)$$

Note that resonance cannot occur (the denominator is always greater than zero, even when the soil is undamped). The effect of the bedrock stiffness, as reflected by the impedance ratio, on amplification behavior is illustrated in Figure 7.8. Note the similarity between the effects of soil damping and bedrock elasticity by comparing the shapes of the amplification factor curves in Figure 7.8 and those in Figure 7.5. The elasticity of the rock affects amplification

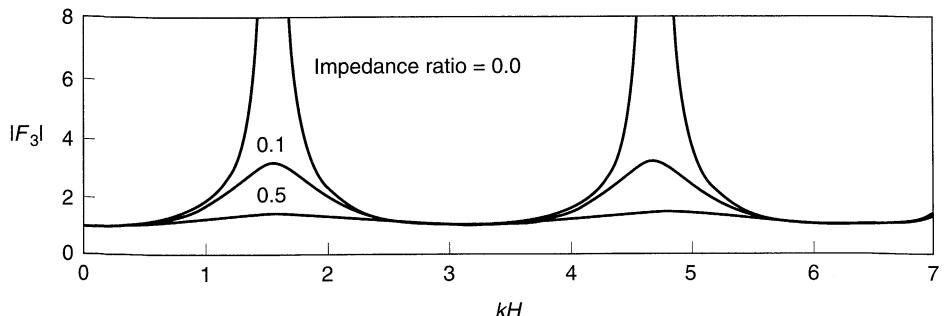


Figure 7.8 Effect of impedance ratio on amplification factor for case of undamped soil.

similarly to the damping ratio of the soil—both prevent the denominator from reaching zero. This radiation damping effect has significant practical importance, particularly in the eastern United States, where bedrock is substantially harder than that typically found in the western states. The stiffer bedrock means that greater amplification may occur in the east and that design criteria established on the basis of empirical evidence from western earthquakes may be somewhat unconservative in the east.

Example 7.3

Repeat Example 7.2 assuming that the bedrock is not rigid. Assume a shear wave velocity of 5000 ft/sec, a unit weight of 160 lb/ft³, and 2% damping for bedrock at the Gilroy No. 2 site (Figure E7.3a).

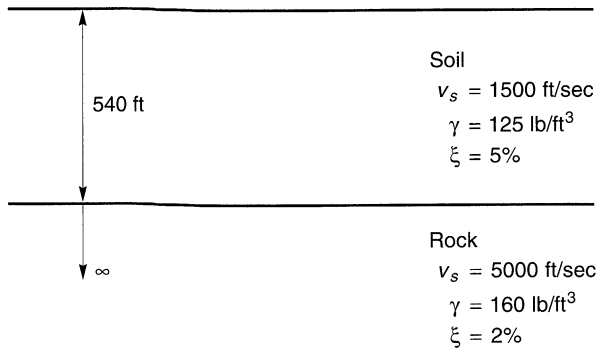


Figure E7.3a

Solution Computation of the ground surface motion from the bedrock motion can be accomplished in the same five steps described in Example 7.2. The only difference is that the transfer function in this example will include the effects of bedrock compliance.

1. Obtain the time history of acceleration of the input motion. This step is identical to step 1 in Examples 7.1 and 7.2; the motion is shown in Figure E7.3b.
2. Compute the Fourier series of the bedrock (input) motion. Again, this step is identical to step 2 in Examples 7.1 and 7.2; the result is shown in Figure E7.3c.
3. Compute the transfer function that relates the ground surface (output) motion to the bedrock (input) motion. From Equation 7.25, the transfer function for the case of damped

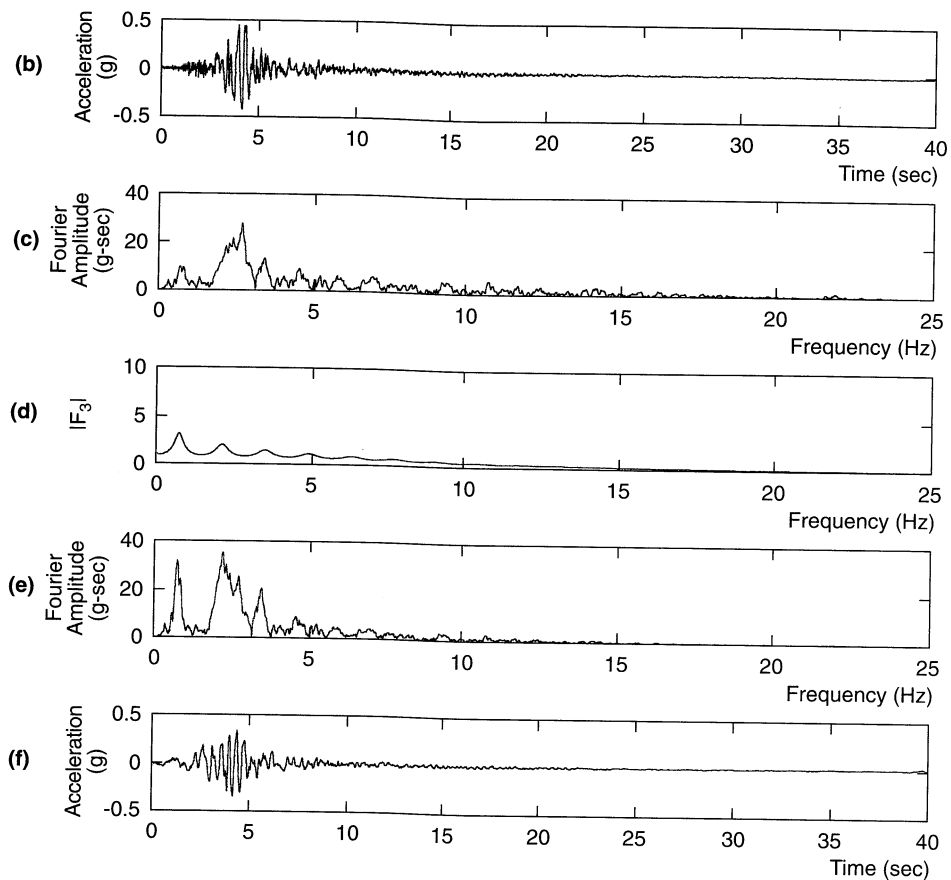


Figure E7.3b-f

soil is complex valued. The modulus of the transfer function, shown in Figure E7.3d, indicates that less amplification will occur than in the case of rigid bedrock.

4. Compute the Fourier series of the ground surface (output) motion as the product of the transfer function and the Fourier series of the bedrock (input) motion. The Fourier series of the ground surface motion (Figure E7.3e) shows less amplification than in the case of rigid bedrock.
5. Obtain the time history of the ground surface motion by inverting the Fourier series. The time history of ground surface motion (Figure E7.3f) indicates that the peak accelerations at the ground surface is lower than the peak acceleration at the bedrock level; the frequency contents are also different.

The compliant bedrock analysis predicts a peak ground surface acceleration of $0.339g$, which agrees well with the peak acceleration of $0.322g$ recorded at the Gilroy No. 2 (soil) station. The good agreement between peak accelerations, however, does not mean that this simple analysis has predicted all aspects of the Gilroy No. 2 (soil) motion. Comparison of the Fourier amplitude spectrum of the predicted motion (Figure E7.3e) with that of the recorded motion (Figure 3.13b) shows significant differences in frequency content.

Layered, Damped Soil on Elastic Rock. While the uniform elastic layer models are useful for illustration of the influence of soil conditions on several ground motion characteristics, they are seldom suitable for analysis of practical ground response problems. Real ground response problems usually involve soil deposits with layers of different stiffness and damping characteristics with boundaries at which elastic wave energy will be reflected and/or transmitted. Such conditions require the development of transfer functions for layered soil deposits.

Consider a soil deposit consisting of N horizontal layers where the N th layer is bedrock (Figure 7.9). Assuming that each layer of soil behaves as a Kelvin–Voigt solid, the wave equation is of the form given in equation (5.94). The solution to the wave equation can be expressed in the form

$$u(z, t) = Ae^{i(\omega t + k^* z)} + Be^{i(\omega t - k^* z)} \quad (7.28)$$

where A and B represent the amplitudes of waves traveling in the $-z$ (upward) and $+z$ (downward) directions, respectively. The shear stress is then given by the product of the complex shear modulus, G^* , and the shear strain, so

$$\tau(z, t) = G^* \frac{\partial u}{\partial z} = (G + i\omega\eta) \frac{\partial u}{\partial z} = G(1 + 2i\xi) \frac{\partial u}{\partial z} \quad (7.29)$$

Introducing a local coordinate system, Z , for each layer, the displacement at the top and bottom of layer m will be

$$u_m(Z_m = 0, t) = (A_m + B_m)e^{i\omega t} \quad (7.30a)$$

$$u_m(Z_m = h_m, t) = (A_m e^{ik_m^* h_m} + B_m e^{-ik_m^* h_m}) e^{i\omega t} \quad (7.30b)$$

Displacements at layer boundaries must be compatible (i.e., the displacement at the top of a particular layer must be equal to the displacement at the bottom of the overlying layer). Applying the compatibility requirement to the boundary between layer m and layer $m+1$, that is,

$$u_m(Z_m = h_m, t) = u_{m+1}(Z_{m+1} = 0, t)$$

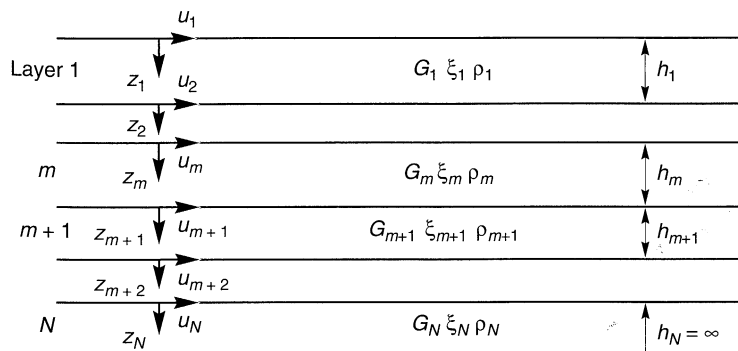


Figure 7.9 Nomenclature for layered soil deposit on elastic bedrock.

yields

$$A_{m+1} + B_{m+1} = A_m e^{ik_m^* h_m} + B_m e^{-ik_m^* h_m} \quad (7.31)$$

The shear stresses at the top and bottom of layer m are

$$\tau_m(Z_m = 0, t) = ik_m^* G_m^*(A_m - B_m) e^{i\omega t} \quad (7.32a)$$

$$\tau_m(Z_m = h_m, t) = ik_m^* G_m^*(A_m e^{ik_m^* h_m} - B_m e^{-ik_m^* h_m}) e^{i\omega t} \quad (7.32b)$$

Since stresses must be continuous at layer boundaries,

$$\tau_m(Z_m = h_m, t) = \tau_{m+1}(Z_{m+1} = 0, t)$$

so

$$A_{m+1} - B_{m+1} = \frac{k_m^* G_m^*}{k_{m+1}^* G_{m+1}^*} (A_m e^{ik_m^* h_m} - B_m e^{-ik_m^* h_m}) \quad (7.33)$$

Adding (7.31) and (7.33) and subtracting (7.33) from (7.31) gives the recursion formulas

$$A_{m+1} = \frac{1}{2} A_m (1 + \alpha_m^*) e^{ik_m^* h_m} + \frac{1}{2} B_m (1 - \alpha_m^*) e^{-ik_m^* h_m} \quad (7.34a)$$

$$B_{m+1} = \frac{1}{2} A_m (1 - \alpha_m^*) e^{ik_m^* h_m} + \frac{1}{2} B_m (1 + \alpha_m^*) e^{-ik_m^* h_m} \quad (7.34b)$$

where α_m^* is the complex impedance ratio at the boundary between layers m and $m+1$:

$$\alpha_m^* = \frac{k_m^* G_m^*}{k_{m+1}^* G_{m+1}^*} = \frac{\rho_m(v_s^*)_m}{\rho_{m+1}(v_s^*)_{m+1}} \quad (7.35)$$

At the ground surface, the shear stress must be equal to zero, which requires [from equation (7.32a)] that $A_1 = B_1$. If the recursion formulas of equation (7.34) are applied repeatedly for all layers from 1 to m , functions relating the amplitudes in layer m to those in layer 1 can be expressed by

$$A_m = a_m(\omega) A_1 \quad (7.36a)$$

$$B_m = b_m(\omega) B_1 \quad (7.36b)$$

The transfer function relating the displacement amplitude at layer i to that at layer j is given by

$$F_{ij}(\omega) = \frac{|u_i|}{|u_j|} = \frac{a_i(\omega) + b_i(\omega)}{a_j(\omega) + b_j(\omega)} \quad (7.37)$$

Because $|u| = \omega |\dot{u}| = \omega^2 |u|$ for harmonic motion, equation (7.37) also describes the amplification of accelerations and velocities from layer i to layer j . Equation (7.37) indicates that the motion in any layer can be determined from the motion in any other layer. Hence if the motion at any one point in the soil profile is known, the motion at any other point can be contributed. This result allows a very useful operation called *deconvolution* (Section 7.2.1.4) to be performed.

Example 7.4

As part of a comprehensive investigation of ground motion estimation techniques, the Electric Power Research Institute performed a detailed subsurface investigation at the site of the Gilroy

No. 2 (soil) recording station (EPRI, 1993). A rough approximation to the measured shear wave velocity profile is listed below.

Depth Range (ft)	Average Shear Wave Velocity (ft/sec)
0–20	500
20–45	700
45–70	1500
70–130	1000
130–540	2000
> 540	5000

Assuming, as in Examples 7.2 and 7.3, an average soil unit weight of 125 lb/ft^3 and 5% soil damping, compute the expected ground surface response when the bedrock is subjected to the Gilroy No. 1 (rock) motion.

Solution As in the previous examples of this chapter, this problem requires evaluation of the transfer function that relates the ground surface motion to the bedrock motion. Because of multiple reflections within the layered system, the transfer function [equation (7.36)] for this example is considerably more complicated than for the single-layered cases of the previous examples. While the transfer function can be evaluated by hand, it has also been coded in the computer program SHAKE (Schnabel et al., 1972). SHAKE was used, with constant soil stiffness and damping ratio, to obtain the transfer function shown in Figure E7.4c. As in the previous examples, the Fourier series of the ground surface motion (Figure E7.4d) was computed as the product of the transfer function and the Fourier series of the bedrock motion. Inversion of this Fourier series produces the time history of ground surface acceleration (Figure E7.4e).

Examination of Figure E7.4c shows that the transfer function for the layered system is indeed more complicated than the transfer functions for the single-layered cases of Examples 7.1, 7.2, and 7.3. The spikes in the transfer function at frequencies of about 3.5 and 5.5 Hz help produce a peak acceleration of $0.499g$ that is considerably larger than the peak acceleration of $0.322g$ that was actually recorded at the Gilroy No. 2 (soil) station. Differences in the frequency contents of the predicted and recorded motions can be seen by comparing Figures E7.4d and 3.13b.

7.2.1.2 Equivalent Linear Approximation of Nonlinear Response

Since the nonlinearity of soil behavior is well known, the linear approach must be modified to provide reasonable estimates of ground response for practical problems of interest. As discussed in Chapter 6, the actual nonlinear hysteretic stress-strain behavior of cyclically loaded soils can be approximated by equivalent linear soil properties. The equivalent linear shear modulus, G , is generally taken as a secant shear modulus and the equivalent linear damping ratio, ξ , as the damping ratio that produces the same energy loss in a single cycle as the actual hysteresis loop. The strain-dependent nature of these equivalent linear properties was described in Section 6.4.2.

Since the linear approach requires that G and ξ be constant for each soil layer, the problem becomes one of determining the values that are consistent with the level of strain induced in each layer. To address this problem, an objective definition of strain level is needed. The laboratory tests from which modulus reduction and damping ratio curves (e.g., those shown in Figures 6.47 and 6.50) have been developed used simple harmonic loading

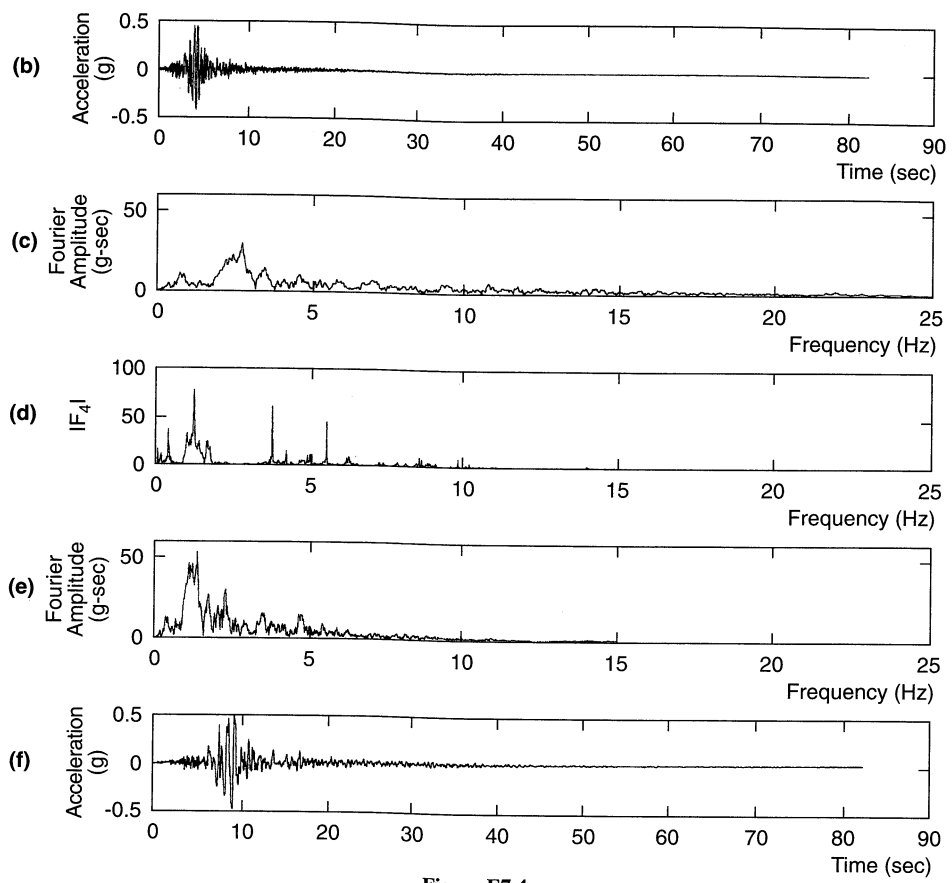


Figure E7.4

and characterized the strain level by the peak shear strain amplitude. The time history of shear strain for a typical earthquake motion, however, is highly irregular with a peak amplitude that may only be approached by a few spikes in the record. Figure 7.10 shows both harmonic (as in a typical laboratory test) and transient (as in a typical earthquake) shear strain time histories that have the same peak cyclic shear strain. Clearly, the harmonic record represents a more severe loading condition than the transient record, although their peak values are identical. As a result, it is common to characterize the strain level of the transient record in terms of an *effective shear strain* which has been empirically found to vary between about 50 and 70% of the maximum shear strain. The computed response is not particularly sensitive to this percentage, however, and the effective shear strain is often taken as 65% of the peak strain.

Since the computed strain level depends on the values of the equivalent linear properties, an iterative procedure is required to ensure that the properties used in the analysis are compatible with the computed strain levels in all layers. Referring to Figure 7.11, the iterative procedure operates as follows:

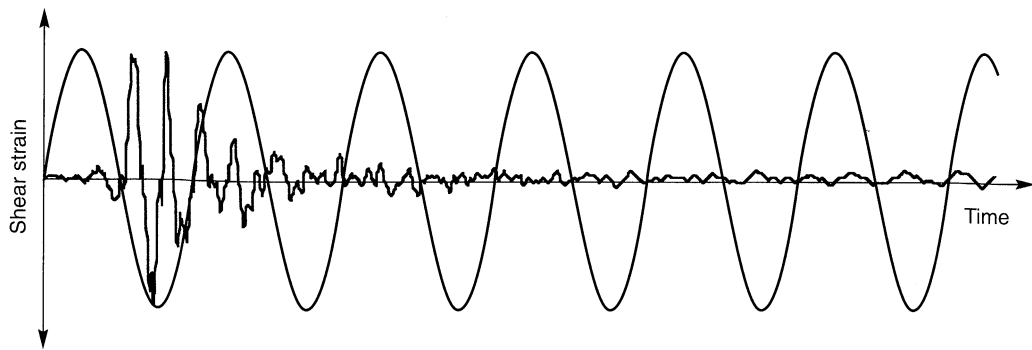


Figure 7.10 Two shear strain time histories with identical peak shear strains. For the transient motion of an actual earthquake, the effective shear strain is usually taken as 65% of the peak strain.

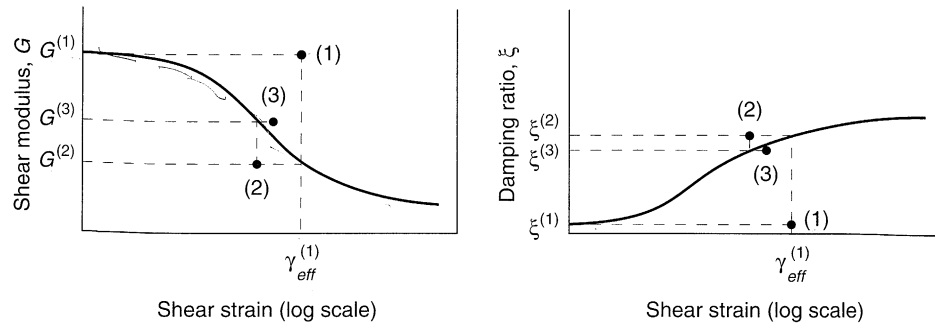


Figure 7.11 Iteration toward strain-compatible shear modulus and damping ratio in equivalent linear analysis. Using initial estimates, $G^{(1)}$ and $\xi^{(1)}$, the equivalent linear analysis predicts an effective shear strain, $\gamma_{\text{eff}}^{(1)}$. Because this strain is greater than those corresponding to $G^{(1)}$ and $\xi^{(1)}$, an iteration is required. The next iteration uses parameters, $G^{(2)}$ and $\xi^{(2)}$, that are compatible with $\gamma_{\text{eff}}^{(1)}$. The equivalent linear analysis is repeated and the parameters checked until strain-compatible value of G and ξ are obtained.

1. Initial estimates of G and ξ are made for each layer. The initially estimated values usually correspond to the same strain level; the low-strain values are often used for the initial estimate.
2. The estimated G and ξ values are used to compute the ground response, including time histories of shear strain for each layer.
3. The effective shear strain in each layer is determined from the maximum shear strain in the computed shear strain time history. For layer j

$$\gamma_{\text{eff},j}^{(i)} = R_\gamma \gamma_{\text{max},j}^{(i)}$$

where the superscript refers to the iteration number and R_γ is the ratio of the effective shear strain to maximum shear strain. R_γ depends on earthquake magnitude (Idriss and Sun, 1992) and can be estimated from

$$R_\gamma = \frac{M - 1}{10}$$

4. From this effective shear strain, new equivalent linear values, $G^{(i+1)}$ and $\xi^{(i+1)}$ are chosen for the next iteration.
5. Steps 2 to 4 are repeated until differences between the computed shear modulus and damping ratio values in two successive iterations fall below some predetermined value in all layers. Although convergence is not absolutely guaranteed, differences of less than 5 to 10% are usually achieved in three to five iterations (Schnabel et al., 1972).

Even though the process of iteration toward strain-compatible soil properties allows nonlinear soil behavior to be approximated, it is important to remember that the complex response method is still a linear method of analysis. The strain-compatible soil properties are constant throughout the duration of the earthquake, regardless of whether the strains at a particular time are small or large. The method is incapable of representing the changes in soil stiffness that actually occur during the earthquake. The equivalent linear approach to one-dimensional ground response analysis of layered sites has been coded into a widely used computer program called SHAKE (Schnabel et al., 1972).

Example 7.5

An extensive laboratory testing program conducted by EPRI (1993) produced detailed information on the modulus reduction and damping characteristics of the soils beneath the Gilroy No. 2 (soil) recording station. Although the soil conditions varied with depth, a rough approximation to the average modulus reduction and damping characteristics is given below.

	Strain (%)										
	10^{-4}	$10^{-3.5}$	10^{-3}	$10^{-2.5}$	10^{-2}	$10^{-1.5}$	10^{-1}	$10^{-0.5}$	10^0	$10^{0.5}$	10^1
G/G_{\max}	1.00	1.00	1.00	0.99	0.90	0.71	0.47	0.24	0.10	0.05	0.04
$\xi (\%)$	3.00	3.00	3.00	3.53	4.83	7.68	12.3	18.5	24.4	27.0	30.0

Repeat the analysis of Example 7.4 with the data listed above using the iterative equivalent linear approach.

Solution As in the case of Example 7.4, the transfer function was evaluated using the computer program SHAKE (Schnabel et al., 1972). In this example the first iteration used the same stiffness and damping values used in Example 7.4. Subsequent iterations used stiffness and damping values that were consistent with the modulus reduction and damping behavior listed above. After a total of eight iterations, the shear moduli and damping ratios had converged to within 1% of strain-compatible values. Because the strain-compatible shear moduli were smaller than the low-strain shear moduli on which the analysis of Example 7.4 was based (the iterations converged to strains at which G/G_{\max} values were less than 1.0), the transfer function (Figure E7.5c) was shifted toward lower frequencies. As in the previous examples, the Fourier series of the ground surface motion (Figure E7.5d) was computed as the product of the transfer function and the Fourier series of the bedrock motion. Inversion of this Fourier series produced the time history of ground surface acceleration shown in Figure E7.5e.

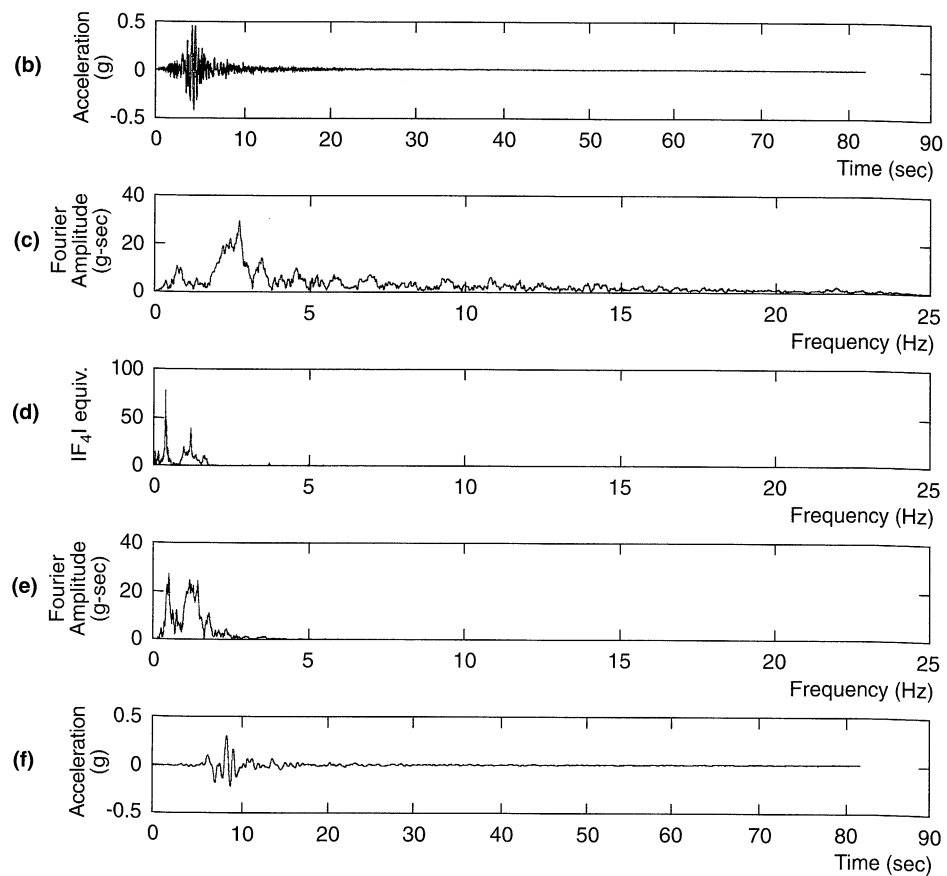


Figure E7.5

The softer soil behavior indicated by the iterative equivalent linear analysis is clearly reflected in the transfer function (Figure E7.5c), the Fourier series of the ground surface motion (Figure E7.5d), and the time history of ground surface acceleration (Figure E7.5e). The predicted peak ground surface acceleration of $0.304g$ compares well with the peak acceleration of $0.322g$ recorded at the Gilroy No. 2 (soil) station, but comparison of the overall motions in the time domain (Figure E7.5e versus Figure 3.1) and frequency domain (Figure E7.5d versus Figure 3.13b) shows significant differences.

The analysis described in this example was intended to illustrate the effects of the equivalent linear approach to approximation of nonlinear soil behavior on computed ground motions. Like Examples 7.2 to 7.4, it characterized the actual soil conditions at the Gilroy No. 2 (soil) site in a simplified manner. More detailed characterization (EPRI, 1993) produced significantly better agreement between predicted and recorded motions.

7.2.1.3 Deconvolution

Because the equivalent linear approach utilizes a linear analysis, the response at any point can be related to the response at any other point. Although the transfer functions developed in Section 7.1.1.1 related to the computation of free surface motion from bedrock

motion, transfer functions relating motions at other depths can also be derived without difficulty. An important problem of practical interest involves the computation of bedrock motion from a known free surface motion. This process, known as *deconvolution*, is particularly useful in the interpretation of actual ground motions recorded on the surfaces of soil deposits.

Although deconvolution of a linear elastic system should theoretically produce a unique solution, practical difficulties often arise. Some of these may be of a numerical nature, particularly when iteration toward strain-compatible soil properties are required (Roessel, 1977) and strain levels are large. Others are associated with limitations in the accuracy of the assumption that all motion results from vertically propagating shear waves. Silva (1988) found that about 75% of the power (87% of the amplitude) in a free surface motion could be attributed to vertically propagating shear waves at frequencies up to 15 Hz; the remainder was attributed to scattered waves and surface waves. Silva suggested a deconvolution procedure based on the use of a prefiltered (15 Hz low-pass to eliminate the tendency to develop unrealistically large accelerations at depth) free surface motion and iteration toward strain-compatible properties using 87% of the input motion amplitudes before deconvolving using the filtered free surface motion at full (100%) amplitude. Deconvolution should be performed with great care and the reasonableness of any deconvolved motion evaluated carefully.

7.2.2 Nonlinear Approach

Although the equivalent linear approach is computationally convenient and provides reasonable results for many practical problems, it remains an approximation to the actual nonlinear process of seismic ground response. An alternative approach is to analyze the actual nonlinear response of a soil deposit using direct numerical integration in the time domain. By integrating the equation of motion in small time steps, any linear or nonlinear stress-strain model (Section 6.4.3) or advanced constitutive model (Section 6.4.4) can be used. At the beginning of each time step, the stress-strain relationship is referred to to obtain the appropriate soil properties to be used in that time step. By this method, a nonlinear inelastic stress-strain relationship can be followed in a set of small incrementally linear steps.

Most currently available nonlinear one-dimensional ground response analysis computer programs characterize the stress-strain behavior of the soil by cyclic stress-strain models (Section 6.4.3) such as the hyperbolic model, modified hyperbolic model, Ramberg-Osgood model, Hardin-Drnevich-Cundall-Pyke (HDCP) model, Martin-Davidenko model, and Iwan-type model. Others have been based on advanced constitutive models (Section 6.4.4), such as the nested yield surface model. Some of the most commonly used computer programs for nonlinear one-dimensional ground response analysis are listed in Table 7-1. A number of techniques can be used to integrate the equations of motion. Of these, the explicit finite-difference technique is most easily explained.

Consider the soil deposit of infinite lateral extent shown in Figure 7.12a. If the soil layer is subjected to horizontal motion at the bedrock level, the response will be governed by the equation of motion

$$\frac{\partial \tau}{\partial z} = \rho \frac{\partial^2 u}{\partial t^2} = \rho \frac{\partial \dot{u}}{\partial t} \quad (7.38)$$

Table 7-1 Computer Programs for Nonlinear One-Dimensional Ground Response Analysis

Program	Soil Model	Reference
CHARSOIL	Ramberg–Osgood	Streeter et al. (1973)
DESRA-2	Hyperbolic	Lee and Finn (1978)
DYNA1D	Nested yield surface	Prevost (1989)
MASH	Martin–Davidenkov	Martin and Seed (1978)
NONLI3	Iwan-type	Joyner (1977)
TESS1	HDCP	Pyke (1985)

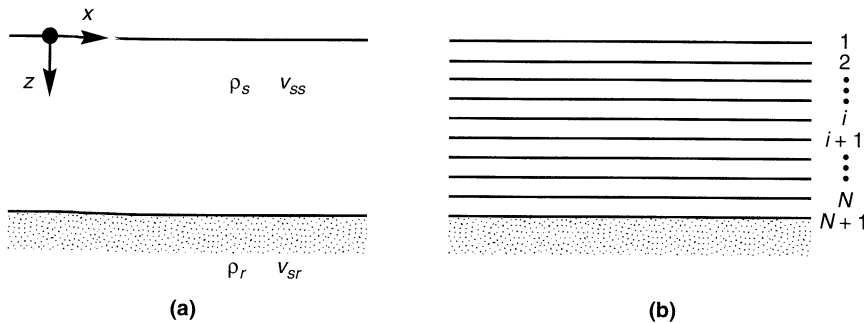


Figure 7.12 (a) Nomenclature for uniform soil deposit of infinite lateral extent overlying bedrock; (b) discretization of soil deposit into N sublayers.

To introduce the explicit finite-difference method, consider the function $f(x)$ shown in Figure 7.13. The first derivative of $f(x)$ at $x = \tilde{x}$ is given by

$$\frac{df(\tilde{x})}{dx} = \lim_{\Delta x \rightarrow 0} \frac{f(\tilde{x} + \Delta x) - f(\tilde{x})}{\Delta x} \quad (7.39)$$

A reasonable approximation to the first derivative can be made by removing the restriction of the limit and using a small but finite value of Δx . In this way the expression of equation (7.39) is referred to as a *forward-difference* approximation to $df(\tilde{x})/dx$. Figure 7.13 illustrates that the forward difference actually provides a better approximation to the derivative at $x = \tilde{x} + \Delta x/2$ than at $x = \tilde{x}$.

Dividing the soil layer into N sublayers of thickness, Δz (Figure 7.12b), and proceeding through time in small time increments of length, Δt , the notation $u_{i,t} = u(z = i \Delta z, t)$ can be used to write finite-difference approximations to the derivatives

$$\frac{\partial \tau}{\partial z} \approx \frac{\tau_{i+1,t} - \tau_{i,t}}{\Delta z} \quad (7.40a)$$

$$\frac{\partial \dot{u}}{\partial t} \approx \frac{\dot{u}_{i,t+\Delta t} - \dot{u}_{i,t}}{\Delta t} \quad (7.40b)$$

Substituting equations (7.40) into the equation of motion allows that differential equation to be approximated by the explicit finite-difference equation

$$\frac{\tau_{i+1,t} - \tau_{i,t}}{\Delta z} = \rho \frac{\dot{u}_{i,t+\Delta t} - \dot{u}_{i,t}}{\Delta t} \quad (7.41)$$

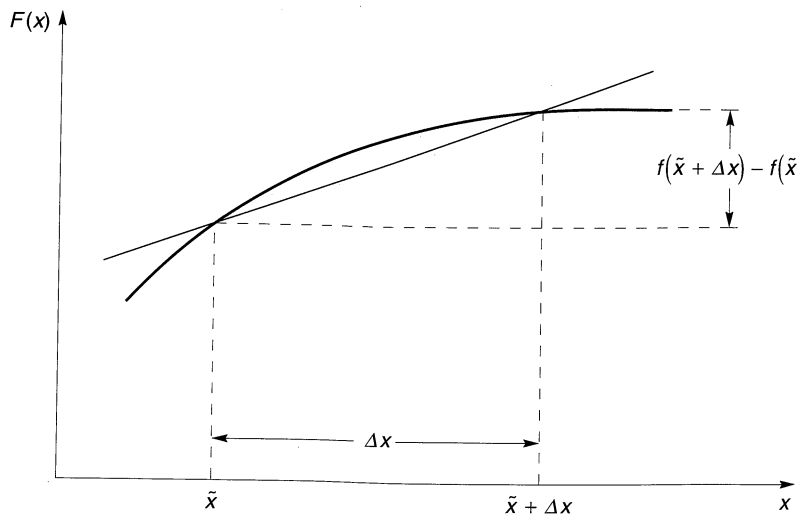


Figure 7.13 Forward-difference approximation of $f'(\tilde{x})$ is given by slope of line passing through function at $x = \tilde{x}$ and $x = \tilde{x} + \Delta x$. Approximation becomes exact as $\Delta x \rightarrow 0$.

Solving for $\dot{u}_{i,t+\Delta t}$ gives

$$\dot{u}_{i,t+\Delta t} = \dot{u}_{i,t} + \frac{\Delta t}{\rho \Delta z} (\tau_{i+1,t} - \tau_{i,t}) \quad (7.42)$$

Equation (7.42) simply shows how the conditions at time, t , can be used to determine the conditions at time, $t + \Delta t$. Using equation (7.42) for all i , the velocity profile can be determined at time $t + \Delta t$. Using the computed velocities at the end of each time step as the initial velocities for the next time step, the repeated application of equation (7.42) allows the equation of motion to be integrated in a series of small time steps.

As with any integration problem, however, the boundary conditions must be satisfied. Since the ground surface is a free surface, $\tau_1 = 0$, so

$$\dot{u}_{1,t+\Delta t} = \dot{u}_{1,t} + \frac{\Delta t}{\rho \Delta z} \tau_{2,t} \quad (7.43)$$

The boundary condition at the bottom of the soil deposit depends on the nature of the underlying bedrock. If the bedrock is rigid, its particle velocity, $\dot{u}_b(t) = \dot{u}_{N+1,t}$, can be specified directly as the input motion. If the bedrock is elastic, continuity of stresses requires that the shear stress at the bottom of the soil layer, $\tau_{N+1,t}$, be equal to the shear stress at the top of the rock layer, $\tau_{r,t}$. Thus

$$\dot{u}_{N+1,t+\Delta t} = \dot{u}_{N+1,t} + \frac{\Delta t}{\rho \Delta z} (\tau_{r,t} - \tau_{N,t}) \quad (7.44)$$

If an incident wave traveling upward through the rock has a particle velocity $\dot{u}_r(t)$ at the soil–rock boundary, the shear stress at the boundary is approximated (Joyner and Chen, 1975) by

$$\tau_{r,t} \approx \rho_r v_{sr} (2\dot{u}_r(t + \Delta t) - \dot{u}_{N+1,t+\Delta t}) \quad (7.45)$$

Substituting equation (7.45) into equation (7.44) and solving for $\dot{u}_{N+1,t+\Delta t}$ gives

$$\dot{u}_{N+1,t+\Delta t} = \frac{\dot{u}_{N+1,t} + \frac{\Delta t}{\rho \Delta z} [2\rho_r v_{sr} \dot{u}_r(t + \Delta t) - \tau_{N,t}]}{1 + (\Delta t/\rho \Delta z) \rho_r v_{sr}} \quad (7.46)$$

Once the boundary conditions have been established, the integration calculations proceed from the bottom ($i = N + 1$) to the top ($i = 1$) of the soil deposit in each time step, and step by step in time. Computation of the velocity at the end of each time step, however, requires knowledge of the shear stress in that time step.

If the soil deposit is initially at rest, then $\dot{u}_{i,t=0} = 0$ and $\tau_{i,t=0}$ for all i . When the input motion, in the form of $\dot{u}_b(t)$ (rigid bedrock) or $\dot{u}_r(t)$ (elastic bedrock), imparts some velocity to the base of the soil deposit, \dot{u}_{N+1} will take on a nonzero value. In subsequent time steps, $\dot{u}_N, \dot{u}_{N-1}, \dot{u}_{N-2}, \dots$ will all take on nonzero values as the soil deposit moves in response to the input motion. The incremental displacement in each time step is given by

$$\Delta u_{i,t} = \dot{u}_{i,t} \Delta t \quad (7.47)$$

Summing the incremental displacements allows the total displacement, $u_{i,p}$ to be determined at the beginning of each time step. The shear strain in each sublayer is given by

$$\gamma_{i,t} = \frac{\partial u_{i,t}}{\partial z} \approx \frac{u_{i+1,t} - u_{i,t}}{\Delta z} \quad (7.48)$$

If the soil is assumed to be linear elastic, the shear stress depends only on the current shear strain, (i.e., $\tau_{i,t} = G_i \gamma_{i,t}$). If the soil is nonlinear and inelastic, however, the shear stress will depend on the current shear strain and the stress-strain history. In such cases the computed shear strain, $\gamma_{i,t}$, and the cyclic stress-strain relationship (or advanced constitutive model) are used to determine the corresponding shear stress, $\tau_{i,t}$. The integration process can then be summarized as follows:

1. At the beginning of each time step, the particle velocity, $\dot{u}_{i,t}$, and total displacement, $u_{i,t}$, are known at each layer boundary.
2. The particle displacement profile is used to determine the shear strain, $\gamma_{i,p}$ within each layer.
3. The stress-strain relationship is used to determine the shear stress, $\tau_{i,p}$ in each layer. The stress-strain curve may be linear or nonlinear. If nonlinear inelastic soil behavior is assumed, stress reversals are checked and accounted for (e.g., by application of the Masing criteria) in each layer.
4. The input motion is used to determine the motion of the base of the soil layer at time $t + \Delta t$.
5. The motion of each layer boundary at time $t + \Delta t$ is calculated, working from bottom to top. The process is then repeated from step 1 to compute the response in the next time step.

Because the particle velocities are computed at times that differ by one-half time step from those at which the shear stresses are best approximated, the explicit method can become numerically unstable if the time step is too large (i.e., if $\Delta t > \Delta z/v_{ss}$) (Davis, 1986).

Using different difference expressions, an *implicit finite-difference* formulation can eliminate the stability problem, thereby allowing the use of longer time steps. Implicit formulations, however, involve the solution of a set of $N + 1$ simultaneous equations (which can be computationally time consuming for large N) at each time step. Whether it is more efficient to perform the rapid calculations of the explicit method at a large number of time steps, or the more time-consuming calculations of the implicit method at fewer time steps, is often difficult to predict. Most existing computer programs for nonlinear ground response analysis use the explicit formulation.

7.2.3 Comparison of One-Dimensional Ground Response Analyses

Although equivalent linear and nonlinear methods are both used to solve one-dimensional ground response analysis problems, their formulations and underlying assumptions are quite different. Consequently, it is reasonable to expect to find some differences in their results.

The results of equivalent linear and nonlinear ground response analyses have been compared on a number of occasions (e.g., Joyner and Chen, 1975; Martin and Seed, 1978; Dikmen and Ghaboussi, 1984) with the following general conclusions:

1. The inherent linearity of equivalent linear analyses can lead to *spurious resonances* (i.e., high levels of amplification that result from coincidence of a strong component of the input motion with one of the natural frequencies of the equivalent linear soil deposit). Since the stiffness of an actual nonlinear soil changes over the duration of a large earthquake, such high amplification levels will not develop in the field.
2. The use of an effective shear strain in an equivalent linear analysis can lead to an over-softened and overdamped system when the peak shear strain is much larger than the remainder of the shear strains, or to an undersoftened, underdamped system when the shear strain amplitude is nearly uniform.
3. Equivalent linear analyses can be much more efficient than nonlinear analyses, particularly when the input motion can be characterized with acceptable accuracy by a small number of terms in a Fourier series. For example, most earthquakes contain relatively little elastic wave energy at frequencies above 15 to 20 Hz. Consequently, the response can usually be computed with reasonable accuracy by considering only the frequencies below 15 to 20 Hz (or lower, in some cases). As the power, speed, and accessibility of computers have increased in recent years, the practical significance of differences in the efficiency of one-dimensional ground response analyses has decreased substantially.
4. Nonlinear methods can be formulated in terms of effective stresses to allow modeling of the generation, redistribution, and eventual dissipation of excess pore pressure during and after earthquake shaking. Equivalent linear methods do not have this capability.
5. Nonlinear methods require a reliable stress-strain or constitutive model. The parameters that describe such models are not as well established as those of the equivalent linear model. A substantial field and laboratory testing program may be required to evaluate nonlinear model parameters.

6. Differences between the results of equivalent linear and nonlinear analyses depend on the degree of nonlinearity in the actual soil response. For problems where strain levels remain low (stiff soil profiles and/or relatively weak input motions), both analyses can produce reasonable estimates of ground response. For problems involving high strain levels, particularly problems in which the induced shear stresses approach the available shear strength of the soil, nonlinear analyses are likely to provide reasonable results.

In summary, both equivalent linear and nonlinear techniques can and have been used successfully for one-dimensional ground response analysis. The use and interpretation of each requires knowledge of their underlying assumptions, understanding of their operation, and recognition of their limitations. Neither can be considered mathematically rigorous or precise, yet their accuracy is not inconsistent with the variability in soil conditions, uncertainty in soil properties, and scatter in the experimental data upon which many of their input parameters are based.

7.3 TWO-DIMENSIONAL DYNAMIC RESPONSE ANALYSIS

The methods of one-dimensional ground response analysis described in previous sections are useful for level or gently sloping sites with parallel material boundaries. Such conditions are not uncommon and one-dimensional analyses are widely used in geotechnical earthquake engineering practice. For many other problems of interest, however, the assumptions of one-dimensional wave propagation are not acceptable. Sloping or irregular ground surfaces, the presence of heavy structures or stiff, embedded structures, or walls and tunnels all require two-dimensional or possibly even three-dimensional analysis. Problems in which one dimension is considerably greater than others can often be treated as two-dimensional plane strain problems. A number of common cases are shown in Figure 7.14.

The following sections discuss a number of methods that can be applied to two-dimensional dynamic response problems. Techniques for the solution of such problems have been developed using both frequency-domain (complex response) methods and time-domain (direct integration) methods. These techniques have been applied to many practical problems such as those shown in Figure 7.14. Two- and three-dimensional dynamic response and soil-structure interaction problems are most commonly solved using dynamic finite-element analyses. Although a detailed treatment of the finite-element method is

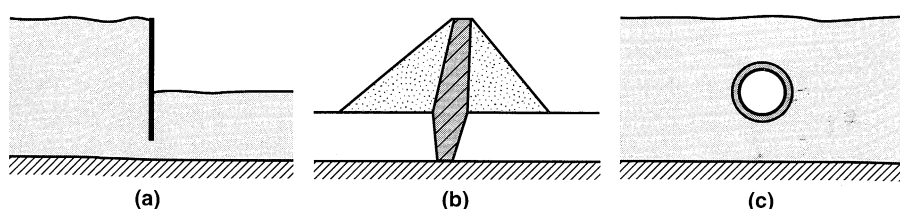


Figure 7.14 Examples of common problems typically analyzed by two-dimensional plane strain dynamic response analyses: (a) cantilever retaining wall; (b) earth dam; (c) tunnel.

beyond the scope of this book, a brief introduction precedes the description of two- and three-dimensional dynamic response analyses.

7.3.1 Dynamic Finite-Element Analysis

The finite-element method treats a continuum as an assemblage of discrete *elements* whose boundaries are defined by *nodal points*, and assumes that the response of the continuum can be described by the response of the nodal points. The following section presents a very brief summary of the finite-element method that is intended only to provide a basic description of its principles to the unfamiliar reader. Complete descriptions of the finite-element method may be found in a number of books devoted to that topic (e.g., Desai and Abel, 1972; Bathe, 1982; Zienkiewicz and Taylor, 1989).

7.3.1.1 Elemental Equations of Motion

In the finite-element method, the problem of interest is first discretized by dividing it into elements as shown in Figure 7.15. The displacement of the soil at any point within an element, $\{\mathbf{v}\}^T = \{u\ v\}$, is expressed in terms of the nodal point displacements, $\{\mathbf{q}\}^T = \{u_1\ u_2\ u_3\ u_4\ v_1\ v_2\ v_3\ v_4\}$, by

$$\{\mathbf{v}\} = [\mathbf{N}] \{\mathbf{q}\} \quad (7.49)$$

where $[\mathbf{N}]$ is a matrix of *shape functions*. The *strain–displacement matrix*, $[\mathbf{B}]$, allows the strains to be determined from the nodal point displacements

$$\{\boldsymbol{\epsilon}\} = [\mathbf{B}] \{\mathbf{q}\} \quad (7.50)$$

and the stress–strain matrix, $[\mathbf{D}]$, relates stresses to strains:

$$\{\boldsymbol{\sigma}\} = [\mathbf{D}] \{\boldsymbol{\epsilon}\} \quad (7.51)$$

Defining a local coordinate system, (s, t) , that maps the quadrilateral elements into squares as shown in Figure 7.16, and using the strain–displacement and stress–strain relationships, an *element stiffness matrix* can be written (assuming unit thickness in the z -direction) as

$$[\mathbf{k}_e] = \int_{-1}^1 \int_{-1}^1 [\mathbf{B}]^T [\mathbf{D}] [\mathbf{B}] |J| ds dt \quad (7.52)$$

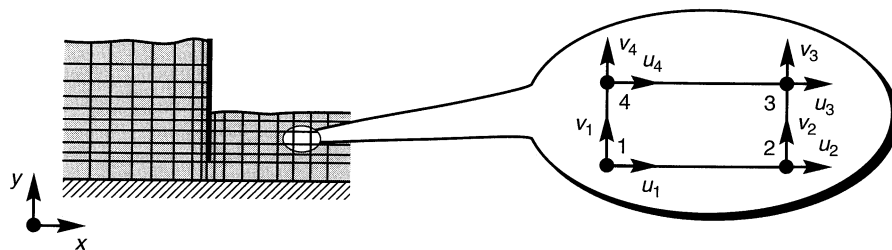


Figure 7.15 Finite-element discretization of retaining structure illustrating the degrees of freedom of a typical four-noded element.

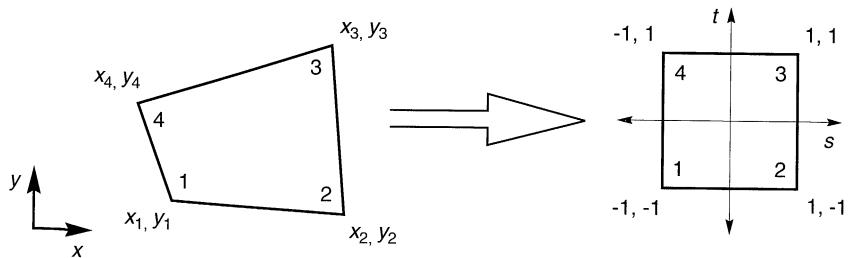


Figure 7.16 Mapping of quadrilateral element from irregular shape in x - y coordinate system to square shape in s - t coordinate system.

where the Jacobian

$$|J| = \sum_{i=1}^4 \sum_{j=1}^4 x_i \left(\frac{\partial N_i}{\partial s} \frac{\partial N_j}{\partial t} - \frac{\partial N_i}{\partial t} \frac{\partial N_j}{\partial s} \right) y_j$$

A *consistent element mass matrix* can be written, assuming constant density within the element, as

$$[\mathbf{m}_e] = \rho \int_{-1}^1 \int_{-1}^1 [\mathbf{N}]^T [\mathbf{N}] |J| ds dt \quad (7.53)$$

As an alternative, a *lumped-element mass matrix* can be developed by assuming that the mass of the element is concentrated at the nodal points. Experience has shown that use of the consistent element matrix tends to overestimate the natural frequencies of a system and that the lumped mass matrix tends to underestimate them by about the same amount. Lysmer et al. (1974) suggested the use of a *mixed element mass matrix*, which is simply the average of the consistent and lumped mass matrices.

Damping matrices can be troublesome because of the implications of various formulations on the frequency dependence of damping. For nonlinear ground response analyses, however, damping results primarily from the hysteretic behavior of the soil and is therefore accounted for by variations in the stiffness matrix under cyclic loading conditions. Some small amount of viscous damping may be included in a two-dimensional ground response analysis to account for damping at very small strains and to minimize numerical problems that can arise in the complete absence of damping. A consistent damping matrix can be obtained from

$$[\mathbf{c}_e] = \rho \int_{-1}^1 \int_{-1}^1 [\mathbf{B}]^T [\boldsymbol{\eta}] [\mathbf{B}] |J| ds dt \quad (7.54)$$

where $[\boldsymbol{\eta}]$ is a matrix of damping terms. The equations of motion for the element can then be written as

$$[\mathbf{m}_e] \ddot{\{\mathbf{q}\}} + [\mathbf{c}_e] \dot{\{\mathbf{q}\}} + [\mathbf{k}_e] \{\mathbf{q}\} = \{\mathbf{Q}(t)\} \quad (7.55)$$

where the element force vector is given by

$$\{\mathbf{Q}(t)\} = \int_{-1}^1 \int_{-1}^1 [\mathbf{N}]^T \{\mathbf{W}\} |J| ds dt + \int_S [\mathbf{N}]^T \{\mathbf{T}\} dS$$

and $\{\mathbf{W}\}$ is the vector of prescribed body forces and $\{\mathbf{T}\}$ is a vector of external tractions that may be applied to some surface, S .

7.3.1.2 Global Equations of Motion

Once the equations of motion for each element are obtained, they are combined in a way that satisfies compatibility of displacements to obtain the *global equations of motion*

$$[\mathbf{M}] \{\ddot{\mathbf{u}}\} + [\mathbf{C}] \{\dot{\mathbf{u}}\} + [\mathbf{K}] \{\mathbf{u}\} = \{\mathbf{R}(t)\} \quad (7.56a)$$

where $[\mathbf{M}]$ is the *global mass matrix*, $[\mathbf{C}]$ the *global damping matrix*, $[\mathbf{K}]$ the *global stiffness matrix*, $\{\mathbf{u}\}$ the *global nodal point displacement vector*, and $\{\mathbf{R}(t)\}$ the *global nodal point force vector*. For the case of loading induced by base motion, the global equation of motion is

$$[\mathbf{M}] \{\ddot{\mathbf{u}}\} + [\mathbf{C}] \{\dot{\mathbf{u}}\} + [\mathbf{K}] \{\mathbf{u}\} = -[\mathbf{M}] [\mathbf{1}] \ddot{\mathbf{u}_b}(t) \quad (7.56b)$$

7.3.1.3 Discretization Considerations

The response of both equivalent linear and nonlinear finite-element models can be influenced by discretization. In particular, the use of coarse finite-element meshes can result in the filtering of high-frequency components whose short wavelengths cannot be modeled by widely spaced nodal points. The maximum dimension of any element should be limited to one-eighth (Kuhlemeyer and Lysmer, 1973) to one-fifth (Lysmer et al., 1975) of the shortest wavelength considered in the analysis.

7.3.1.4 Boundary Conditions

For computational efficiency it is desirable to minimize the number of elements in a finite-element analysis. Since the maximum dimensions of the elements are generally controlled by the wave propagation velocity and frequency range of interest, minimizing the number of elements usually becomes a matter of minimizing the size of the discretized region. As the size of the discretized region decreases, the influence of boundary conditions becomes more significant.

For many dynamic response and soil–structure interaction problems, rigid or near-rigid boundaries such as bedrock are located at considerable distances, particularly in the horizontal direction, from the region of interest. As a result, wave energy that travels away from the region of interest may effectively be permanently removed from that region. In a dynamic finite-element analysis, it is important to simulate this type of radiation damping behavior. The most commonly used boundaries for finite-element analyses can be divided into three groups (Christian et al., 1977; Wolf, 1985).

Elementary Boundaries. Conditions of zero displacement or zero stress are specified at *elementary boundaries* (Figure 7.17a). Elementary boundaries can be used to model the ground surface accurately as a free (zero stress) boundary. For lateral or lower

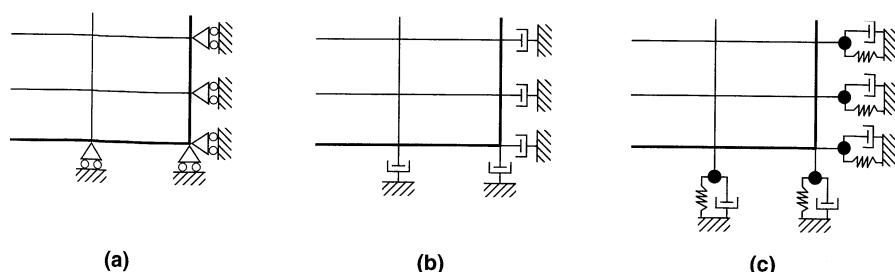


Figure 7.17 Three types of finite-element mesh boundaries: (a) elementary boundary in which zero displacements are specified; (b) local boundary consisting of viscous dashpots; (c) lumped-parameter consistent boundary (actual lumped parameter would consist of more masses, springs, and dashpots than shown).

boundaries, however, the perfect reflection characteristics of elementary boundaries can trap energy in the mesh that in reality would radiate past the boundaries and away from the region of interest. The resulting “box effect” can produce serious errors in a ground response or soil–structure interaction analysis. If elementary boundaries are placed far enough from the region of interest, reflected waves may be damped sufficiently to negate their influence.

Local Boundaries. Section 5.4.1 showed how a viscous dashpot could be used to simulate a semi-infinite region for the case of normally incident body waves. The use of viscous dashpots (Figure 7.17b) represents a common type of *local boundary*. It can be shown (e.g., Wolf, 1985) that the value of the dashpot coefficient necessary for perfect energy absorption depends on the angle of incidence of the impinging wave. Since waves are likely to strike the boundary at different angles of incidence, a local boundary with specific dashpot coefficients will always reflect some of the incident wave energy. Additional difficulties arise when dispersive surface waves reach a local boundary; since their phase velocity depends on frequency, a frequency-dependent dashpot would be required to absorb all their energy. The effects of reflections from local boundaries can be reduced by increasing the distance between the boundary and the region of interest.

Consistent Boundaries. Boundaries that can absorb all types of body waves and surface waves at all angles of incidence and all frequencies are called *consistent boundaries*. Consistent boundaries can be represented by frequency-dependent boundary stiffness matrices obtained from boundary integral equations or the boundary element method. Wolf (1991), for example, developed a lumped-parameter model consisting of an assemblage of discrete springs, masses, and dashpots which can approximate the behavior of a consistent boundary. A greatly simplified example of such an assemblage is shown in Figure 7.17c.

7.3.2 Equivalent Linear Approach

The two-dimensional equivalent linear approach is very similar to the one-dimensional approach. A soil–structure system is represented by a two-dimensional finite-element model. The input motion is represented by a Fourier series and the equations of motion are solved for each frequency of the series (or at selected frequencies with interpretation in between) with the results summed to obtain the total response.

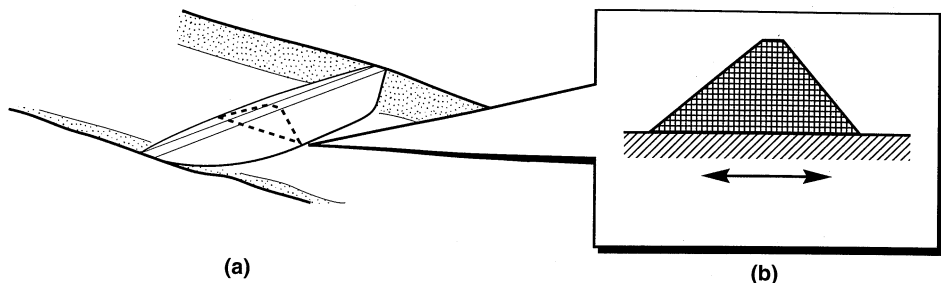


Figure 7.18 Practical situation where two-dimensional ground response analyses are used: (a) plane strain conditions can be assumed at center of long dam, allowing (b) center section of dam to be modeled in two dimensions.

Consider the problem of the earth dam shown in Figure 7.18a. Assuming that the axis of the dam is long relative to its height, the response of the center portion of the dam can be assumed to be two-dimensional. Dynamic equilibrium of the model shown in Figure 7.18b requires that the following equations of motion be satisfied:

$$[\mathbf{M}] \{ \ddot{\mathbf{u}} \} + [\mathbf{K}^*] \{ \mathbf{u} \} = -[\mathbf{M}] [\mathbf{1}] \ddot{u}_b(t) \quad (7.57)$$

where $[\mathbf{M}]$ is the mass matrix, $[\mathbf{K}^*]$ the *complex stiffness matrix*, $[\mathbf{K}^*] = [\mathbf{K}] + i\omega[\mathbf{C}]$, $\{ \mathbf{u} \}$ the vector of unknown nodal point displacements (relative to the base), and $\ddot{u}_b(t)$ is the time history of base acceleration. The mass and stiffness matrices are assembled from the corresponding element stiffness matrices using standard finite-element procedures and damping is introduced into the analysis through the use of complex shear moduli when forming the complex element stiffness matrices.

If the base motion is assumed to be harmonic, the relative displacement vector can be expressed as

$$\{ \mathbf{u} \} = \{ \mathbf{H}(\omega) \} \tilde{u}_b(\omega) e^{i\omega t} \quad (7.58)$$

where $\{ \mathbf{H}(\omega) \}$ is a vector of transfer functions and $\tilde{u}_b(\omega)$ is the Fourier transform of $\ddot{u}_b(t)$. Substituting equation (7.58) into the equation of motion gives

$$-\omega^2 [\mathbf{M}] \{ \mathbf{H}(\omega) \} \tilde{u}_b(\omega) e^{i\omega t} + [\mathbf{K}^*] \{ \mathbf{H}(\omega) \} \tilde{u}_b(\omega) e^{i\omega t} = -[\mathbf{M}] [\mathbf{1}] \tilde{u}_b(\omega) e^{i\omega t}$$

Rearranging allows the transfer function vector to be expressed as

$$\{ \mathbf{H}(\omega) \} = \frac{[\mathbf{M}]}{\omega^2 [\mathbf{M}] - [\mathbf{K}^*]} \quad (7.59)$$

Once the transfer function vector has been obtained, computation of the response follows the same procedures used for one-dimensional complex response analysis (Section 7.1.1.2). In this approach the primary computational effort is associated with evaluation of the transfer functions. For large problems, the mass and stiffness matrices are large, and evaluation of the transfer functions can be quite time consuming. For computational efficiency, the transfer functions are often explicitly evaluated at only a limited number of frequencies, with values at intermediate frequencies obtained by interpolation (Lysmer et al.,

1975; Tajirian, 1981). Iteration toward strain-compatible material properties (Section 7.1.1.3) can be incorporated on an element-by-element basis. Analyses of this type are performed by the widely used computer program FLUSH (Lysmer et al., 1975). The use of *generalized hyperelements* in the computer program GROUND2D greatly reduces the number of degrees of freedom required for two-dimensional dynamic response analyses (Deng et al., 1995).

7.3.3 Nonlinear Approach

Two-dimensional nonlinear analyses can be used to estimate permanent displacements of slopes (Chapter 10), retaining structures (Chapter 11), and other constructed facilities. Two-dimensional nonlinear dynamic response analyses are performed by writing the global equations of motion [equation (7.57)] from a finite-element idealization in incremental form and then integrating them in the time domain. Such analyses can be divided into two main groups according to the manner in which the soil behavior is represented. One group uses cyclic nonlinear stress-strain models (Section 6.4.3) and the other uses advanced constitutive models (Section 6.4.4).

Finn et al. (1986) extended the hyperbolic model with extended Masing criteria and a residual pore pressure model from one to two dimensions in the computer program TARA-3. The program has been used to back-analyze full-scale case histories and the results of various centrifuge model tests. Even with its relatively simple cyclic stress-strain model, the program has been able to capture the most important aspects of ground response with good accuracy. According to Finn (1988), the simplicity of the stress-strain model can produce substantial computational efficiency relative to models based on more complicated soil models.

Methods based on advanced constitutive models have been developed. The program DYNAFLOW (Prevost, 1981) uses a multiple yield surface model to predict deformations and pore pressures. It has been applied to problems of earth dams with good results. A consortium of Japanese construction firms have developed the program DIANA (Kawai, 1985) that can perform static and dynamic analyses with different advanced constitutive models. A number of other programs incorporating advanced constitutive models have been developed in recent years.

7.3.4 Other Approaches to Two-Dimensional Dynamic Response Problems

In an attempt to capture the most significant aspects of various two-dimensional dynamic response problems without the computational cost and complexity of dynamic finite-element analyses, a number of investigators have developed alternative approaches to specific problems. These approaches typically involve simplifying assumptions that allow two-dimensional problems to be solved by one-dimensional analyses.

7.3.4.1 Shear Beam Approach

One of the earliest approaches to the dynamic analysis of two-dimensional geotechnical systems was the *shear beam analysis* applied to earth dams by Mononobe et al. (1936). The approach has since been verified and extended to cover a variety of conditions; a comprehensive review was prepared by Gazetas (1987). The shear beam approach is based on the assumption that a dam deforms in simple shear, thereby producing only horizontal displacements.

Hatanaka (1952) and others have verified the accuracy of this assumption, at least for rigid foundation conditions. The shear beam approach also assumes that either shear stresses or shear strains are uniform across horizontal planes. These assumptions have also been verified (Chopra, 1966; Dakoulas, 1985); stresses and strain are nearly constant across the dam except in small zones near the upstream and downstream faces where they decrease to zero (Gazetas, 1987).

Consider the homogeneous, infinitely long dam shown in Figure 7.19. Assuming horizontal displacements to be constant at a given depth, the horizontal displacement relative to the base, $\bar{u}(z, t)$, is independent of x . The resultant shearing force on the upper surface of a slice of thickness, dz , is

$$S_z(t) = \int_{-x_u}^{x_d} \tau(x, z, t) dx$$

The corresponding resultant shearing force on the bottom of the slice is

$$S_{z+dz}(t) = \int_{-x_u}^{x_d} \left[\tau(x, z, t) + \frac{\partial \tau(x, z, t)}{\partial z} dz \right] dx$$

The resultant inertial force acting on the slice depends on the total acceleration, that is,

$$I_z(t) = \rho \left[\ddot{u}(z, t) + \ddot{u}_b(t) \right] \frac{2Bz}{H} dz$$

For equilibrium in the x -direction,

$$S_{z+dz}(t) - S_z(t) = I_z(t) \quad (7.60)$$

or

$$-\frac{\partial}{\partial z} \left[\int_{-x_u}^{x_d} \tau(x, z, t) dx \right] dz = \rho \left[\ddot{u}(z, t) + \ddot{u}_b(t) \right] \frac{2Bz}{H} dz$$

Substituting $\tau(x, z, t) = G(x, z)\gamma(z, t)$ and $\gamma(z, t) = \partial u(z, t)/\partial z$, the shear beam equation can be written as

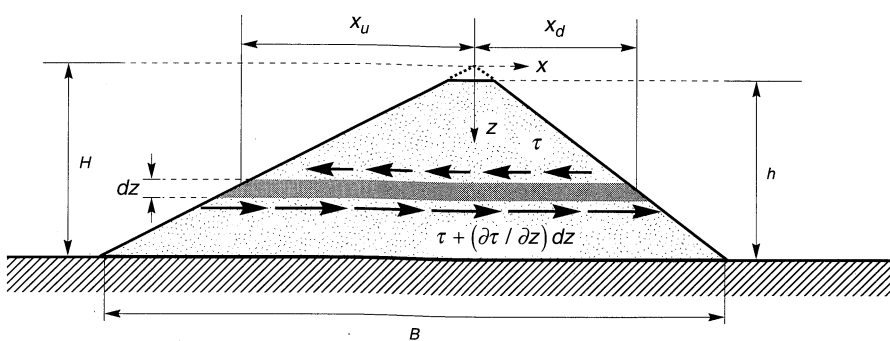


Figure 7.19 Earth dam, showing stresses acting on an element of thickness, dz .

$$\rho(\ddot{u} + \ddot{u}_b) = \frac{1}{z} \frac{\partial}{\partial z} \left[\bar{G}(z) z \frac{\partial u}{\partial z} \right] \quad (7.61)$$

where the average shear modulus, \bar{G} , is given by

$$\bar{G}(z) = \frac{1}{x_u + x_d} \int_{-x_u}^{x_d} G(x, z) dx$$

Equation (7.62) is simply a one-dimensional wave equation (i.e., the shear beam approach allows the two-dimensional dam section to be represented as a one-dimensional system).

Gazetas (1982) developed solutions to the shear beam wave equation for the case where the shear modulus increases as a power function of depth according to $G(z) = G_b(z/H)^m$, where G_b is the average shear modulus at the base of the dam. For such conditions, the n th natural circular frequency (assuming $h/H = 1$) is given by

$$\omega_n = \frac{\bar{v}_{ss}}{H} \frac{\beta_n}{8} (4+m)(2-m) \quad (7.62)$$

where \bar{v}_{ss} is the average shear wave velocity of the soil in the dam and β_n is the n th root of a period relation (Dakoulas and Gazetas, 1985) tabulated in Table 7-2 for the first five modes of vibration.

Table 7-2 Values of β_n for First Five Modes of Vibration of an Earth Dam

m	n				
	1	2	3	4	5
0	2.404	5.520	8.654	11.792	14.931
$\frac{1}{2}$	2.903	6.033	9.171	12.310	15.451
$\frac{4}{7}$	2.999	6.133	9.273	12.413	15.544
$\frac{2}{3}$	3.142	6.283	9.525	12.566	15.708
1	3.382	7.106	10.174	13.324	16.471

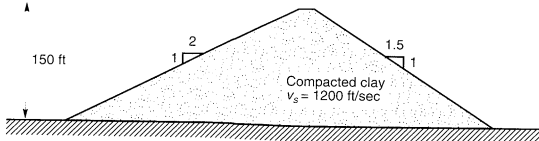


Figure E7.6

Equation (7.62) produces a fundamental period of

$$T_1 = \frac{16\pi}{(4+m)(2-m)\beta_1} \frac{H}{\bar{v}_{ss}} \quad (7.63)$$

Example 7.6

The earth dam shown in Figure E 7.6 is constructed of compacted clay with a shear wave velocity of 1200 ft/sec. Compute the first three natural frequencies of the dam.

Solution Because the crest of the dam is so narrow, $H \approx h$. Then, from equation (7.62), the first three natural frequencies can be calculated as

$$\omega_1 = \frac{\bar{v}_{ss}\beta_1}{H} \frac{(4+m)(2-m)}{8} = \frac{1200}{150} \frac{2.404}{8} (4)(2) = 19.2 \text{ rad/sec} \quad f_1 = 3.1 \text{ Hz}$$

$$\omega_2 = \frac{\bar{v}_{ss}\beta_2}{H} \frac{(4+m)(2-m)}{8} = \frac{1200}{150} \frac{5.520}{8} (4)(2) = 44.2 \text{ rad/sec} \quad f_2 = 7.0 \text{ Hz}$$

$$\omega_3 = \frac{\bar{v}_{ss}\beta_3}{H} \frac{(4+m)(2-m)}{8} = \frac{1200}{150} \frac{8.654}{8} (4)(2) = 69.2 \text{ rad/sec} \quad f_3 = 11.0 \text{ Hz}$$

The mode shape at the n th natural frequency is given by

$$U_n(z) = \left(\frac{z}{H}\right)^{-m/2} J_q \left[\beta_n \left(\frac{z}{H}\right)^{1-m/2} \right] \quad (7.64)$$

where J_q is a Bessel function of the first kind of order, $q = m/(2 - m)$, which can be evaluated from

$$J_q(x) = \sum_{k=0}^{\infty} \frac{(-1)^k}{k! \Gamma(q+k+1)} \left(\frac{x}{2}\right)^{q+2k} \quad (7.65)$$

where $\Gamma(\cdot)$ is the gamma function (Table 7-3).

Table 7-3 Recursion Relationship and Values of Gamma Function

$$\Gamma(x) = \int_0^{\infty} e^{-x} x^{n-1} dx; \quad \Gamma(x+1) = x\Gamma(x)$$

x	$\Gamma(x)$	x	$\Gamma(x)$	x	$\Gamma(x)$	x	$\Gamma(x)$
1.00	1.00000	1.25	0.90640	1.50	0.88623	1.75	0.91906
1.01	0.99433	1.26	0.90440	1.51	0.88659	1.76	0.92137
1.02	0.98884	1.27	0.90250	1.52	0.88704	1.77	0.92376
1.03	0.98335	1.28	0.90072	1.53	0.88757	1.78	0.92623
1.04	0.97884	1.29	0.89904	1.54	0.88818	1.79	0.92877
1.05	0.97350	1.30	0.89747	1.55	0.88887	1.80	0.93138
1.06	0.96874	1.31	0.89600	1.56	0.88964	1.81	0.93408
1.07	0.96415	1.32	0.89464	1.57	0.89049	1.82	0.93685
1.08	0.95973	1.33	0.89338	1.58	0.89142	1.83	0.93969
1.09	0.95546	1.34	0.89222	1.59	0.89243	1.84	0.94261
1.10	0.95135	1.35	0.89115	1.60	0.89352	1.85	0.94561
1.11	0.94739	1.36	0.89018	1.61	0.89468	1.86	0.94869
1.12	0.94359	1.37	0.88931	1.62	0.89592	1.87	0.95184
1.13	0.93993	1.38	0.88854	1.63	0.89724	1.88	0.95507
1.14	0.93642	1.39	0.88785	1.64	0.89864	1.89	0.95838
1.15	0.93304	1.40	0.88726	1.65	0.90012	1.90	0.96177
1.16	0.92980	1.41	0.88676	1.66	0.90167	1.91	0.96523
1.17	0.92670	1.42	0.88636	1.67	0.90330	1.92	0.96878
1.18	0.92373	1.43	0.88604	1.68	0.90500	1.93	0.97240
1.19	0.92088	1.44	0.88580	1.69	0.90678	1.94	0.97610
1.20	0.91817	1.45	0.88565	1.70	0.90864	1.95	0.97988
1.21	0.91558	1.46	0.88560	1.71	0.91057	1.96	0.98374
1.22	0.91311	1.47	0.88563	1.72	0.91258	1.97	0.98768
1.23	0.91075	1.48	0.88575	1.73	0.91466	1.98	0.99171
1.24	0.90852	1.49	0.88595	1.74	0.91683	1.99	0.99581
					2.00		1.00000

The first and second mode shapes are shown in Figure 7.20 for various values of the stiffness parameter, m . As m increases, the shear beam analysis produces a “whiplash effect” characterized by large shear strain and high acceleration near the crest of the dam in the second and higher modes. Under strong shaking, nonlinear behavior of the materials in an actual earth dam may prevent the development of the high accelerations predicted by the shear beam analysis.

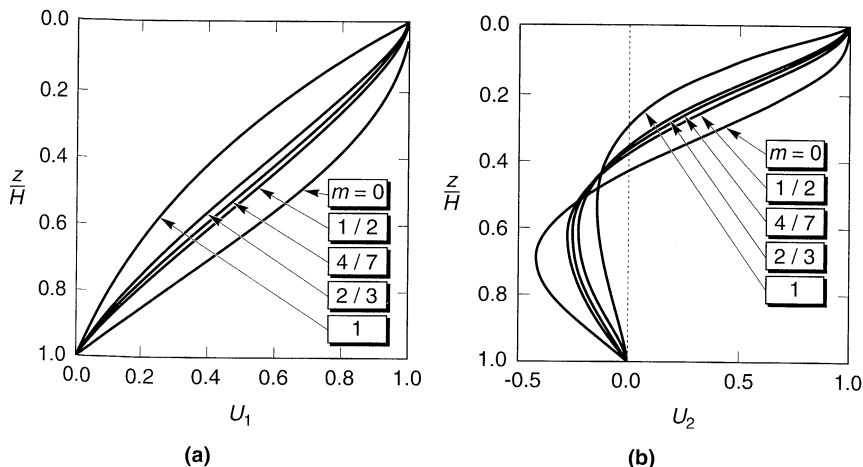


Figure 7.20 Mode shapes for (a) first mode and (b) second mode of earth dam response. Note rapid change of U with depth near crest of dam for second mode at $m = 1$ (whiplash effect). (After Dakoulas and Gazetas, 1985.)

The midcrest and base accelerations are related by the transfer function

$$H(\omega) = \frac{\ddot{u}(z=0) + \ddot{u}_b}{\ddot{u}_b} = \frac{(a_0/2)^q}{\Gamma(q+1)J_q(a_0)} \frac{1}{i\alpha_z J_{q+1}(a_0)} \quad (7.66)$$

where $a_0 = \omega H / \bar{v}_{ss}$, and $\alpha_z = \rho_s v_{ss} / \rho_r v_{sr}$ is the impedance ratio at the soil–rock interface.

In the preceding derivation, the soil was assumed to be linear and undamped. The effects of soil damping can easily be included by repeating the derivation with the soil characterized by a complex stiffness. The results, as expressed in equations (7.62) through (7.66), would be identical except for the replacement of v_{ss} by the complex shear wave velocity, $\bar{v}_{ss}^* = v_{ss}(1 + i\xi)$.

The shear beam approach is an excellent example of a procedure that through the judicious use of appropriate assumptions, greatly simplifies an important class of ground response problems. It allows rapid estimation of many important response parameters, and can be used to check the reasonableness of the results of more sophisticated analyses. The shear beam transfer function can be used in an equivalent linear analysis, or nonlinear inelastic stress-strain behavior can be assumed in an incremental nonlinear analysis.

7.3.4.2 Other Approaches

The *layered inelastic shear beam* (Stara-Gazetas, 1986) combines the shear beam approach with a one-dimensional nonlinear ground response analysis. In this approach, a series of static nonlinear finite-element analyses are performed with incrementally increasing horizontal pseudoinertial forces to determine the nonlinear backbone curve for an entire horizontal layer, or “superelement.” The backbone curves for each layer are then used with the extended Masing criteria (Section 6.4.3) in a nonlinear shear beam analysis of the dam. Other approaches include the simplified nonlinear method of Dakoulas (1985) and the nonlinear hysteretic method of Elgamal et al. (1985).

7.3.5 Comparison of Two-Dimensional Dynamic Response Analyses

Differences in the underlying assumptions and formulations of two-dimensional dynamic response analyses lead to differences in their results. The proper use of these analyses requires understanding of these differences. The two-dimensional equivalent linear method can suffer from the spurious resonances and difficulties associated with effective strain determination described for the one-dimensional equivalent linear method in Section 7.2.3. In addition, the different modes of vibration associated with the extra degrees of freedom (vertical translation and rotation) in the two-dimensional case complicate the computation of the maximum shear strain, require the use of another material parameter (such as Poisson's ratio) in addition to the shear modulus, and produce much more complicated stress paths. Again, the equivalent linear approach is restricted to total stress analyses.

Two-dimensional nonlinear methods have the enormously beneficial capability of computing pore pressures (hence effective stresses) and permanent deformations. The accuracy with which they can be computed, however, depends on the accuracy of the constitutive models on which they are based. While great progress in the constitutive modeling of soils has been made in the past 20 years, additional refinement is required before precise *a priori* predictions of permanent displacement are possible.

The shear beam models are fundamentally different from the equivalent linear and nonlinear finite-element models in that they restrict particle movement to the horizontal plane. Finite-element analyses are capable of modeling an actual dam's tendency to respond vertically as well as horizontally, but the shear beam model forces all of the elastic wave energy to produce horizontal deformations. As a result, shear beam models generally overestimate the fundamental frequency of most dams by about 5%, and higher natural frequencies by increasingly greater amounts. Shear beam displacements compare well (within about 10%) with those computed by finite-element analyses, but shear beam crest accelerations for flexible dams can be up to 50% greater than those from finite-element analyses. This discrepancy is related to the whiplash effect produced by the higher shear beam modes. For stiff dams where these higher modes are associated with frequencies greater than those associated with earthquake motions, the computed accelerations match much more closely.

7.4 THREE-DIMENSIONAL DYNAMIC RESPONSE ANALYSIS

In some instances the two-dimensional idealizations of the preceding sections may not be appropriate and three-dimensional dynamic response analyses are necessary. Such conditions can arise, as illustrated in Figure 7.21, when soil conditions vary three-dimensionally, when problem boundaries vary three-dimensionally, and when the response of three-dimensional structures is of interest.

Three-dimensional dynamic response problems are treated in much the same way as two-dimensional problems. Dynamic finite-element analyses are available, using both equivalent linear and nonlinear approaches. A number of three-dimensional analyses have been developed with an emphasis on soil-structure interaction problems (Section 7.5.2). For the important problem of earth dams, shear beam analyses have been developed for the approximate response of dams in narrow canyons.

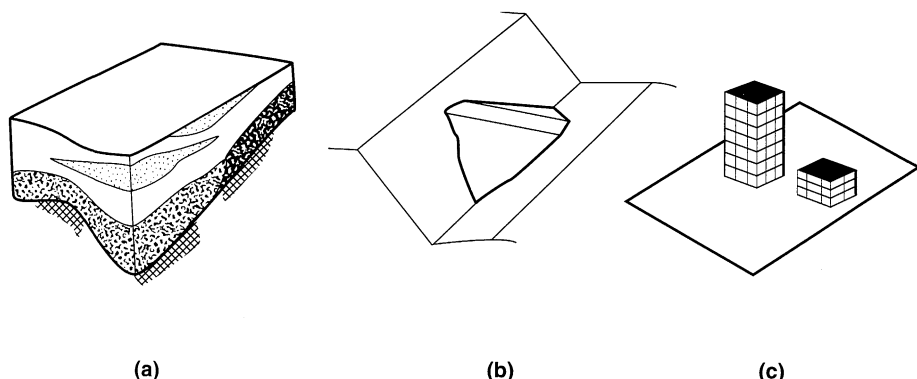


Figure 7.21 Three situations requiring three-dimensional dynamic response or soil-structural interaction analysis: (a) site where soil conditions vary significantly in three dimensions; (b) earth dam in narrow canyon; (c) site where response of soil is influenced by response of structures (and vice versa) and where response of one structure may influence response of another.

7.4.1 Equivalent Linear Finite-Element Approach

Computationally, three-dimensional equivalent linear dynamic response analyses are virtually identical to the two-dimensional analyses described in Section 7.2.2. Three-dimensional finite elements (usually in the shapes of “bricks” or tetrahedra) have more nodal points with more degrees of freedom than corresponding two-dimensional elements, but the basic process of element mass, damping, and stiffness formulation, and assembly into global equations of motion, is identical.

To analyze the seismic response of earth dams in narrow canyons, Kagawa (1977) implemented three-dimensional finite elements into a predecessor of the two-dimensional equivalent linear program FLUSH (Lysmer et al., 1975). Mejia and Seed (1981) eliminated several restrictions that resulted from Kagawa’s original assumptions while developing the three-dimensional equivalent linear program TLUSH (Kagawa et al., 1981).

Three-dimensional equivalent linear analyses have also been developed for soil-structure interaction (Section 7.4) problems. Computer programs such as SASSI (Lysmer et al., 1981), CLASSI (Luco and Wong, 1982), and HASSI (Katayama et al., 1991) use both soil and structural elements to model soil-structure systems.

7.4.2 Nonlinear Finite-Element Approach

Three-dimensional nonlinear ground response analyses are also relatively straightforward extensions of their two-dimensional counterparts. The computer program DYNAFLOW (Prevost, 1981), based on a multiple yield surface plasticity model, has three-dimensional as well as two-dimensional capabilities. When applied to the back-analysis of earth dams (e.g., Prevost et al., 1985), it realistically represented dam response while accounting for all three components of ground shaking and all modes of vibration. Three-dimensional nonlinear soil-structure interaction analyses can also be performed with programs such as TRANL (Baylor et al., 1974) and FLEX (Vaughan, 1983). Many of the large multipurpose finite-element codes (e.g., ANSYS, ADINA, etc.) are also capable of performing three-dimensional nonlinear

analyses, although they are not specifically oriented toward soil–structure problems or earthquake loading.

7.4.3 Shear Beam Approach

Many earth dams are constructed in relatively narrow canyons where abutment boundary conditions influence the response of the dam. Hatanaka (1952) and Ambraseys (1960) developed shear beam-type solutions for earth dams in rectangular canyons of different width/height ratios. Dakoulas and Gazetas (1986) developed a closed-form solution for a homogeneous ($v_{ss} = \text{constant}$) earth dam in a semicylindrical valley of width, L , and depth, H , showing

$$\begin{aligned}\omega_n &= \frac{n\pi v_{ss}}{H} \\ T_1 &= \frac{2H}{v_{ss}} \\ U_n(y=0, z) &= \frac{\sin(n\pi z/H)}{n\pi z/H}\end{aligned}\quad (7.67)$$

and

$$H(\omega) = \frac{\ddot{u}(y=0, z=0) + \ddot{u}_b}{\ddot{u}_b} \quad (7.68)$$

where all variables are as defined for equations (7.62) to (7.66) and the origin of axes is at the center of the crest of the dam. Note that the natural frequencies of a three-dimensional dam are always greater than the corresponding natural frequencies of its two-dimensional maximum section, thereby illustrating the “stiffening” effects of the abutments. This stiffening effect is also observed for dams in canyons of different shapes, although the effect decreases as the crest length/dam height ratio increases (Figure 7.22a).

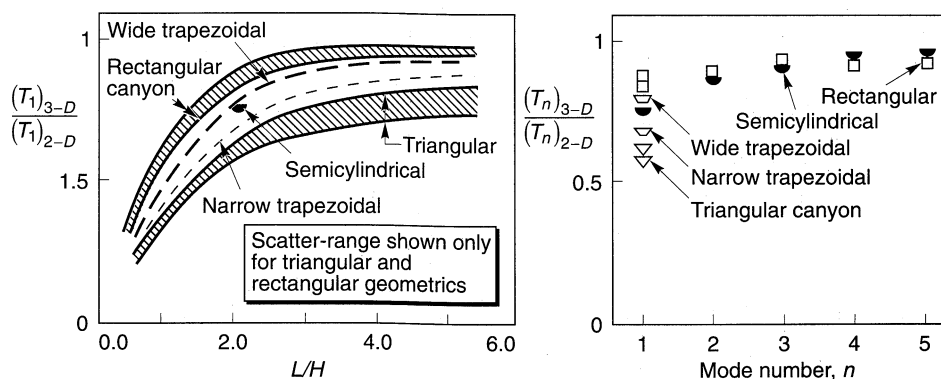


Figure 7.22 Effect of three-dimensional boundary effects on (a) fundamental frequencies for different crest length/dam height ratios, and (b) natural periods for first five modes of earth dams ($L/H = 2$) in canyons of different shape. (After Gazetas, 1987. Used with kind permission from Elsevier Science, Ltd, The Boulevard, Langford Lane, Kidlington OX5 1GB UK.)

7.4.4 Comparison of Three-Dimensional Dynamic Response Analyses

The relative capabilities and limitations of the various approaches to three-dimensional dynamic response analysis are very similar to those of their two-dimensional counterparts. Of special interest for three-dimensional problems, however, are the relative computational efficiencies of the various approaches.

The shear beam approach is simple and consequently very efficient for earth dam problems, but it makes quite restrictive assumptions about the mode of dam response. The nonlinear finite-element approach offers the greatest potential, in terms of its ability to compute permanent displacements and variations in effective stress, but it requires solution of the incremental equations of motion at every time step. For large three-dimensional problems, this can involve very large systems of simultaneous equations and many time steps. The equivalent linear approach, through the use of the cutoff frequency and interpolation of the transfer functions, requires large matrix computations at only a relatively small number of frequencies. The equivalent linear approach can therefore be more computationally efficient than the nonlinear approach.

7.5 SOIL-STRUCTURE INTERACTION

All of the ground response analyses described thus far have considered cases in which no structures are present. Ground motions that are not influenced by the presence of structures are referred to as *free-field motions*. When a structure founded on solid rock is subjected to an earthquake, the extremely high stiffness of the rock constrains the rock motion to be very close to the free-field motion. Structures founded on rock are considered to be *fixed-base structures*. Computation of their response is relatively simple using the methods described in Appendix B.

On the other hand, the same structure would respond differently if supported on a soft soil deposit. First, the inability of the foundation to conform to the deformations of the free-field motion would cause the motion of the base of the structure to deviate from the free-field motion. Second, the dynamic response of the structure itself would induce deformation of the supporting soil. This process, in which the response of the soil influences the motion of the structure and the response of the structure influences the motion of the soil, is referred to as *soil-structure interaction*.

Soil-structure interaction has little effect on the dynamic response of many structures and foundation systems. In other cases, however, its effects can be significant. Whether the neglect of its effects is conservative or unconservative depends on the details of the problem at hand and must be evaluated on a case-by-case basis. The analysis of soil-structure interaction can be quite complicated; a detailed treatment is beyond the scope of this book. For more details, the work of Wolf (1985) and the Committee on Nuclear Structures and Materials (1979) are helpful. The purpose of the following sections is simply to provide a basic description of soil-structure interaction phenomena, to provide insight into the conditions under which it can be significant, and to introduce some of the methods that are commonly used to evaluate its effects.

7.5.1 Illustration of Soil-Structure Interaction Effects

A simple analysis is sufficient to illustrate the most important effects of soil-structure interaction. Following the approach of Wolf (1985), consider the case of the simple SDOF system mounted on a rigid, massless, L-shaped foundation (Figure 7.23a) supported on an elastic soil deposit. The structure is characterized by its mass, m , stiffness, k , and damping coefficient, c . If the material supporting the foundation is rigid, the natural frequency of the resulting fixed-base system would depend only on the mass and stiffness of the structure, that is,

$$\omega_0 = \sqrt{\frac{k}{m}} \quad (7.69)$$

and the hysteretic damping ratio would be

$$\xi = \frac{c\omega_0}{2k} \quad (7.70)$$

If the supporting material is compliant, however, the foundation can translate and rotate. The stiffness and damping characteristics of the compliant soil-foundation system can be represented by the translational and rotational springs and dashpots shown in Figure 7.23b. The foundation dashpots represent two sources of damping: material damping caused by inelastic behavior of the soil supporting the foundation, and radiation damping that occurs as dynamic forces in the structure cause the foundation to deform the soil, producing stress waves that travel away from the foundation. The amount of material damping will depend on the level of strain induced in the soil; if the strains are high, material damping can be substantial, but if they are low, the material damping may be negligible. In contrast, radiation damping is a purely geometric effect that exists at low as well as high strain amplitudes. For typical foundations, radiation damping is often much greater than material damping.

The total displacements of the mass and the base of the structure can be split into their individual components (Figure 7.23c):

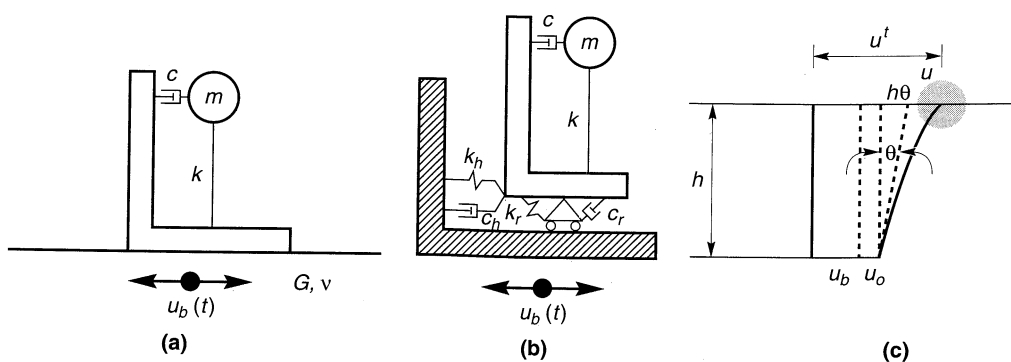


Figure 7.23 Compliant base model with one dynamic degree of freedom: (a) SDOF system on an elastic soil deposit; (b) idealized discrete system in which compliance of base is represented by translational and rotational springs and dashpots; (c) components of motion of base and mass.

$$u^t = u_b + u_0 + h\theta + u \quad (7.71a)$$

$$u_0^t = u_b + u_0 \quad (7.71b)$$

where the symbols are defined as shown in Figure 7.23c. Neglecting material damping in the soil ($\xi_g = 0$), the horizontal force imposed on the soil by the foundation would be

$$P_x = k_x u_0 + c_x \dot{u}_0 \quad (7.72)$$

where the subscript x refers to the horizontal direction for $\xi_g = 0$ conditions. For harmonic excitation at frequency ω , material damping can be introduced by the use of a complex stiffness, so that

$$P_h = k_x (1 + i2\xi_x + i2\xi_g) u_0 \quad (7.73)$$

Since $P_h = k_h u_0 + c_h \dot{u}_0$, the horizontal stiffness and damping coefficients are

$$k_h = k_x \quad (7.74a)$$

$$c_h = c_x + \frac{2}{\omega} \xi_g k_x \quad (7.74b)$$

The first term on the right side of equation (7.74b) corresponds to radiation damping, and the second to material damping. If the structure was rigid ($k = \infty$) and the foundation unable to rotate ($k_r = \infty$), the natural frequency for translational vibration would be

$$\omega_h = \sqrt{\frac{k_h}{m}} \quad (7.75)$$

Repeating the same process for the rocking mode of vibration produces

$$k_r = k_\theta \quad (7.76a)$$

$$c_r = c_\theta + \frac{2}{\omega} \xi_g k_\theta \quad (7.76b)$$

where the subscript θ denotes the absence of material damping. If the structure was rigid ($k = \infty$) and the foundation unable to translate ($k_h = \infty$), the natural frequency for rocking would be

$$\omega_r = \sqrt{\frac{k_r}{mh^2}} \quad (7.77)$$

Insight into the soil-structure interaction problem can now be gained by developing an equivalent SDOF system (i.e., a SDOF system that responds in essentially the same way as the system of Figure 7.23). Using the subscript e to describe the properties of this equivalent system, the equation of motion (for harmonic motion) can be written as

$$(-m\omega^2 + i\omega c_e + k_e)u = m\omega^2 U_b$$

where U_b is the equivalent seismic input motion. Note that the mass is the same for the equivalent and actual models. For the equivalent system

$$k_e = m\omega_e^2$$

$$\xi_e = \frac{c_e \omega}{2k_e}$$

The natural frequency of the equivalent model, ω_e , is the frequency at which the response of the equivalent system goes to infinity for $\xi_e = 0$. This occurs when

$$\frac{1}{\omega_e^2} = \frac{1}{\omega_0^2} + \frac{1}{\omega_h^2} + \frac{1}{\omega_r^2}$$

or at

$$\omega_e = \frac{\omega_0}{\sqrt{1 + k/k_h + kh^2/k_r}} \quad (7.78)$$

Equation (7.78) indicates that the natural frequency of the equivalent system is always lower than that of the fixed-base structure. In other words, an important effect of soil-structure interaction is to reduce the natural frequency of the soil-structure system to a value lower than that of the structure under fixed-base conditions.

By neglecting second-order damping ratio terms, the equivalent hysteretic damping ratio can be expressed as

$$\xi_e = \frac{\omega_e^2 \xi}{\omega_0^2} + \left(1 - \frac{\omega_e^2}{\omega_0^2}\right) \xi_g + \frac{\omega_e^2 \xi_x}{\omega_h^2} + \frac{\omega_e^2 \xi_\theta}{\omega_r^2} \quad (7.79)$$

Equation (7.79) indicates that the damping ratio of the equivalent system will, for typical soils and foundations, be larger than the damping ratio of the structure itself. Consequently, another important effect of soil-structure interaction is to increase the effective damping ratio to a value greater than that of the structure itself.

For the fixed-base case, no translation or rotation of the base is possible, but the base translation of the equivalent system can be shown to be

$$u_0 = \frac{\omega_0^2}{\omega_h^2} (1 + 2\xi_i - 2\xi_x i - 2\xi_g i) u \quad (7.80)$$

and the base rotation

$$\theta = \frac{1}{h} \frac{\omega_0^2}{\omega_r^2} (1 + 2\xi_i - 2\xi_\theta i - 2\xi_g i) u \quad (7.81)$$

Then the motion of the mass relative to the free-field motion is given by the sum of the base displacement, u_0 , the displacement of the top of the rod due to rotation of the base, $h\theta$, and the displacement due to distortion of the structure, u ,

$$u + u_0 + h\theta = \omega_0^2 \left[\frac{1}{\omega_e^2} + 2(\xi - \xi_g)i \left(\frac{1}{\omega_e^2} - \frac{1}{\omega_0^2} \right) - \frac{2\xi_x i}{\omega_h^2} - \frac{2\xi_\theta i}{\omega_r^2} \right] u \quad (7.82)$$

The effects of soil–structure interaction are easily illustrated in terms of the following dimensionless parameters:

$$\text{Stiffness ratio: } \bar{s} = \frac{\omega_0 h}{v_s} \quad \text{where } v_s \text{ is the soil shear wave velocity}$$

$$\text{Slenderness ratio: } \bar{h} = \frac{h}{a} \quad \text{where } a \text{ is characteristic length of the foundation (radius for circular shape)}$$

$$\text{Mass ratio: } \bar{m} = \frac{m}{\rho a^3} \quad \text{where } \rho \text{ is the mass density of the soil}$$

Large values of the stiffness ratio correspond to situations where a relatively stiff structure rests on a relatively soft soil. The fixed-base condition is realized at zero stiffness ratio.

Actual foundation stiffness and damping coefficients are frequency dependent. To illustrate the effects of soil–structure interaction, however, the following simplified, frequency-independent expressions can be used to estimate the stiffness and damping coefficients of a rigid circular footing of radius a

$$k_x = \frac{8Ga}{2-\nu} \quad c_x = \frac{4.6}{2-\nu} \rho v_s a^2$$

$$k_\theta = \frac{8Ga^3}{3(1-\nu)} \quad c_\theta = \frac{0.4}{1-\nu} \rho v_s a^4$$

The graphs in Figures 7.24 and 7.25 show the influence of soil–structure interaction on the natural frequency, damping ratio, and displacement characteristics of the equivalent SDOF system. Comparing the response characteristics of the equivalent system with the fixed-base system illustrates the effects of soil–structure interaction.

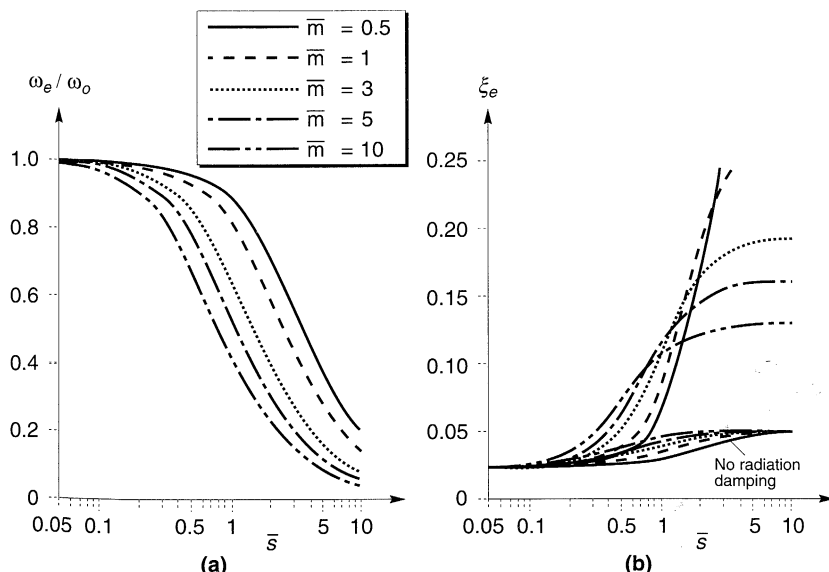


Figure 7.24 Effect of stiffness ratio and mass ratio on (a) natural frequency, and (b) damping ratio of soil–structure systems ($\bar{h} = 1$, $\nu = 0.33$, $\xi = 0.025$, $\xi_g = 0.05$). (After Wolf, 1985.)

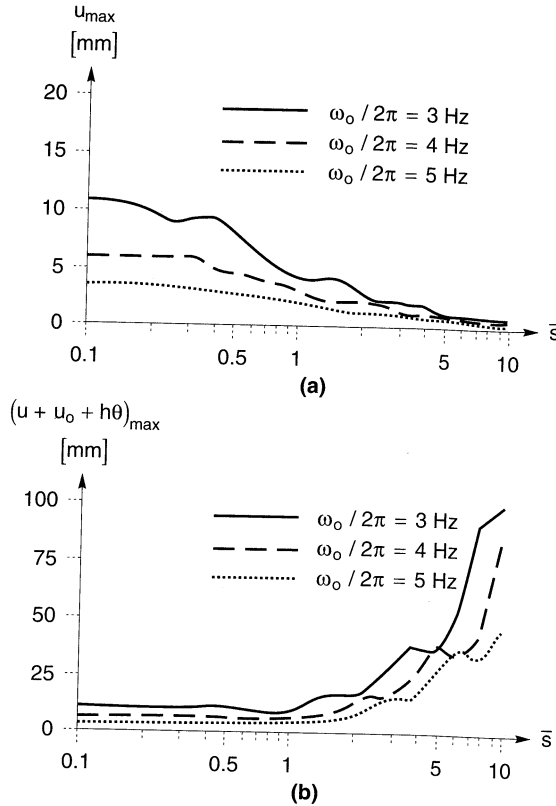


Figure 7.25 Response of equivalent soil-structure system to artificial time history ($\bar{h} = 1$, $\bar{m} = 3$, $v = 0.33$, $\xi = 0.025$, $\xi_g = 0.05$): (a) maximum structural distortion; (b) maximum displacement of mass relative to free field. (After Wolf, 1985.)

Figure 7.24a shows how the natural frequency of the equivalent SDOF system drops below that of the fixed-base system as the stiffness ratio increases. The effects of soil-structure interaction on the natural frequency is small at low stiffness ratios, i.e., when the stiffness of the soil (as reflected in the shear wave velocity) is large relative to the stiffness of the structure. For the fixed-base condition ($\bar{s} = 0$), the natural frequency of the equivalent system is equal to the fixed-base natural frequency. Figure 7.24b illustrates the influence of soil-structure interaction on the damping ratio of the equivalent SDOF system. For the fixed-base condition, the damping ratio of the equivalent system is equal to the structural damping ratio, but as the stiffness ratio increases, the effects of radiation and soil damping become more apparent. At high stiffness ratios, structural damping represents only a small part of the total damping of the system.

The effects of soil-structure interaction on displacements is illustrated in Figure 7.25. The indicated maximum responses are for an artificial input motion that produced an NRC response spectrum scaled to $a_{max} = 1.0g$. In this case, the effects of soil-structure interaction were to reduce the maximum structural distortion, u_{max} , by an amount that increased with increasing stiffness ratio and to increase the overall displacement (relative to the free field) by an amount that increased with increasing stiffness ratio. Thus soil-structure interaction tends to reduce the demands on the structure, but because the foundation can translate and rotate, increase the overall displacement. These effects can be important for tall, slender

structures or for closely spaced structures that may be subject to *pounding* when relative displacements become large.

7.5.2 Methods of Analysis

While the preceding analysis illustrated several important effects of soil–structure interaction, it is not suitable for the detailed analysis of practical soil–structure interaction problems. Methods for the analysis of soil–structure interaction can be divided into two main categories: *direct methods* and *multistep methods*.

7.5.2.1 Direct Method

In the direct method, the entire soil–foundation–structure system is modeled and analyzed in a single step. As illustrated in Figure 7.26, free-field input motions are specified along the base and sides of the model and the resulting response of the interacting system is computed (for a finite-element model) from the equations of motion

$$[\mathbf{M}]\{\ddot{\mathbf{u}}\} + [\mathbf{K}^*]\{\mathbf{u}\} = -[\mathbf{M}]\{\ddot{\mathbf{u}}_{ff}(t)\} \quad (7.83)$$

where $\{\ddot{\mathbf{u}}_{ff}(t)\}$ are the specified free-field accelerations at the boundary nodal points. The use of the direct method requires a computer program that can treat the behavior of both the soil and the structure with equal rigor.

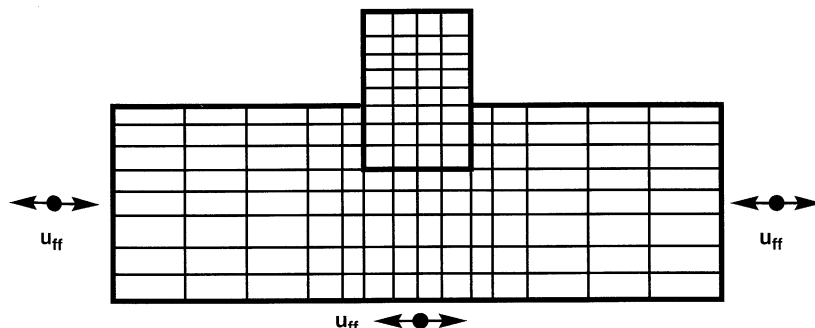


Figure 7.26 Direct method of soil–structure interaction analysis. Entire problem is modeled and response to free-field motion applied at boundaries is determined in a single step.

7.5.2.2 Multistep Method

Multistep methods use the principle of superposition to isolate the two primary causes of soil–structure interaction: the inability of the foundation to match the free-field deformation and the effect of the dynamic response of the structure–foundation system on the movement of the supporting soil. Because they rely on superposition, they are limited to the analysis of linear (or equivalent linear) systems.

Kinematic Interaction. In the free field, an earthquake will cause soil displacements in both the horizontal and vertical directions. If a foundation on the surface of, or embedded in, a soil deposit is so stiff that it cannot follow the free-field deformation pattern, its motion will be influenced by *kinematic interaction*, even if it has no mass. For

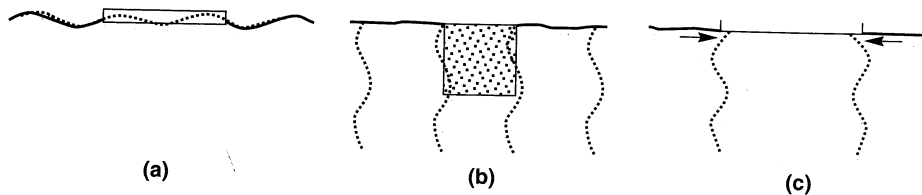


Figure 7.27 Kinematic interaction with free-field motions indicated by dashed lines:
 (a) flexural stiffness of surface foundation prevents it from following vertical component of free-field displacement; (b) rigidity of block foundation prevents it from following horizontal component of free-field displacement; (c) axial stiffness of surface foundation prevents immediately underlying soil from deforming incoherently.

example, the flexural stiffness of the massless mat foundation in Figure 7.27a prevents it from following the horizontally varying vertical component of the free-field motion. The rigidity of the massless embedded foundation in Figure 7.27b keeps it from following the vertically varying horizontal free-field motion. The axial stiffness of the slab in Figure 7.27c prevents development of the incoherent free-field motion. In each of these cases, the motion of the foundation is influenced by kinematic interaction. Kinematic interaction, however, is not present in all problems. If the surface foundation of Figure 7.27a was subjected to vertically propagating s-waves (horizontal particle motion only), it would not restrict the movement of the soil; consequently, no kinematic interaction would exist. Kinematic interaction will occur whenever the stiffness of the foundation system impedes development of the free-field motions.

Kinematic interaction can also induce different modes of vibration in a structure. Consider the embedded foundation of Figure 7.28a. When subjected to vertically propagating s-waves with a wavelength equal to the depth of embedment, a net overturning moment can be applied to the foundation, thereby causing the foundation to rock as well as translate, even though the free-field motion is purely translational. At a different frequency (Figure 7.28b), the wavelength may be such that rotation is inhibited. Horizontally propagating waves can, in a similar manner, induce torsional vibration of the foundation.

The deformations due to kinematic interaction alone can be computed by assuming that the foundation has stiffness but no mass. The equations of motion for this case are

$$[\mathbf{M}_{\text{soil}}]\{\ddot{\mathbf{u}}_{\text{KI}}\} + [\mathbf{K}^*]\{\mathbf{u}_{\text{KI}}\} = -[\mathbf{M}_{\text{soil}}]\ddot{\mathbf{u}}_b(t) \quad (7.84)$$

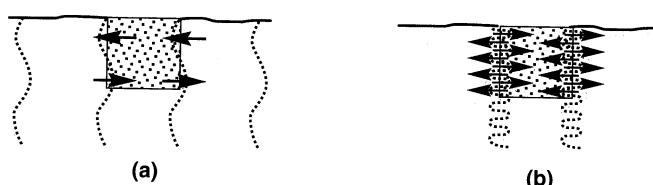


Figure 7.28 Excitation of rocking vibrations in an embedded foundation by vertically propagating s-waves: (a) at certain frequencies, the wavelength is such that unbalanced overturning moments cause rocking; (b) at other frequencies (and wavelengths), rocking may be suppressed.

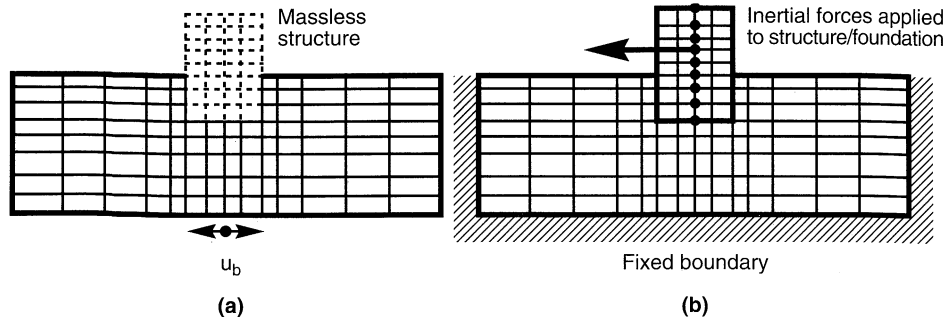


Figure 7.29 (a) Kinematic interaction analysis and (b) inertial interaction analysis. Mass of structure in inertial interaction analysis shown as being lumped at the center of the structure.

where $[M_{soil}]$ is the mass matrix assuming that the structure and foundation are massless. Equation (7.84) describes the problem illustrated in Figure 7.29a. Equation (7.84) is solved for $\{u_{KI}\}$, which is referred to as the *foundation input motion*.

Inertial Interaction. The structure and foundation do have mass, however, and this mass causes them to respond dynamically. If the supporting soil is compliant, the forces transmitted to it by the foundation will produce foundation movement that would not occur in a fixed-base structure. The effects of soil compliance on the resulting response are due to *inertial interaction*.

The deformations due to inertial interaction can be computed from the equations of motion

$$[\mathbf{M}]\{\ddot{\mathbf{u}}_{\text{II}}\} + [\mathbf{K}^*]\{\mathbf{u}_{\text{II}}\} = -[\mathbf{M}_{\text{structure}}]\{\ddot{\mathbf{u}}_{\text{KI}}(t) + \ddot{\mathbf{u}}_b(t)\} \quad (7.85)$$

where $[M_{\text{structure}}]$ is the mass matrix assuming that the soil is massless. Note that the right side of equation (7.85) represents the inertial loading on the structure–foundation system. This inertial loading depends on the base motion and the foundation input motion, which reflects the effects of kinematic interaction. In the inertial interaction analysis, the inertial loading is applied only to the structure; the base of the soil deposit is stationary. Equation (7.85) corresponds to the problem illustrated in Figure 7.29b.

Combination of Kinematic and Inertial Interaction. The kinematic interaction analysis produces the motion of the massless foundation–structure system (relative to the base) due to kinematic interaction. This motion is combined with the base motion to produce the total kinematic motion of the foundation–structure system. When the inertial loading that results from this kinematic motion is applied to the foundation–structure system resting on massless soil, equation (7.85) allows computation of the relative (to the total kinematic) motion. Adding equations (7.84) and (7.85) gives

$$[\mathbf{M}_{\text{soil}}]\{\ddot{\mathbf{u}}_{\text{KI}}\} + [\mathbf{M}]\{\ddot{\mathbf{u}}_{\text{II}}\} + [\mathbf{K}^*](\{\mathbf{u}_{\text{KI}}\} + \{\ddot{\mathbf{u}}_{\text{II}}\}) = -([\mathbf{M}_{\text{soil}}] + [\mathbf{M}_{\text{structure}}])\ddot{\mathbf{u}}_b - [\mathbf{M}_{\text{structure}}]\{\ddot{\mathbf{u}}_{\text{KI}}\} \quad (7.86)$$

Since $\{\mathbf{u}_{\text{KI}}\} + \{\mathbf{u}_{\text{II}}\} = \{\mathbf{u}\}$ and $[\mathbf{M}_{\text{soil}}] + [\mathbf{M}_{\text{structure}}] = [\mathbf{M}]$, equation (7.86) is equivalent to the original equations of motion

$$[\mathbf{M}]\{\ddot{\mathbf{u}}\} + [\mathbf{K}^*]\{\mathbf{u}\} = -[\mathbf{M}]\{\ddot{\mathbf{u}}_b(t)\}$$

which proves that the solution to the entire soil–structure interaction problem is equal to the sum of the solutions of the kinematic and inertial interaction analyses. Therefore, the multi-step procedure can be summarized as follows:

1. A kinematic interaction analysis, in which the foundation–structure system is assumed to have stiffness but no mass, is performed. This analysis produces the foundation input motion.
2. The foundation input motion is used to apply inertial loads to the structure in an inertial interaction analysis, in which the soil, foundation, and structure are all assumed to have stiffness and mass.

If the foundation itself is rigid, the soil can be replaced by a set of equivalent springs and dashpots in the inertial interaction analysis. The inertial interaction analysis can then be performed by applying inertial forces to the masses of the structure (Figure 7.30a) or by applying the input motion to the supports (Figure 7.30b); the two methods are mathematically equivalent. Considerable research, involving analytical, numerical, and experimental modeling, has produced a variety of techniques for the evaluation of spring and dashpot constants for foundation systems. Gazetas (1991) provided a very useful, practical series of charts and tables for estimation of spring and dashpot coefficients for a variety of foundation types and soil conditions. For more complicated soil and foundation conditions, computer programs such as DYNA4 (Novak et al., 1993) allow computation of complete foundation stiffness and damping matrices.

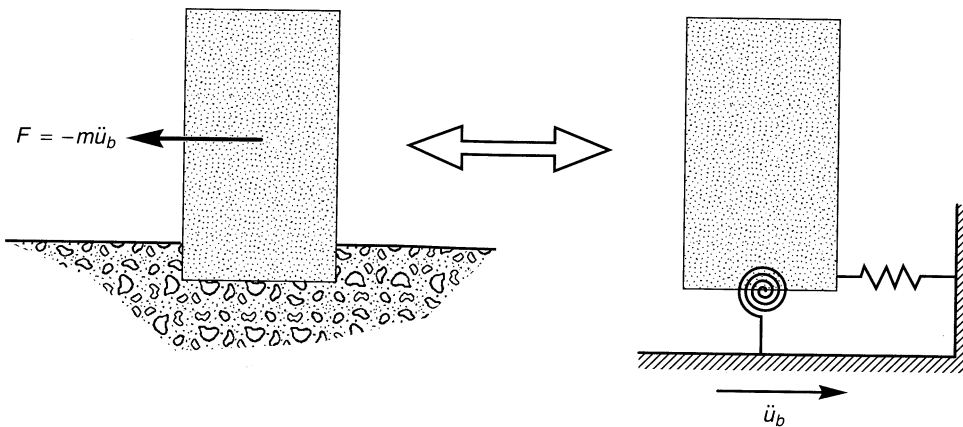


Figure 7.30 Equivalent formulations of inertial interaction analysis for structures with rigid foundation: (a) inertia forces applied to each element; (b) foundation motion applied through frequency-dependent springs and dashpots (not shown).

7.6 SUMMARY

1. Analysis of the response of soil deposits and earthen structures to earthquake motions is one of the most important aspects of geotechnical earthquake engineering practice. Ground response problems are often grouped into categories for which one-, two-, and three-dimensional ground response analyses are appropriate.

2. Ground response analyses are generally performed by one of two methods: equivalent linear analysis or nonlinear analysis. Equivalent linear analyses are linear analyses in which the soil stiffness and damping characteristics are adjusted until they are compatible with the level of strain induced in the soil. Nonlinear analyses actually consider the nonlinear inelastic stress-strain behavior of soils by integrating the equations of motion in small time steps. Equivalent linear analyses are generally more computationally efficient than nonlinear analyses.
3. One-dimensional ground response analyses are based on the assumption that the ground surface and all material boundaries below the ground surface are horizontal and extend infinitely in all lateral directions. Although these assumptions can never be strictly satisfied, they are satisfied sufficiently for engineering purposes at many sites.
4. The equivalent linear approach makes use of transfer functions to relate parameters of interest (such as ground surface acceleration or velocity) to known parameters (such as bedrock acceleration). The nature of a transfer function is influenced by the thickness, stiffness, and damping characteristics of each soil layer. The transfer function is also influenced by bedrock properties.
5. During an earthquake, stress waves that reach the ground surface are perfectly reflected (i.e., with no loss of energy) to travel downward toward bedrock. When a downward traveling wave reaches bedrock, part of the wave will be reflected, and unless the rock is perfectly rigid, part will be transmitted to continue traveling downward through the rock. If the elastic bedrock is relatively homogeneous, the transmitted wave effectively removes energy from the soil deposit and causes its response to be lower than it would have been for the case of rigid bedrock. This phenomenon represents a form of radiation damping.
6. Because the equivalent linear approach is fundamentally linear, the response at any two points in a soil deposit are uniquely related to each other. As a result, an object motion can be specified at any point in the soil deposit and the corresponding motion computed at any other point. This feature allows use of a motion recorded on the surface of a soil deposit to compute the bedrock motion that would have caused it. This useful operation, known as deconvolution, does not provide a unique solution when performed with nonlinear analyses.
7. Nonlinear analyses integrate the equations of motion in small time steps. At the beginning of each time step, the stress-strain relationship is referred to to obtain the appropriate soil properties to be used in that time step. By this method, a nonlinear inelastic stress-strain relationship can be followed in a set of small incrementally linear steps.
8. Both equivalent linear and nonlinear approaches have been used successfully for ground response analysis. Their use and interpretation, however, requires knowledge of their underlying assumptions, understanding of their operation, and recognition of their limitations. Neither can be considered mathematically rigorous or precise, yet their accuracy is not inconsistent with the variability in soil conditions, uncertainty in soil properties, and scatter in the experimental data upon which many of their input parameters are based.
9. Two- and three-dimensional ground response analyses are usually performed using dynamic finite-element analyses. These analyses can be performed using equivalent

linear or nonlinear approaches. Both equivalent linear and nonlinear dynamic finite element analyses are analogous to their one-dimensional counterparts, and many of the same advantages and limitations apply to each.

10. Analysis of the response of certain two- and three-dimensional earth structures, such as earth dams and embankments, can be greatly simplified by the shear beam approach. The shear beam approach allows two- and three-dimensional problems to be idealized as equivalent one-dimensional problems.
11. Ground motions that are not influenced by the presence of structures are called free-field motions. When structures are present, they interact with the soil through a process referred to as soil-structure interaction. Soil-structure interaction has little effect on the response of some systems and a large effect on the response of others. Its effects are most significant for stiff and/or heavy structures supported on relatively soft soils. For soft and/or light structures founded on stiff soils, soil-structure interaction effects are generally small.
12. In general, soil-structure interaction will cause the natural frequency of a soil-structure system to be lower than the natural frequency of the structure itself. Also, radiation damping will generally cause the total damping of a soil-structure system to be greater than that of the structure itself. Because of these effects, soil-structure interaction tends to reduce the demands on the structure, but because the foundation can translate and rotate, can increase the overall displacement.
13. Soil-structure interaction is caused by two phenomena: the inability of the foundation to match the free-field deformation (kinematic interaction) and the effect of the dynamic response of the structure-foundation system on the movement of the supporting soil (inertial interaction). Kinematic interaction can induce modes of deformation (e.g., rocking and torsion) that are not present in a free-field motion. Inertial interaction occurs when the forces transmitted to the soil by the dynamic response of the structure produce foundation movements that would not occur in a fixed-base structure. The effects of inertial interaction are usually more pronounced than the effects of kinematic interaction.
14. For linear or equivalent linear analyses, the effects of kinematic interaction and inertial interaction can be separated. The effects of kinematic interaction are first determined and then used as input to an inertial interaction analysis. Combining the results of both analyses allows the overall response to be determined.

HOMEWORK PROBLEMS

- 7.1 For the case of a uniform layer of undamped soil overlying rigid bedrock, develop a transfer function that relates shear stress, $\tau(z = H/2, t)$, to the bedrock acceleration, $\ddot{u}_b(t)$. Plot the modulus of the transfer function from $kH = 0$ to $kH = 2\pi$.
- 7.2 An acceleration reduction factor can be defined as the ratio of the peak acceleration at depth, z , to the peak ground surface acceleration, i.e.

$$r_d = \frac{\ddot{u}_{max}(z)}{\ddot{u}_{max}(z=0)}$$

For the case of a uniform layer of undamped soil overlying rigid bedrock, develop an expression for the reduction factor as a function of the thickness and shear wave velocity of the soil layer, and the frequency of the input motion.

- 7.3** Plot the reduction factor determined in Problem 7.2 with depth for a 15 m thick soil deposit with a shear wave velocity of 300 m/sec at input motion frequencies of 0.5 Hz, 1.0 Hz, 2.0 Hz, 3.0 Hz, and 5.0 Hz.
- 7.4** Derive a transfer function that relates the displacement of the ground surface to the displacement of bedrock for the site illustrated below.
- Define the complex wave numbers, k_1^* and k_2^* .
 - Define the complex impedance ratio, α^* .
 - Express the transfer function in terms of h_1 , h_2 , k_1^* , k_2^* , and α^* .

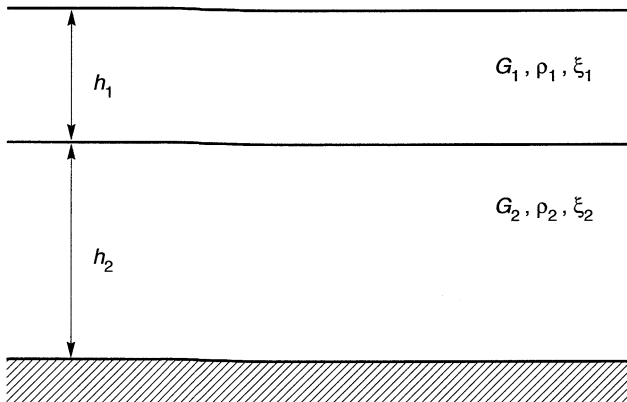


Figure P7.4

- 7.5** The shear modulus of the soil within the earth dam shown below increases linearly with depth. The shear wave velocity of the soil just above the base of the dam is 800m/sec. Compute the first two natural frequencies of the dam.

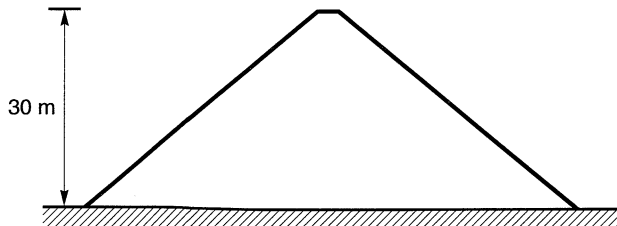


Figure P7.5

- 7.6** If the dam section shown in Problem 7.5 represented the maximum section of a dam in a semi-cylindrical channel, estimate the first two natural frequencies of the dam.

7.7 The SDOF system shown below is supported by a 10 ft diameter circular footing. The mass of the footing is small compared to the mass of the structure. Compute the damped natural period of the soil-structure system:

- (a) assuming fixed base conditions,
- (b) assuming that the footing can translate horizontally (but not rotate), and
- (c) assuming that the footing can both translate and rotate.

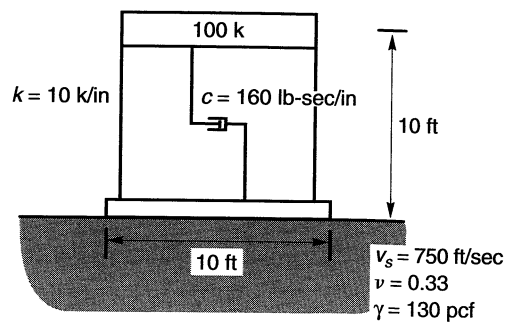


Figure P7.7

8

Local Site Effects and Design Ground Motions

8.1 INTRODUCTION

The influence of local geologic and soil conditions on the intensity of ground shaking and earthquake damage has been known for many years. MacMurdo (1824) noted that “buildings situated on rock were not by any means so much affected . . . as those whose foundations did not reach to the bottom of the soil” in the 1819 earthquake in Cutch, India. In his report on the 1857 Neapolitan earthquake, Mallet (1862) noted the effect of local geologic conditions on damage. Wood (1908) and Reid (1910) showed that the intensity of ground shaking in the 1906 San Francisco earthquake was related to local soil and geologic conditions. Gutenberg (1927) developed site-dependent amplification factors from recordings of microseisms at sites with different subsurface conditions. Since these early observations, the effects of local site conditions on ground motions have been illustrated in earthquakes around the world. More recently, the availability of strong-motion instruments has allowed local site effects to be measured quantitatively in recent years.

Local site effects play an important role in *earthquake-resistant design* and must be accounted for on a case-by-case basis. This is usually accomplished by the development of one or more *design ground motions* (i.e., motions that reflect the levels of strong motion amplitude, frequency content, and duration that a structure or facility at a particular site should be designed for). The development of site-specific design ground motions involves

concepts presented in all of the preceding chapters of this book; it is one of the most important aspects of geotechnical earthquake engineering.

Despite considerable evidence, the existence of local site effects was a matter of some debate in past years. Indeed, provisions specifically accounting for local site effects did not appear in building codes until the 1970s. This chapter presents theoretical, instrumental, and historical evidence for the existence of local site effects. It discusses procedures that are commonly used for the development of site-specific design ground motions and reviews the manner in which local site effects are treated in the specification of design ground motions by contemporary building codes and standards.

8.2 EFFECTS OF LOCAL SITE CONDITIONS ON GROUND MOTION

Local site conditions can profoundly influence all of the important characteristics—amplitude, frequency content, and duration—of strong ground motion. The extent of their influence depends on the geometry and material properties of the subsurface materials, on site topography, and on the characteristics of the input motion. The nature of local site effects can be illustrated in several ways: by simple, theoretical ground response analyses, by measurements of actual surface and subsurface motions at the same site, and by measurements of ground surface motions from sites with different subsurface conditions.

8.2.1 Evidence from Theoretical Ground Response Analyses

There are important theoretical reasons why ground surface motions should be influenced by local site conditions. At most sites the density and s-wave velocity of materials near the surface are smaller than at greater depths. If the effects of scattering and material damping are neglected, the conservation of elastic wave energy requires that the flow of energy (energy flux, $\rho v_s \dot{u}^2$) from depth to the ground surface be constant. Therefore, since ρ and v_s decrease as waves approach the ground surface, the particle velocity, \dot{u} , must increase.

The characteristics of local soil deposits can also influence the extent to which ground motion amplification will occur when the specific impedance is constant. The basis for such amplification can be illustrated analytically using simple, theoretical ground response analyses. Consider, for example, the two soil deposits shown in Figure 8.1; their geometries are identical, but one is considerably stiffer than the other. If each soil is assumed to be linearly

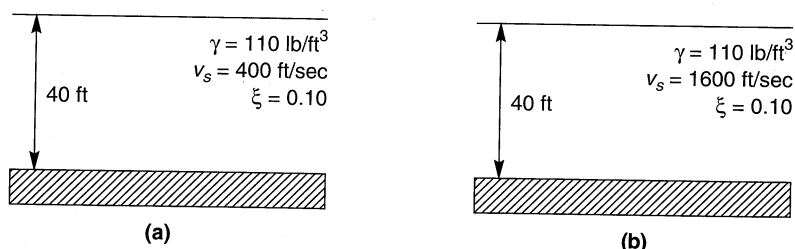


Figure 8.1 Two hypothetical soil deposits overlying rigid bedrock: (a) site A; (b) site B. Soils are identical, except the s-wave velocity of the soil at site B is four times greater than that at site A.

elastic and bedrock to be rigid, the amplification functions of each site [from equation (7.13)] are as illustrated in Figure 8.2. Clearly, the softer site (site A) will amplify low-frequency (long-period) bedrock motions more than the stiff site (site B); the reverse would be observed for high-frequency (short-period) motions. Since earthquakes produce bedrock motion over a range of frequencies, some components of an actual bedrock motion will be amplified more than others, as illustrated in Examples 7.1 to 7.5. For the more realistic condition of elastic bedrock, the nature of the local site amplification will be influenced by the specific impedance of the bedrock. Consequently, any description of local site conditions should include the density and stiffness of the bedrock. For example, the harder crystalline bedrock found in much of the eastern United States would be expected to produce amplification factors about 50% higher than those associated with the softer rock conditions typically found in California (Jacob, 1991) for equivalent soil conditions.

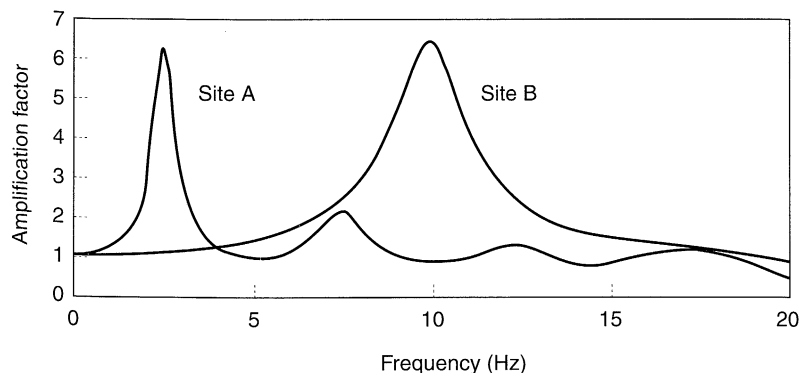


Figure 8.2 Amplification functions for sites A and B. Note that the softer soil at site A will amplify low-frequency input motions much more strongly than will the stiffer soils of site B. At higher frequencies, the opposite behavior would be expected.

8.2.2 Evidence from Measured Amplification Functions

The idealized assumptions of simple one-dimensional ground response analyses (uniform materials, horizontal layering, vertically propagating s-waves, etc.) produce smooth amplification functions such as those shown in Figure 8.2. Since these conditions rarely exist in the field, actual amplification functions are not so smooth.

Interpretation of strong motion data from sites where both surface and subsurface instruments had been installed allows actual amplification functions to be computed (e.g., Joyner et al., 1976; Johnson and Silva, 1981; Chang et al., 1986). The strong amplification at the natural frequencies of the soil deposit shown in Figure 8.3 clearly illustrates the importance of local soil conditions on ground response. The site consists of various soils of relatively uniform shear wave velocity overlying bedrock; consequently, the frequency dependence of the actual amplification function is qualitatively similar to that predicted by simple ground response analyses. For sites with more complicated subsurface conditions, or

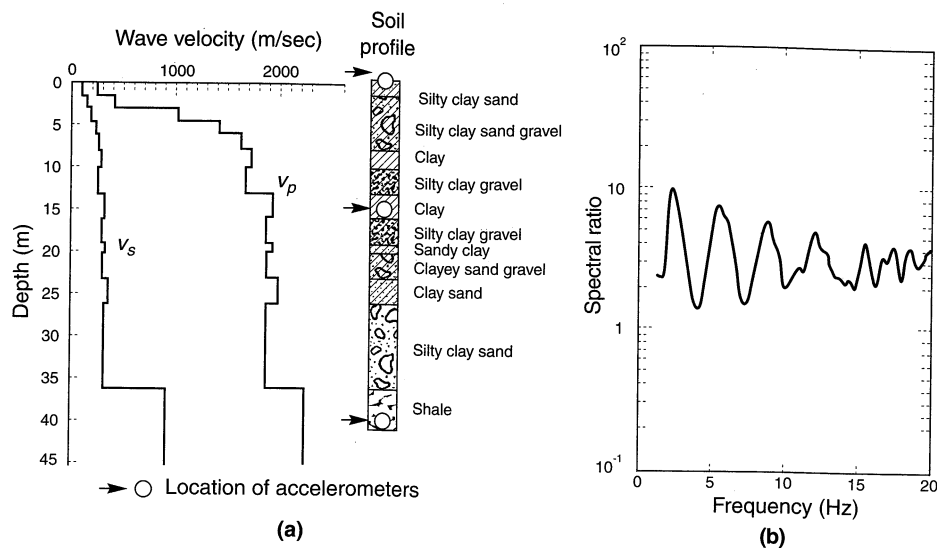


Figure 8.3 (a) Subsurface profile at Richmond field station (after Johnson and Silva, 1981). (b) Surface–bedrock amplification functions from response measured during the Briones Hills ($M_L = 4.3$) earthquake (after Silva, 1988). Fourier spectra were smoothed over a 1-Hz window prior to spectral ratio computation.

for stronger earthquakes in which soil nonlinearity may become significant, the ability of simple ground response analyses to predict the irregular peaks and valleys of actual amplification functions decreases. The effects of soil nonlinearity also cause amplification functions from strong motions to differ from those of weak motions (e.g., Aki, 1993).

Example 8.1

Compute the spectral ratio of the Gilroy No. 1 (rock) and Gilroy No. 2 (soil) motions.

Solution The actual transfer function relating the Gilroy No. 1 (rock) and Gilroy No. 2 (soil) motions can be computed from the Fourier series of the individual motions. The process can be performed in three steps:

1. Compute the Fourier series for the Gilroy No. 1 (rock) motion. The Fourier amplitude spectrum of this motion was originally shown in Figure 3.13a, and is repeated in Figure E8.1a. Also shown is a smoothed version of the spectrum (the smoothed version was smoothed numerically, but not as extensively as required for evaluation of the predominant period in Example 3.3).
2. Compute the Fourier series for the Gilroy No. 2 (soil) motion. Raw and smoothed Fourier amplitude spectra for this motion are shown in Figure E8.1b.
3. Compute the transfer function as the ratio of the Fourier amplitudes of the Gilroy No. 2 (soil) motion to the Fourier amplitudes of the Gilroy No. 1 (rock) motion. The result, shown in Figure E8.1c, shows that low-frequency components of the Gilroy No. 1 (rock) motion were amplified by the soils underlying the Gilroy No. 2 (soil) station; high-frequency components were attenuated.

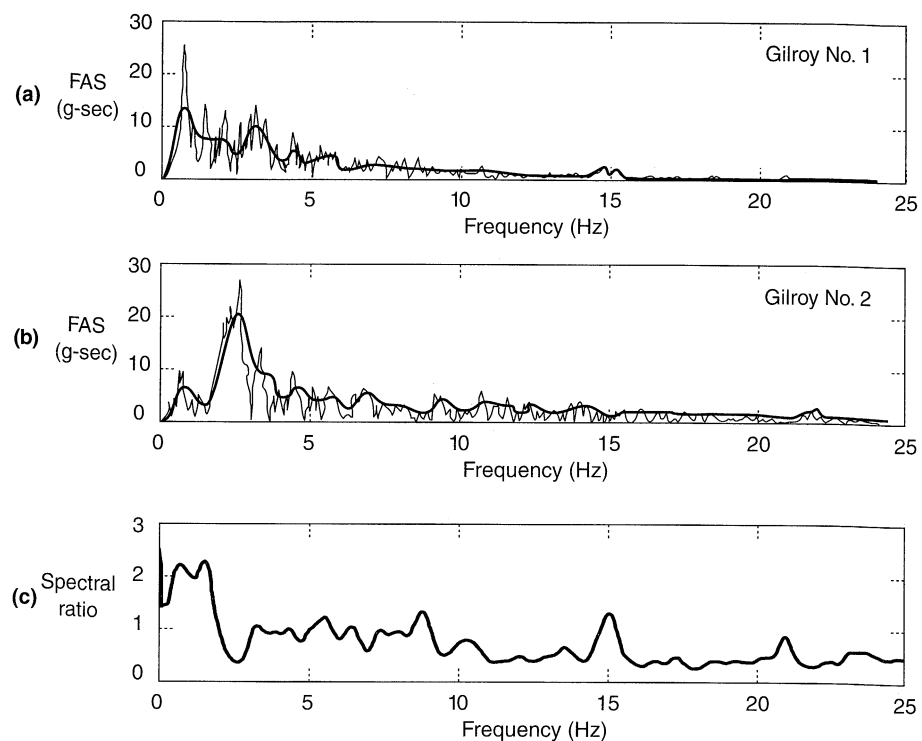


Figure E8.1

8.2.3 Evidence from Measured Surface Motions

Further evidence of the importance of local site conditions can be gained by comparing ground surface motions measured at different sites. For example, recordings of ground motion at several locations in San Francisco were made during a nearby $M \approx 5.3$ earthquake in 1957. Variations in ground motion, expressed in terms of peak horizontal acceleration and response spectra, are shown along with variation in soil conditions along a 4-mile section through the city in Figure 8.4. Ground surface motions at the rock outcrops (Market and Guerrero, Mason and Pine, Harrison and Main) were quite similar, but the amplitude and frequency content of the motions at sites underlain by thick soil deposits were markedly different.

Similar effects have been observed in many other earthquakes. From the standpoint of local site effects, two of the most significant recent earthquakes were the 1985 Michoacan (Mexico) earthquake (Stone et al., 1987) and the 1989 Loma Prieta (California) earthquake (Seed et al., 1990). These well-documented earthquakes produced strong motion records at sites underlain by a variety of different subsurface conditions in Mexico City and the San Francisco Bay area. A brief examination of these case histories illustrates the importance of local site effects.

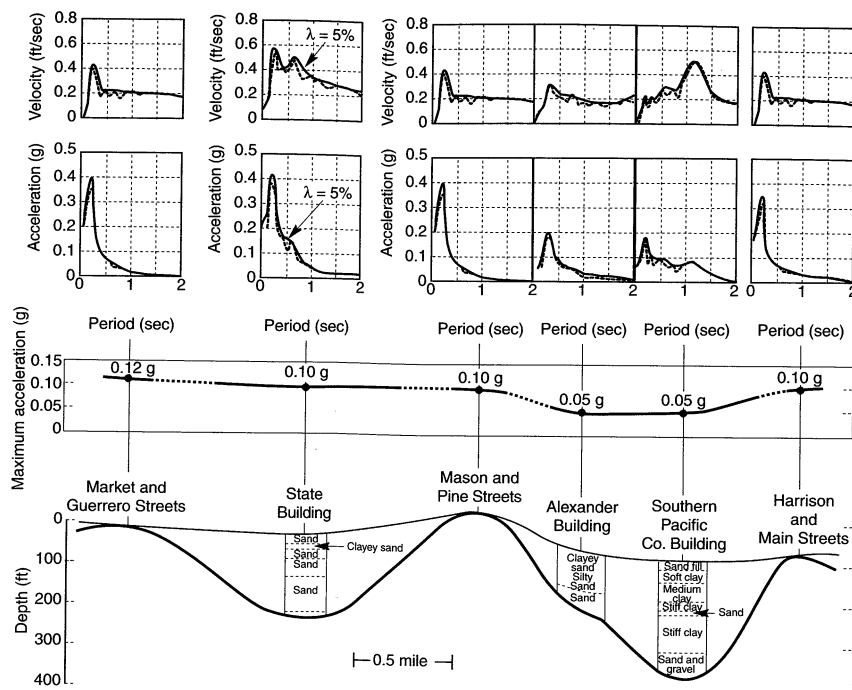


Figure 8.4 Variation of spectral velocity, spectral acceleration, and peak horizontal acceleration along a 4-mile section through San Francisco in the 1957 San Francisco earthquake. (After Idriss and Seed, 1968. Used by permission of the Seismological Society of America.)

8.2.3.1 Mexico City, 1985

The September 19, 1985 Michoacan ($M_s = 8.1$) earthquake caused only moderate damage in the vicinity of its epicenter (near the Pacific coast of Mexico) but caused extensive damage some 350 km away in Mexico City. Studies of ground motions recorded at different sites in Mexico City illustrated the significant relationship between local soil conditions and damaging ground motions and led to important advances in understanding the cyclic response of plastic clays (e.g., Dobry and Vucetic, 1987).

For seismic zonation purposes, Mexico City is often divided into three zones with different subsurface conditions (Figure 8.5a). Shallow, compact deposits of mostly granular soil, basalt, or volcanic tuff are found in the *Foothill Zone*, located west of downtown. In the *Lake Zone*, thick deposits of very soft soils formed from the pluviation of airborne silt, clay, and ash from nearby volcanoes through the waters of ancient Lake Texcoco extend to considerable depths, as shown by the contours of Figure 8.5b. These soft soils generally consist of two soft clay (Mexico City Clay) layers separated by a 0- to 6-m-thick (0 to 20 ft) compact sandy layer called the *capa dura*. Groundwater is generally found at a depth of about 2 m over most of the Lake Zone. Between the Foothill and Lake Zones lies the *Transition Zone*, where the soft soil deposits are thin and interspersed erratically with alluvial deposits.

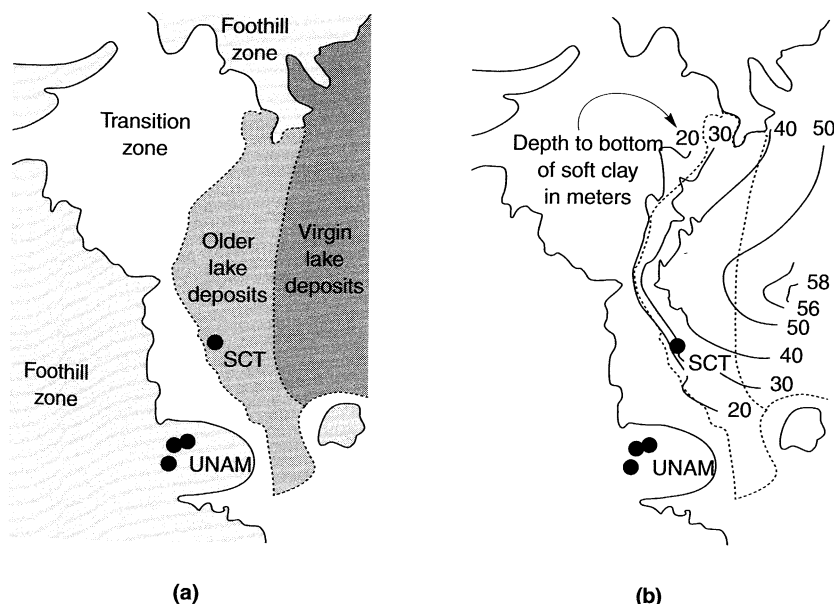


Figure 8.5 Strong-motion instruments and geotechnical conditions in Mexico City: (a) locations of strong motion instruments relative to Foothill, Transition, and Lake Zones; (b) contours of soft soil thickness. (After Stone et al., 1987.)

Prior to 1985, a number of strong-motion instruments had been deployed in Mexico City. Shown in Figure 8.5 are the locations of those at the Universidad Nacional Autonoma de Mexico (UNAM) and the Secretary of Communications and Transportation (SCT) site. The UNAM site was located in the Foothill Zone on 3 to 5 m (10 to 16 ft) of basaltic rock underlain by softer strata of unknown thickness. The SCT site was located on the soft soils of the Lake Zone.

Although the Michoacan earthquake was quite large, its great distance from Mexico City produced accelerations at the UNAM (rock) site of only 0.03g to 0.04g (Figure 8.6). In

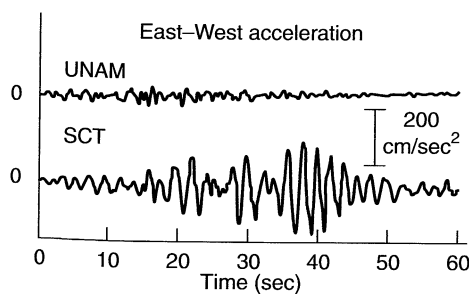


Figure 8.6 Time histories of acceleration recorded by strong motion instruments at UNAM and SCT sites. (After Stone et al., 1987.)

the Transition Zone, peak accelerations at the VIV site were slightly greater than those at UNAM but still quite low. In the Lake Zone, however, peak accelerations at the CDA and SCT sites were up to five times greater than those at UNAM. The frequency contents of the SCT and CDA motions were also much different than that of the UNAM motion; the predominant period was about 2 sec at SCT and slightly longer at CDA. Strong levels of shaking persisted over a very long duration at the SCT and CDA sites. The response spectra shown in Figure 8.7 illustrate the pronounced effects of the Lake Zone soils: at periods of approximately 2 sec, spectral accelerations at the SCT site were about 10 times greater than those at the UNAM site. The SCT site was underlain by 35 to 40 m (115 to 131 ft) of soft clay with an average s-wave velocity of about 75 m/sec (250 ft/sec). As a result, its characteristic site period [equation (7.16)] was $T_s = 4H/v_s \approx 4(37.5)/75 = 2$ sec, a value consistent with the peak in the SCT response spectrum of Figure 8.7.

Structural damage in Mexico City was highly selective; large parts of the city experienced no damage while other areas suffered pronounced damage. Damage was negligible in the Foothill Zone and minimal in the Transition Zone. The greatest damage occurred in those portions of the Lake Zone underlain by 38 to 50 m (125 to 164 ft) of soft soil (Stone et al., 1987), where the characteristic site periods were estimated at 1.9 to 2.8 sec. Even within this area, damage to buildings of less than five stories and modern buildings greater than 30 stories was slight. Most buildings in the five- to 20-story range, however, either collapsed or were badly damaged. Using the crude rule of thumb that the fundamental period of an N -story building is approximately $N/10$ sec, most of the damaged buildings had fundamental periods equal to or somewhat less than the characteristic site period. Accounting for the period-lengthening effect of soil-structure interaction (Section 7.4) and the tendency for the fundamental period of a structure to increase during a strong earthquake (due to the reduction in stiffness caused by cumulative architectural and structural damage), it seems likely that the damaged structures were subjected to many cycles of large dynamic forces at periods near their fundamental periods. This “double-resonance” condition (amplification of bedrock motion by the soil deposit and amplification of the soil motion by the structure) combined with structural design and construction deficiencies to cause locally devastating damage.

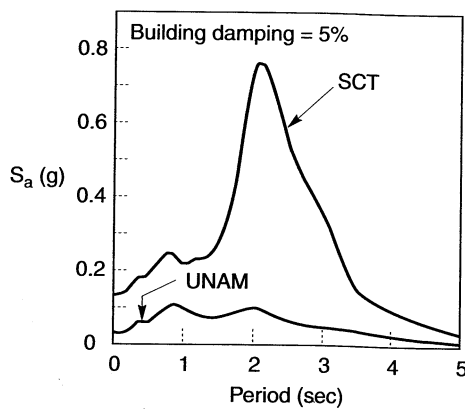


Figure 8.7 Response spectra computed from recorded motions at UNAM and SCT sites. (After Romo and Seed, 1986.)

8.2.3.2 San Francisco Bay Area, 1989

On October 19, 1989, a $M_s = 7.1$ earthquake occurred near Mt. Loma Prieta located about 100 km south of San Francisco and Oakland, California. The Loma Prieta earthquake produced MMI VIII shaking in the epicentral region, but intensities were actually higher, MMI IX, in portions of San Francisco and Oakland. The fact that the earthquake caused extensive damage in certain areas, and relatively little damage in others, suggested that local site effects were important.

The San Francisco Bay basin is largely filled with alluvial deposits of clays and silty to sandy clays with some layers of sandy and gravelly soils. The deeper deposits were overconsolidated by historical glacial sea-level drawdown, but the upper unit was deposited after the last drawdown episode. This material, known as San Francisco Bay Mud, is a normally consolidated silty clay. It is highly compressible and its strength grades from soft near the ground surface to medium stiff at depth. For purposes of seismic zonation, the Bay area can be divided into the three zones shown in Figure 8.8. The San Francisco Bay Mud is generally found at the margins of the bay, where its thickness varies from zero up to several tens of feet.

Both the epicentral region and the San Francisco Bay area were well instrumented with seismographs and accelerometers. Peak horizontal accelerations were recorded at the locations shown in Figure 8.8. These accelerations were high near the epicenter but attenuated with distance from the source. The attenuation, however, occurs much more rapidly for sites in the Rock/Shallow Residual Soil zone than in the Alluvium or Bay Mud zones (Figure 8.8).

The response of two instruments, those located at Yerba Buena Island and Treasure Island in the middle of San Francisco Bay, are particularly instructive. Yerba Buena Island

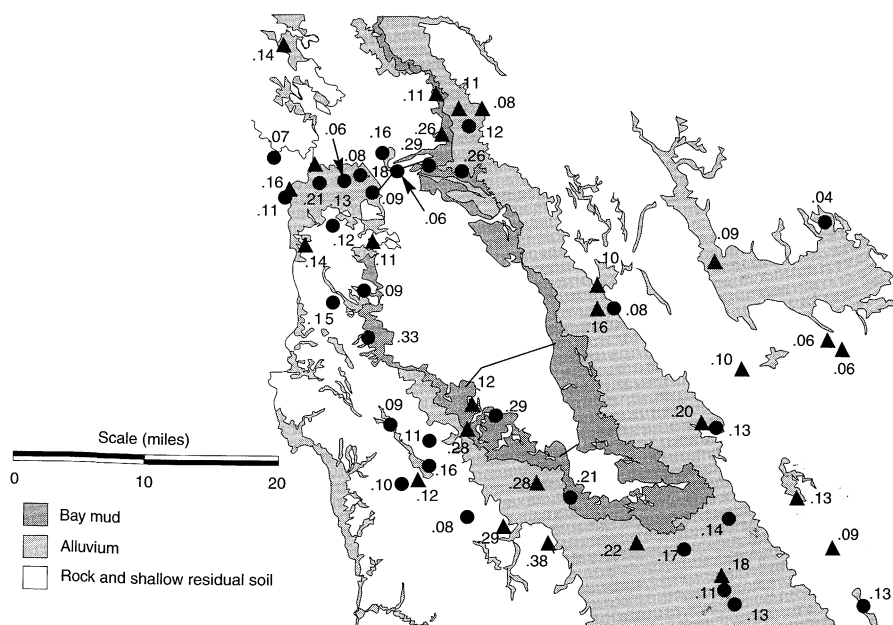


Figure 8.8 Measured peak horizontal accelerations (in g's) in the San Francisco Bay area during the 1989 Loma Prieta earthquake. Note the variation of peak acceleration for different site conditions. (After Seed et al., 1990.)

is a rock outcrop and Treasure Island is a 400-acre man-made hydraulic fill placed partially on the Yerba Buena shoals, a sandbar located immediately northwest of Yerba Buena Island. Treasure Island is underlain by a variable thickness of San Francisco Bay Mud; the Treasure Island seismograph was underlain by 45 ft (13.7 m) of loose sandy soil (hydraulic fill and natural soils) over 55 ft (16.8 m) of San Francisco Bay Mud. The Yerba Buena Island seismograph was located directly on rock. Though the Yerba Buena Island and Treasure Island instruments were virtually the same distance from the source, they recorded dramatically different ground surface motions (Figure 8.9a). Peak accelerations at Yerba Buena Island were 0.06g in the E-W direction and 0.03g in the N-S direction; the corresponding values at Treasure Island were 0.16g and 0.11g. Response spectra for the two sites are shown in Figure 8.9b. Clearly, the presence of the soft soils at the Treasure Island site caused significant amplification of the underlying bedrock motion.

Amplification of ground motion by soft soil deposits in other areas contributed significantly to damage in other parts of the San Francisco Bay area. The northern portion of the I-880 Cypress Viaduct that collapsed in the earthquake was underlain by San Francisco Bay Mud; the southern part that remained standing was not.

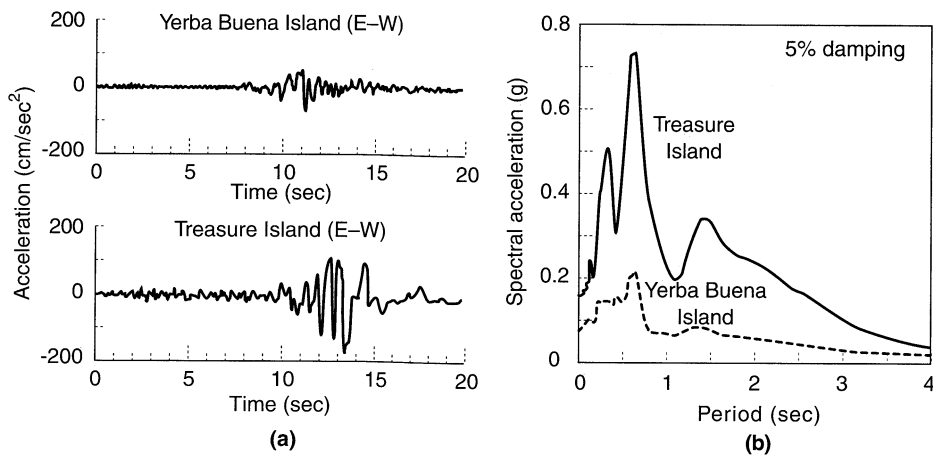


Figure 8.9 Ground surface motions at Yerba Buena Island and Treasure Island in the 1989 Loma Prieta earthquake: (a) time histories; (b) response spectra. (After Seed et al., 1990.)

8.2.4 Compilations of Data on Local Site Effects

The preceding section illustrates the important influence of local site conditions on the characteristics of ground surface motions. Case histories of ground response in Mexico City, the San Francisco Bay area, and many other locations have clearly shown that local site conditions strongly influence peak acceleration amplitudes and the amplitudes and shapes of response spectra.

Comparisons of peak acceleration attenuation relationships for sites underlain by different types of soil profiles show distinct trends in amplification behavior (Seed et al., 1976). Although attenuation data are scattered, overall trends suggest that peak accelerations at the surfaces of soil deposits are slightly greater than on rock when peak accelerations are small and somewhat smaller at higher acceleration levels (Figure 8.10). Based on data from Mexico

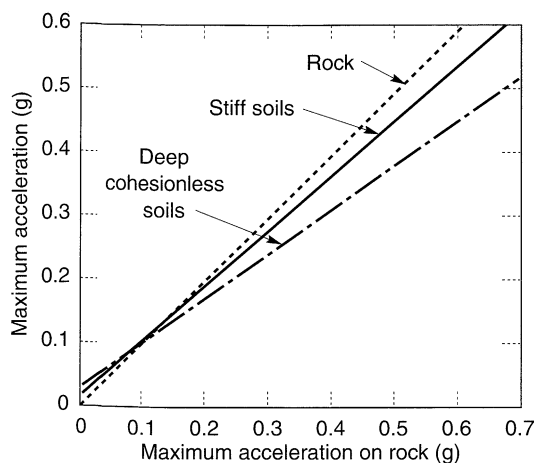


Figure 8.10 Approximate relationships between peak accelerations on rock and other local site conditions. (After Seed et al., 1976.)

City and the San Francisco Bay area, and on additional ground response analyses, Idriss (1990) related peak accelerations on soft soil sites to those on rock sites (Figure 8.11). At low to moderate acceleration levels (less than about 0.4g), peak accelerations at soft sites are likely to be greater than on rock sites. In some cases, such as Mexico City in 1985 and the San Francisco Bay area in 1989, relatively small rock accelerations may cause high accelerations at the surfaces of soft soil deposits. At higher acceleration levels, however, the low stiffness and nonlinearity of soft soils often prevent them from developing peak accelerations as large as those observed on rock.

Local site conditions also influence the frequency content of surface motions and hence the response spectra they produce. Seed et al. (1976) computed response spectra from ground motions recorded at sites underlain by four categories of site conditions: rock sites, stiff soil sites (less than 200 ft (61 m) deep), deep cohesionless soil sites (greater than 250 ft (76 m) deep), and sites underlain by soft to medium-stiff clay deposits. Normalizing the computed spectra (by dividing spectral accelerations by the peak ground acceleration) illustrates

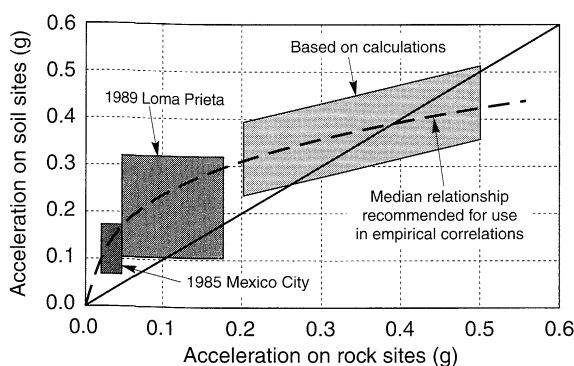


Figure 8.11 Approximate relationship between peak accelerations on rock and soft soil sites. (After Idriss, 1990, *H. Bolton Seed Memorial Symposium Proceedings*, Vol. 2, p. 285. Used by permission of BiTech Publishers, Ltd.)

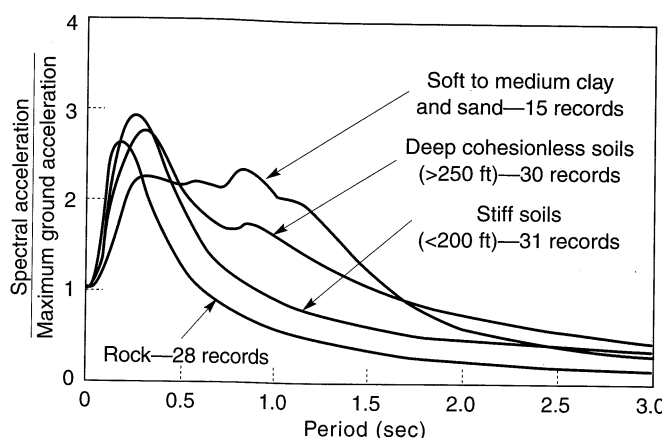


Figure 8.12 Average normalized response spectra (5% damping) for different local site conditions. (After Seed et al., 1976.)

the effects of local soil conditions on the shapes of the spectra (Figure 8.12). The effects are apparent: at periods above about 0.5 sec, spectral amplifications are much higher for soil sites than for rock sites. At longer periods, the spectral amplification increases with decreasing subsurface profile stiffness. Figure 8.12 clearly shows that deep and soft soil deposits produce greater proportions of long-period (low-frequency) motion. This effect can be very significant, particularly when long-period structures such as bridges and tall buildings are founded on such deposits. These results also show that the use of a single response spectrum shape for all site conditions is not appropriate, a finding that has strongly influenced the development of building codes and standards (Section 8.4.2).

8.2.5 Effects of Surface Topography and Basin Geometry

The effects of topographic irregularities and alluvial basin geometry on ground motions can be significant. Perhaps the best known example of apparent topographic effects was produced by an accelerograph on the abutment of Pacoima Dam in southern California. The Pacoima Dam accelerograph recorded peak horizontal accelerations of about $1.25g$ in each of two perpendicular directions in the 1971 San Fernando ($M_L = 6.4$) earthquake, values that were considerably larger than expected for an earthquake of this magnitude. The accelerograph, however, was located at the crest of a narrow, rocky ridge adjacent to the dam (Trifunac and Hudson, 1971). Subsequent investigations have attributed a good part of the unusually high peak accelerations to dynamic response of the ridge itself—a topographic effect. In the cases where alluvial valleys have been filled with soft soils, one-dimensional ground response analyses are often able to capture most essential aspects of response. They may not, however, be able to describe the complex wave fields and long durations produced by multiple reflections in some of these basins. The effects of surface topography and basin geometry are illustrated in the following sections.

8.2.5.1 Topography

The topographic effects caused by simple irregularities can be estimated from exact solutions to idealized problems (Aki, 1988). For a triangular infinite wedge subjected to vertically propagating SH-waves (with particle motion parallel to its axis), apex displacements are amplified by a factor $2\pi/\phi$, where ϕ is the vertex angle of the wedge (Figure 8.13a). This approach can be used to approximate topographic effects for certain cases of ridge-valley terrain (Figure 8.13b). Different geometries and different wave fields have also been considered (e.g., Geli et al., 1988; Sanchez-Sesma, 1990; Faccioli, 1991).

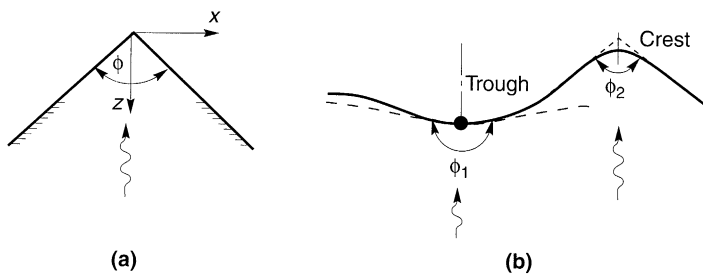


Figure 8.13 Characterization of simple topographic irregularities: (a) notation for a triangular wedge; (b) approximation of actual ground surface (solid line) at trough and crest by wedges. (After Faccioli, 1991.)

Increased amplification near the crest of a ridge was measured in five earthquakes in Matsuzaki, Japan (Jibson, 1987). Figure 8.14 shows how the normalized peak acceleration varied at different points along the ridge. The average peak crest acceleration was about 2.5 times the average base acceleration. Similar patterns of amplification on ridges are suggested

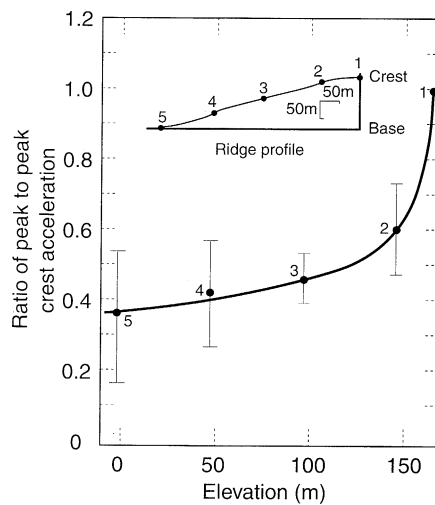


Figure 8.14 Normalized peak accelerations (means and error bars) recorded on mountain ridge at Matsuzaki, Japan. (After Jibson, 1987.)

by damage patterns in earthquakes in Italy and Chile (Finn, 1991). Analysis of topographic irregularities is a complicated problem; the interaction of waves can produce complex patterns of amplification and deamplification, depending on the geometry of the irregularity and on the types, frequencies, and angles of incidence of the incoming waves (Sanchez-Sesma and Campillo, 1993).

8.2.5.2 Basins

Since many large cities are located on or near alluvial valleys, the effects of basin geometry on ground motion is of great interest in geotechnical earthquake engineering. The curvature of a basin in which softer alluvial soils have been deposited can trap body waves and cause some incident body waves to propagate through the alluvium as surface waves (Vidale and Helmberger, 1988). These waves can produce stronger shaking and longer durations than would be predicted by one-dimensional analyses that consider only vertically propagating s-waves.

King and Tucker (1984) measured ground motions along transverse and longitudinal profiles across the Chusai Valley near the Afghanistan border of the former Soviet Union. Interpretation of the response in a series of small ($M_L \leq 4.0$) earthquakes suggested that one-dimensional ground response analyses could predict the average response of sediments near the center of the valley but not at the edges. Significant differences between the amplification functions at the center and edges of the valley were observed, explaining why the motions at those locations were considerably different. Similar effects have been observed for other valleys (e.g., Caracas in 1967, San Fernando in 1971, and Leninakan, Armenia in 1988) in different earthquakes.

Bard and Garel (1986) used an analytical approach to study the two-dimensional response of shallow and deep alluvial valleys. By comparing computed amplification functions for the two-dimensional case with those based on the assumption of one-dimensional wave propagation, the accuracy of the one-dimensional assumption could be demonstrated. As shown in Figure 8.15a, the one- and two-dimensional amplification functions at the center of a shallow, flat valley (Station 8) were quite similar, which indicates that one-dimensional analyses would be appropriate in that area. Closer to the edge of the valley (Station 4), however, the amplification functions were considerably different. For the deep valley shown in Figure 8.15b, agreement between the one- and two-dimensional amplification functions was much better at the center of the valley than near the edges, but was not as good as for the shallow valley. For alluvial valleys of irregular shape, such combined concave/convex regions, theoretical studies (e.g., Rial et al., 1992) indicate that very complex, even chaotic, motions can result.

The potential for significant differential motion across such alluvial valleys has important implications for the design of long-span structures, such as bridges and pipelines, that often cross valleys. Differential movements can induce large loads and cause heavy damage to these types of structures.

8.2.5.3 Evaluation of Effects

Evaluation of the effects of topographic and subsurface irregularities requires two- and in some cases, three-dimensional analyses. Such analyses are often complicated and time consuming and may require more detailed site characterization than may be feasible.

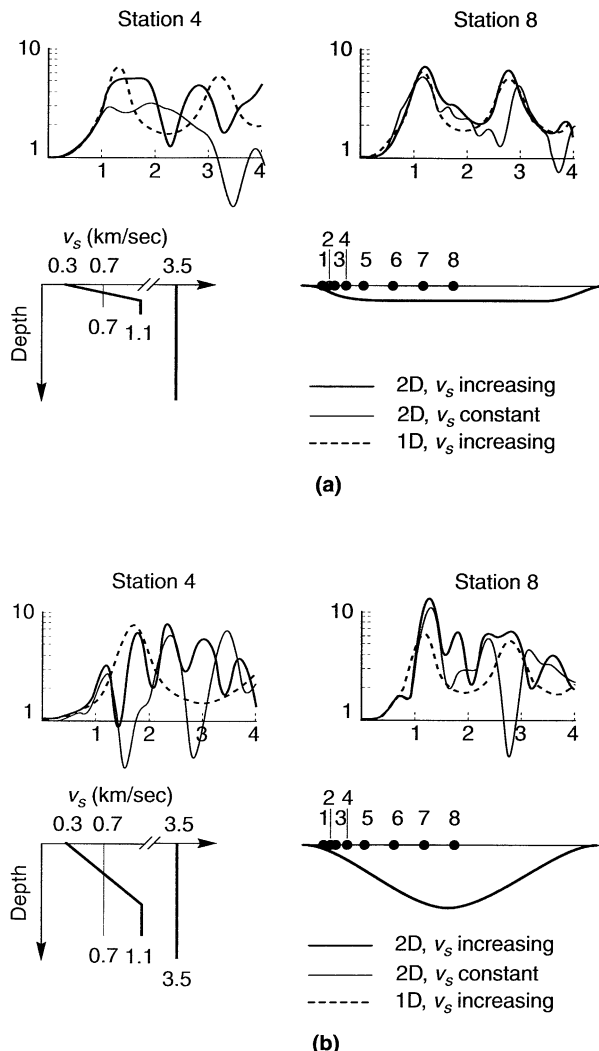


Figure 8.15 Comparison of amplification factors for one- and two-dimensional analyses of (a) shallow, flat basin, and (b) deep basin. (After Bard and Gariel, 1986. Used by permission of the Seismological Society of America.)

Although they may be difficult to predict, there is little doubt that such effects exist. Silva (1988) summarized the effects of topographic and subsurface irregularities, with comments on their quantitative predictability, as shown in Table 8-1.

Although provisions for considering topographic effects have been incorporated into a French building code (French Association for Earthquake Engineering, 1990), participants in a recent site effects workshop (Whitman, 1992) considered the introduction of such provisions into U.S. codes to be premature.

Table 8-1 Effects of Topographic and Subsurface Irregularities

Structure	Conditions	Type	Size	Quantitative Predictability
Surface topography	Sensitive to shape ratio, largest for ratio between 0.2 and 0.6; most pronounced when $\lambda \approx$ mountain width	Amplification at top of structure, amplification and deamplification at base, rapid changes in amplitude phase along slopes	Ranges up to a factor of 30 but generally from about 2 to 10	Poor: generally underpredict size; may be due to ridge-ridge interaction and three-dimensional effects
Sediment-filled valleys	Local changes in shallow sediment thickness	Increased duration	Duration of significant motions can be doubled	Fair
	Generation of long-period surface waves from body waves at shallow incidence angles	Increased amplification and duration due to trapped surface waves	Duration and amplification of significant motions may be increased over one-dimensional projections	Good at periods exceeding 1 sec
Shallow and wide (depth/width < 0.25) sediment-filled valleys	Effects most pronounced near edges; largely vertically propagating shear waves away from edges	Broadband amplification near edges due to generation of surface waves	One-dimensional models may underpredict at higher frequencies by about 2 near edges	Good: away from edges one dimension works well, near edges extend one dimension to higher frequencies
Deep and narrow (depth/width > 0.25) sediment-filled valleys	Effects throughout valley width	Broadband amplification across valley due to whole valley modes	One-dimensional models may underpredict for a wide bandwidth by about 2 to 4; resonant frequencies shifted from one dimension	Fair: given detailed description of vertical and lateral changes in material properties

Source: After Silva (1988).

8.3 DESIGN PARAMETERS

Earthquake-resistant design of new structures and evaluation of the safety of existing structures requires analysis of their response to earthquake shaking. Evaluation of geotechnical hazards, such as liquefaction and slope failure, also requires analysis with respect to some level of shaking. The level of shaking for which satisfactory performance is expected is often referred to as a *design level* of shaking and is described by a *design ground motion*. Design ground motions can, depending on how they are to be used, be specified in many different ways. Many analyses of soil and structural response require an entire time history of motion; others require only one or more of the ground motion parameters described in Chapter 3. The parameters most commonly used to specify design ground motions are peak horizontal acceleration, peak horizontal velocity, predominant period, response spectrum ordinates, and duration.

8.3.1 Design Earthquakes

Historically, design parameters were most commonly determined from a specified *design earthquake*, and some regulatory agencies still require that earthquake-resistant design be performed with respect to the motion produced by a design earthquake. The specification of a design earthquake implies a level of determinism in the seismic hazard analysis; that is, after the design earthquake is characterized (which can be done deterministically or probabilistically), its effects at the site of interest are computed deterministically. Historically, design earthquakes have been associated with *two-level design*, in which a structure or facility is required both to remain operational at one level of motion, and to avoid catastrophic failure at another, more severe level.

Many different terms have been used to describe the levels of severity associated with design earthquakes; some of them have been defined differently by different organizations. The Maximum Credible Earthquake (MCE) is usually defined as the largest earthquake that can reasonably be expected (although the meaning of the word *reasonably* may be open to interpretation) from a particular source. The Safe Shutdown Earthquake (SSE), used in the design of nuclear power plants, is specifically defined (Christian, 1988) as the earthquake that produces the maximum peak horizontal acceleration for the following cases: (1) moving the epicenter of the largest anticipated event in the surrounding seismotectonic province (region of uniform seismicity) to the site, (2) moving the epicenters of the largest events in the adjacent seismotectonic provinces to the nearest points on their boundaries and attenuating their motions to the site, and (3) moving the foci of the largest events on any capable faults to the closest points on the faults to the site and then attenuating their motions to the site. In many geographic regions, the MCE and SSE have similar characteristics. Other terms that have been used to describe similar worst-case levels of shaking include Maximum Capable Earthquake, Maximum Design Earthquake, Contingency Level Earthquake, Safety Level Earthquake, Credible Design Earthquake, and Contingency Design Earthquake. The two-level design approach generally requires that structures of facilities be designed to avoid catastrophic failure at the levels of shaking produced by these upper-level design earthquakes.

A lower but more likely level of shaking would be produced by an Operating Basis Earthquake (OBE); it is an earthquake that should be expected during the life of a structure (Krinitsky et al., 1993). The OBE has been taken as an earthquake with half the peak acceleration of the SSE (Christian, 1988), as an earthquake that produces motion with a 50% probability of exceedance in 50 years (USCOLD, 1985), and as an earthquake with a return period of about 110 years (Christian et al., 1978). Other terms that have been used to describe design earthquakes of similar size are Operating Level Earthquake, Maximum Probable Earthquake, Probable Design Earthquake, and Strength Level Earthquake. Two-level design requires that structures and facilities be designed to remain operational after being subjected to the levels of shaking associated with these lower-level design earthquakes.

Design earthquakes are often specified without regard to their likelihood of occurrence, even though a MCE may have a return period of 200 years in one location and 10,000 years in another. Their use in the development of design ground motions has decreased as probabilistic seismic hazard analysis techniques have developed. Still, some believe (e.g., Krinitzky et al., 1993) that the assumptions of the probabilistic approach are insufficiently supported by observational data to allow its reliable use for critical structures and facilities. This lack of data is particularly significant for large earthquakes.

8.3.2 Design Spectra

Response spectra are often used to represent seismic loading for the dynamic analysis of structures. As a result, design ground motions are often expressed in terms of *design spectra*. Design spectra and the response spectra of actual earthquakes are not the same. Response spectra from earthquakes are highly irregular (e.g., Figure 3.16); their shapes reflect the details of their specific frequency contents and phasing. Design spectra, on the other hand, are generally quite smooth; they are usually determined by smoothing, averaging, or enveloping the response spectra of multiple motions. The use of smooth design response spectra implicitly recognizes the uncertainty with which soil and structural properties are known by avoiding sharp fluctuations in spectral accelerations with small changes in structural period.

Newmark and Hall (1973), for example, recommended that design response spectra be developed from a series of straight lines on a tripartite plot (Section A.2.2 of Appendix A) corresponding to the acceleration-, velocity-, and displacement-controlled portions (Section 3.3.2.1) of the spectrum. A Newmark–Hall design spectrum is obtained by multiplying the peak ground acceleration, velocity, and displacement values by the factors shown in Table 8-2. At periods below about 0.17 sec (frequencies above about 6 Hz), the spectral accelerations are tapered down to the peak ground acceleration. A peak ground velocity of 48 in./sec (122 cm/sec) and peak ground displacement of 36 in. (91 cm) are assumed to be consistent with a peak ground acceleration of 1.0g; each of these parameters can be scaled by the ratio of the design peak ground acceleration to 1.0g to produce a design spectrum.

Table 8-2 Amplification factors for Newmark–Hall Design Spectra

Structural Damping Ratio	Amplification Factors for:		
	Displacement	Velocity	Acceleration
0	2.5	4.0	6.4
2	1.8	2.8	4.3
5	1.4	1.9	2.6
10	1.1	1.3	1.5
20	1.0	1.1	1.2

Source: After Newmark and Hall (1973).

Example 8.2

Develop a Newmark–Hall design spectrum for 5% damping and a peak ground acceleration of 0.25g.

Solution For 5% damping, the acceleration, velocity, and displacement amplification factors are 2.6, 1.9, and 1.4, respectively. Consequently, the peak spectral values are:

$$\text{Spectral acceleration: } S_a = 2.6(0.25g) = 0.65g$$

$$\text{Spectral velocity: } S_v = 1.9 \frac{0.25g}{1.00g} (48 \text{ in/sec}) = 22.8 \text{ in/sec}$$

$$\text{Spectral displacement: } S_d = 1.4 \frac{0.25g}{1.00g} (36 \text{ in}) = 12.6 \text{ in}$$

A tripartite plot of the resulting design spectrum is shown in Figure E8.2.

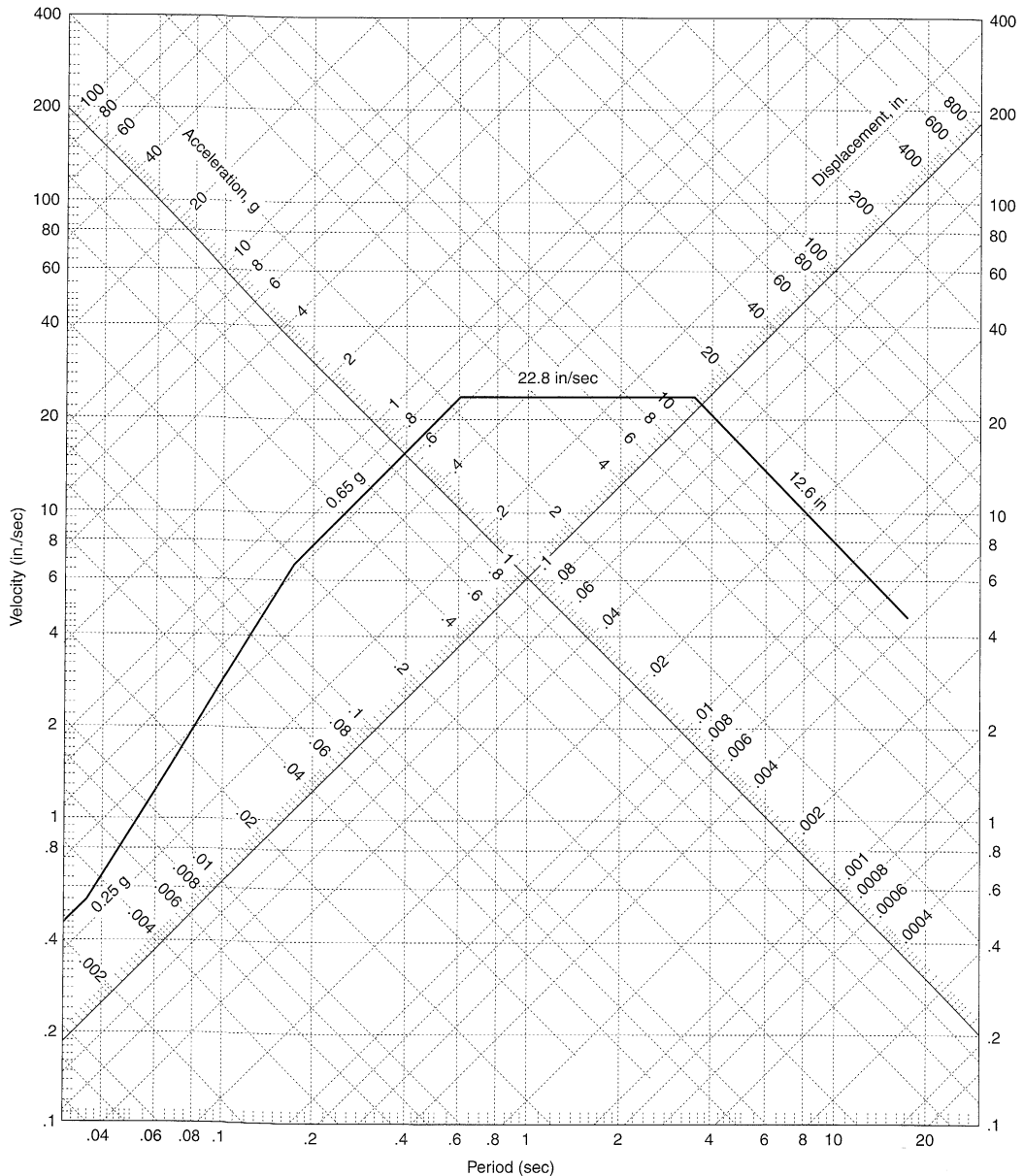


Figure E8.2

For sites that could be subjected to shaking from more than one seismic source, development of a design spectrum can be complicated. A site in California, for example, may be subjected to strong short-period (high-frequency) motion from small earthquakes on nearby faults and strong long-period (low-frequency) motion from large earthquakes on more distant faults. The development of predictive relationships for the ordinates of response spectra

(Section 3.4.4.4) have allowed *uniform risk spectra* (e.g., Trifunac et al., 1987), in which spectral ordinates are obtained by individual PSHAs, to be generated with proper consideration of all seismic sources. With this approach, the design spectrum has an equal probability of exceedance at all periods of vibration. Because of the averaging procedures inherent in the attenuation relationships on which they are based, uniform risk spectra have smooth shapes that are unlike the response spectra from individual ground motions.

8.4 DEVELOPMENT OF DESIGN PARAMETERS

The characteristics of the design ground motion at a particular site are influenced by the location of the site relative to potential seismic sources, the seismicity of those sources, the nature of rupture at the source, travel path effects between the source and the site, local site effects, and the importance of the structure or facility for which the ground motion is to be used. The manner in which the motion is to be used should also be considered.

Design ground motions are usually developed in one of two ways: from site-specific analyses or from the provisions of building codes and standards.

8.4.1 Site-Specific Development

Site-specific design ground motions reflect the detailed effects of the particular subsurface conditions at the sites of interest. The usual process for developing site-specific ground motions involves a seismic hazard analysis and a ground response analysis. The seismic hazard analysis can be performed deterministically or probabilistically using the techniques described in Chapter 4. The use of probabilistic seismic hazard analyses requires that the design motion be associated with some level of risk, or return period. Selection of such a quantity can be quite complex; various social, economic, and political considerations are often involved. For many structures and facilities in the United States, design ground motions have been based on parameters with a 10% probability of exceedance in 50 years (or a 475-year return period). The requirements of most contemporary building codes, for example, are based on that level of risk though some experts believe that higher return periods would be more appropriate (Matthiesen et al., 1982; Whitman, 1989). Different regulatory agencies may require different return periods for different types of structures and facilities.

The seismic hazard analysis will produce a set of ground motion parameters that may, or may not, correspond to the subsurface conditions at the site of interest. Both deterministic and probabilistic seismic hazard analyses utilize predictive relationships (Section 3.4) that usually correspond to a fairly narrow range of subsurface conditions; if the site of interest is located on a similar profile, these parameters may be taken directly as the *design ground motion parameters*. If it is not, however, the parameters from the seismic hazard analysis must be modified to account for the effects of local site conditions.

This parameter modification process may be performed empirically, using prior observations such as those shown in Figures 8.12 and 8.13, or analytically. In the analytical approach, both deconvolution (Section 7.1.1.4) and conventional ground response analyses may be required, as illustrated in Figure 8.16. The seismic hazard analysis will produce parameters that describe a ground motion at the surface (point A) of a site with subsurface

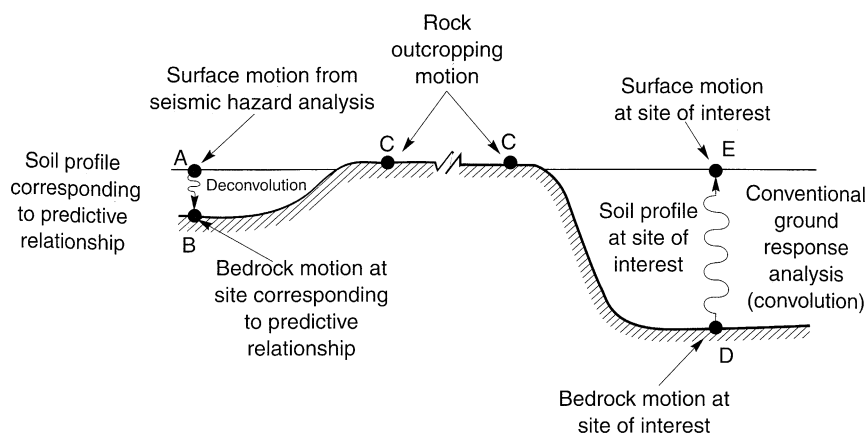


Figure 8.16 Procedure for modifying ground motion parameters from a seismic hazard analysis to account for the effects of local site conditions.

conditions that corresponds to those of the sites in the database from which the predictive relationship was developed. To determine the corresponding parameters at the surface of the site of interest, a time history of ground surface motion that is consistent with the predicted parameters is generated; procedures for generating such time histories are described in Section 8.5. This motion is then deconvolved through a soil profile corresponding to the predictive relationship to determine the time history of bedrock motion (at point *B*) that would produce the time history of motion at point *A*. The corresponding rock at cropping motion produces the bedrock motion applied at the base (point *D*) of the soil profile at the site of interest. A conventional ground response analysis is then performed to predict the motion at the surface of the soil profile of interest (point *E*). This motion, which is consistent with the results of the seismic hazard analysis and also with the local site conditions, can be taken as the design ground motion. It can be used to compute site-specific design parameters such as peak acceleration and velocity, response spectral ordinates, and duration.

8.4.2 Code-Based Development

Alternatively, design ground motions can be developed on the basis of building code provisions. Consideration of earthquake and other effects in the design of new structures is mandated by modern building codes which may be adopted as law by various city, county, and state governments. The purpose of codes such as the *Uniform Building Code* (UBC) is “to provide minimum standards to safeguard life or limb, health, property, and public welfare by regulating and controlling the design, construction, quality of materials, use and occupancy, location and maintenance of buildings” (ICBO, 1991). Codes for highway bridges, nuclear power plants, and other types of structures have been produced by various regulatory agencies.

The provisions of building codes are developed by consensus of a broad group of experienced practitioners and researchers. Although contemporary codes do consider site effects, they usually do so by lumping groups of similar soil profiles together so that their provisions apply to broad ranges of soil conditions within which the local conditions of a particular site are expected to fall. Because of this, design ground motions developed from

code provisions are usually more conservative (i.e., correspond to stronger levels of shaking) than those developed from site-specific analyses. This relationship between site-specific and code-based design ground motions provides an economic incentive that implicitly encourages the development of site-specific design ground motions.

8.4.2.1 Background

The first building code, motivated primarily by insurance losses due to fire, was published in 1905. In 1927, the first edition of the *UBC* was published by what is now the International Conference of Building Officials. The *UBC* has become widely adopted, particularly in the western United States, where seismic hazards are high. As a result, the *UBC* has been near the forefront of activity on issues relating to earthquake-resistant design. In the United States, the Building Officials and Code Administrators International (BOCA) Code, Standard Building Code (SBC), and National Building Code (NBC) are frequently used in the midwest, south, and northeast, respectively.

Historically, building code provisions relating to earthquake safety have developed incrementally, with each increment occurring shortly after the occurrence of a damaging earthquake in the United States. Although building codes go back as far as about 2100 B.C. (Berg, 1983), explicit provisions for earthquake resistance did not appear in U.S. building codes until after the 1925 Santa Barbara earthquake ($M_L = 6.3$). Those provisions, however, were listed only in an appendix and were not mandatory. After the 1933 Long Beach, California earthquake ($M_L = 6.3$), in which the potentially tragic consequences of the collapse of many school buildings were averted by the earthquake's occurrence after school hours, the state of California passed a bill known as the Field Act, which required that all new school construction be designed for higher levels of earthquake resistance and that school construction be closely supervised in the field. Shortly thereafter, California also passed the Riley Act, which established mandatory design requirements for nearly all occupied buildings in the state.

In 1959, the Structural Engineers Association of California (SEAOC) published a document titled *Recommended Lateral Force Requirements and Tentative Commentary*, more commonly known as the *SEAOC Blue Book*, whose provisions were incorporated into the 1961 *UBC*. Since then the Blue Book has been modified about every three years with its revised provisions adopted first by the ICBO in the *UBC* and then by the other major regional codes. These codes developed in an incremental, evolutionary manner as new research and experience was gained. The provisions of the *UBC*, for example, have historically been based on those of the *SEAOC Blue Book* (e.g., SEAOC, 1990). In 1975 the Applied Technology Council began, with support from the National Science Foundation and the National Bureau of Standards (now the National Institute for Standards and Technology), to take a fresh look at all aspects of earthquake-resistant design, with the aim of developing code provisions that could be adopted nationwide. In 1978, ATC published a report titled *Tentative Provisions for the Development of Seismic Regulations for Buildings* (ATC, 1978), popularly known as *ATC 3-06*. This document included many innovations, including several relating to the treatment of local site effects and development of design ground motions. Years later, many of the provisions of *ATC 3-06* were incorporated into the NEHRP (National Earthquake Hazards Reduction Program) *Recommended Provisions for the Development of Seismic Regulations for New Buildings* produced by the Building Seismic Safety Council (BSSC, 1991a, b).

The *UBC* and *NEHRP Provisions* are the most influential contemporary documents that describe minimum standards for earthquake-resistant design of buildings in the United States. Although codes and provisions change with time, both the *UBC* and *NEHRP Provisions* address the issue of local site conditions and present commonly used approaches to the development of design ground motions. The following sections describe the manner in which local site effects and design ground motions are specified in the most recent (1994) versions of the *UBC* and *NEHRP Provisions*. These descriptions are intended only to illustrate the philosophies and basic approaches of the documents; they are not complete.

8.4.2.2 Uniform Building Code

Building codes are not intended to eliminate earthquake damage completely. Indeed, the commentary to the 1990 *SEAOC Blue Book*, upon which the 1991 *UBC* is based, says that “structures designed in conformance [with the *Blue Book* recommendations] should, in general, be able to: (1) resist a minor level of earthquake ground motion without damage; (2) resist a moderate level of earthquake ground motions without structural damage, but possibly experience some nonstructural damage; (3) resist a major level of earthquake ground motion having an intensity equal to the strongest either experienced or forecast for the building site, without collapse, but possibly with some structural as well as nonstructural damage” (*SEAOC*, 1990). These expectations illustrate the basic philosophy of earthquake-resistant structural design, as the commentary goes on to state that it “would in most cases be economically prohibitive to design buildings to remain elastic for all levels of earthquake ground motions. A fundamental tenet of seismic design is that inelastic yielding is allowed to accommodate seismic loadings as long as such yielding does not impair the vertical load capacity of the structure. In other words, damage is allowed in the maximum expected earthquake loading case only if it does not pose a significant probability of the structure’s collapse.”

The *UBC* allows two basic approaches to the earthquake-resistant design of buildings: a static approach in which the effects of ground motions are represented by static lateral forces, and a dynamic approach in which ground motion is characterized by a design response spectrum. The simpler static approach is allowed only for certain conditions of geometric regularity, occupancy, and height.

Static Approach. The static approach is based on determination of a *design base shear* force, which is then distributed in a specified pattern over the height of the structure for structural analysis of lateral load resistance. The total design base shear in a given direction (the structure must be able to resist it in any direction) is given by

$$V = \frac{ZIC}{R_w} W \quad (8.1)$$

where *Z* is a *seismic zone factor* (Figure 8.17), *I* is an *importance factor* (Table 8-3), *R_w* is a numerical coefficient that reflects the ductility of the structure (Table 8-4), *W* is the *seismic dead load* (which includes permanent equipment and portions of live loads, partition loads, and snow loads), and

$$C = \frac{1.25S}{T^{2/3}} \quad (8.2)$$

In equation (8.2), *S* is a soil coefficient (Table 8-5) and *T* is the fundamental period of the structure in seconds. The value of *C* need not exceed 2.75, and the minimum value of *C/R_w*,

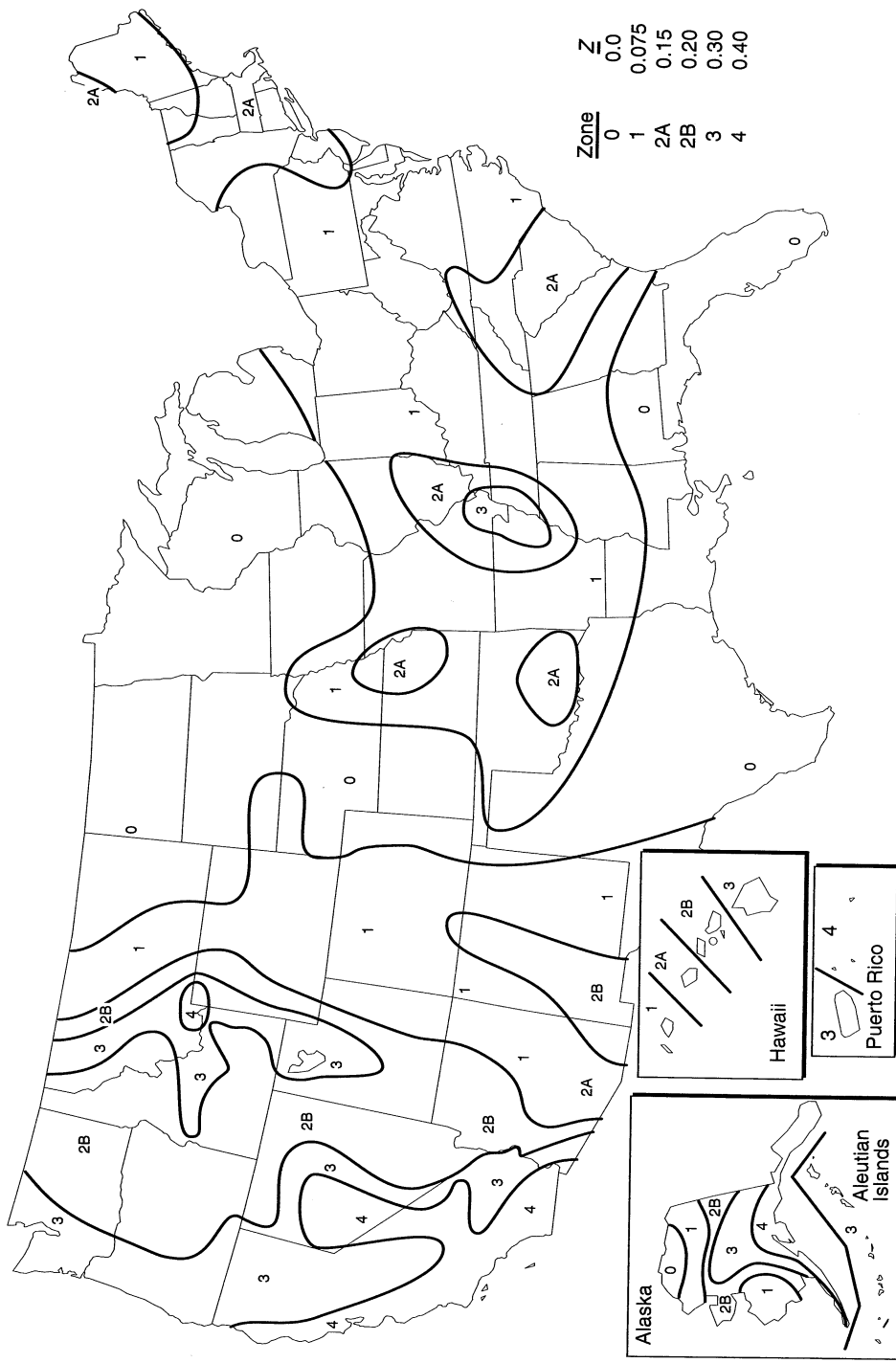


Figure 8.17 Map and table for evaluation of UBC seismic zone factor, Z (Reproduced from the 1994 edition of the *Uniform Building Code™*, copyright © 1994, with permission of the publisher, the International Conference of Building Officials.)

Table 8-3 UBC Importance Factor, I .

Occupancy Category	I
Essential Facilities ^a	1.25
Hazardous Facilities ^b	1.25
Special Occupancy Structures ^c	1.00
Standard Occupancy Structures ^d	1.00
Miscellaneous Structures ^e	

^a Includes hospitals and other medical facilities having surgery and emergency treatment areas; fire and police stations; tanks or other structures containing, housing or supporting water or other fire-suppression materials or equipment required for the protection of essential or hazardous facilities, or special occupancy structures; structures and shelters in emergency-preparedness centers; standby power-generating equipment for essential facilities; structures and equipment in government communication centers and other facilities required for emergency response; garages and shelters for emergency vehicles and emergency aircraft; aviation control towers; standby power generating equipment for essential facilities.

^b Includes occupancies and structures therein housing or supporting toxic or explosive chemicals or substances. Nonbuilding structures housing, supporting, or containing quantities of toxic or explosive substances which, if contained in a building, would cause that building to be classified as a hazardous facility.

^c Occupancies with a capacity > 300 persons; buildings for schools through secondary or day-care centers - capacity > 250 students; occupancies used for colleges or adult education schools - capacity > 500 students; medical facilities with 50 or more resident incapacitated patients, but not included above; jails and detention facilities, all structures with occupancy > 5,000 persons; structures and equipment in power-generating stations and other public utility facilities not included above, and required for continued operation.

^d All structures having occupancies or functions not listed above, and occupancy towers.

^e Group U occupancies except for towers.

under most conditions, is set at 0.075. The fundamental period of the structure can be determined by different methods; in the simplest it is approximated by

$$T = C_t(h_n)^{3/4} \quad (8.3)$$

where C_t has values of 0.035 for steel moment-resisting frames, 0.030 for reinforced concrete moment-resisting frames and eccentrically braced steel frames, and 0.020 for all other structures, and h_n is the height (in feet) of the uppermost level of the main portion of the structure above the base.

Dynamic Approach. The dynamic approach of the *UBC* allows the response of the structure to be determined by response spectrum analysis or by time-history analysis. Hence design ground motions can be specified in terms of design response spectra or design ground motion time histories. In both cases, the *UBC* requires that the design ground motion correspond to a 10% probability of exceedance in a 50-year period (475-year return period).

Design response spectra can be determined in one of two ways: from site-specific ground response analyses of the type described in Section 8.4.1, or from smooth, normalized spectral shapes (Figure 8.18). The normalized spectral shapes follow from the results of Seed et al. (1976) and Newmark and Hall (1982) (see Figure 8.12), and account for the frequency-dependent amplification of ground motion by different local site conditions. These normalized spectra are presented for three subsurface profiles; as would be expected, greater long-period spectral accelerations are associated with softer and deeper soil profiles.

Table 8-4 Values of UBC reduction factor, R_w .

Basic Structural System	Lateral Load Resisting System	R_w
Bearing Wall System	Light-framed walls with shear panels a. Wood structural panel walls for structures three stories or less b. All other light-framed walls	8 6
	Shear walls a. Concrete b. Masonry	6 6
	Light steel-framed bearing walls with tension-only bracing	4
	Braced frames where bracing carries gravity loads a. Steel b. Concrete c. Heavy timber	6 4 4
Building Frame System	Steel eccentrically braced frame Light-framed walls with shear panels a. Wood structural panel walls for structures three stories or less b. All other light-framed walls	10 9 7
	Shear walls a. Concrete b. Masonry	8 8
	Ordinary braced frames a. Steel b. Concrete c. Heavy timber	8 8 8
	Special concentrically braced frames a. Steel	9
Moment-Resisting Frame System	Special moment-resisting frames (SMRF) a. Steel b. Concrete	12 12
	Concrete intermediate moment-resisting frames (IMRF)	8
	Ordinary moment-resisting frames (OMRF) a. Steel b. Concrete	6 5
	Masonry moment-resisting wall frame	9
Dual Systems	Shear walls a. Concrete with SMRF b. Concrete with steel OMRF c. Concrete with concrete IMRF d. Masonry with SMRF e. Masonry with OMRF f. Masonry with concrete IMRF	12 6 9 8 6 7
	Steel eccentrically braced frame a. With steel SMRF b. With steel OMRF	12 6
	Ordinary braced frames a. Steel with steel SMRF b. Steel with steel OMRF c. Concrete with concrete SMRF d. Concrete with concrete IMRF	10 6 9 6
	Special concentrically braced frames a. Steel with steel SMRF b. Steel with steel OMRF	11 6

Table 8-5 UBC Soil Coefficient, S .

Type	Description	S
S1	A soil profile with either: (a) A rock-like material characterized by a shear wave velocity greater than 2,500 feet per second or by other suitable means of classification, or (b) Medium-dense to dense or medium-stiff to stiff soil condition where the soil depth is less than 200 feet.	1.0
S2	A soil profile with predominantly medium dense to dense or medium-stiff to stiff soil conditions, where the soil depth exceeds 200 feet or more.	1.2
S3	A soil profile containing more than 20 feet of soft to medium stiff clay but not more than 40 feet of soft clay.	1.5
S4	A soil profile containing more than 40 feet of soft clay characterized by a shear wave velocity less than 500 feet per second.	2.0

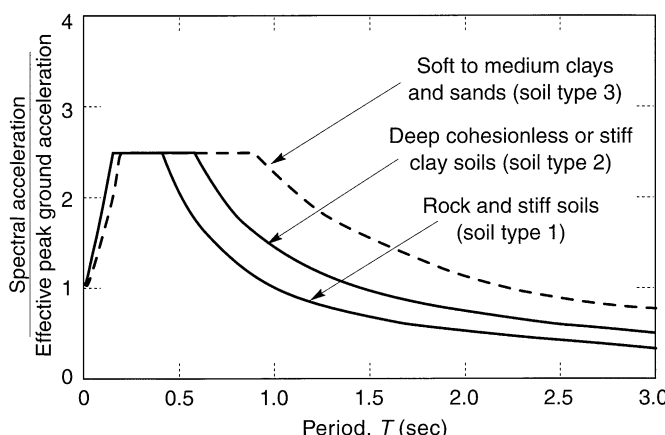


Figure 8.18 Site-dependent normalized response spectra. (Reproduced from the 1994 edition of the *Uniform Building Code™*, copyright © 1994, with permission of the publisher, the International Conference of Building Officials.)

The design response spectrum is obtained by multiplying the ordinates of the normalized spectrum by the effective peak ground acceleration, which can be taken as the value of the seismic zone factor, Z , expressed as a fraction of gravity. Note that the shape of the design spectrum is constant—the spectral ordinates are linearly scaled by the peak acceleration alone. Since important ground motion characteristics such as frequency content and duration are influenced by earthquake magnitude and distance, the probabilities of exceedance of a constant-shape design spectrum may be different at low periods than at high periods. The use of such a design spectrum may produce structural designs with different probabilities of failure. Uniform risk spectra (Section 8.3.2) minimize this possibility.

The *UBC* requires that design ground motion time histories be developed on a site-specific basis. The use of several time histories is recommended. Response spectra computed from the time histories must, either individually or in combination, approximate the site-specific design response spectrum. Site-specific analyses are required for flexible structures (fundamental periods greater than 0.7 seconds) located on soil profile S4.

Other Code Provisions. The UBC also sets forth requirements dealing with site grading, foundations, and retaining structures. In seismic zones 3 and 4, building officials may require that “the potential for soil liquefaction and soil strength loss during earthquakes shall be evaluated during the geotechnical investigation. The geotechnical report shall assess potential consequences of any liquefaction and soil strength loss, including estimation of differential settlement, lateral movement or reduction in foundation soil-bearing capacity, and discuss mitigating measures.” The topic of soil liquefaction is discussed in detail in Chapter 9.

8.4.2.3 NEHRP Provisions

The *NEHRP Provisions* is not a building code; rather, it is a source document intended to aid in the development of building codes in areas of seismic exposure. Their purpose is to “present criteria for the design and construction of buildings and nonbuilding structures subject to earthquake ground motions. Their purposes are to minimize the hazard to life for all buildings and nonbuilding structures, to increase the expected performance of higher occupancy structures as compared to ordinary structures, and to improve the capability of essential facilities to function during and after an earthquake . . . (they provide) the minimum criteria considered to be prudent and economically justified for the protection of life safety in buildings subject to earthquakes at any location in the United States. . . The ‘design’ earthquake ground motion levels specified . . . may result in both structural and non-structural damage. For most structures designed and constructed according to these provisions, it is expected that structural damage from a major earthquake may be repairable but it may not be economical. . . For motions larger than the design levels, the intent of these provisions is that there be a low likelihood of building collapse.” (BSSC, 1991b).

Ground Motion Parameters. The *NEHRP Provisions* use the effective peak acceleration, EPA, and effective peak velocity, EPV (Section 3.3.4), to describe ground motions. These parameters can be thought of as normalizing factors for the development of smooth response spectra; the EPA is proportional to the average spectral acceleration at low periods (0.1 to 0.5 sec) and the EPV is proportional to the spectral velocity at longer periods (about 1 sec). The EPA is usually somewhat lower than the peak acceleration of a specific ground motion and can be substantially lower for ground motions with very high frequencies. The EPV is usually greater than the peak velocity, particularly at large distances from strong earthquakes. To compute various design coefficients, the EPA and EPV are replaced by the dimensionless acceleration coefficients, A_a and A_v . The *effective peak acceleration coefficient*, A_a , is numerically equal to the EPA when expressed as a decimal fraction of gravity (i.e., $A_a = 0.2$ when $\text{EPA} = 0.2g$). The *effective peak velocity-related acceleration coefficient*, A_v , is numerically equal to $\text{EPV}/30$ when the EPV is expressed in in./sec (i.e., $A_v = 0.2$ when $\text{EPV} = 6 \text{ in./sec}$). Note that A_v is an acceleration coefficient, even though it is obtained from the spectral velocity; it provides a useful measure of the longer-period (lower-frequency) components of a ground motion. At any particular location, the design of a building may be governed by A_a or A_v . The NEHRP provisions contain maps, based on probabilistic seismic hazard analyses with a 10% probability of exceedance in a 50-year period, that divide the United States into seven seismic loading zones (Figure 8.19). The coefficients A_a and A_v can be determined from these maps and Table 8-6.

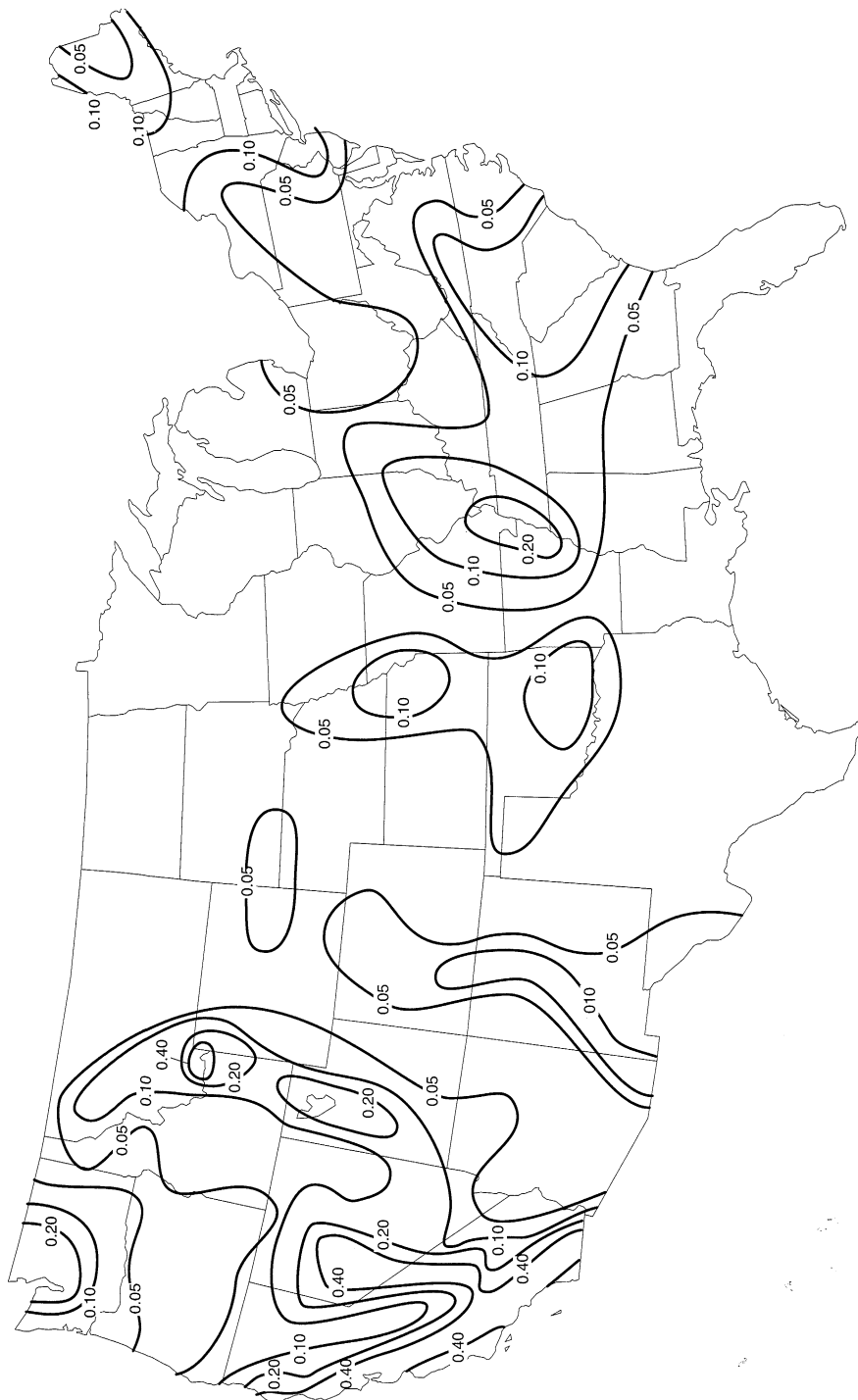


Figure 8.19 Maps of NEHRP seismic loading zones: (a) map 1 for A_a ; and (b) map 2 for A_v . (After BSSC, 1994.)

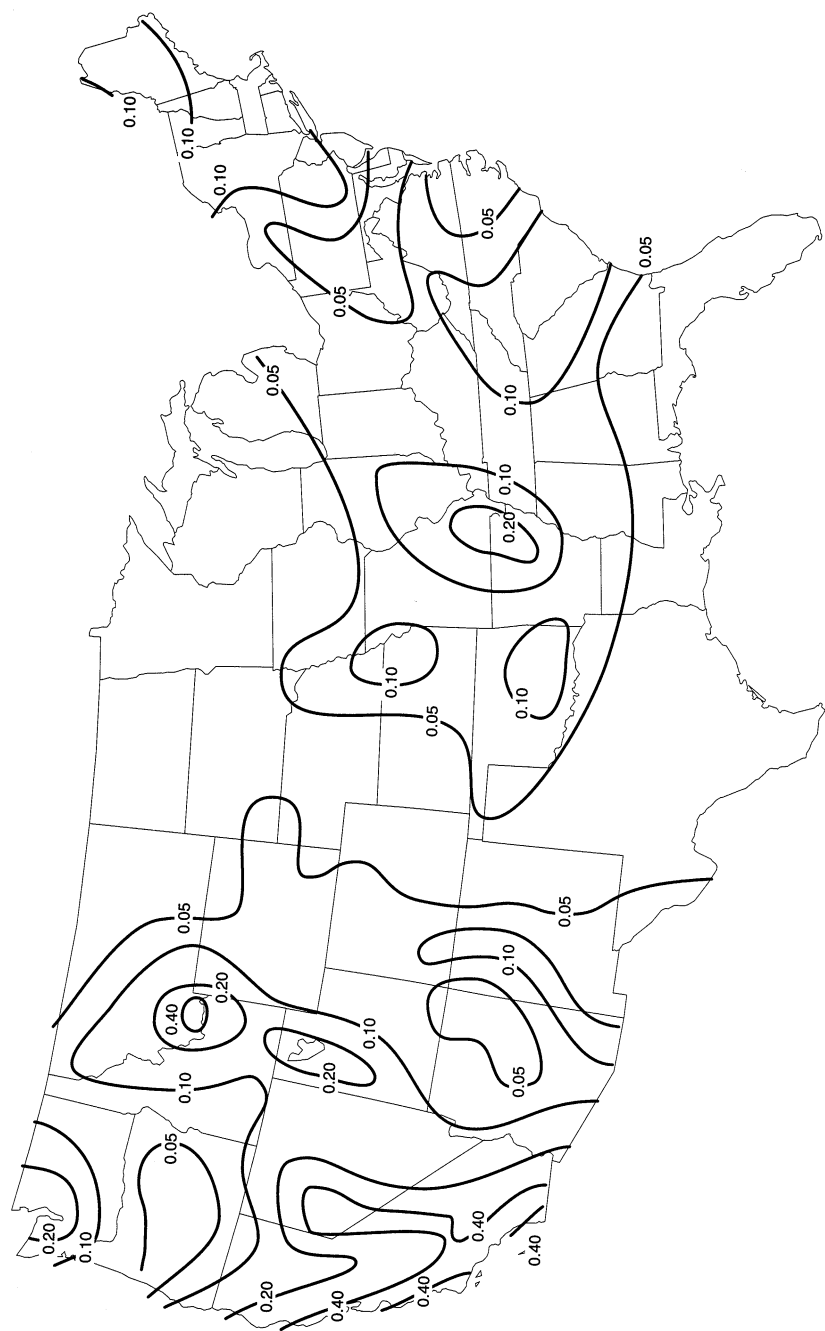


Figure 8.19 (continued)

Table 8-6 NEHRP Coefficients A_a and A_v

Map Area from Map 1 (for A_a) or Map 2 (for A_v)	Value of A_a and A_v
7	0.40
6	0.30
5	0.20
4	0.15
3	0.10
2	0.05
1	< 0.05 ^a

^a For equations or expressions incorporating the terms A_a or A_v , a value of 0.05 shall be used.

Equivalent Lateral Force Procedure. Like the *UBC*, the *NEHRP Provisions* account for local soil conditions in the determination of design loading. The *NEHRP Provisions*, however, address the effects of local soil conditions in greater detail than the *UBC*. The remainder of this section focuses on the differences between this aspect of the *UBC* and *NEHRP Provisions*, as illustrated by their static (or equivalent lateral force) approaches to seismic design.

The equivalent lateral force procedure of the *NEHRP Provisions* requires that the seismic base shear that is proportional to the weight of the structure.

$$V = C_s W \quad (8.4)$$

where W includes the total dead load and applicable portions of other loads (e.g., permanent equipment, partitions, live loads) and the seismic response coefficient, C_s , is the smaller of

$$C_s = \frac{1.2 C_v}{R T^{2/3}} \quad (8.5a)$$

or

$$C_s = \frac{2.5 C_a}{R} \quad (8.5b)$$

In Equations 8.5, R is a response modification factor (analogous but not identical to the R_w factor in the *UBC*) and T is the fundamental period of the structure. The long-period seismic coefficient, C_v , and the short-period seismic coefficient, C_a , reflect both local soil conditions and site seismicity. These coefficients are defined as

$$C_a = F_a A_a \quad (8.6a)$$

$$C_v = F_v A_v \quad (8.6b)$$

where F_a and F_v depend on soil type and A_a and A_v depend on site seismicity. The effective peak acceleration, A_a , and effective peak velocity-related acceleration, A_v , are obtained from Table 8-6 and Figure 8.20. The site coefficients, F_a and F_v , are shown in Table 8-7.

Table 8-7 Values of F_a and F_v for different site conditions and shaking intensities.

Soil Profile Type	Values of F_a				
	Shaking Intensity				
	$A_a \leq 0.1$	$A_a = 0.2$	$A_a = 0.3$	$A_a = 0.4$	$A_a \geq 0.5$
A	0.8	0.8	0.8	0.8	0.8
B	1.0	1.0	1.0	1.0	1.0
C	1.2	1.2	1.1	1.0	1.0
D	1.6	1.4	1.2	1.1	1.0
E	2.5	1.7	1.2	0.9	SS ¹
F	SS	SS	SS	SS	SS

Soil Profile Type	Values of F_v				
	Shaking Intensity				
	$A_v \leq 0.1$	$A_v = 0.2$	$A_v = 0.3$	$A_v = 0.4$	$A_v \geq 0.5$
A	0.8	0.8	0.8	0.8	0.8
B	1.0	1.0	1.0	1.0	1.0
C	1.7	1.6	1.5	1.4	1.3
D	2.4	2.0	1.8	1.6	1.5
E	3.5	3.2	2.8	2.4	SS ¹
F	SS	SS	SS	SS	SS

¹ Site-specific geotechnical investigation and dynamic site response analyses shall be performed.

Soil Profile Type	Description
A	Hard rock with measured shear wave velocity, $\bar{v}_s > 5000$ ft/sec (1500 m/sec)
B	Rock with 2500 ft/sec $< \bar{v}_s \leq 5000$ ft/sec (760 m/sec $< \bar{v}_s \leq 1500$ m/sec)
C	Very dense soil and soft rock with 1200 ft/sec $< \bar{v}_s \leq 2500$ ft/sec (360 m/sec $< \bar{v}_s \leq 760$ m/sec) or with either $\bar{N} > 50$ or $\bar{s}_u \geq 2000$ psf (100 kPa)
D	Stiff soil with 600 ft/sec $< \bar{v}_s \leq 1200$ ft/sec (180 m/sec $< \bar{v}_s \leq 360$ m/sec) or with either $15 \leq \bar{N} \leq 50$ or 1000 psf $\leq \bar{s}_u \leq 2000$ psf (50 kPa $\leq \bar{s}_u \leq 100$ kPa)
E	A soil profile with $\bar{v}_s < 600$ ft/sec (180 m/sec) or any profile with more than 10 ft (3 m) of soft clay defined as soil with $PI > 20$, $w \geq 40\%$, and $s_u < 500$ psf (25 kPa)
F	Soil requiring site-specific evaluations: <ol style="list-style-type: none"> 1. Soils vulnerable to potential failure or collapse under seismic loading such as liquefiable soils, quick and highly sensitive clays, collapsible weakly cemented soils. 2. Peats and/or highly organic clays ($H > 10$ ft (3 m) of peat and/or highly organic clay where H = thickness of soil) 3. Very high plasticity clays ($H > 25$ ft (8 m) with $PI > 75$) 4. Very thick soft/medium stiff clays ($H > 120$ ft (36 m)) <p>Exception: When the soil properties are not shown in sufficient detail to determine the Soil Profile Type, Type D shall be used. Soil Profile Types E or F need not be assumed unless the regulatory agency determines that Types E or F may be present at the site or in the event that Types E or F are established by the geotechnical data.</p>

8.5 DEVELOPMENT OF GROUND MOTION TIME HISTORIES

On many occasions, ground motion parameters alone do not adequately describe the effects of ground shaking. For analysis of nonlinear problems such as the response of inelastic structures or the permanent deformation of an unstable slope, time histories of motion are required. Time histories can also be required in the development of site-specific design ground motions, as illustrated in Figure 8.19. In these cases, time histories that match *target ground motion parameters* such as peak accelerations, velocities, or spectral ordinates are required.

In some cases, the local and regional geologic and tectonic conditions of the site of interest may be so similar to those of sites where actual strong motions have previously been measured that those strong motion records can be used directly. Usually, this is not the case, and artificial ground motions must be developed. Artificial ground motions can be developed in a number of different ways. The main challenges in their development are to ensure that they are consistent with the target parameters and that they are realistic (i.e., that their characteristics are consistent with those of actual earthquakes). This is not as easy as it might appear; many motions that appear reasonable in the time domain may not when examined in the frequency domain, and vice versa. Many reasonable-looking time histories of acceleration produce, after integration, unreasonable time histories of velocity and/or displacement. The quality of an artificial ground motion is very difficult to discern by eye.

The most commonly used methods for generation of artificial ground motions fall into four main categories: (a) modification of actual ground motion records, (b) generation of artificial motions in the time domain, (c) generation of artificial motions in the frequency domain, and (d) generation of artificial motions using Green's function techniques.

8.5.1 Modification of Actual Ground Motion Records

Perhaps the simplest approach to the generation of artificial ground motions is the modification of actual recorded ground motions. Maximum motion levels, such as peak acceleration and peak velocity, have been used to rescale actual strong motion records to higher or lower levels of shaking (Figure 8.20). Krinitzky and Chang (1979) recommended that the scaling factor (the ratio of the target amplitude to the amplitude of the record being scaled) should be kept as close to 1 as possible, and always between 0.25 and 4.0, and that analyses be conducted with several scaled records. Vanmarcke (1979), noting that simple amplitude scaling fails to account for differences in important characteristics such as frequency content and duration, suggested that limits on the scaling factor should be related to the type of problem to which the resulting motion is to be applied. For analysis of linear elastic structures, the limits of Krinitzky and Chang (1979) were considered suitable, but for liquefaction a scaling factor range of 0.5 to 2.0 was recommended.

This type of rescaling procedure requires careful selection of the actual motion that is to be used. A desirable ground motion record will not only have a peak acceleration or velocity close to the target value, but will have magnitude, distance, and local site characteristics that are similar to those of the target motion. Such a record is most likely to have a similar frequency content and duration to the target motion. Computer programs (e.g., Dus som et al., 1991; Ferritto, 1992) that contain, or at least interact with, strong motion databases are available to aid in the selection of actual ground motions for rescaling.

Rescaling of the time scale has been used to modify the frequency content of an actual ground motion record. This is usually accomplished by multiplying the time step of a digitized

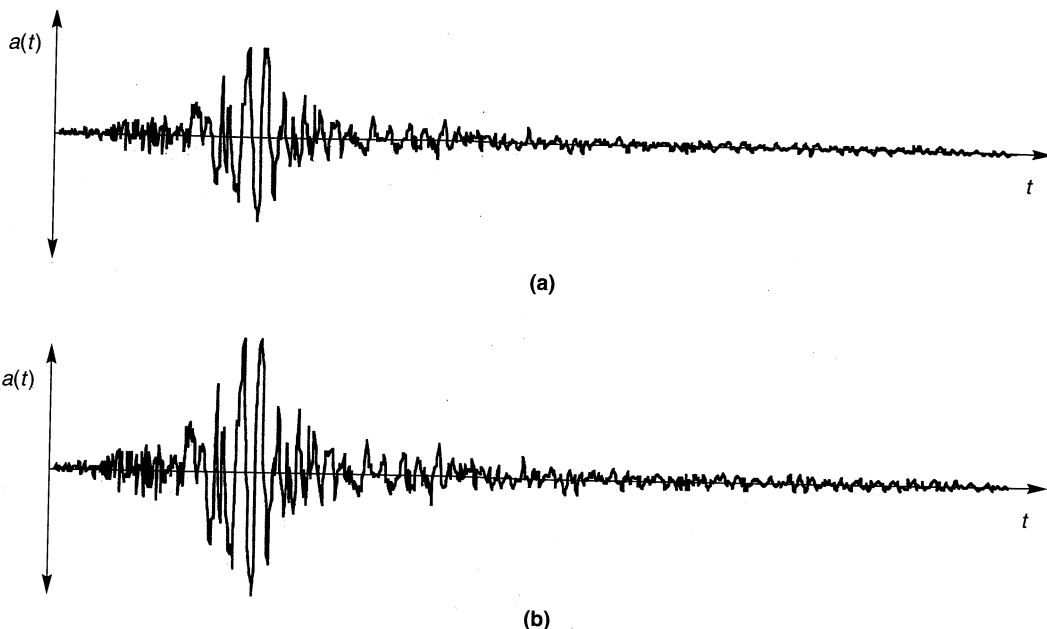


Figure 8.20 (a) Original accelerogram from actual earthquake; (b) rescaled version of original accelerogram in which accelerations were scaled upward by a factor of 1.5 to match target peak acceleration.

actual record by the ratio of the predominant period (Section 3.3.2.2) of the target motion to the predominant period of the actual motion (Figure 8.21). Since this approach changes the frequency content over the entire spectrum as well as the duration of the rescaled record, it should be used carefully to avoid unintended consequences.

To generate artificial ground motions of long duration without significantly changing the frequency content, some (e.g., Seed and Idriss, 1969) have spliced parts of actual ground motion records together. Procedures of this type must also be used with caution. Careful examination of the reasonableness of spliced motions in both the time and frequency domains is advised.

8.5.2 Time-Domain Generation

The resemblance of ground motion time histories to transient stochastic processes was noted years ago (Housner, 1947). Since then, a number of procedures that treat ground motions as stochastic processes have been developed. Many of these operate entirely in the time domain.

A stationary stochastic process is one whose statistics remain constant with time. A stationary accelerogram, for example, would have a constant mean acceleration, constant standard deviation of acceleration, and a constant frequency content—the accelerations would continue indefinitely. The fact that the acceleration amplitude of actual ground motions varies with time (ground motions have a beginning and an end, after all) renders their amplitudes nonstationary. Studies have also shown that the frequency content of a typical ground motion is also nonstationary—it changes over the duration of shaking.

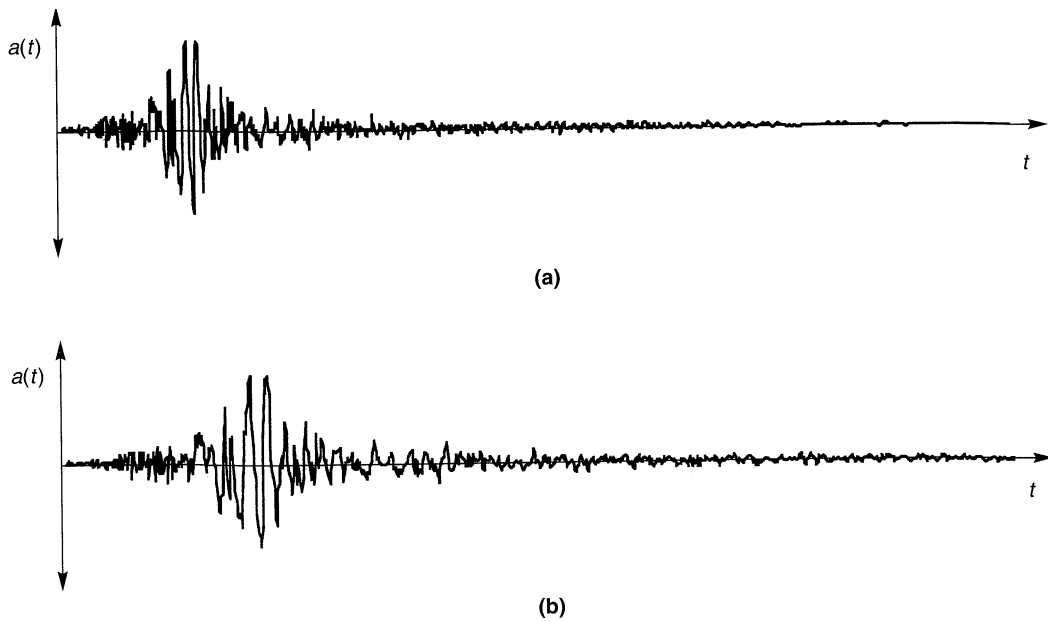


Figure 8.21 (a) Original accelerogram from actual earthquake; (b) rescaled version of original accelerogram in which time scale was scaled upward by a factor of 1.3 to match target predominant period. Note that the duration has also been increased by a factor of 1.3.

Generation of an artificial ground motion time history in the time domain typically involves multiplying a stationary, filtered white noise (or filtered Poisson process) signal by an envelope function that describes the buildup and subsequent decay (nonstationarity) of ground motion amplitude (Shinozuka and Deodatis, 1988), as illustrated in Figure 8.22. More recently, models that consider the nonstationarity of both amplitude and frequency content (e.g., Sharma and Shah, 1986; Shinozuka and Deodatis, 1988) have been developed. The use of autoregressive moving average (ARMA) models (e.g., Chang et al., 1982; Kozin, 1988) has also increased in recent years.

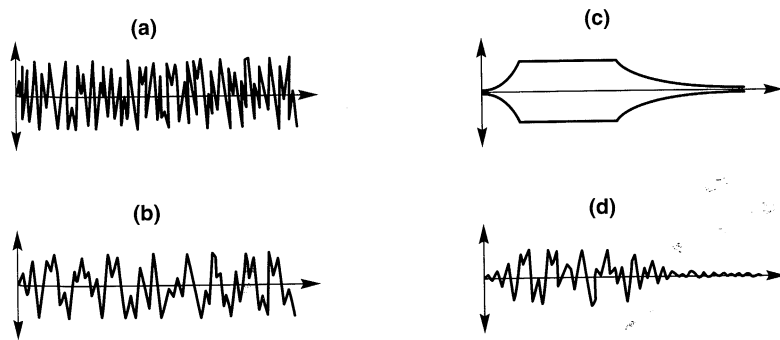


Figure 8.22 Example of time-domain generation of synthetic time history: (a) time history of white noise is filtered in the time domain to produce (b) time history of filtered white noise. Filtered white noise is multiplied by envelope function in (c) to produce the artificial ground motion shown in (d).

8.5.3 Frequency-Domain Generation

Ground motions can be generated quite conveniently in the frequency domain by combining a Fourier amplitude spectrum with a Fourier phase spectrum. The amplitude spectrum may be computed from an actual ground motion spectrum or may be represented by some theoretical means, such as a Brune spectrum or a power spectral density function (Section 3.3.2.1). The phase spectrum may be obtained from an actual ground motion or may be computed from a time history given by the product of white noise and an envelope function (Figure 8.23). Some investigators (e.g., Ohsaki, 1979; Abrahamson and Singh, 1986) have used phase difference distributions as an indicator of phase structure to develop nonrandom, artificial phase spectra.

Frequency-domain methods are particularly useful for generating motions that are consistent with target response spectra. Computer programs such as EQGEN (Chang et al., 1986b) and RASCAL (Silva, 1987) assume initial Fourier amplitude and phase spectra, and then iteratively adjust the ordinates of the Fourier amplitude spectrum until a motion consistent with the target response spectrum is produced. The origin of the target response spectrum must be kept in mind when generating spectrum-compatible motions. Constant risk spectra (Chapter 4), for example, represent the aggregate effect of potential earthquakes of many different magnitudes occurring at many different distances. Because a constant risk spectrum does not correspond to any particular seismic event, a motion generated from a constant risk target spectrum should not be expected to correspond to a particular seismic event (Naiem and Lew, 1995).

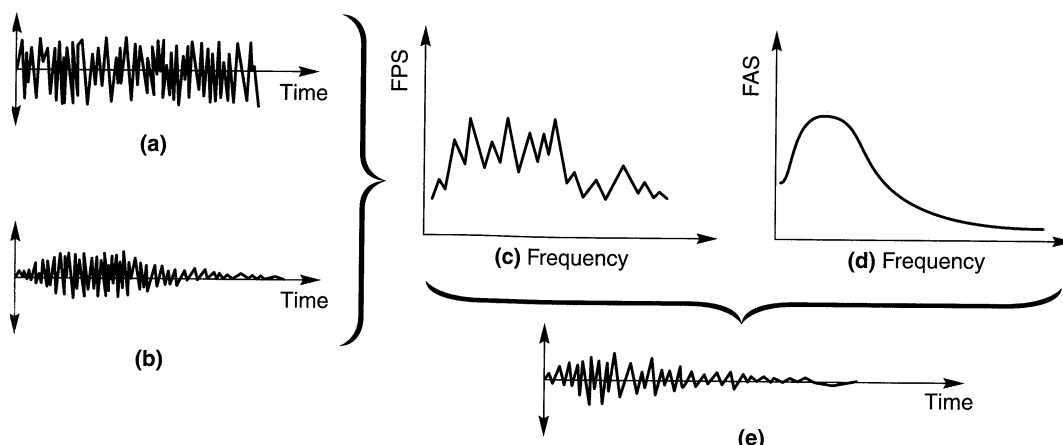


Figure 8.23 Example of frequency-domain generation of synthetic time history: (a) time history of white noise is shaped by envelope function to produce (b) time history of enveloped white noise. Fourier transform of enveloped white noise is performed to obtain (c) phase spectrum. Phase spectrum is combined with (d) amplitude spectrum to produce (e) synthetic time history.

8.5.4 Green's Function Techniques

The Green's function approach to ground motion modeling is based on the idea that the total motion at a particular site is equal to the sum of the motions produced by a series of individual ruptures of many small patches on the causative fault. Obtaining the site motion

requires defining the geometry of the earthquake source, dividing the source into a finite number of patches, defining the sequence in which the patches rupture, defining the slip functions (functions describing the variation of slip displacement with time for each patch) across the source, and defining Green's functions (functions that describe the motion at the site due to an instantaneous unit slip at the source; see Figure 8.24) across the source. Combining the Green's function with the slip function gives the motion at the site due to slip of each individual patch. Summing the effects of the slips of each patch while accounting for the order in which they rupture produces the overall ground motion at the site. Obviously, the summation procedure assumes that all materials remain linear.

Calculation of Green's functions requires knowledge of the velocity structure of the crustal materials between the source and site. However, estimation of the velocity structure, particularly with respect to heterogeneities responsible for the scattering that produces late-arriving coda waves, is a very difficult problem. Considerable computational effort is also required to calculate Green's function; finite-element, finite-difference, and ray theory techniques are usually used for this purpose. Hartzell (1978) bypassed these computations by using the weak motions of small earthquakes as *empirical Green's functions* to simulate the strong motion of large earthquakes. Empirical Green's functions have the benefit of automatically retaining the effects of the crustal velocity structure.

The Green's function approach is particularly useful for generating *near-field* motions, that is, motions at sites close enough to the fault that the fault dimensions become significant (for *far-field* sites, the fault can be treated as a point source without undue loss of accuracy). The nature of the rupture pattern, including the general direction in which rupture progresses, and the site azimuth (relative to the fault) can strongly influence ground motion in the near field. The Green's function approach allows phenomena such as directivity and fling (Section 2.5) to be reflected in artificial motions.

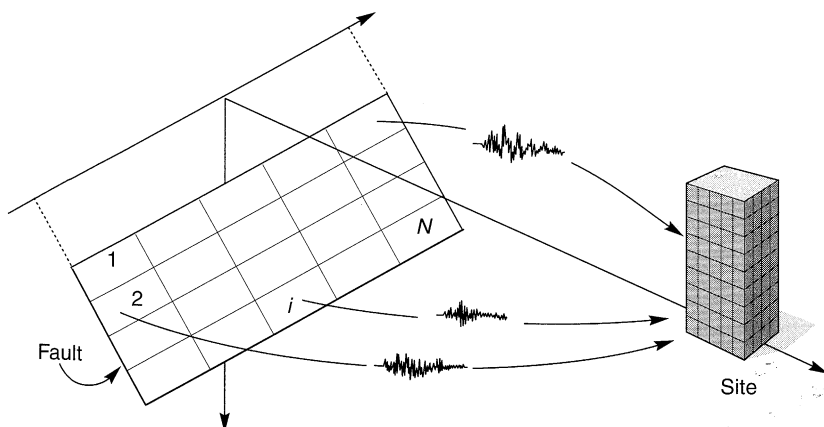


Figure 8.24 Schematic of Green's functions for a fault divided into N patches. Differences in the Green's functions for the different patches are due to differences in focal depth, epicentral distance, and geologic structure along the source–site path. Once Green's functions have been determined, site motions can easily be simulated for a variety of fault rupture patterns and slip functions.

8.5.5 Limitations of Artificial Ground Motions

As discussed in Chapter 3, actual ground motions are complicated—they are influenced by, and consequently reflect, characteristics of the seismic source, the rupture process, the source–site travel path, and local site conditions. Although it is convenient to characterize them with a small number of parameters, it is important to remember that such characterizations can never be complete.

Artificial motions that match a small number of target parameters are not unique; many different motions can produce the same target parameters. If such a set of motions are used to analyze problems for which damage correlates well to the target parameters, the predicted damage is likely to be consistent. For example, a set of different motions with the same peak acceleration will produce similar base shears in a stiff, linear elastic structure founded on rock. The same set of motions, however, might produce a broad range of base shears in a flexible and/or inelastic structure or in a structure founded on soft soil. They could also produce significantly different estimates of permanent slope movement or liquefaction potential. When using artificial motions, the eventual use(s) of the motions must always be reconciled with the criteria from which they were developed.

8.6 SUMMARY

1. Historical references to the correlation between earthquake damage and local site conditions extend back nearly 200 years. Provisions that specifically accounted for local site conditions did not appear in building codes, however, until the early 1970s.
2. Evidence for the existence of local site effects is compelling. In addition to theoretical evidence, amplification functions computed from measurements of surface and bedrock motions at the same location, and comparisons of surface motion characteristics from nearby sites with different subsurface conditions, all confirm the important effects of local site conditions on earthquake ground motions.
3. Geometric effects can also influence ground motions. Though topographic irregularities scatter seismic waves to produce complicated patterns of amplification and deamplification, motions at the crests of ridges are generally amplified. Alluvial basins filled with soft sediments can, depending on their shapes, trap body waves and produce surface waves within the alluvium. Ground motion in an alluvial basin may be considerably different than those that would be predicted by one-dimensional ground response analyses, particularly near the edges of the basin.
4. Earthquake-resistant design of new structures and evaluation of the seismic vulnerability of existing structures involves prediction of their response to design ground motions. Design ground motions are obtained from design parameters developed from a prescribed design earthquake or from a seismic hazard analysis.
5. Design parameters may be developed on a site-specific basis or they may be obtained from building codes. For a typical site, parameters based on site-specific analyses are likely to be more accurate than code-based parameters. They are also likely to result in more economical designs.

6. Building codes have historically developed on an incremental basis as new knowledge is obtained. The seismic provisions of building codes have followed the same trend with the most significant changes occurring after major earthquakes.
7. Building codes are not intended to eliminate earthquake damage completely. Instead, they aim to produce designs that will resist small ground motions without damage, moderate motions without structural damage, and severe motions without collapse.
8. Ground motion time histories with specified target parameters can be developed by several different procedures. When design parameters are used as targets, these procedures will produce design ground motions. Procedures based on scaling of recorded ground motions and generation of artificial ground motions are widely used.

HOMEWORK PROBLEMS

- 8.1 Compute and compare the response spectrum intensities at the State Building, Alexander Building, and Southern Pacific Company Building in the 1957 San Francisco earthquake (see Figure 8.4).
- 8.2 An earthquake produces a peak acceleration of $0.25g$ on a rock outcrop in the far-field. Estimate the peak ground surface accelerations that would be expected at stiff soil, deep cohesionless soil, and soft soil sites at the same distance from the source of the earthquake.
- 8.3 How would the frequency content of the bedrock motion influence the relationships shown in Figures 8.10 and 8.11. Comment on the ranges of applicability of these relationships.
- 8.4 Consider the Gilroy No. 1 (rock) and Gilroy No. 2 (soil) ground motions described in Chapter 3. Soil conditions at the Gilroy No. 2 (soil) site were described in Example 7.4. How well do the motions at these sites agree with the approximate relationships between peak accelerations on rock and soil outcrops shown in Figure 8.12?
- 8.5 How well do the shapes of the response spectra of the Gilroy No. 1 (rock) and Gilroy No. 2 (soil) motions (Figure 3.15) agree with the average normalized spectra shown in Figure 8.12?
- 8.6 Vertically propagating shear waves with a displacement amplitude of 1 cm at a great depth approach the ground surface illustrated below. Assuming that the topographic effects can be approximated by the triangular infinite wedge solution, estimate the displacement amplitudes at points A, B, C, and D.

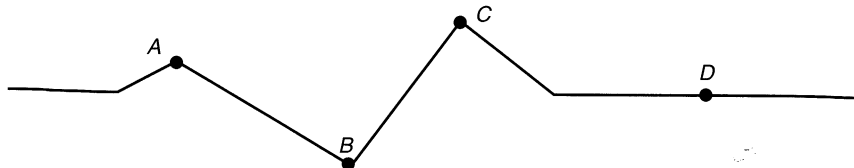
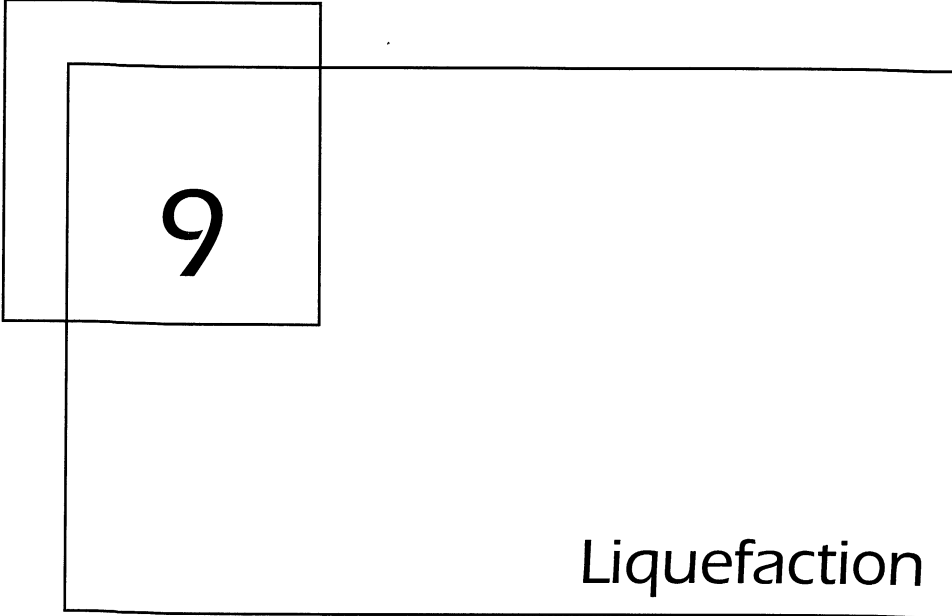


Figure P8.6

- 8.7 Determine and plot (on arithmetic scales) Newmark-Hall design spectra (5% damping) for a peak acceleration of $0.442g$. Label the acceleration-controlled, velocity-controlled, and displacement-controlled portions of the spectrum. How well does this design spectrum correspond to the response spectrum of the Gilroy No. 1 (rock) ground motion?

- 8.8** Using the provisions of the Uniform Building Code, evaluate design base shear coefficients (the ratio of the design base shear to the weight of the structure) for 8-story hospital buildings in Denver, Seattle, and San Francisco. Assume that the hospitals are constructed as ordinary moment-resisting steel frames. Bedrock outcrops at the ground surface at the Denver site. The Seattle site is located on 700 feet of dense, glacially overconsolidated soils. The San Francisco hospital site is underlain by 45 feet of soft San Francisco Bay Mud.
- 8.9** Use the provisions of the Uniform Building Code to develop design response spectra for the Denver and Seattle hospital sites from Problem 8.8. Briefly describe the steps that would be required to develop a design response spectrum for the San Francisco site.



9

Liquefaction

9.1 INTRODUCTION

Liquefaction is one of the most important, interesting, complex, and controversial topics in geotechnical earthquake engineering. Its devastating effects sprang to the attention of geotechnical engineers in a three-month period in 1964 when the Good Friday earthquake ($M_W = 9.2$) in Alaska was followed by the Niigata earthquake ($M_S = 7.5$) in Japan. Both earthquakes produced spectacular examples of liquefaction-induced damage, including slope failures, bridge and building foundation failures, and flotation of buried structures. In the 30 years since these earthquakes, liquefaction has been studied extensively by hundreds of researchers around the world. Much has been learned, but the road has not been smooth. Different terminologies, procedures, and methods of analysis have been proposed, and a prevailing approach has been slow to emerge.

In recent years, many of these differences have been reconciled by the realization that their causes were due, in large part, to semantics. The term *liquefaction* has been used to describe a number of different, though related phenomena. Rather than try to trace the convoluted development of the current state of knowledge regarding liquefaction, this chapter will present a basic framework for the conceptual understanding of liquefaction-related soil behavior and use it to describe the various methods by which liquefaction hazards can be evaluated. To do this, the chapter introduces some new terminology to distinguish between

phenomena that have frequently been lumped together under the heading of *liquefaction*. The new terminology allows these phenomena to be illustrated in a way that simplifies understanding of their mechanics and the manner in which they contribute to earthquake damage.

9.2 LIQUEFACTION-RELATED PHENOMENA

The term *liquefaction*, originally coined by Mogami and Kubo (1953), has historically been used in conjunction with a variety of phenomena that involve soil deformations caused by monotonic, transient, or repeated disturbance of saturated cohesionless soils under undrained conditions. The generation of excess pore pressure under undrained loading conditions is a hallmark of all liquefaction phenomena. The tendency for dry cohesionless soils to densify under both static and cyclic loading is well known. When cohesionless soils are saturated, however, rapid loading occurs under undrained conditions, so the tendency for densification causes excess pore pressures to increase and effective stresses to decrease. Liquefaction phenomena that result from this process can be divided into two main groups: *flow liquefaction* and *cyclic mobility*.

Both flow liquefaction and cyclic mobility are very important, and any evaluation of liquefaction hazards should carefully consider both. In the field, flow liquefaction occurs much less frequently than cyclic mobility but its effects are usually far more severe. Cyclic mobility, on the other hand, can occur under a much broader range of soil and site conditions than flow liquefaction; its effects can range from insignificant to highly damaging. In this book, the generic term *liquefaction* will be taken to include both flow liquefaction and cyclic mobility. Flow liquefaction and cyclic mobility will be identified individually when necessary.

9.2.1 Flow Liquefaction

Flow liquefaction produces the most dramatic effects of all the liquefaction-related phenomena—tremendous instabilities known as *flow failures*. Flow liquefaction can occur when the shear stress required for static equilibrium of a soil mass (the *static shear stress*) is greater than the shear strength of the soil in its liquefied state. Once triggered *the large deformations produced by flow liquefaction are actually driven by static shear stresses*. The cyclic stresses may simply bring the soil to an unstable state at which its strength drops sufficiently to allow the static stresses to produce the flow failure. Flow liquefaction failures are characterized by the sudden nature of their origin, the speed with which they develop, and the large distance over which the liquefied materials often move. The flow slide failures of Sheffield Dam (Figure 1.5) and Lower San Fernando Dam (Figure 1.7) are examples of flow liquefaction. The fluid nature of liquefied soil is illustrated in Figure 9.1.

9.2.2 Cyclic Mobility

Cyclic mobility is another phenomenon that can also produce unacceptably large permanent deformations during earthquake shaking. In contrast to flow liquefaction, cyclic mobility occurs when the static shear stress is less than the shear strength of the liquefied soil. *The deformations produced by cyclic mobility failures develop incrementally during earthquake*



Figure 9.1 A small flow slide along the shore of Lake Merced in San Francisco in 1957 (photo by M. Bonilla; courtesy of USGS).

shaking. In contrast to flow liquefaction, the deformations produced by cyclic mobility are driven by both cyclic and static shear stresses. These deformations, termed *lateral spreading*, can occur on very gently sloping ground or on virtually flat ground adjacent to bodies of water (Figure 9.2). When structures are present, lateral spreading can cause significant damage (Figure 1.8 and 1.9).

A special case of cyclic mobility is *level-ground liquefaction*. Because static horizontal shear stresses that could drive lateral deformations do not exist, level-ground liquefaction can produce large, chaotic movement known as *ground oscillation* during earthquake shaking, but produces little permanent lateral soil movement. Level-ground liquefaction failures are caused by the upward flow of water that occurs when seismically induced excess pore pressures dissipate. Depending on the length of time required to reach hydraulic equilibrium, level-ground liquefaction failure may occur well after ground shaking has ceased. Excessive vertical settlement and consequent flooding of low-lying land and the development of sand boils (Figure 9.3) are characteristic of level-ground liquefaction failure.

9.3 EVALUATION OF LIQUEFACTION HAZARDS

Both flow liquefaction and cyclic mobility can produce damage at a particular site, and a complete evaluation of liquefaction hazards requires that the potential for each be addressed. When faced with such a problem, the geotechnical earthquake engineer can systematically evaluate potential liquefaction hazards by addressing the following questions:

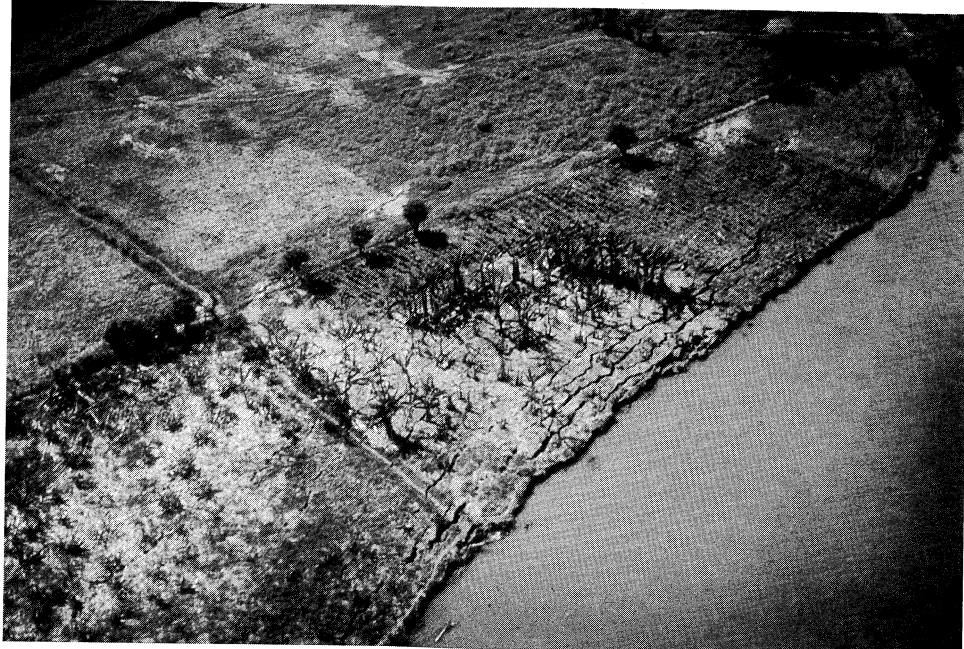


Figure 9.2 Lateral spreading of very flat ground toward the Motagua River following the 1976 Guatemala earthquake. Note orientation of ground surface cracks parallel to river bank (photo by G. Plafker; courtesy of USGS).

1. Is the soil susceptible to liquefaction?
2. If the soil is susceptible, will liquefaction be triggered?
3. If liquefaction is triggered, will damage occur?

If the answer to the first question is no, the liquefaction hazard evaluation can be terminated with the conclusion that liquefaction hazards do not exist. If the answer is yes, the next question must be addressed. In some cases it may be more efficient to reverse the order of the second and third questions, particularly when damage appears unlikely. If the answers to all three are yes, a problem exists; if the anticipated level of damage is unacceptable, the site must be abandoned or improved (Chapter 12) or on-site structures strengthened. These questions pertain to the three most critical aspects of liquefaction hazard evaluation: *susceptibility*, *initiation*, and *effects*. All three must be considered in a comprehensive evaluation of liquefaction hazards.

9.4 LIQUEFACTION SUSCEPTIBILITY

Not all soils are susceptible to liquefaction; consequently, the first step in a liquefaction hazard evaluation is usually the evaluation of liquefaction susceptibility. If the soil at a particular site is not susceptible, liquefaction hazards do not exist and the liquefaction hazard evaluation can be ended. If the soil is susceptible, however, the matters of liquefaction initiation and

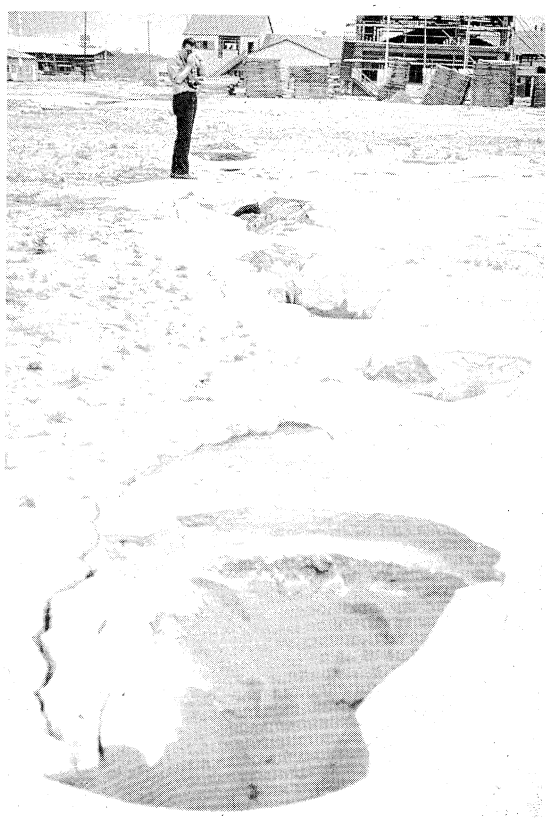


Figure 9.3 Sand boils near Niigata, Japan following the 1964 Niigata earthquake. Sand boils are often aligned along cracks in the ground (photo by K. Steinbrugge; courtesy of Earthquake Engineering Research Center, University of California).

effects must be addressed. There are several criteria by which liquefaction susceptibility can be judged, and some are different for flow liquefaction and cyclic mobility. These include historical, geologic, compositional, and state criteria.

9.4.1 Historical Criteria

A great deal of information on liquefaction behavior has come from postearthquake field investigations, which have shown that liquefaction often recurs at the same location when soil and groundwater conditions have remained unchanged (Youd, 1984a). Thus liquefaction case histories can be used to identify specific sites, or more general site conditions, that may be susceptible to liquefaction in future earthquakes. Youd (1991) described a number of instances where historical evidence of liquefaction has been used to map liquefaction susceptibility.

Postearthquake field investigations have also shown that liquefaction effects have historically been confined to a zone within a particular distance of the seismic source. Ambraseys (1988) compiled worldwide data from shallow earthquakes to estimate a limiting epicentral distance beyond which liquefaction has not been observed in earthquakes of different magnitudes (Figure 9.4). The distance to which liquefaction can be expected

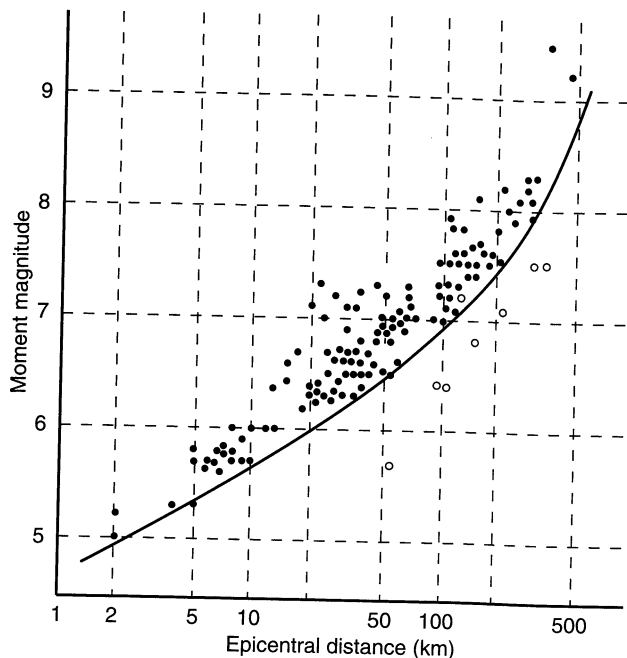


Figure 9.4 Relationship between limiting epicentral distance of sites at which liquefaction has been observed and moment magnitude for shallow earthquakes. Deep earthquakes (focal depths > 50 km) have produced liquefaction at greater distances. After Ambraseys (1988).

increases dramatically with increasing magnitude. While relationships of the type shown in Figure 9.4 offer no guarantee that liquefaction cannot occur at greater distances, they are helpful for estimation of regional liquefaction hazard scenarios.

9.4.2 Geologic Criteria

Soil deposits that are susceptible to liquefaction are formed within a relatively narrow range of geological environments (Youd, 1991). The depositional environment, hydrological environment, and age of a soil deposit all contribute to its liquefaction susceptibility (Youd and Hoose, 1977).

Geologic processes that sort soils into uniform grain size distributions and deposit them in loose states produce soil deposits with high liquefaction susceptibility. Consequently, fluvial deposits, and colluvial and aeolian deposits when saturated, are likely to be susceptible to liquefaction. Liquefaction has also been observed in alluvial-fan, alluvial-plain, beach, terrace, playa, and estuarine deposits, but not as consistently as in those listed previously. The susceptibility of older soil deposits to liquefaction is generally lower than that of newer deposits. Soils of Holocene age are more susceptible than soils of Pleistocene age, although susceptibility decreases with age within the Holocene. Liquefaction of pre-Pleistocene deposits is rare.

Liquefaction occurs only in saturated soils, so the depth to groundwater (either free or perched) influences liquefaction susceptibility. Liquefaction susceptibility decreases with increasing groundwater depth; the effects of liquefaction are most commonly observed at

sites where groundwater is within a few meters of the ground surface. At sites where groundwater levels fluctuate significantly, liquefaction hazards may also fluctuate.

Human-made soil deposits also deserve attention. Loose fills, such as those placed without compaction, are very likely to be susceptible to liquefaction. The stability of hydraulic fill dams and mine tailings piles, in which soil particles are loosely deposited by settling through water, remains an important contemporary seismic hazard. Well-compacted fills, on the other hand, are unlikely to satisfy state criteria (Section 9.4.4) for liquefaction susceptibility.

9.4.3 Compositional Criteria

Since liquefaction requires the development of excess pore pressure, liquefaction susceptibility is influenced by the compositional characteristics that influence volume change behavior. Compositional characteristics associated with high volume change potential tend to be associated with high liquefaction susceptibility. These characteristics include particle size, shape, and gradation.

For many years, liquefaction-related phenomena were thought to be limited to sands. Finer-grained soils were considered incapable of generating the high pore pressures commonly associated with liquefaction, and coarser-grained soils were considered too permeable to sustain any generated pore pressure long enough for liquefaction to develop. More recently, the bounds on gradation criteria for liquefaction susceptibility have broadened.

Liquefaction of nonplastic silts has been observed (Ishihara, 1984, 1985) in the laboratory and the field, indicating that plasticity characteristics rather than grain size alone influence the liquefaction susceptibility of fine-grained soils. Coarse silts with bulky particle shape, which are nonplastic and cohesionless, are fully susceptible to liquefaction (Ishihara, 1993); finer silts with flaky or platelike particles generally exhibit sufficient cohesion to inhibit liquefaction. Clays remain nonsusceptible to liquefaction, although sensitive clays can exhibit strain-softening behavior similar to that of liquefied soil. Fine-grained soils that satisfy each of the following four Chinese criteria (Wang, 1979) may be considered susceptible to significant strength loss:

Fraction finer than 0.005 mm \leq 15%

Liquid limit, LL \leq 35%

Natural water content \geq 0.9 LL

Liquidity index \leq 0.75

To account for differences in Chinese and U.S. practice, the U.S. Army Corps of Engineers modified the measured index properties (by decreasing the fines content by 5%, increasing the liquid limit by 1%, and increasing the natural water content by 2%) before applying the Chinese criteria to a clayey silt in the foundation of Sardis Dam (Finn et al., 1994).

At the other end of the grain size spectrum, liquefaction of gravels has been observed in the field (Coulter and Migliaccio, 1966; Chang, 1978; Wong, 1984; Youd et al., 1985, Yegian et al., 1994) and in the laboratory (Wong et al., 1975; Evans and Seed, 1987). The effects of membrane penetration (Section 6.3.2.3) are now thought to be responsible for the high liquefaction resistance observed in early laboratory investigations of gravelly soils. When pore pressure dissipation is impeded by the presence of impermeable layers so that truly undrained conditions exist, gravelly soils can also be susceptible to liquefaction.

Liquefaction susceptibility is influenced by gradation. Well-graded soils are generally less susceptible to liquefaction than poorly graded soils; the filling of voids between larger particles by smaller particles in a well-graded soil results in lower volume change potential under drained conditions and, consequently, lower excess pore pressures under undrained conditions. Field evidence indicates that most liquefaction failures have involved uniformly graded soils.

Particle shape can also influence liquefaction susceptibility. Soils with rounded particle shapes are known to densify more easily than soils with angular grains. Consequently, they are usually more susceptible to liquefaction than angular-grained soils. Particle rounding frequently occurs in the fluvial and alluvial environments where loosely deposited saturated soils are frequently found, and liquefaction susceptibility is often high in those areas.

9.4.4 State Criteria

Even if a soil meets all of the preceding criteria for liquefaction susceptibility, it still may or may not be susceptible to liquefaction. Liquefaction susceptibility also depends on the initial state of the soil (i.e., its stress and density characteristics at the time of the earthquake). Since the tendency to generate excess pore pressure of a particular soil is strongly influenced by both density and initial stress conditions, liquefaction susceptibility depends strongly on the initial state of the soil. These liquefaction susceptibility criteria, unlike those discussed previously, are different for flow liquefaction and cyclic mobility.

To introduce contemporary methods for evaluating state criteria (and to provide a background for evaluating the effects of liquefaction), a brief historical review of some basic concepts of cohesionless soil behavior is required.

9.4.4.1 Critical Void Ratio

In his pioneering work on the shear strength of soils, Casagrande (1936) performed drained, strain-controlled triaxial tests on initially loose and initially dense sand specimens. The results (Figure 9.5), which form the cornerstone of modern understanding of soil

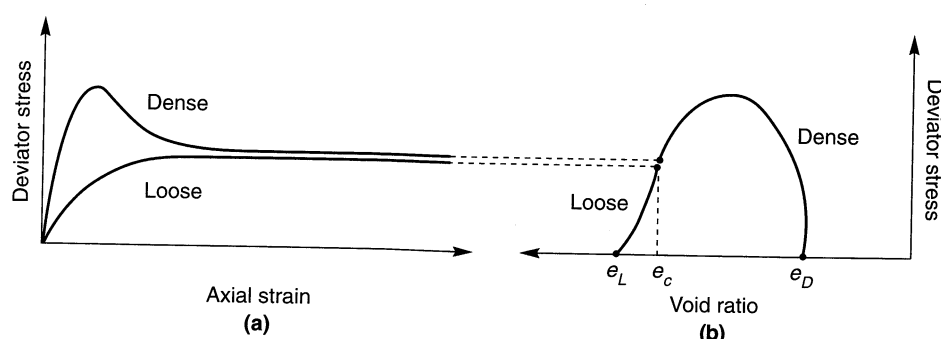


Figure 9.5 (a) Stress-strain and (b) stress-void ratio curves for loose and dense sands at the same effective confining pressure. Loose sand exhibits contractive behavior (decreasing void ratio) and dense sand exhibits dilative behavior (increasing void ratio) during shearing. By the time large strains have developed, both specimens have reached the critical void ratio and mobilize the same large-strain shearing resistance.

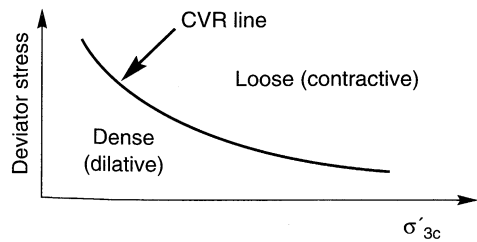


Figure 9.6 Use of the CVR line as a boundary between loose contractive states and dense dilative states.

strength behavior, showed that all specimens tested at the same effective confining pressure approached the same density when sheared to large strains. Initially loose specimens contracted, or densified, during shearing and initially dense specimens first contracted, but then very quickly began to dilate. At large strains, all specimens approached the same density and continued to shear with constant shearing resistance. The void ratio corresponding to this constant density was termed the *critical void ratio*, e_c . By performing tests at different effective confining pressures, Casagrande found that the critical void ratio was uniquely related to the effective confining pressure, and called the locus the *critical void ratio (CVR) line* (Figure 9.6). By defining the state of the soil in terms of void ratio and effective confining pressure, the CVR line could be used to mark the boundary between loose (contractive) and dense (dilative) states.

The equipment needed to measure pore pressure was not available at the time, but Casagrande hypothesized that strain-controlled undrained testing would produce positive excess pore pressure (due to the tendency for contraction) in loose specimens, and negative excess pore pressure (due to the tendency for dilation) in dense specimens (Figure 9.7), until the CVR line was reached. This hypothesis was subsequently verified experimentally. The CVR line therefore described the state toward which any soil specimen would migrate at large strains, whether by volume changes under drained conditions, changes in effective confining pressure under undrained conditions, or some combination under partially drained conditions.

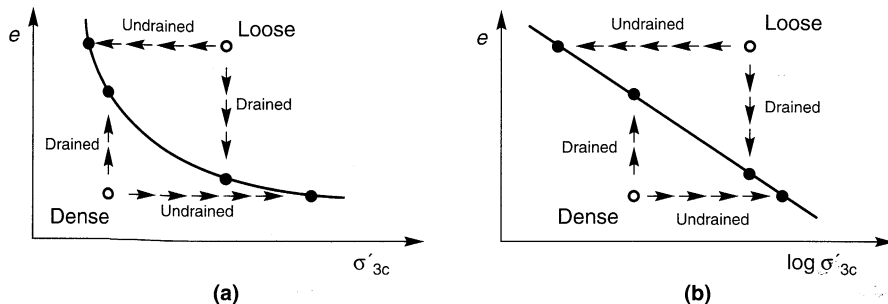


Figure 9.7 Behavior of initially loose and dense specimens under drained and undrained conditions for (a) arithmetic and (b) logarithmic effective confining pressure scales.

Since the CVR line marked the boundary between contractive and dilative behavior, it was considered to mark the boundary between states in which a particular soil was or was not susceptible to flow liquefaction (Figure 9.8). Saturated soils with initial void ratios high

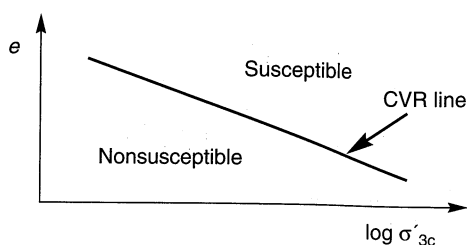


Figure 9.8 Use of CVR line as a boundary between initial states that are and are not susceptible to flow liquefaction.

enough to plot above the CVR line were considered susceptible to flow liquefaction, and soils with initial states plotting below the CVR line were considered nonsusceptible. However, when Fort Peck Dam in Montana suffered a static flow liquefaction failure of its upstream slope during construction in 1938 (Middlebrooks, 1942), a postfailure investigation showed that the initial state of soils that had obviously liquefied actually plotted somewhat below the CVR line (i.e., in the nonsusceptible region). Casagrande attributed this discrepancy to the inability of strain-controlled drained tests to replicate all of the phenomena that influence soil behavior under the stress-controlled undrained conditions of an actual flow liquefaction failure. Over the years, Casagrande developed the hypothesis that a flowing liquefied sand has a "flow structure" in which grains continuously rotate to orient themselves in a structure of minimum frictional resistance (Casagrande, 1976). Casagrande was unable to achieve a flow structure in the laboratory until the late 1960s, when one of his students performed an important series of stress-controlled undrained triaxial tests (Castro, 1969).

9.4.4.2 Steady State of Deformation

Castro (1969) performed static and cyclic triaxial tests on isotropically consolidated specimens and several static tests on anisotropically consolidated specimens. Three different types of stress-strain behavior, illustrated for anisotropically consolidated specimens in Figure 9.9 were observed. Very loose specimens (such as specimen A in Figure 9.9) exhibited a peak undrained strength at a small shear strain and then "collapsed" to flow rapidly to large strains at low effective confining pressure and low large-strain strength. This type of behavior now recognized as flow liquefaction was described at that time as "liquefaction." Dense specimens (specimen B) initially contracted but then dilated until a relatively high constant effective confining pressure and large-strain strength was reached. At intermediate densities (specimen C) the exceedance of a peak strength at low strain was followed by a limited period of strain-softening behavior, which ended with the onset of dilation at intermediate strains. [This reversal from contractive to dilative behavior occurs at the *phase transformation point* (Ishihara et al., 1975).] Further loading produced continued dilation to higher effective confining pressures and, consequently, higher large-strain strengths. This type of behavior was termed *limited liquefaction*.

The testing program showed a unique relationship between void ratio and effective confining pressure at large strains. Graphically, this relationship plotted below and roughly parallel to the CVR line obtained from drained strain-controlled tests; the difference being attributed to development of the flow structure under stress-controlled conditions. The state in which the soil flowed continuously under constant shear stress and constant effective confining pressure at constant volume and constant velocity was later defined (Castro and

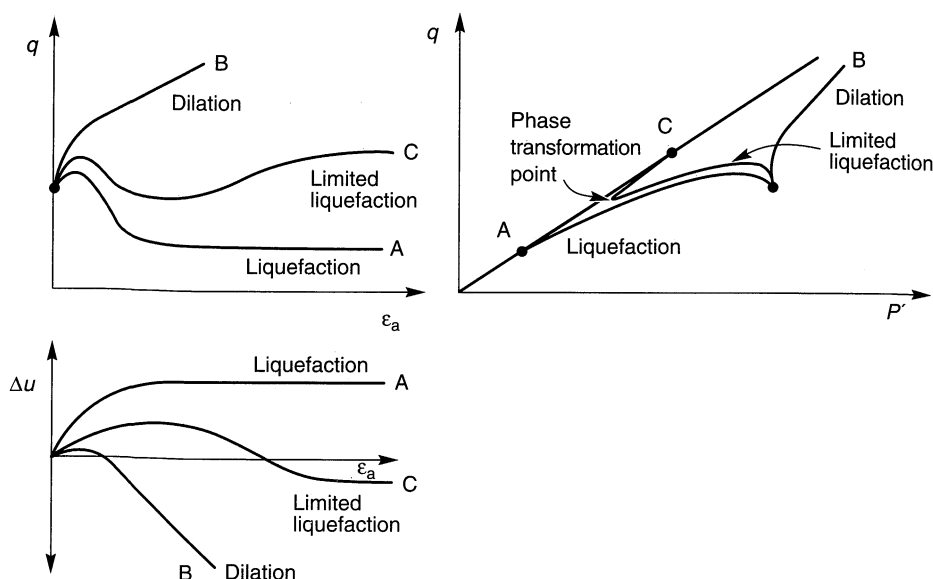


Figure 9.9 Liquefaction, limited liquefaction, and dilation in monotonic loading tests.

Poulos, 1977; Poulos, 1981) as the *steady state of deformation*. Since the steady state of deformation is reached only at large strains (after the effects of initial conditions such as soil fabric, stress and strain history, and loading conditions have been obscured), the effective confining pressure in an element of soil in the steady state of deformation was considered to depend only on the density of the soil. Relatively recently it has been shown that the steady-state conditions are different for compressive and extensional stress paths (e.g., Vaid et al., 1990; Reimer and Seed, 1992; Vaid and Thomas, 1995), particularly when the soil is deposited with inherently anisotropic structure. Specifically, pluviated sands exhibit contractive behavior over a wider range of densities when loaded in extension than in compression; a particular element of sand at an intermediate density may exhibit dilative behavior in compression but contractive behavior when loaded in extension. As a result, the depositional conditions, stress conditions, and loading conditions that exist in the field should be matched as closely as possible in laboratory investigations of steady-state behavior.

The locus of points describing the relationship between void ratio and effective confining pressure in the steady state of deformation is called the *steady-state line* (SSL). In its most general form, the SSL can be viewed as a three-dimensional curve in $e-\sigma'-\tau$ (Figure 9.10) or $e-p'-q$ space. The SSL shown in Figure 9.7a therefore represents the projection of the three-dimensional SSL onto a plane of constant τ . The SSL can also be projected onto planes of constant effective confining pressure ($\sigma' = \text{constant}$) and constant density ($e = \text{constant}$). The SSL can also be expressed in terms of the steady-state strength, S_{su} ; since the shearing resistance of the soil in the steady state of deformation is proportional to the effective confining pressure, the strength-based SSL is parallel to the effective confining pressure-based SSL when both are plotted on logarithmic scales (Figure 9.11).

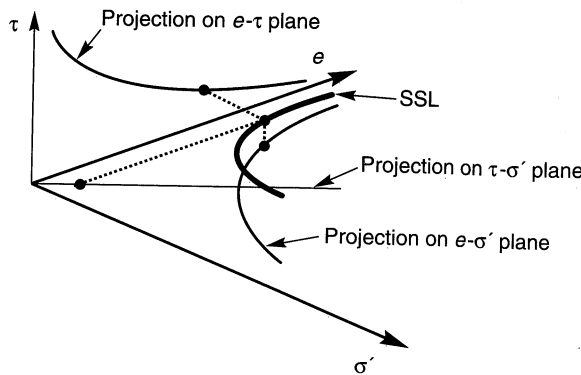


Figure 9.10 Three-dimensional steady-state line showing projections on $e-\tau$ plane, $e-\sigma'$ plane, and $\tau-\sigma'$ plane. A similar plot can be developed using the stress path parameters q and p' instead of τ and σ' .

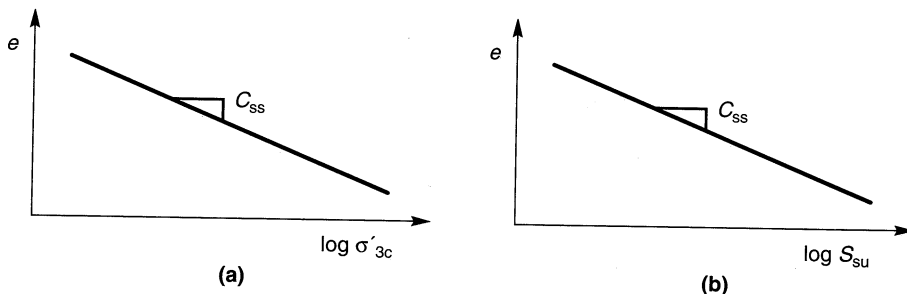


Figure 9.11 Proportionality of S_{su} to σ'_{3c} produces strength-based and effective confining pressure-based steady-state lines with identical slopes.

The SSL is useful for identifying the conditions under which a particular soil may or may not be susceptible to flow liquefaction (Figure 9.12). Soils whose state plots below the SSL are not susceptible to flow liquefaction. A soil whose state lies above the SSL will be susceptible to flow liquefaction *only if the static shear stress exceeds its steady state (or residual) strength*. Since the SSL can be used to evaluate the shearing resistance of liquefied soils, it is also useful for evaluating the potential effects of liquefaction (Section 9.6). Although determination of the position of the SSL can be difficult in practice (Section 9.6.4.1), the SSL is very useful for understanding the basic concepts of liquefaction.

Cyclic mobility, on the other hand, can occur in soils whose state plot above or below the SSL. In other words, *cyclic mobility can occur in both loose and dense soils*.

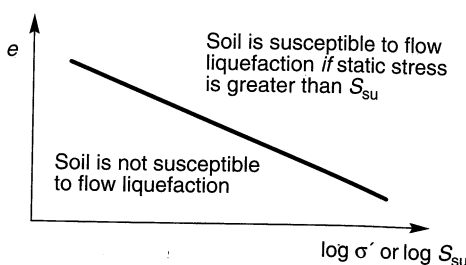


Figure 9.12 State criteria for flow liquefaction susceptibility. Soils with combinations of initial density and stress conditions that plot above the SSL are susceptible to flow liquefaction when the static shear strength is greater than the steady-state strength. Initial conditions that plot below the SSL are not susceptible to flow liquefaction.

The location of the SSL is sensitive to the compositional characteristics of the soil—its vertical position is strongly influenced by gradation and its slope by particle angularity. Soils with rounded particles usually have flat SSLs—a characteristic that often leads to difficulty in the estimation of in situ steady-state strength.

9.4.4.3 State Parameter

The nature of the steady-state line illustrates the limited applicability of absolute measures of density, such as void ratio and relative density, for characterization of a potentially liquefiable soil. As illustrated in Figure 9.12, an element of soil at a particular void ratio (hence a particular density and relative density) can be susceptible to flow liquefaction under a high effective confining pressure but nonsusceptible at a low effective confining pressure.

Using concepts of critical-state soil mechanics, the behavior of a cohesionless soil should be more closely related to the proximity of its initial state to the steady-state line than to absolute measures of density (Roscoe and Pooroshab, 1963). In other words, soils in states located at the same distance from the steady-state line should exhibit similar behavior. Using this logic, a *state parameter* (Been and Jeffries, 1985) can be defined as

$$\psi = e - e_{ss} \quad (9.1)$$

where e_{ss} is the void ratio of the steady-state line at the effective confining pressure of interest (Figure 9.13). When the state parameter is positive, the soil exhibits contractive behavior and may be susceptible to flow liquefaction. When it is negative, dilative behavior will occur and the soil is not susceptible to flow liquefaction. The state parameter has been related to friction angle, dilation angle, CPT resistance (Been et al., 1986, 1987; Sladen, 1985), PMT results (Yu, 1994), and DMT results (Konrad, 1988). Ishihara (1993) showed that the ability of the state parameter to characterize soil behavior of very loose sands under low effective confining pressures may be limited and proposed an analogous parameter (the *state index*) based on the relative distance between the initial state and the *quasi-steady-state line* (a line analogous to and located slightly below the SSL which corresponds to the stress and density conditions at the phase transformation points observed in cases of limited liquefaction).

The concept of the state parameter is very useful and the possibility of determining its value from in situ tests is appealing. The accuracy with which the state parameter can be determined, however, is influenced by the accuracy with which the position of the SSL can be determined (Section 9.6.3.1).

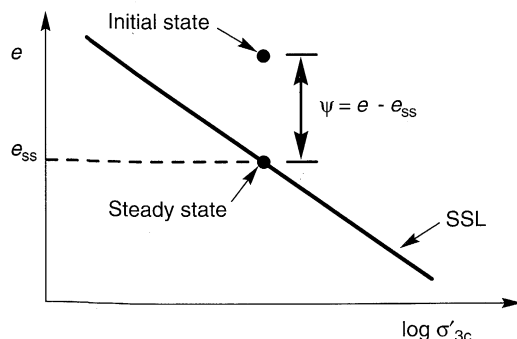


Figure 9.13 State parameter.

9.5 INITIATION OF LIQUEFACTION

The fact that a soil deposit is susceptible to liquefaction does not mean that liquefaction will necessarily occur in a given earthquake. Its occurrence requires a disturbance that is strong enough to initiate, or trigger, it. Evaluation of the nature of that disturbance is one of the most critical parts of a liquefaction hazard evaluation. Any discussion of the initiation of liquefaction must specify which liquefaction-related phenomena are being considered. Many previous studies of liquefaction initiation have implicitly lumped flow liquefaction and cyclic mobility together, but since they are distinctly different phenomena, it is more appropriate to consider each separately.

Although cyclic mobility is an earthquake related phenomenon, flow liquefaction can be initiated in a variety of ways. Flow slides triggered by monotonic loading (*static liquefaction*) have been observed in natural soil deposits (Koppejan et al., 1948; Andersen and Bjerrum, 1968; Bjerrum, 1971; Kramer, 1988), man-made fills (Middlebrooks, 1942; Cornforth et al., 1975; Mitchell, 1984), and mine tailings piles (Kleiner, 1976; Jennings, 1979; Eckersley, 1985). Flow liquefaction has also been triggered by nonseismic sources of vibration, such as pile driving (Jakobsen, 1952; Broms and Bennermark, 1967), train traffic (Fellenius, 1953), geophysical exploration (Hryciw et al., 1990), and blasting (Conlon, 1966; Carter and Seed, 1988). Perhaps somewhat ironically, the study of static liquefaction over the past 10 to 15 years has contributed greatly to improved understanding of seismically induced liquefaction by identifying the effective stress conditions at which liquefaction phenomena are initiated.

Understanding the initiation of liquefaction requires identification of the state of the soil when liquefaction is triggered. In the following sections, these conditions will be presented in a framework that allows the mechanics of both flow liquefaction and cyclic mobility to be clearly understood. Subsequently, practical and commonly used procedures for determining the nature of the disturbance required to move from initial state to the state at which liquefaction is triggered will be presented.

9.5.1 Flow Liquefaction Surface

The conditions at which flow liquefaction is initiated are most easily illustrated with the aid of the stress path (Section 6.2.2). Hanzawa et al. (1979) first showed that the effective stress conditions at which strain-softening behavior occurred in loose, saturated sands could be described very simply in stress path space. As discussed in the following sections, the effective stress conditions at the initiation of flow liquefaction can be described in stress path space by a three-dimensional surface that will be referred to hereafter as the *flow liquefaction surface* (FLS). While some practical difficulties in the measurement of the FLS for general stress paths remain, it provides (in conjunction with steady-state concepts) a very useful framework for conceptual understanding of the relationships between the various liquefaction phenomena. This conceptual understanding is vital for proper evaluation of the behavior of liquefiable soils both during and after earthquake shaking.

9.5.1.1 Monotonic Loading

The conditions at the initiation of flow liquefaction can be seen most easily when the soil is subjected to monotonically increasing stresses. Consider, for example, the response of an isotropically consolidated specimen of very loose, saturated sand in undrained,

stress-controlled triaxial compression (Figure 9.14). Immediately prior to undrained shearing (point A), the specimen is in drained equilibrium under an initial effective confining pressure, σ'_{3c} , with zero shear stress (Figure 9.14a,b) and zero excess pore pressure (Figure 9.14c). Since its initial state is well above the SSL (Figure 9.14d), the sand will exhibit contractive behavior. When undrained shearing begins, the contractive specimen generates positive excess pore pressure as it mobilizes shearing resistance up to a peak value (point B) that occurs at a relatively small strain. The excess pore pressure at point B is also relatively small; the *pore pressure ratio*, $r_u = u_{\text{excess}}/\sigma'_{3c}$, is well below 1.00. At point B, however, *the specimen becomes unstable*, and because it is loaded under stress-controlled conditions, collapses (the axial strain may increase from less than 1% to more than 20% in a fraction of a second). As the specimen strains from point B to point C, the excess pore pressure increases dramatically. At and beyond point C, the specimen is in the steady state of deformation and the effective confining pressure is only a small fraction of the initial effective confining pressure. This specimen has exhibited flow liquefaction behavior; the static shear stresses required for equilibrium (at point B) were greater than the available shear strength (at point C) of the liquefied soil. Flow liquefaction was initiated at the instant it became irreversibly unstable (i.e., at point B).

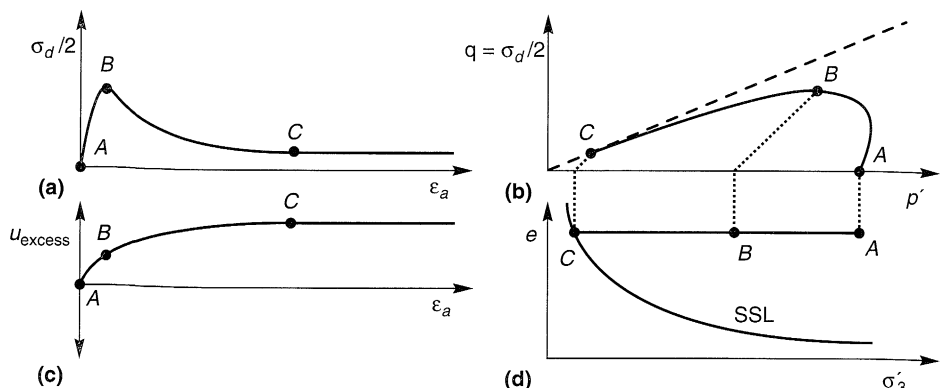


Figure 9.14 Response of isotropically consolidated specimen of loose, saturated sand:
 (a) stress-strain curve; (b) effective stress path; (c) excess pore pressure; (d) effective confining pressure.

Now consider the response of a series of triaxial specimens initially consolidated to the same void ratio at different effective confining pressures. Since all of the specimens have the same void ratio, they will all reach the same effective stress conditions at the steady state, but they will get there by different stress paths. Figure 9.15 illustrates the response of each specimen under monotonic loading. The initial states of specimens A and B are below the SSL, so they exhibit dilative behavior upon shearing. Specimens C, D, and E all exhibit contractive behavior; each reaches a peak undrained strength after which they strain rapidly toward the steady state. For specimens C, D, and E, flow liquefaction is initiated at the peak of each stress path (at the points marked with an X). Hanzawa et al. (1979), Vaid and Chern (1983), and a number of more recent investigations have shown that the locus of points

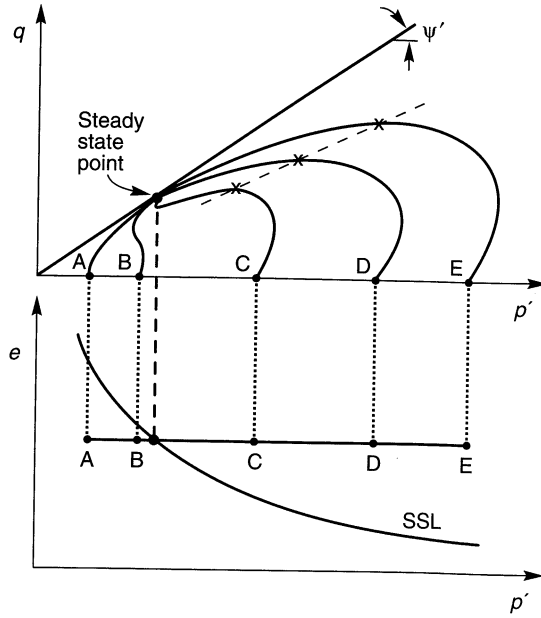


Figure 9.15 Response of five specimens isotropically consolidated to the same initial void ratio at different initial effective confining pressures. Flow liquefaction in specimens C, D, and E is initiated at the points marked with an \times . The dotted line passing through these points is a line of constant principal effective stress ratio, K_L .

describing the effective stress conditions at the initiation of flow liquefaction is a straight line (the dotted line in Figure 9.15) that projects through the origin of the stress path. Graphically, these points may be used to define the *flow liquefaction surface* (FLS) in stress path space; since flow liquefaction cannot occur if the stress path is below the steady-state point, the FLS is truncated at that level (Figure 9.16). This form of the FLS was first proposed (with a different name) by Vaid and Chern (1985). It should be noted that Sladen et al. (1985) proposed an analogous surface (called the *collapse surface*) that was assumed to project linearly through the steady-state point; since the preponderance of current experimental evidence appears to support projection through the origin, the term *FLS* is used in this book. For very loose samples, the steady-state point may be so close to the origin that the practical difference between the FLS and the collapse surface is negligible.

The FLS marks the boundary between stable and unstable states in undrained shear. If the stress conditions in an element of soil reach the FLS under undrained conditions, whether by monotonic or cyclic loading, flow liquefaction will be triggered and the shearing

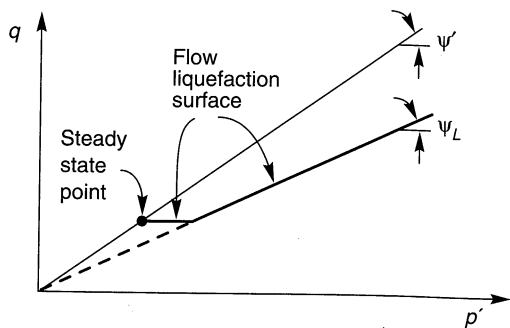


Figure 9.16 Orientation of the flow liquefaction surface in stress path space.

resistance will be reduced to the steady-state strength. Therefore, *the FLS describes the conditions at which flow liquefaction is initiated.*

For isotropic initial conditions, the slope of the FLS is often about two-thirds the slope of the drained failure envelope for clean sands. Specimens tested under anisotropic initial conditions, however, indicate that the FLS is steeper for soils with high initial (drained) shear stress compared to soils with lower initial shear stress at the same void ratio (Figure 9.17). The FLS may be very close to the initial stress point when initial shear stresses are large, in which case flow liquefaction may be initiated by only a very small undrained disturbance (Kramer and Seed, 1988). Case histories that have been attributed to *spontaneous liquefaction* probably involved initial shear stresses that were high enough that the small undrained disturbance required to initiate flow liquefaction was not observed.

The *limited liquefaction* behavior exhibited by specimens C and D (Figure 9.16) is significant for cases in which the static shear stress increases (as in the case of monotonic loading described in this section). In such cases the shearing resistance may drop to values at the point of phase transformation (or the quasi-steady state) that are lower than the steady-state strength. This temporary drop in shearing resistance may produce shear strains of 5% to 20% (Ishihara, 1993) and result in unacceptably large permanent deformations. Because the effects of initial conditions are not erased completely at these strain levels, they influence the quasi-steady-state strength. Procedures for estimation of quasi-steady-state strength are given by Ishihara (1993). Because the static component of shear stress generally remains constant or decreases during earthquakes, the quasi-steady state is less likely to be reached as a result of earthquake shaking.

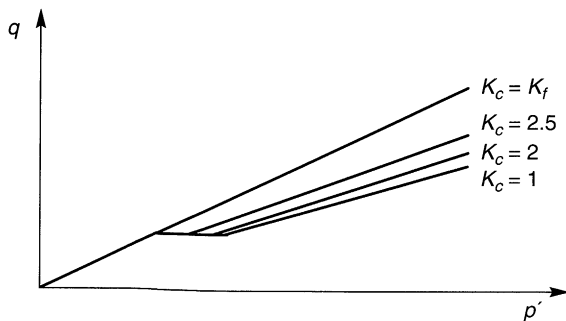


Figure 9.17 Variation of flow liquefaction surface inclination with initial principal effective stress ratio for constant void ratio.

9.5.1.2 Cyclic Loading

Vaid and Chern (1983) first showed that the FLS applied to both cyclic and monotonic loading, and a considerable amount of independent experimental evidence supports that observation. Other experimental evidence (e.g., Alarcon-Guzman et al., 1988) suggests that the effective stress path can move somewhat beyond the FLS before liquefaction is initiated by cyclic loading. Whether liquefaction is initiated precisely at the FLS under cyclic as well as monotonic loading is not currently known with certainty. Because the FLS is used as part of a conceptual model of liquefaction behavior in this book, and because it is slightly more conservative to do so, the FLS will be assumed to apply to both cyclic and monotonic loading.

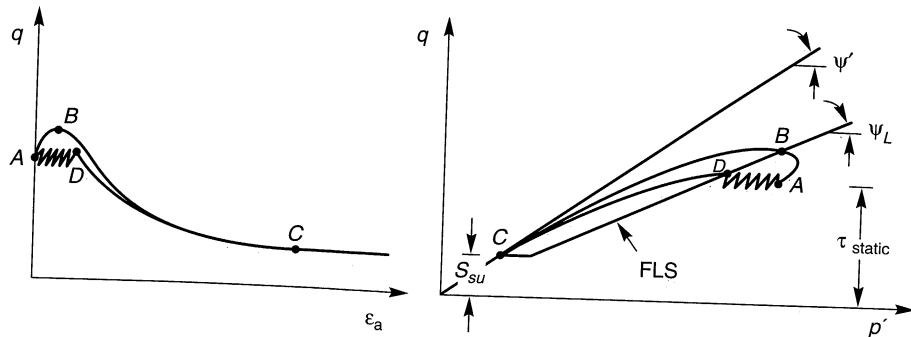


Figure 9.18 Initiation of flow liquefaction by cyclic and monotonic loading. Although the stress conditions at the initiation of liquefaction are different for the two types of loading (points *B* and *D*), both lie on the FLS.

Consider the responses of two identical, anisotropically consolidated, triaxial specimens of loose, saturated sand (Figure 9.18). Initially, the specimens are in drained equilibrium (point *A*) under a static shear stress, τ_{static} , that is greater than the steady-state strength, S_{su} . The first specimen is loaded monotonically (under undrained conditions): the shearing resistance builds up to a peak value when the stress path reaches the FLS (point *B*). At that point the specimen becomes unstable and strains rapidly toward the steady state (point *C*). The second specimen is loaded cyclically (also under undrained conditions): the effective stress path moves to the left as positive excess pore pressures develop and permanent strains accumulate. When the effective stress path reaches the FLS (at point *D*), the specimen becomes unstable and strains toward the steady state of deformation (point *C*). Although the effective stress conditions at the initiation of liquefaction (points *B* and *D*) were different, they fell in both cases on the FLS. The FLS, therefore, marks the onset of the instability that produces flow liquefaction. Lade (1992) provided a detailed description of this instability from a continuum mechanics standpoint.

9.5.1.3 Development of Flow Liquefaction

Flow liquefaction occurs in two stages. The first stage, which takes place at small strain levels, involves the generation of sufficient excess pore pressure to move the stress path from its initial position to the FLS. This excess pore pressure may be generated by undrained monotonic or cyclic loading. When the effective stress path reaches the FLS, the soil becomes inherently unstable and the second stage begins. The second stage involves strain softening (and additional excess pore pressure generation) that is driven by the shear stresses required for static equilibrium. These shear stresses are the *driving stresses*—they must be distinguished from the *locked-in stresses* that develop during deposition and consolidation of the soil (Castro, 1991). Locked-in shear stresses, such as those that exist beneath level ground when $K_0 \neq 1$, cannot drive a flow liquefaction failure. Large strains develop in the second stage as the effective stress path moves from the FLS to the steady state. If the first stage takes the soil to the FLS under undrained, stress-controlled conditions, the second stage is inevitable.

9.5.2 Influence of Excess Pore Pressure

The generation of excess pore pressure is the key to the initiation of liquefaction. Without changes in pore pressure, hence changes in effective stress, neither flow liquefaction nor cyclic mobility can occur. The different phenomena can, however, require different levels of pore pressure to occur.

9.5.2.1 Flow Liquefaction

Flow liquefaction can be initiated by cyclic loading only when the shear stress required for static equilibrium is greater than the steady-state strength. In the field, these shear stresses are caused by gravity and remain essentially constant until large deformations develop. Therefore, initial states that plot in the shaded region of Figure 9.19 are susceptible to flow liquefaction. The occurrence of flow liquefaction, however, requires an undrained disturbance strong enough to move the effective stress path from its initial point to the FLS.

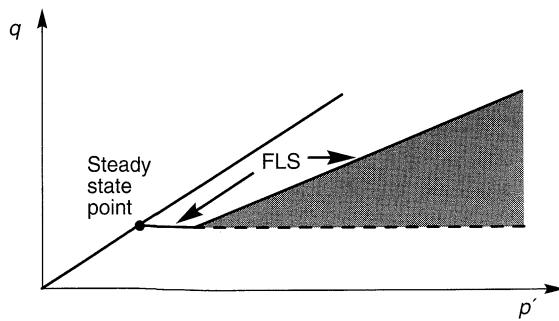


Figure 9.19 Zone of susceptibility to flow liquefaction. If initial conditions fall within the shaded zone, flow liquefaction will occur if an undrained disturbance brings the effective stress path from the point describing the initial conditions to the FLS.

If the initial stress conditions plot near the FLS, as they would in an element of soil subjected to large shear stresses under drained conditions, flow liquefaction can be triggered by small excess pore pressures (Kramer and Seed, 1988). The liquefaction resistance will be greater if the initial stress conditions are farther from the flow liquefaction surface. The FLS can be used to estimate the pore pressure ratio at the initiation of flow liquefaction; it decreases substantially with increasing initial stress ratio (Figure 9.20) for soils at a particular void ratio. At high initial stress ratios, flow liquefaction can be triggered by very small static or dynamic disturbances.

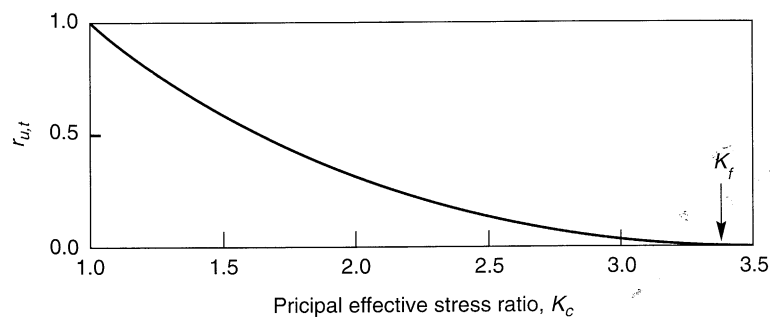


Figure 9.20 Variation of pore pressure ratio ($r_{u,t} = u_t / \sigma_{3c}$) required to trigger flow liquefaction in triaxial specimens of Sacramento River Fine Sand with initial principal effective stress ratio.

9.5.2.2 Cyclic Mobility

Although flow liquefaction cannot occur, cyclic mobility can develop when the static shear stress is smaller than the steady-state shear strength. Therefore, initial states that plot in the shaded region of Figure 9.21 are susceptible to cyclic mobility. Note that cyclic mobility can occur in both loose and dense soils (the shaded region of Figure 9.21 extends from very low to very high effective confining pressures and corresponds to states that would plot both above and below the SSL). The development of cyclic mobility can be illustrated by the response of soils in cyclic triaxial tests. Three combinations of initial conditions and cyclic loading conditions generally produce cyclic mobility.

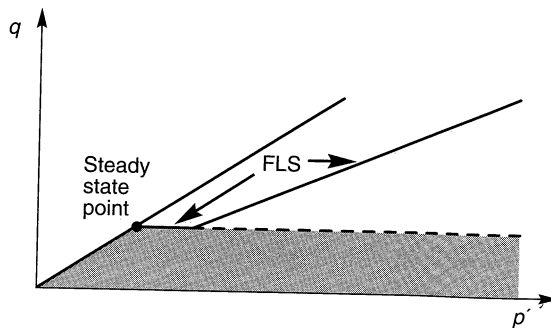


Figure 9.21 Zone of susceptibility to cyclic mobility. If initial conditions plot within shaded zone, cyclic mobility can occur.

The first, illustrated in Figure 9.22a, occurs when $\tau_{\text{static}} - \tau_{\text{cyc}} > 0$ (i.e., no shear stress reversal) and $\tau_{\text{static}} + \tau_{\text{cyc}} < S_{su}$ (no exceedance of steady-state strength). In this case the effective stress path moves to the left until it reaches the drained failure envelope. Since it cannot cross the drained failure envelope, additional loading cycles simply cause it to move up and down along the envelope. As a result, the effective stress conditions stabilize. Flow-type deformations cannot develop because any unidirectional straining would induce dilation. The effective confining pressure has decreased significantly, and the resulting low stiffness can allow significant permanent strains to develop within each loading cycle.

The second condition (Figure 9.22b) occurs when $\tau_{\text{static}} - \tau_{\text{cyc}} > 0$ (no stress reversal) and $\tau_{\text{static}} + \tau_{\text{cyc}} > S_{su}$ (steady-state strength is exceeded momentarily). Again, cyclic loading will cause the effective stress path to move to the left. When it touches the FLS, momentary periods of instability will occur. Significant permanent strain may develop during these

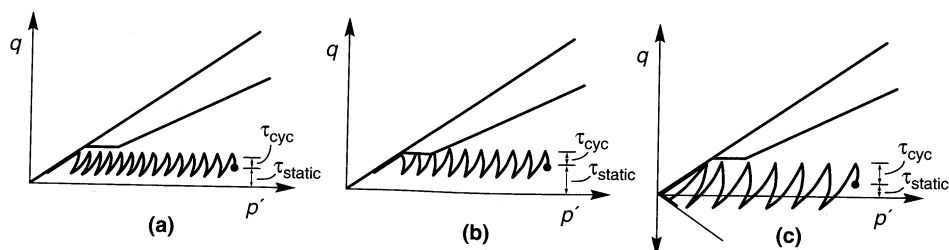


Figure 9.22 Three cases of cyclic mobility: (a) no stress reversal and no exceedance of the steady-state strength; (b) no stress reversal with momentary periods of steady-state strength exceedance; (c) stress reversal with no exceedance of steady-state strength.

periods, particularly if τ_{static} is greater than the quasi-static shear strength, but the straining will generally cease at the end of cyclic loading when the shear stress returns to τ_{static} .

The final condition is that in which $\tau_{\text{static}} - \tau_{\text{cyc}} < 0$ (stress reversal occurs) and $\tau_{\text{static}} + \tau_{\text{cyc}} < S_{su}$ (steady-state strength is not exceeded). In this case (Figure 9.22c) the direction of the shear stress changes so that each cycle includes both compressional and extensional loading. Experimental evidence (e.g., Dobry et al., 1982; Mohamad and Dobry, 1986) has shown that the rate of pore pressure generation increases with increasing degree of stress reversal. Hence the effective stress path moves relatively quickly to the left (because excess pore pressure builds up quickly) and eventually oscillates along the compression and extension portions of the drained failure envelope. Each time the effective stress path passes through the origin (it does so twice during each loading cycle), the specimen is in an instantaneous state of zero effective stress ($r_u = 100\%$). Although this state of zero effective stress is referred to as *initial liquefaction* (Seed and Lee, 1966), it should not be taken to imply that the soil has no shear strength. If monotonic loading is applied at the state of initial liquefaction, the specimen will dilate until the steady-state strength is mobilized (Figure 9.23). Significant permanent strains may accumulate during cyclic loading, but flow failure cannot occur. Note that initial liquefaction can only occur when stress reversals occur.

In contrast to flow liquefaction, there is no clearcut point at which cyclic mobility is initiated. Permanent strains, and the permanent deformations they produce, accumulate incrementally. Their magnitude depends on the static shear stress and the duration of the ground motion. For ground motions of short duration at nearly level sites, permanent deformations may be small. For moderately sloping sites or gently sloping sites subjected to ground motions of long duration, cyclic mobility can produce damaging levels of soil deformation.

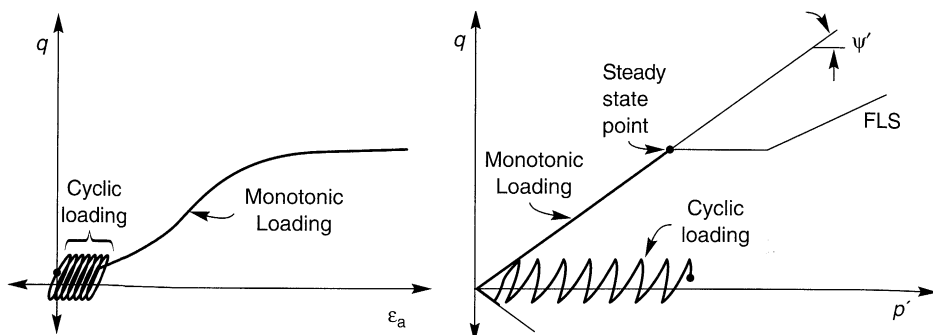


Figure 9.23 Dilative behavior of specimen loaded monotonically after occurrence of cyclic mobility. Cyclic loading with stress reversal causes the effective confining pressure to decrease rapidly, eventually reaching momentary values of zero. Subsequent monotonic loading, however, causes dilation as the steady-state strength is mobilized.

9.5.3 Evaluation of Initiation of Liquefaction

The combination of steady-state and flow liquefaction surface concepts described in Section 9.5.2 provides a framework in which the basic mechanisms of liquefaction can be understood. This framework integrates liquefaction susceptibility with liquefaction initiation and

liquefaction effects. It also illustrates the important influence of excess pore pressure generation on the extent of liquefaction-related hazards.

A number of approaches to evaluation of the potential for initiation of liquefaction have developed over the years. In the following sections, the most common of these—the *cyclic stress approach* and a useful alternative, the *cyclic strain approach*—are presented. Each has advantages and limitations, and each is preferred by different groups of engineers. For particularly important projects, it is not unusual to use more than one approach in a liquefaction hazard evaluation.

9.5.3.1 Cyclic Stress Approach

In the 1960s and 1970s, many advances in the state of knowledge of liquefaction phenomena resulted from the pioneering work of H. B. Seed and his colleagues at the University of California at Berkeley. This research was directed largely toward evaluation of the loading conditions required to trigger liquefaction. This loading was described in terms of cyclic shear stresses, and liquefaction potential was evaluated on the basis of the amplitude and number of cycles of earthquake-induced shear stress. The general approach has come to be known as the *cyclic stress approach*.

Seed and Lee (1966) defined *initial liquefaction* as the point at which the increase in pore pressure is equal to the initial effective confining pressure [i.e., when $u_{\text{excess}} = \sigma'_{3c}$ (or when $r_u = 100\%$)]. Because most of the early laboratory testing investigations were based on cyclic triaxial tests on isotropically consolidated specimens (consequently, with complete stress reversal), initial liquefaction could be produced in both loose and dense specimens. According to the definitions of Section 9.2, this behavior would now be classified (since the static shear stress was zero) as cyclic mobility. The use of the term *initial liquefaction* led many to the erroneous belief that flow liquefaction could be initiated in any loose or dense cohesionless soil.

The cyclic stress approach is conceptually quite simple: the earthquake-induced loading, expressed in terms of cyclic shear stresses, is compared with the liquefaction resistance of the soil, also expressed in terms of cyclic shear stresses. At locations where the loading exceeds the resistance, liquefaction is expected to occur. Application of the cyclic stress approach, however, requires careful attention to the manner in which the loading conditions and liquefaction resistance are characterized.

Characterization of Earthquake Loading. The level of excess pore pressure required to initiate liquefaction is related to the amplitude and duration of earthquake-induced cyclic loading. The cyclic stress approach is based on the assumption that excess pore pressure generation is fundamentally related to the cyclic shear stresses, hence seismic loading is expressed in terms of cyclic shear stresses. The loading can be predicted in two ways: by a detailed ground response analysis or by the use of a simplified approach.

Ground response analyses (Chapter 7) can be used to predict time histories of shear stress at various depths within a soil deposit. Such analyses produce time histories with the transient, irregular characteristics of actual earthquake motions. However, the laboratory data from which liquefaction resistance can be estimated are usually obtained from tests in which the cyclic shear stresses have uniform amplitudes. Therefore, comparison of earthquake-induced loading with laboratory-determined resistance requires conversion of an irregular time history of shear stress to an equivalent series of uniform stress cycles. Seed et

al. (1975a) applied a weighting procedure to a set of shear stress time histories from recorded strong ground motions to determine the number of uniform stress cycles, N_{eq} (at an amplitude of 65% of the peak cyclic shear stress, i.e., $\tau_{cyc} = 0.65\tau_{max}$) that would produce an increase in pore pressure equivalent to that of the irregular time history (Figure 9.24). Similar relationships have been developed for other stress levels (e.g., Haldar and Tang, 1981) but the 65% level is most commonly used. In all cases, the equivalent number of uniform stress cycles increases with increasing earthquake magnitude (just as strong-motion duration increases with increasing earthquake magnitude).

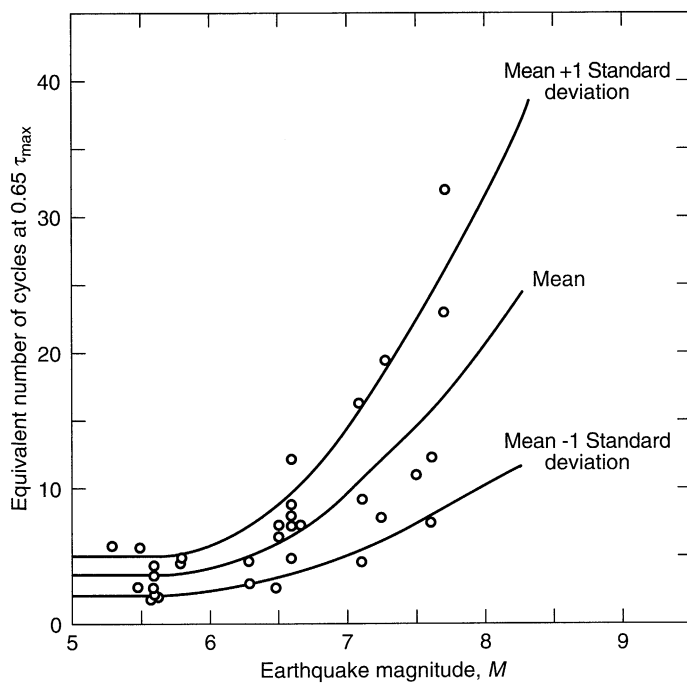


Figure 9.24 Number of equivalent uniform stress cycles, N_{eq} , for earthquakes of different magnitude. (After Seed, et al., 1975a.)

Example 9.1

Figure E9.1 shows a typical irregular time history of shear stress that was produced by a $M_w = 7.0$ earthquake. Estimate the amplitude and number of loading cycles of an equivalent series of uniform stress cycles.

Solution Figure E9.1 shows that the maximum shear stress is $780 \text{ lb}/\text{ft}^2$ (37.4 kPa). Consequently, the amplitude of the equivalent series of uniform stress cycles is

$$\tau_{cyc} = 0.65\tau_{max} = (0.65)(780 \text{ lb}/\text{ft}^2) = 507 \text{ lb}/\text{ft}^2 (24.3 \text{ kPa})$$

Referring to Figure 9.28, the corresponding equivalent number of cycles is approximately 10 (although values ranging from 5 to 14 would fall within one standard deviation of that value).

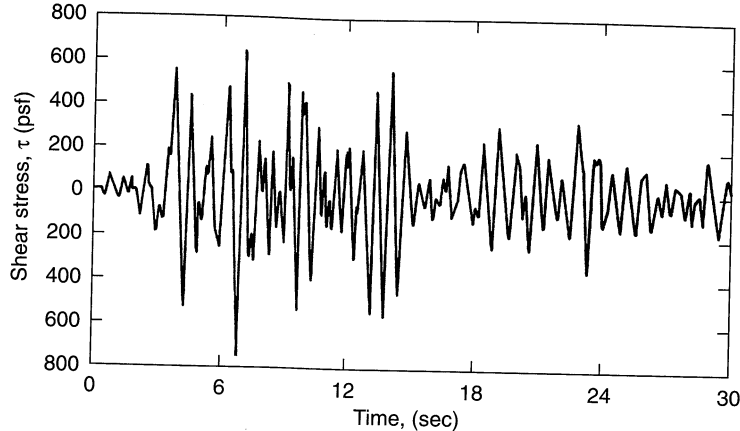


Figure E9.1 Typical irregular time history of shear stress. For liquefaction purposes, 10 cycles of harmonic shear stress at 510 lb/ft² would be considered equivalent to this time history.

The uniform cyclic shear stress amplitude for level (or gently sloping) sites can also be estimated from a simplified procedure (Seed and Idriss, 1971) as

$$\tau_{\text{cyc}} = 0.65 \frac{a_{\max}}{g} \sigma_v r_d \quad (9.2)$$

where a_{\max} is the peak ground surface acceleration, g the acceleration of gravity, σ_v the total vertical stress, and r_d the value of a stress reduction factor (Figure 9.25) at the depth of interest. This uniform cyclic shear stress is assumed to be applied for the equivalent number of cycles shown in Figure 9.24.

Regardless of whether a detailed ground response analysis or the simplified procedure is used, the earthquake-induced loading is characterized by a level of uniform cyclic shear stress that is applied for an equivalent number of cycles.

Example 9.2

The site shown in Figure E9.2a is subjected to earthquake shaking that produces a peak ground acceleration of 0.22g. Estimate and plot the variation of maximum shear stress with depth. Compute and plot the variation of equivalent uniform cyclic shear stress with depth.

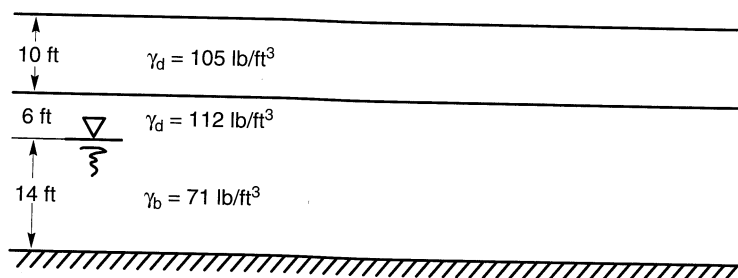


Figure E9.2a

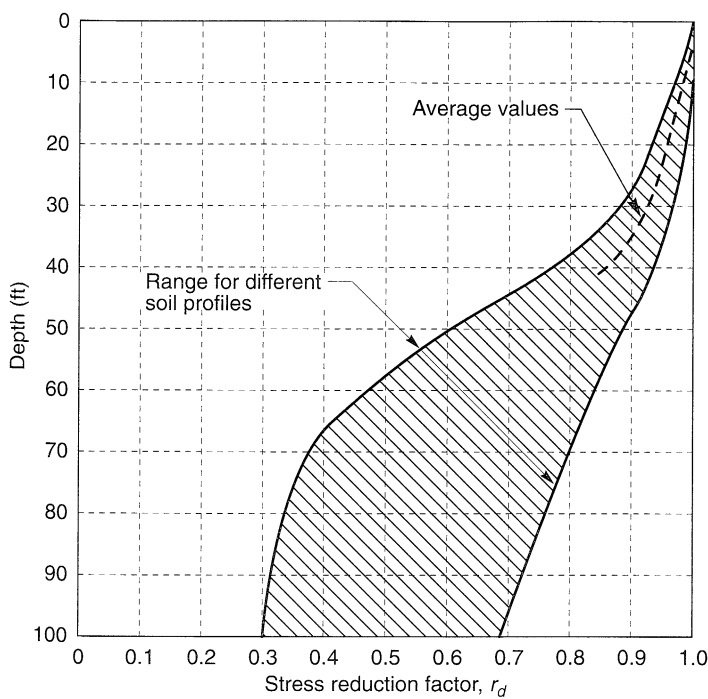


Figure 9.25 Reduction factor to estimate the variation of cyclic shear stress with depth below level or gently sloping ground surfaces. (After Seed and Idriss, 1971.)

Solution Using the simplified procedure of Seed and Idriss (1971), the maximum shear stress can be estimated from

$$\tau_{\max} = \frac{a_{\max}}{g} \sigma_v r_d$$

Estimation of the variation of τ_{\max} with depth requires evaluation of the variation of total vertical stress, σ_v , and stress reduction factor, r_d , with depth. At depths of 5 ft and 25 ft, for example, the total vertical stresses are

$$\begin{aligned}\sigma_v(z = 5 \text{ ft}) &= (5 \text{ ft})(105 \text{ lb/ft}^3) = 525 \text{ lb/ft}^2 \\ \sigma_v(z = 25 \text{ ft}) &= (10 \text{ ft})(105 \text{ lb/ft}^3) + (6 \text{ ft})(112 \text{ lb/ft}^3) + (9 \text{ ft})(71 \text{ lb/ft}^3 + 62.4 \text{ lb/ft}^3) \\ &= 2923 \text{ lb/ft}^2\end{aligned}$$

At the same depths, Figure 9.29 indicates that the stress reduction factor has values of

$$\begin{aligned}r_d(z = 5 \text{ ft}) &= 0.992 \\ r_d(z = 25 \text{ ft}) &= 0.947\end{aligned}$$

The maximum shear stresses at depths of 5 ft and 25 ft can then be estimated as

$$\begin{aligned}\tau_{\max}(z = 5 \text{ ft}) &= (0.22)(525 \text{ lb/ft}^2)(0.992) = 115 \text{ lb/ft}^2 \\ \tau_{\max}(z = 25 \text{ ft}) &= (0.22)(2923 \text{ lb/ft}^2)(0.947) = 609 \text{ lb/ft}^2\end{aligned}$$

The equivalent uniform cyclic shear stresses are simply taken as 65% of the maximum shear stresses, i.e.

$$\tau_{\text{cyc}} = (z = 5 \text{ ft}) = 0.65\tau_{\text{max}}(z = 5 \text{ ft}) = (0.65)(115 \text{ lb/ft}^2) = 75 \text{ lb/ft}^2$$

$$\tau_{\text{cyc}} = (z = 5 \text{ ft}) = 0.65\tau_{\text{max}}(z = 5 \text{ ft}) = (0.65)(609 \text{ lb/ft}^2) = 396 \text{ lb/ft}^2$$

By repeating this process for other depths, the variations of τ_{max} and τ_{cyc} can be determined and plotted as in Figure E9.2b.

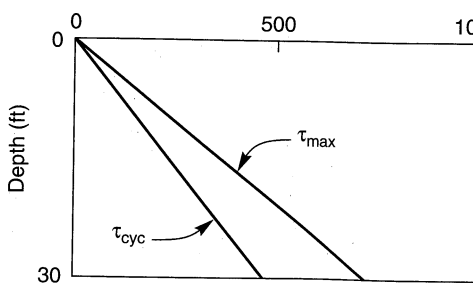


Figure E9.2b

Characterization of Liquefaction Resistance. The liquefaction resistance of an element of soil depends on how close the initial state of the soil is to the state corresponding to “failure” and on the nature of the loading required to move it from the initial state to the failure state. As the preceding sections have shown, however, the failure state is different for flow liquefaction and cyclic mobility. The failure state for flow liquefaction is easily defined using the FLS, and its initiation is easily recognized in the field. The definition of failure for cyclic mobility is imprecise—a certain level of deformation caused by cyclic mobility may be excessive at some sites and acceptable at others. In contrast to flow liquefaction, there is no distinct point at which cyclic mobility “failure” can be defined. Cyclic mobility failure is generally considered to occur when pore pressures become large enough to produce ground oscillation, lateral spreading, or other evidence of damage at the ground surface. This definition of failure is imprecise; in practice the presence of sand boils is frequently taken as evidence of cyclic mobility. The development of sand boils, however, depends not only on the characteristics of the liquefiable sand but also on the characteristics (e.g., thickness, permeability, and intactness) of any overlying soils (Section 9.6.2).

In the field, where stresses and pore pressures are seldom measured, it is often difficult to distinguish between different liquefaction phenomena after an earthquake has occurred. When the cyclic stress approach was developed, little distinction was made between the different liquefaction phenomena—cases of flow liquefaction and cyclic mobility were lumped together under the general heading of “liquefaction.” Characterization of liquefaction resistance developed along two lines: methods based on the results of laboratory tests, and methods based on in situ tests and observations of liquefaction behavior in past earthquakes.

Characterization Based on Laboratory Tests. The early development of the cyclic stress approach emphasized laboratory testing for characterization of liquefaction resistance. To create an initial condition of zero driving stress (to simulate the stress conditions on

horizontal planes beneath level ground), most laboratory tests were performed on isotropically consolidated triaxial specimens or on K_0 -consolidated simple shear specimens. In these tests, “liquefaction failure” was usually defined as the point at which initial liquefaction was reached or at which some limiting cyclic strain amplitude (commonly 5% for dense specimens) was reached.

Laboratory tests show that the number of loading cycles required to produce liquefaction failure, N_L , decreases with increasing shear stress amplitude and with decreasing density (Figure 9.26). While liquefaction failure can occur in only a few cycles in a loose specimen subjected to large cyclic shear stresses, thousands of cycles of low-amplitude shear stresses may be required to cause liquefaction failure of a dense specimen. The relationship between density, cyclic stress amplitude, and number of cycles to liquefaction failure can be expressed graphically by laboratory *cyclic strength curves*, such as those shown in Figure 9.27. Cyclic strength curves are frequently normalized by the initial effective overburden pressure to produce a *cyclic stress ratio* (CSR). The CSR must be defined differently for different types of tests. For the cyclic simple shear test, the CSR is taken as the ratio of the cyclic shear stress to the initial vertical effective stress [i.e., $(CSR)_{ss} = \tau_{cyc}/\sigma'_{v0}$]. For the cyclic triaxial test, it is taken as the ratio of the maximum cyclic shear stress to the initial effective confining pressure [i.e., $(CSR)_{tx} = \sigma_{dc}/2\sigma'_{3c}$]. As discussed in Chapter 6, the cyclic simple shear and cyclic triaxial tests impose quite different loading, and their cyclic stress ratios are not equivalent. For liquefaction testing, the two are usually related by

$$(CSR)_{ss} = c_r (CSR)_{tx} \quad (9.3)$$

where the correction factor, c_r , is estimated from Table 9-1.

In contrast to laboratory cyclic simple shear and cyclic triaxial tests, earthquakes produce shear stresses in different directions. Multidirectional shaking has been shown (Pyke, et al., 1975) to cause pore pressures to increase more rapidly than does unidirectional shaking. Seed, et al. (1975b) suggested that the CSR required to produce initial liquefaction in

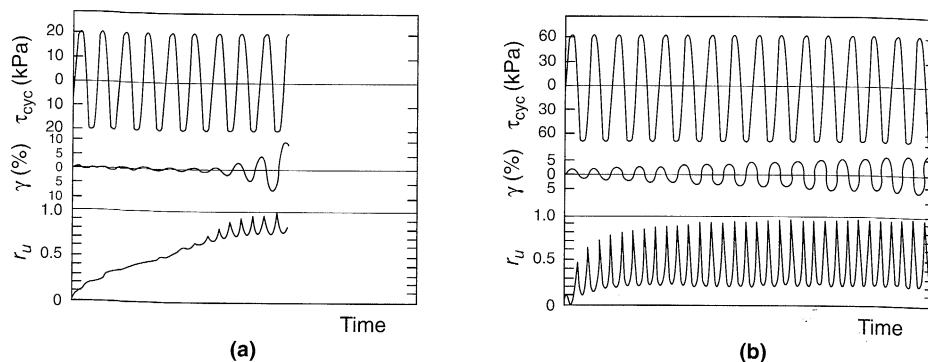


Figure 9.26 Results of torsional shear tests on isotropically consolidated ($\sigma'_0 = 98$ kPa) specimens of (a) loose sand (47% relative density) and (b) dense sand (75% relative density). Loose specimen reached initial liquefaction ($r_u = 1.00$) on 10th loading cycle. Despite much higher loading, dense specimen has not quite reached initial liquefaction after 17 cycles. (After Ishihara, 1985; used by permission of Kluwer Academic Publishers.)

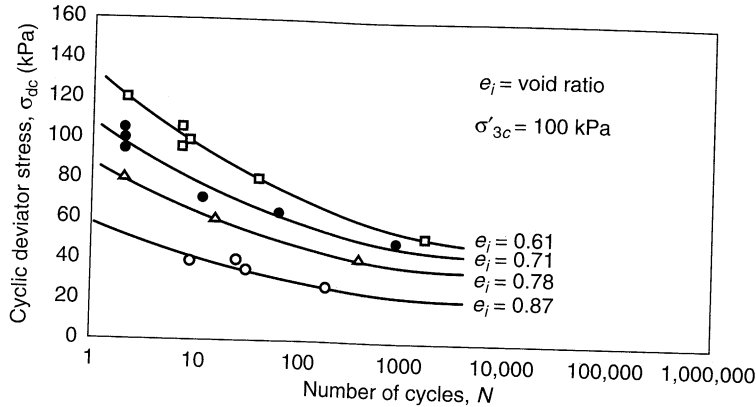


Figure 9.27 Cyclic stresses required to produce initial liquefaction and 20% axial strain in isotropically consolidated Sacramento River Sand triaxial specimens. (After Seed and Lee, 1965.)

Table 9-1 Values of CSR Correction Factor, c_r

Reference	Equation	c_r for:	
		$K_0 = 0.4$	$K_0 = 1.0$
Finn et al. (1971)	$c_r = (1 + K_0)/2$	0.7	1.0
Seed and Peacock (1971)	Varies	0.55–0.72	1.0
Castro (1975)	$c_r = 2(1 + 2K_0)/3\sqrt{3}$	0.69	1.15

the field was about 10% less than that required in unidirectional cyclic simple shear tests. Therefore, the liquefaction resistance of an element of soil in the field is given by the cyclic stress ratio

$$(\text{CSR})_{\text{field}} = \frac{\tau_{\text{cyc}}}{\sigma'_{v0}} = 0.9(\text{CSR})_{ss} = 0.9c_r(\text{CSR})_{tx} \quad (9.4)$$

Example 9.3

A 2-m-thick layer of Sacramento River Sand ($e = 0.87$; $\phi' = 33^\circ$) is overlain by 4 m of compacted fill ($\rho_i = 2.1 \text{ Mg/m}^3$). The water table is at the bottom of the fill. Using the cyclic triaxial test results shown in Figure 9.27, estimate the maximum cyclic shear stress required to initiate liquefaction in the sand in a magnitude 7.5 earthquake.

Solution The sand is under an average effective vertical stress of

$$\sigma'_{v0} = [(4 \text{ m})(2.1 \text{ Mg/m}^3) + (1.0 \text{ m})(0.91 \text{ Mg/m}^3)] \left(9.81 \frac{\text{m}}{\text{sec}^2} \right) = 91.3 \text{ kPa}$$

which is close to the effective confining pressures of the cyclic triaxial test data shown in Figure 9.27.

Using Figure 9.24, a magnitude 7.5 earthquake would be expected to produce about 14 uniform stress cycles (at 65% of the maximum shear stress). From Figure 9.27, the cyclic deviator

stress that would cause initial liquefaction in 14 cycles would be about 39 kPa. Then the triaxial cyclic stress ratio is

$$(\text{CSR})_{tx} = \frac{\sigma_{dc}}{2\sigma'_{3c}} = \frac{39 \text{ kPa}}{(2)(100 \text{ kPa})} = 0.195$$

The corresponding field cyclic stress ratio can be determined using equation (9.4). Letting $K_0 = 1 - \sin \phi' = 0.46$, we have

$$(\text{CSR})_{\text{field}} = 0.9c_r(\text{CSR})_{tx} = 0.9 \frac{1+0.46}{2}(0.195) = 0.128$$

Then

$$\tau_{\text{cyc}} = (\text{CSR})_{\text{field}}\sigma'_{v0} = (0.128)(91.3 \text{ kPa}) = 11.7 \text{ kPa}$$

$$\tau_{\max} = \frac{\tau_{\text{cyc}}}{0.65} = \frac{11.7 \text{ kPa}}{0.65} = 18.0 \text{ kPa}$$

Therefore, a peak shear stress of 18 kPa would be required to initiate liquefaction in the Sacramento River Sand in a magnitude 7.5 earthquake.

Laboratory tests can also reveal the manner in which excess pore pressure is generated. For stress-controlled cyclic tests with uniform loading, Lee and Albaisa (1974) and DeAlba et al. (1975) found that the pore pressure ratio, r_u , is related to the number of loading cycles by

$$r_u = \frac{1}{2} + \frac{1}{\pi} \sin^{-1} \left[2 \left(\frac{N}{N_L} \right)^{1/\alpha} - 1 \right] \quad (9.5)$$

where N_L is the number of cycles required to produce initial liquefaction ($r_u = 1.00$) and α is a function of the soil properties and test conditions. As illustrated in Figure 9.28, excess pore pressures increase quickly in the first and last loading cycles. Equation (9.5) can be used to estimate the excess pore pressure generated when initial liquefaction does not occur (i.e., when $N_{eq} < N_L$). In an approach that could address irregular loading, Martin et al.

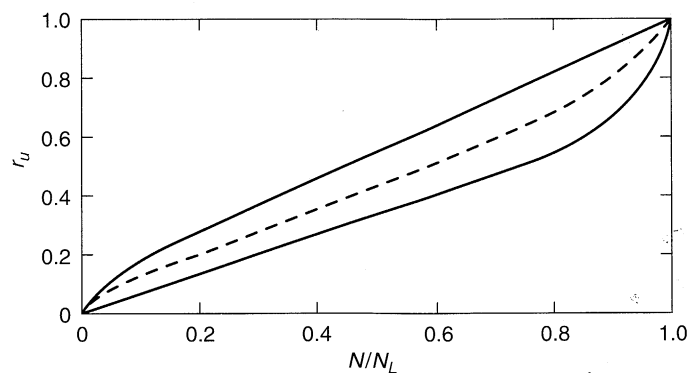


Figure 9.28 Rate of pore pressure generation in cyclic simple shear tests. The dashed line was generated from equation (9.5) with $\alpha = 0.7$. (After De Alba et al., 1975.)

(1975) developed a fundamental model that combined data on the rate of settlement of cyclically loaded dry sand with data on the rebound and stress-deformation characteristics of the soil to predict pore pressure generation. The model has been incorporated into nonlinear ground response analyses to provide an effective stress-based approach to liquefaction analysis (Section 9.5.3.3).

For a number of years, liquefaction resistance was commonly characterized by cyclic stresses determined from laboratory tests. However, subsequent work showed that cyclic stress-based measures of liquefaction resistance are influenced by factors other than the initial density and stress conditions. For example, liquefaction resistance is influenced by differences in the structure of the soil (or *soil fabric*) produced by different methods of specimen preparation (Ladd, 1974; Mulilis et al., 1975; Toki et al., 1986; Tatsuoka et al., 1986). The history of prior seismic straining also influences liquefaction resistance [i.e., the liquefaction resistance of a specimen that has been subjected to prior seismic straining is greater than that of a specimen of the same density that has not (Finn et al., 1970; Seed et al., 1975b)]. Also, liquefaction resistance increases with increasing overconsolidation ratio and lateral earth pressure coefficient (Seed and Peacock, 1971). Finally, the length of time under sustained pressure has been shown (Ohsaki, 1969; Seed, 1979; Yoshimi et al., 1989) to increase the liquefaction resistance. These additional parameters are all functions of the depositional and historical environment of a soil deposit, and they tend to influence soil behavior primarily at the low strain levels associated with the initiation of liquefaction. These low-strain effects are easily destroyed by sampling disturbance, and are very difficult to replicate in reconstituted specimens. Because of these factors, characterization of liquefaction resistance by laboratory testing is extremely difficult and has been supplanted by methods based on in situ test results for many projects. Truly undisturbed sampling (e.g., by careful ground freezing and coring) is required for laboratory tests to be able to characterize liquefaction resistance reliably.

Cyclic triaxial tests of liquefaction resistance can also be complicated by specimen nonuniformity. As high pore pressures develop in a cyclic triaxial test specimen, the soil grains tend to settle causing densification of the lower part and loosening of the upper part of the specimen. The nonuniform density leads to nonuniform strain, and eventually to thinning or *necking* of the upper portion of the specimen. This nonuniformity can cause considerable uncertainty in the application of cyclic triaxial test results to field conditions.

Characterization Based on In Situ Tests. An alternative approach, first described by Whitman (1971), is to use liquefaction case histories to characterize liquefaction resistance in terms of measured in situ test parameters. Previous case histories can be characterized by the combination of a loading parameter, \mathcal{L} , and a liquefaction resistance parameter, \mathfrak{R} , which can be plotted with a symbol that indicates whether liquefaction was or was not observed (Figure 9.29). A boundary can then be drawn between the \mathcal{L} - \mathfrak{R} combinations that have and have not produced liquefaction in past earthquakes. The boundary is usually drawn conservatively such that all cases in which liquefaction has been observed lie above it. In this approach, the cyclic stress ratio is usually used as the loading parameter, and in situ test parameters that reflect the density and pore pressure generation characteristics of the soil are used as liquefaction resistance parameters.

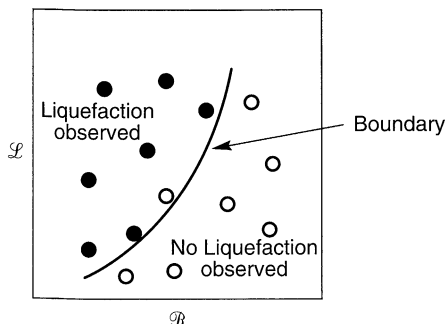


Figure 9.29 Typical plot showing combinations of loading parameter, \mathcal{L} , and liquefaction resistance parameter, \mathcal{R} , for cases where liquefaction has been observed (solid circles) and not observed (open circles). Boundary indicates minimum value of liquefaction resistance parameter required to prevent liquefaction.

1. Standard Penetration Resistance. In the United States and most other countries, the standard penetration test (SPT) has been the most commonly used in situ test for characterization of liquefaction resistance; factors that tend to increase liquefaction resistance (e.g. density, prior seismic straining, overconsolidation ratio, lateral earth pressures, and time under sustained pressure) also tend to increase SPT resistance. Seed et al. (1983) compared the corrected SPT resistance (Section 6.3.1.2) and cyclic stress ratio for clean sand (Figure 9.30) and silty sand (Figure 9.31) sites at which liquefaction was or was not observed in earthquakes of $M = 7.5$ to determine the minimum cyclic stress ratio at which liquefaction could be expected in a clean sand of a given SPT resistance.

The presence of fines can affect SPT resistance and therefore must be accounted for in the evaluation of liquefaction resistance (Seed et al., 1985; Ishihara and Koseki, 1989; Koester, 1994). Examination of Figures 9.30 and 9.31 shows that the liquefaction resistance of sands is not influenced by fines unless the fines comprise more than 5% of the soil. At higher fines contents, the fines tend to inhibit liquefaction [i.e., the CSR required to initiate liquefaction (for a given $(N_1)_{60}$ value)]. The plasticity of the fines can also influence liquefaction resistance; the adhesion of plastic fines tends to resist the relative movement of individual soil particles and thereby reduce the generation of excess pore pressure during earthquakes. Laboratory tests (Ishihara and Koseki, 1989) indicate little influence at plasticity indices below 10, and a gradual increase in liquefaction resistance at plasticity indices greater than 10. Ishihara (1993) suggested that the effects of plasticity could be accounted for by multiplying the CSR by the factor

$$F = \begin{cases} 1.0 & PI \leq 10 \\ 1.0 + 0.022(PI - 10) & PI > 10 \end{cases} \quad (9.6)$$

Since most sandy soils in alluvial deposits and man-made fills have plasticity indices less than about 15, the effect of fines plasticity is usually small.

Because strong-motion duration (hence equivalent number of uniform stress cycles) increases with earthquake magnitude, the minimum cyclic stress ratio required to initiate liquefaction decreases with increasing magnitude. The minimum cyclic stress ratio for other magnitudes may be obtained by multiplying the cyclic stress ratio for $M = 7.5$ earthquakes by the factors shown in Table 9-2.

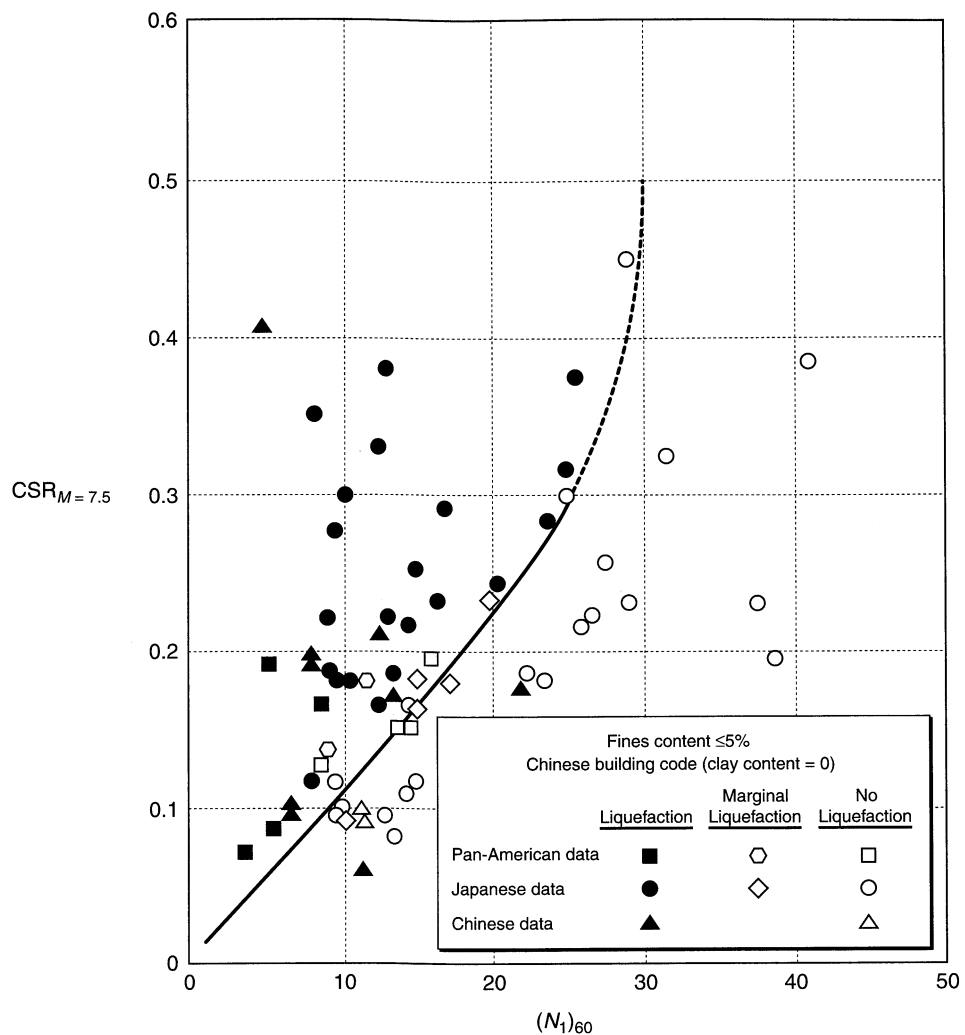


Figure 9.30 Relationship between cyclic stress ratios causing liquefaction and $(N_1)_{60}$ values for clean sands in $M = 7.5$ earthquakes. (After Seed et al. (1975). Influence of SPT procedures in soil liquefaction resistance evaluations, *Journal of Geotechnical Engineering*, Vol. 111, No. 12. Reprinted by permission of ASCE.)

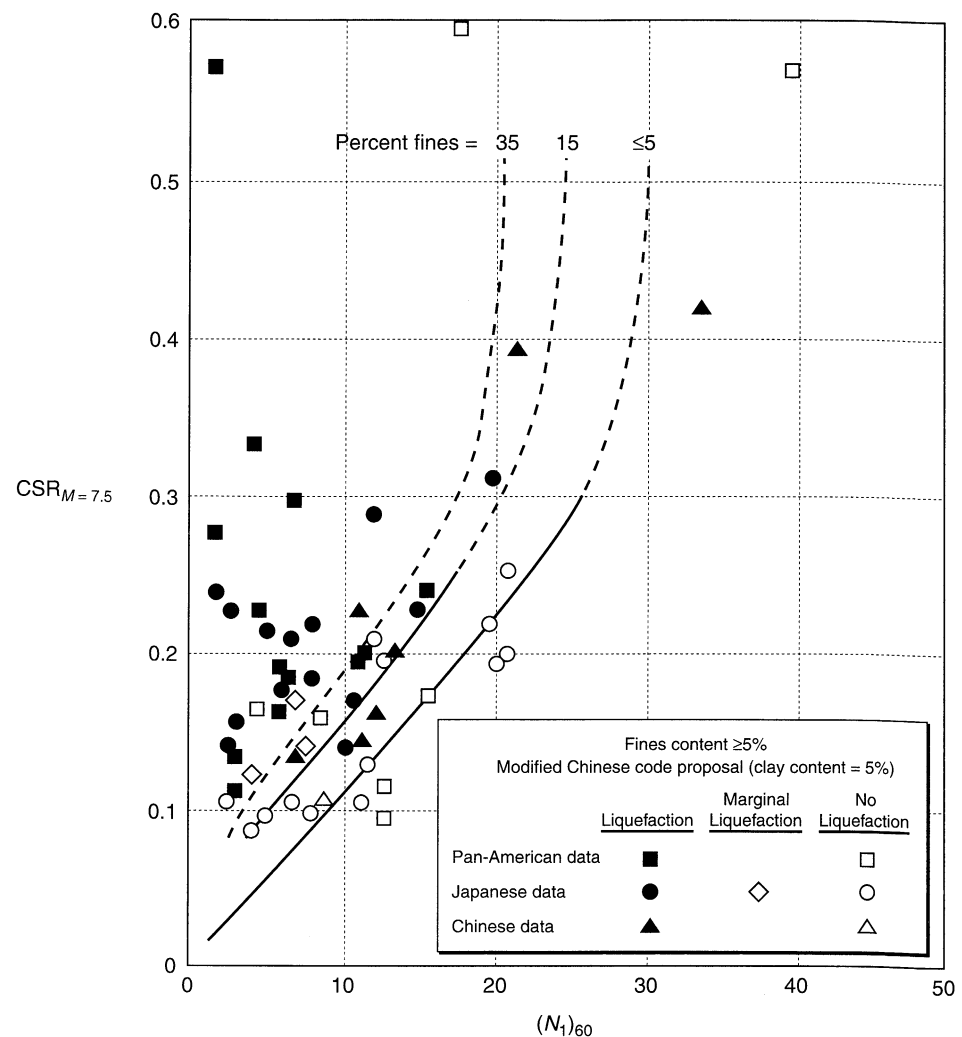


Figure 9.31 Relationship between cyclic stress ratios causing liquefaction and $(N_1)_{60}$ values for silty sands in $M = 7.5$ earthquakes. (After Seed et al. (1975). Influence of SPT procedures in soil liquefaction resistance evaluations, *Journal of Geotechnical Engineering*, Vol. 111, No. 12. Reprinted by permission of ASCE.)

Table 9-2 Magnitude Correction Factors for Cyclic Stress Approach

Magnitude, M	$\text{CSR}_M/\text{CSR}_{M=7.5}$
$5\frac{1}{4}$	1.50
6	1.32
$6\frac{3}{4}$	1.13
$7\frac{1}{2}$	1.00
$8\frac{1}{2}$	0.89

The data from which Figures 9.30 and 9.31 were developed correspond primarily to level-ground sites with relatively shallow deposits of potentially liquefiable soil. At sites with sloping ground conditions or at sites that support heavy structures, the presence of initial static shear stresses will influence liquefaction resistance. For conditions in which the static shear stress is greater than the steady-state strength, the initial conditions are closer to the FLS and the liquefaction resistance is reduced. Laboratory tests show that the cyclic shear stress required to trigger liquefaction increases at high effective confining pressures (greater than those of the field performance database). Seed (1983) proposed that the effects of initial shear stress and high effective confining pressures be accounted for by modifying the cyclic stress ratio as follows:

$$(\text{CSR}_{\text{field}})_{\alpha, \sigma} = (\text{CSR}_{\text{field}})_{\alpha=0, \sigma < 1 \text{ ton}/\text{ft}^2} K_{\alpha} K_{\sigma} \quad (9.7)$$

where $\alpha = \tau_{h, \text{static}}/\sigma'_{v0}$, and K_{α} and K_{σ} are correction factors for initial shear stress (Figure 9.32) and effective overburden pressure (Figure 9.33), respectively. The values of K_{α} and K_{σ} vary for different soils and should be evaluated on a site-specific basis whenever possible.

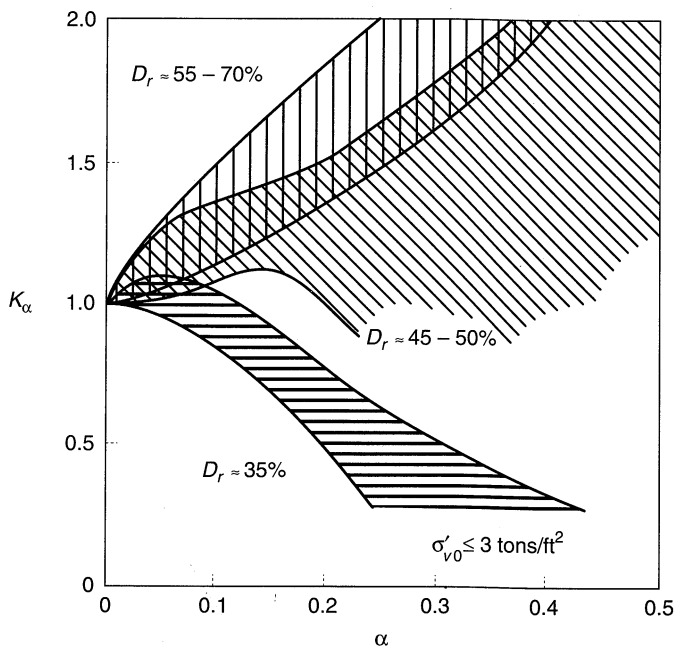


Figure 9.32 Variation of correction factor, K_{α} , with initial shear/normal stress ratio. (After Seed and Harder, 1990. *H. Bolton Seed Memorial Symposium Proceedings*, Vol. 2, p. 364. Used by permission of BiTech Publishers, Ltd.)

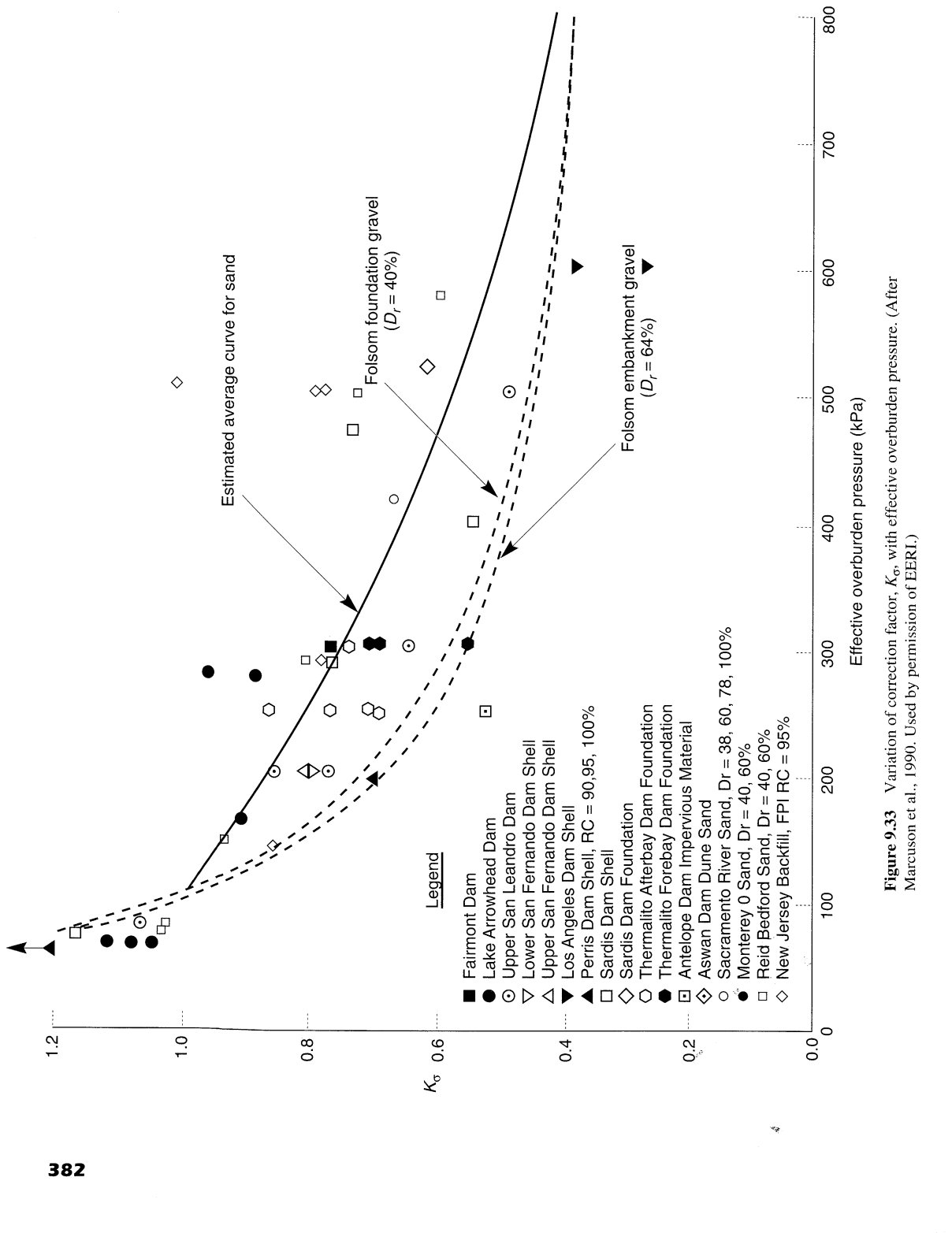


Figure 9.33 Variation of correction factor, K_{σ} , with effective overburden pressure. (After Marcuson et al., 1990. Used by permission of EERI.)

2. Cone Penetration Resistance. The tip resistance from the cone penetration test (CPT) can also be used as a measure of liquefaction resistance; indeed, it has a pronounced advantage over the SPT in its ability to detect thin seams of loose soil. The database of sites at which CPT resistance has been measured and where the occurrence or nonoccurrence of liquefaction has been documented, although growing rapidly, remains fairly small. By supplementing these data with correlations between CPT and SPT resistances, the minimum cyclic stress ratio at which liquefaction can be expected in a clean sand of a given CPT resistance can be determined (e.g., Robertson and Campanella, 1985; Seed and DeAlba, 1986). Since the CPT–SPT correlation depends on grain size, CPT-based liquefaction curves have been developed for different mean grain sizes (Figure 9.34a). Mitchell and Tseng (1990) developed curves based on laboratory tests and theoretically derived values of CPT resistance (Figure 9.34b). CPT–SPT correlation that make use of the friction ratio as well as the tip resistance (Douglas et al., 1981; Martin, 1992) eliminate the need for measurement of mean grain size (and the drilling and sampling required to do so). In CPT-based liquefaction evaluations, the tip resistance is normalized to a standard effective overburden pressure of 1 ton/ft² (96 kPa) by

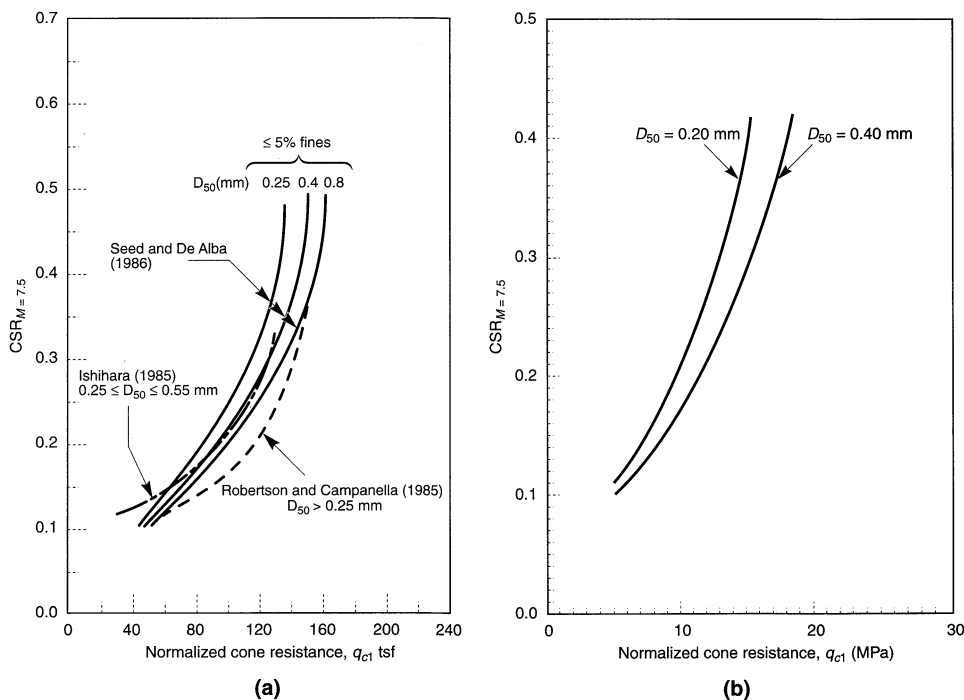


Figure 9.34 CPT-based liquefaction curves: (a) based on correlations with SPT data; (b) based on theoretical/experimental results. (After Mitchell and Tseng, 1990, H. Bolton Seed Memorial Symposium Proceedings, Vol. 2, p. 347. Used by permission of BiTech Publishers, Ltd.)

$$q_{c1} = q_c \left(\frac{p_a}{\sigma'_{v0}} \right)^{0.5} \quad (9.8a)$$

or

$$q_{c1} = \frac{1.8}{0.8 + \sigma'_{v0}} q_c \quad (9.8b)$$

where σ'_{v0} is in tons/ft² (Kayen et al., 1992). Adjustment for magnitudes other than 7.5 can be made using the CSR correction factors presented in Table 9-2. Kayen et al. (1992) found that liquefaction observations in the 1989 Loma Prieta earthquake agreed well with the curves of Robertson and Campanella (1985) and Mitchell and Tseng (1990).

For silty sands (> 5% fines), the effects of fines can be estimated by adding the following tip resistance increments to the measured tip resistance to obtain an equivalent clean sand tip resistance (Ishihara, 1993)

Fines Content (%)	Tip Resistance Increment (tons/ft ²)
≤ 5	0
~ 10	12
~ 15	22
~ 35	40

3. Shear Wave Velocity. Improved methods of in situ shear wave velocity measurements and studies related to development of the cyclic strain approach (Section 9.5.3.2) have contributed to the recognition of shear wave velocity as a useful measure of liquefaction resistance. Measured shear wave velocities can be normalized to a standard effective overburden pressure of 1 ton/ft² (96 kPa) by

$$v_{s1} = v_s (\sigma'_{v0})^{-1/n} \quad (9.9)$$

where σ'_{v0} is in tons/ft² and n has been taken as 3 (Tokimatsu et al., 1991) or 4 (Finn, 1991; Kayen et al., 1992). Stokoe et al. (1988) used the cyclic strain approach and equivalent linear ground response analyses to explore the relationship between peak ground surface acceleration (for stiff soil site conditions) and shear wave velocity. The results were used to develop bounds for the conditions under which liquefaction could be expected; the results agreed well with observed behavior in two earthquakes in the Imperial Valley of California (Figure 9.35). Tokimatsu et al. (1991) used the results of laboratory tests to develop curves showing the CSR required to produce a cyclic strain amplitude of 2.5% in various numbers of cycles as a function of corrected shear wave velocity (Figure 9.36).

The observation that the shear wave velocity of sand is insensitive to factors (e.g., soil fabric, overconsolidation ratio, prior cyclic straining) that are known to influence liquefaction resistance suggests that shear wave velocity measurements alone may not be sufficient to evaluate the liquefaction potential of all soil deposits (Jamiolkowsky and LoPresti, 1992; Verdugo, 1992).

4. Dilatometer Index. Correlations for liquefaction potential with the horizontal stress index of the dilatometer test (DMT) have also been proposed (Marchetti, 1982; Robertson

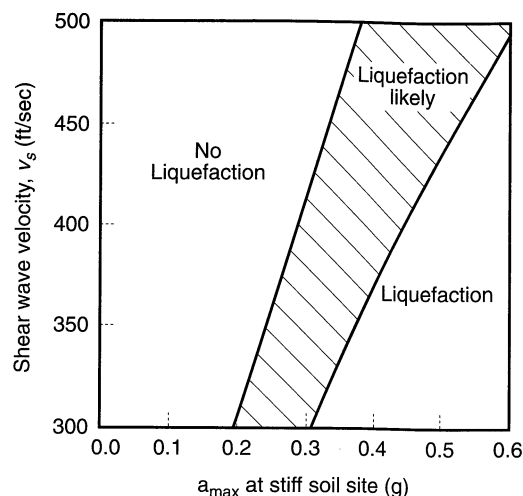


Figure 9.35 Chart for evaluation of liquefaction potential from shear wave velocity and peak ground acceleration (10 cycles). (After Stokoe et al., 1988.)

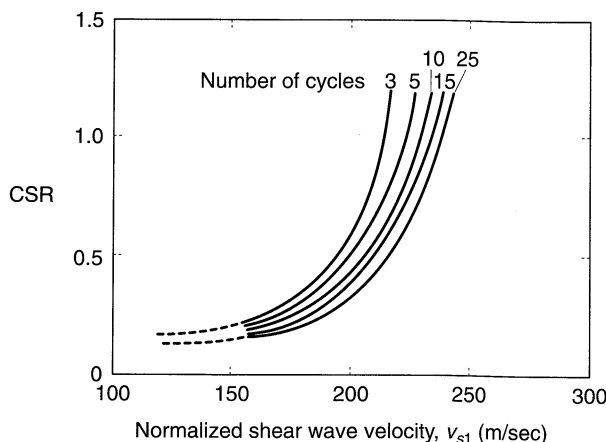


Figure 9.36 Correlations between cyclic stress ratio required to produce cyclic strain amplitude of 2.5% in clean sand and shear wave velocity. (After Tokimatsu et al., 1991.)

and Camponella, 1986; Reyna and Chameau, 1991). Figure 9.37 illustrates the performance of three such correlations when applied to data from several sites in the Imperial Valley of California. New correlations for the DMT should be expected as additional experience with this relatively new in situ test is obtained.

5. Use of In Situ Test Results. SPT resistance is by far the most commonly used in situ test parameter for characterization of liquefaction resistance. The SPT allows a sample to be retrieved (for identification, measurement of fines content, etc.) and has the largest case history database of any in situ test. However, the CPT is becoming much more commonly used for characterization of liquefaction resistance. The CPT provides a continuous record of penetration resistance (an important benefit when thin layers of seams of potentially liquefiable soil may exist) and is much faster and less expensive than the SPT. Because CPT-based liquefaction resistance is influenced by grain size characteristics (Figure 9.34), complementary borings with sampling may be required.

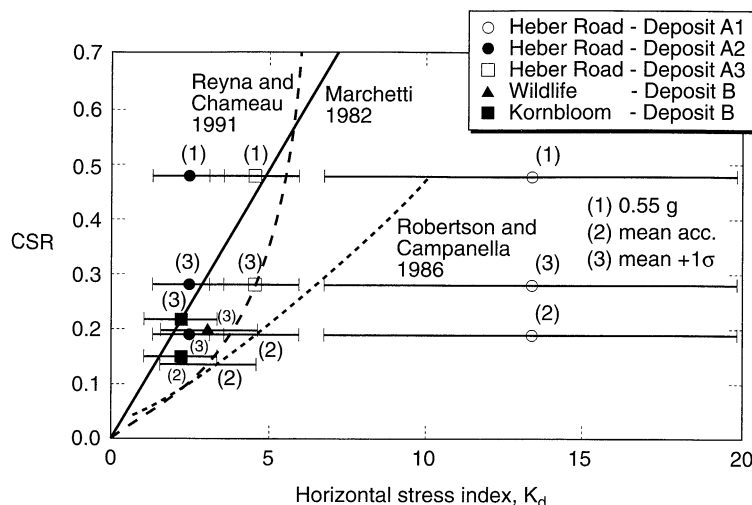


Figure 9.37 Suggested relationships between cyclic stress ratio required to produce liquefaction and horizontal stress index from dilatometer test. (After Reyna and Chameau, 1991.)

Regardless of which is used, the in situ test parameters allow estimation of CSR_L —the CSR required to initiate liquefaction. Using the definition of cyclic stress ratio, the cyclic shear stress required to initiate liquefaction is given by

$$\tau_{cyc,L} = CSR_L \sigma'_{v0} \quad (9.10)$$

Evaluation of Initiation of Liquefaction. Once the cyclic loading imposed by an earthquake and the liquefaction resistance of the soils have been characterized, liquefaction potential can be evaluated. The cyclic stress approach characterizes earthquake loading by the amplitude of an equivalent uniform cyclic stress and liquefaction resistance by the amplitude of the uniform cyclic stress required to produce liquefaction in the same number of cycles. The evaluation of liquefaction potential is thus reduced to a comparison of loading and resistance throughout the soil deposit of interest.

The evaluation is easily performed graphically. First, the variation of equivalent cyclic shear stress (earthquake loading, τ_{cyc}), with depth is plotted as in Figure 9.38 (the number of equivalent cycles, N_{eq} , corresponding to the earthquake magnitude must be determined if liquefaction resistance is to be characterized using laboratory test results). The variation of the cyclic shear stress required to cause liquefaction (liquefaction resistance, $\tau_{cyc,L}$) with depth is then plotted on the same graph (the values of $\tau_{cyc,L}$ must correspond to the same earthquake magnitude, or same number of equivalent cycles, as τ_{cyc}). Liquefaction can be expected at depths where the loading exceeds the resistance or when the factor of safety against liquefaction, expressed as

$$FS_L = \frac{\text{cyclic shear stress required to cause liquefaction}}{\text{equivalent cyclic shear stress induced by earthquake}} = \frac{\tau_{cyc,L}}{\tau_{cyc}} = \frac{CSR_L}{CSR} \quad (9.11)$$

is less than 1.

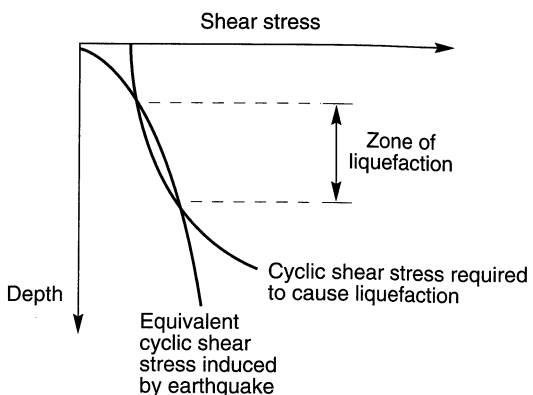


Figure 9.38 Process by which zone of liquefaction is identified.

It should be noted that significant excess pore pressure can develop even if the computed factor of safety is greater than 1. At level-ground sites, for example, the magnitude of this excess pore pressure can be estimated from Figure 9.39. The reduction in effective stress associated with such excess pore pressures can reduce the stiffness of the soil, and significant settlement can occur as the excess pore pressures dissipate (Section 9.6.3.2).

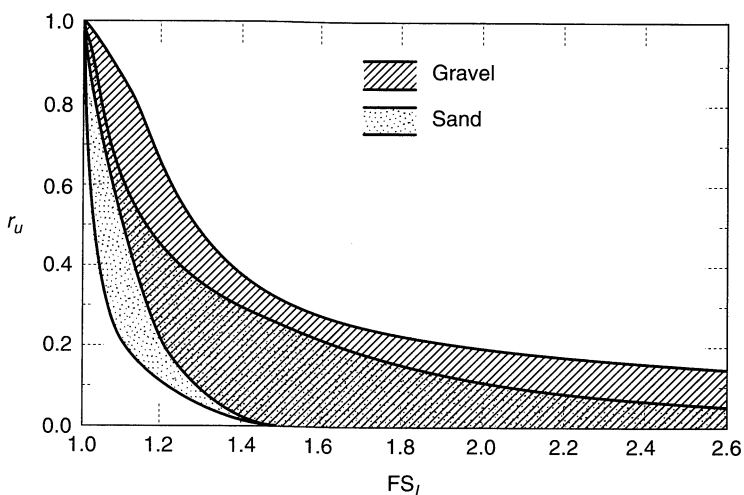


Figure 9.39 Relationship between residual excess pore pressure and factor of safety against liquefaction for level-ground sites. (After Marcuson and Hynes, 1990.)

Example 9.4

A site in Japan underlain by clean, potentially liquefiable sand was described in Example 6.6. SPT tests were performed at the site using standard Japanese SPT techniques; the process by which the measured SPT resistances are corrected to obtain $(N_1)_{60}$ values was described in Example 6.6. Using the information available, determine the extent to which liquefaction would have been expected in the 1964 Niigata earthquake ($M = 7.5$) if the peak horizontal acceleration at the ground surface was $0.16g$.

Solution Evaluation of liquefaction potential by the cyclic stress approach involves comparison of the level of cyclic stress induced by the earthquake with the level of cyclic stress required to initiate liquefaction. The level of cyclic stress induced by the earthquake can be estimated from the information available using the simplified procedure of Seed and Idriss (1971). The variation of total vertical stress with depth is easily computed (column 2 below). For example, the total vertical stress at a depth of 6.2 m is given by

$$\sigma_{v0} = (1.5 \text{ m}) \left(1.874 \frac{\text{Mg}}{\text{m}^3} \right) + (4.7 \text{ m}) \left(2.180 \frac{\text{Mg}}{\text{m}^3} \right) \left(9.81 \frac{\text{m}}{\text{sec}^2} \right) = 128.1 \text{ kPa}$$

The value of the stress reduction factor can be obtained graphically from Figure 9.25 (column 3 below). At a depth of 6.2 m, $r_d = 0.960$. Knowing the peak ground surface acceleration, the cyclic shear stress is computed (column 4 below) by equation (9.2). At a depth of 6.2 m,

$$\tau_{\text{cyc}} = 0.65 \frac{0.16g}{g} (128.1 \text{ kPa}) (0.960) = 12.8 \text{ kPa}$$

The level of cyclic shear stress required to initiate liquefaction depends on the liquefaction resistance of the soil. For this example, liquefaction resistance can be characterized by the $(N_1)_{60}$ values (column 5 below—from column 6 in Example 6.6). Using the chart for less than 5% fines in Figure 9.31, the cyclic stress ratios required to initiate liquefaction can be found graphically (column 6 below). At a depth of 6.2 m, the value $(N_1)_{60} = 11.7$ corresponds to $\text{CSR}_{M=7.5} = 0.130$. Because the magnitude of the Niigata earthquake was 7.5, the magnitude correction factor (Table 9-2) has a value of 1.0. Then

$$\text{CSR}_L = (\text{CSR}_{M=7.5})(1.0) = 0.130$$

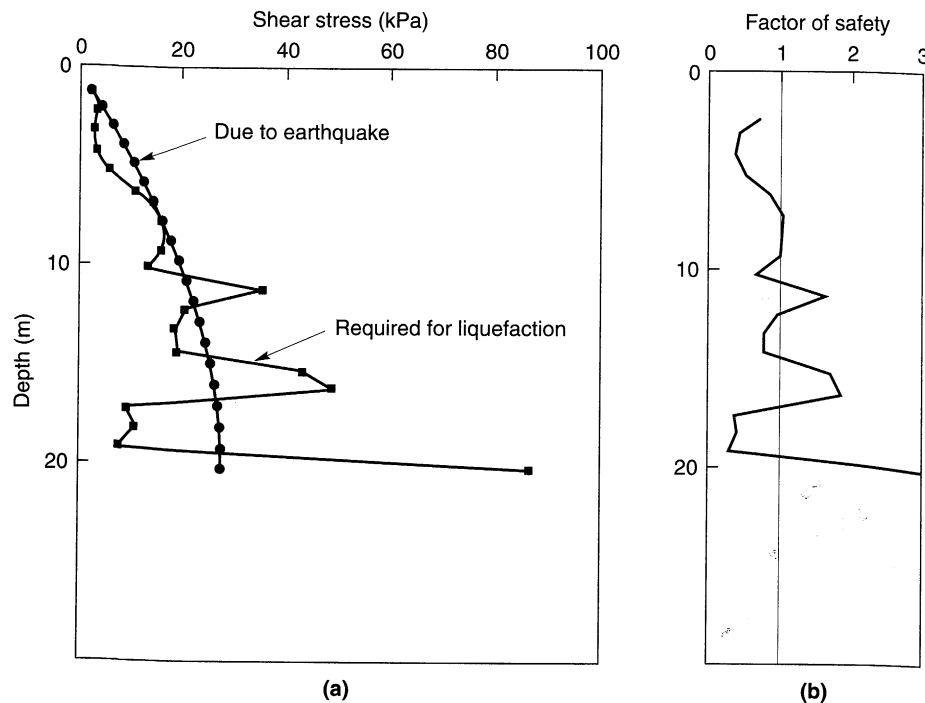


Figure E9.4

Knowing CSR_L and the variation of vertical effective stress with depth (column 7 below—from column 3 of Example 6.6), the cyclic stress required to initiate liquefaction can be computed (column 8 below and Figure E9.4a). At a depth of 6.2 m,

$$\tau_{\text{cyc},L} = \text{CSR}_L \sigma'_{v0} = (0.130)(82.0 \text{ kPa}) = 10.7 \text{ kPa}$$

Finally, the cyclic stress induced by the earthquake can be compared to the cyclic stress required to initiate liquefaction. Using the concept of a factor of safety against liquefaction [equation (9.11)], the variation of factor of safety with depth can be determined (column 9 below and Figure E9.4b). At a depth of 6.2 m,

$$\text{FS}_L = \frac{\tau_{\text{cyc},L}}{\tau_{\text{cyc}}} = \frac{10.7 \text{ kPa}}{12.8 \text{ kPa}} = 0.84$$

As illustrated in Figure E9.4b, the factor of safety against liquefaction is greater than one where the cyclic stress induced by the earthquake is lower than the cyclic stress required to initiate liquefaction ($\tau_{\text{cyc}} < \tau_{\text{cyc},L}$). At this site, extensive liquefaction would have been expected in the upper 8 to 10 m and at some greater depths as well.

The conditions of this example are representative of those in the Kawagishi-Cho area of Niigata, Japan (Figure 1.6) though the actual peak accelerations may have been on the order of 0.2 to 0.3g. The extensive liquefaction predicted in this example is consistent with what was actually observed in that area in the 1964 Niigata earthquake.

(1) <i>D</i> (m)	(2) σ_{vo}	(3) r_d	(4) τ_{cyc}	(5) $(N_1)_{60}$	(6) CSR_L	(7) σ'_{vo}	(8) $\tau_{\text{cyc},L}$	(9) FS_L
1.2	22.1	0.994	2.28	17.3	—	22.1	—	—
2.2	42.6	0.989	4.38	7.9	0.087	36.4	3.17	0.72
3.2	64.0	0.982	6.53	5.1	0.056	47.3	2.65	0.41
4.2	85.3	0.976	8.66	4.6	0.051	58.8	3.00	0.35
5.2	106.7	0.968	10.8	7.0	0.077	70.4	5.42	0.50
6.2	128.1	0.960	12.8	11.7	0.130	82.0	10.7	0.84
7.2	149.5	0.951	14.8	14.6	0.161	93.6	15.1	1.02
8.2	170.9	0.940	16.7	13.7	0.151	105.3	15.9	0.95
9.2	192.3	0.926	18.5	15.2	0.167	116.8	19.5	1.05
10.2	213.8	0.910	20.2	9.3	0.102	128.4	13.1	0.65
11.2	235.1	0.886	21.7	22.8	0.250	140.0	35.0	1.61
12.2	256.5	0.864	23.1	12.4	0.136	151.5	20.6	0.89
13.2	277.9	0.835	24.1	10.1	0.111	163.1	18.1	0.75
14.2	299.3	0.813	25.3	9.8	0.108	174.7	18.9	0.75
15.2	320.7	0.767	25.6	20.7	0.228	186.3	42.5	1.66
16.2	342.1	0.739	26.3	22.5	0.245	197.9	48.5	1.84
17.2	363.5	0.704	26.6	4.1	0.045	209.4	9.42	0.35
18.2	384.8	0.671	26.9	4.7	0.052	221.1	11.5	0.43
19.2	406.2	0.642	27.1	3.1	0.034	232.7	7.91	0.29
20.2	427.7	0.625	27.8	28.5	0.350	244.3	85.5	3.08

Because of their physical significance, the initiation of liquefaction has been presented in terms of cyclic stresses in this section. After developing an understanding of the relationship between the cyclic shear stresses induced by an earthquake and the cyclic shear stresses required to initiate liquefaction, many engineers will find it more convenient to characterize earthquake loading and liquefaction resistance in terms of the cyclic stress

ratios, CSR and CSR_L, both of which vary over a much smaller range than the cyclic shear stresses themselves.

9.5.3.2 Cyclic Strain Approach

The large number of factors that influence the cyclic stresses required to produce liquefaction can make laboratory evaluation of liquefaction resistance in the cyclic stress approach difficult. As Seed (1976) pointed out, "the liquefaction characteristics of in situ sand deposits are determined by a number of complex factors, of which relative density is only one, and careful evaluations of all of these factors is required in selecting soil characteristics for use in design."

In an effort to develop a more robust approach to the liquefaction problem, Dobry and Ladd (1980) and Dobry et al. (1982) described an approach that used cyclic strains rather than cyclic stresses to characterize earthquake-induced loading and liquefaction resistance. The approach is based on experimental evidence that shows densification of dry sands to be controlled by cyclic strains rather than cyclic stresses (e.g., Silver and Seed, 1971; Youd, 1972) and the existence of the threshold volumetric shear strain (Section 6.4.1) below which densification does not occur. Since the tendency for a sand to densify when dry is directly related to its tendency to develop excess pore pressure when saturated, it follows that pore pressure generation should be more fundamentally related to cyclic strains than cyclic stresses.

Characterization of Loading Conditions. In the cyclic strain approach, earthquake-induced loading is expressed in terms of cyclic strains. The time history of cyclic strain in an actual earthquake is transient and irregular. To compare the loading with laboratory-measured liquefaction resistance, it must be represented by an equivalent series of uniform strain cycles. The conversion procedure is analogous to that used in the cyclic stress approach.

The time history of cyclic shear strain may be computed in a ground response analysis. This is perhaps the weakest link in the cyclic strain approach since cyclic strains are considerably more difficult to predict accurately than cyclic stresses (Seed, 1980). Dobry et al. (1982) proposed a simplified method for estimating the amplitude of the uniform cyclic strain from the amplitude of the uniform cyclic stress of equation (9.2):

$$\gamma_{\text{cyc}} = 0.65 \frac{a_{\max}}{g} \frac{\sigma_v r_d}{G(\gamma_{\text{cyc}})} \quad (9.12)$$

where $G(\gamma_{\text{cyc}})$ is the shear modulus of the soil at $\gamma = \gamma_{\text{cyc}}$. Since γ_{cyc} influences both sides of equation (9.12), the value of $G(\gamma_{\text{cyc}})$ must be obtained iteratively from a measured G_{\max} profile and appropriate modulus reduction curves (Section 6.4.2.1). The equivalent number of strain cycles, N_{eq} , depends on the earthquake magnitude, and can be estimated from Figure 9.24.

Once γ_{cyc} is determined, it can be compared with the threshold shear strain, γ_t . If $\gamma_{\text{cyc}} < \gamma_t$, no pore pressure will be generated and, consequently, liquefaction cannot be initiated. The liquefaction hazard evaluation would end at that point. If $\gamma_{\text{cyc}} > \gamma_t$, liquefaction is possible and the liquefaction resistance of the soil must be evaluated.

Characterization of Liquefaction Resistance. The cyclic strain approach simplifies the interpretation of liquefaction resistance from laboratory tests. Experimental evidence indicates that factors that increase the cyclic stresses required to initiate

liquefaction (e.g., density, soil fabric, strain history, overconsolidation ratio, length of time under sustained pressure) also increase the shear modulus of the soil. Because these factors influence both τ_{cyc} and G similarly, their influence on the ratio $\gamma_{cyc} = \tau_{cyc}/G$ is much smaller. Consequently, they have little influence on pore pressure generation when interpreted in terms of cyclic strains. Dobry and Ladd (1980) provided striking evidence of this result; Figure 9.40 shows the pore pressure ratio produced by 10 strain-controlled cycles of loading on two different sands prepared by three different methods at three different initial effective confining pressures. The insensitivity of the generated pore pressure to factors other than cyclic strain amplitude illustrated in Figure 9.40 is a hallmark of the cyclic strain approach.

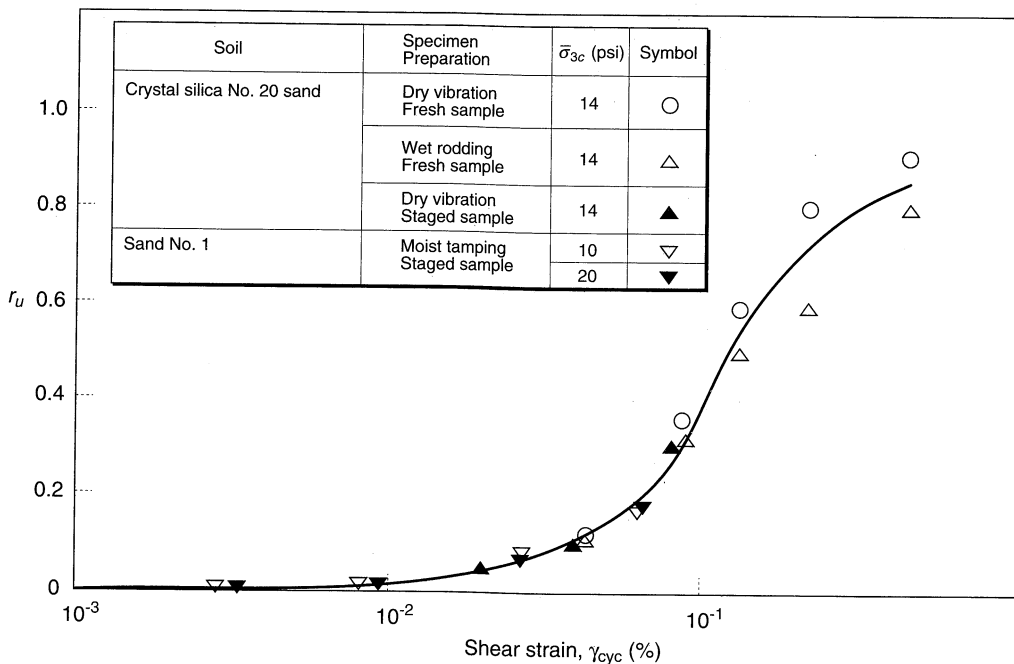


Figure 9.40 Measured pore pressure ratio after 10 cycles of loading in strain-controlled cyclic triaxial tests. After Dobry and Ladd, (1980). Discussion, *Journal of the Geotechnical Engineering Division*, Vol. 106, No. GT6. Reprinted by permission of ASCE.

Dobry et al. (1984) developed an innovative axial/torsional triaxial test called the CyT-CAU test for measurement of liquefaction resistance. In this test a solid cylindrical specimen is anisotropically consolidated under a *stress-controlled* static deviator stress. Cyclic strains are then imposed under undrained conditions by *strain-controlled* cyclic torsion while the stress-controlled deviator stress remains constant. The cyclic shear strains induce excess pore pressure in the specimen. If the effective stress conditions reach the FLS and the steady-state strength is less than the static shear stress, flow liquefaction will occur. This test closely models the behavior of soils that experience flow liquefaction

in the field: excess pore pressures are generated by cyclic shear strains, but flow failure is driven by static shear stresses.

Vasquez-Herrera and Dobry (1988) used the CyT- $\overline{\text{CAU}}$ test to investigate the generation of excess pore pressure and initiation of flow liquefaction. Confirming the existence of a FLS for several sands, Vasquez-Herrera and Dobry also observed that the excess pore pressure required to trigger liquefaction decreased with increasing initial principal effective stress ratio (see Figure 9.20), and a corresponding decrease in the number of strain cycles required to trigger liquefaction (Figure 9.41). The cyclic strain amplitude required to trigger liquefaction in N_{eq} cycles can be expressed in the form

$$\gamma_{cyc} = 0.01 + \left[\frac{r_{u,t}}{\alpha N_{eq}(2 - r_{u,t})} \right]^{1/\beta} \quad (9.13)$$

where α and β are experimentally determined functions of K_c used to characterize liquefaction resistance in the cyclic strain approach. The rate at which excess pore pressures develop is also influenced by K_c ; normalized pore pressures increase more quickly in the first cycles for specimens at lower K_c values (Figure 9.42).

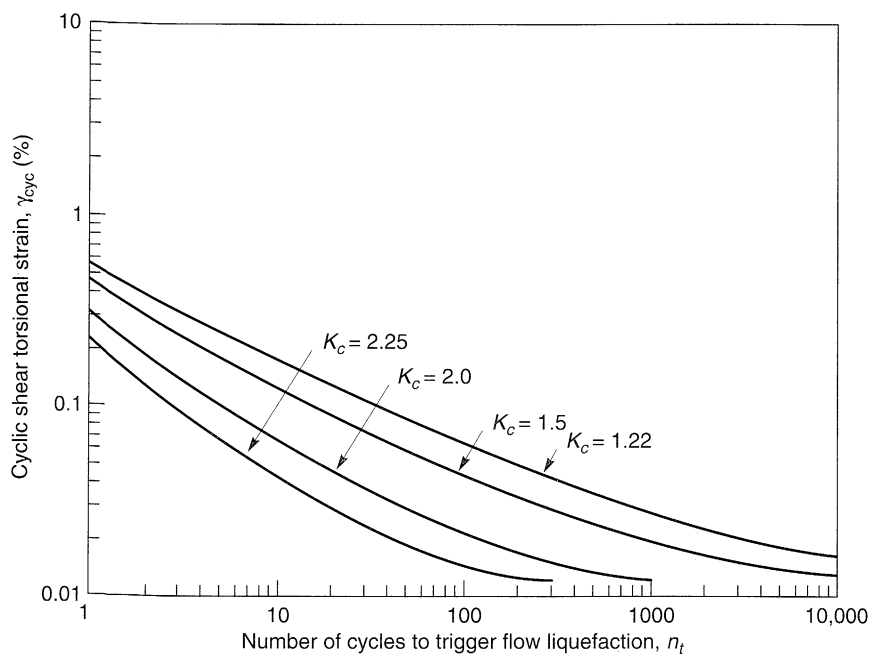


Figure 9.41 Liquefaction resistance curves for a sand obtained from an actual liquefaction failure. For this sand, $\alpha = 4.78$ to $1.91K_c$ and $\beta = 2.96$ to $0.78K_c$. Note the significant reduction in liquefaction resistance with increasing level of initial shear stress. (After Vasquez-Herrera and Dobry, 1988.)

Evaluation of Liquefaction Potential. Liquefaction potential may be evaluated in the cyclic strain approach in a manner similar to that used in the cyclic stress approach. The cyclic loading imposed by the earthquake, characterized by the amplitude of

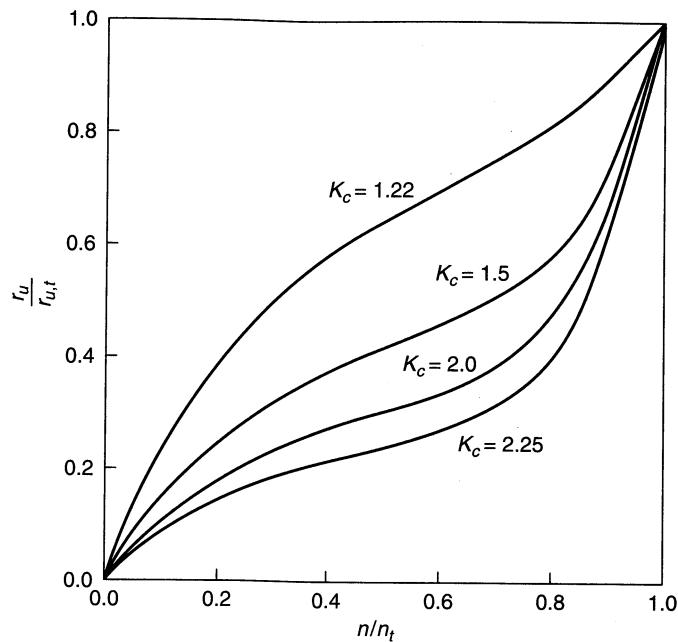


Figure 9.42 Normalized rate of pore pressure generation for sands subjected to different levels of initial shear stress. (After Vasquez-Herrera and Dobry, 1988.)

a series of N_{eq} uniform strain cycles, is compared with the liquefaction resistance, which is expressed in terms of the cyclic strain amplitude required to initiate liquefaction in the same number of cycles. Liquefaction can be expected at depths where the cyclic loading exceeds the liquefaction resistance (Figure 9.43). Since loading and resistance are characterized in terms of strains rather than stresses, the cyclic strain approach does not yield a factor of safety against liquefaction.

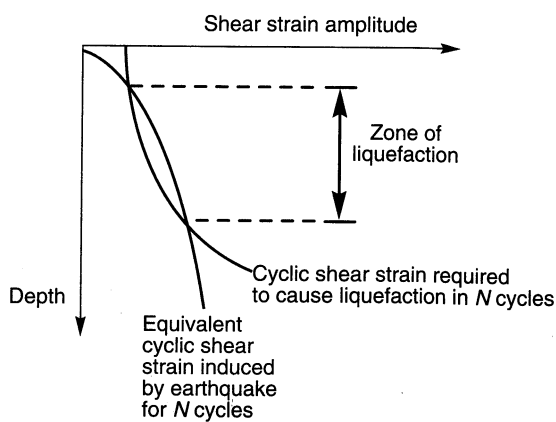


Figure 9.43 Process by which the zone of liquefaction is identified in the cyclic strain approach.

The primary advantage of the cyclic strain approach derives from the strong relationship between pore pressure generation and cyclic strain amplitude. For a given soil, excess pore pressure can be predicted more accurately from cyclic strains than from cyclic stresses. However, cyclic strains are considerably more difficult to predict accurately than cyclic stresses. The cyclic strain approach is not used as commonly as the cyclic stress approach in geotechnical earthquake engineering practice.

9.5.3.3 Other Approaches to the Initiation of Liquefaction

Although the cyclic stress and cyclic strain approaches are the most commonly used in geotechnical earthquake engineering practice, other approaches have also been developed. Two that offer considerable promise are the *dissipated energy approach* and the *effective stress-based response analysis approach*. As these approaches are refined, and as additional data with which to calibrate them become available, their use is likely to increase.

Energy Dissipation Approach. The use of dissipated energy as a measure of liquefaction resistance offers a number of advantages; it is related to both cyclic stresses and cyclic strains, and it can be related to inherently stochastic earthquake ground motions in a way that methods based on peak ground motion parameters alone cannot, it is a scalar quantity, and it can be related to fundamental earthquake parameters.

The densification of dry soil involves rearrangement of grains and hence the expenditure of energy. As a cyclically loaded dry soil densifies and approaches its minimum void ratio, the amount of energy required to rearrange individual soil grains increases. For a saturated soil, however, the tendency for densification causes the pore pressure to increase and the interparticle contact forces to decrease. As these contact forces decrease, the amount of energy needed to rearrange soil grains decreases. By combining these observations, Nemat-Nasser and Shokooh (1979) developed a simple, unified theory that related densification under drained conditions and pore pressure generation under undrained conditions to dissipated energy. Others have since attempted to characterize the relationship between excess pore pressure and dissipated energy experimentally (e.g., Simcock et al., 1983; Law et al., 1990; Figueroa and Dahisaria, 1991). Although some of the data are quite scattered, the excess pore pressure can be predicted by a relationship of the form

$$\frac{\Delta u}{\sigma'_{v0}} = \alpha W_N^\beta \quad (9.14)$$

where W_N is a dimensionless energy term (Law et al., 1990) and α and β are coefficients determined from laboratory tests.

Davis and Berrill (1982) demonstrated the potential for using energy to relate liquefaction behavior to fundamental earthquake parameters such as magnitude and distance. By combining an estimate of the energy content of seismic waves at a distance R from an earthquake of magnitude M with a simple energy dissipation function calibrated by experimental results and field observations of liquefaction behavior, an expression for excess pore pressure was developed.

$$\Delta u = \frac{450}{R^2 N_1^2 \sqrt{\sigma'_{v0}}} 10^{1.5M} \quad (9.15)$$

where R is in meters, N_1 is the SPT resistance corrected to an effective overburden pressure of 1 ton/ft² (96 kPa), and Δu and σ'_{v0} are in kPa. Law et al. (1990) used energy principles to develop the following criterion for liquefaction failure in sands:

$$\frac{10^{1.5M}}{2.28 \times 10^{-10} N_1^{11.5} R^{4.3}} \geq 1.0 \quad (9.16)$$

where R is the hypocentral distance in kilometers.

Effective Stress-Based Response Analysis Approach. Stress-strain modeling of soil behavior has been a subject of intense research activity for many years, and the task of replicating the complex behavior of potentially liquefiable soils with simple constitutive models has proven challenging. As discussed in Section 6.4, the nonlinear stress-strain behavior of soils can be described by cyclic nonlinear stress-strain models and by advanced constitutive models.

Cyclic nonlinear stress-strain models (Section 6.4.3) use an empirical backbone curve and a series of unloading-reloading rules that govern cyclic behavior. Pore pressure prediction is accomplished by pore pressure models (e.g., Martin et al., 1975; Ishihara and Towhata, 1980; Finn and Bhatia, 1981) that can predict the generation of pore pressure under irregular cyclic loading conditions. The computed pore pressure is used to degrade, or soften, the backbone curve as the effective stress (and soil stiffness) decreases.

In the Martin et al. (1975) model, for example, the pore pressure generated in an increment of undrained loading is related to the volumetric strain that would have occurred in the same loading increment under drained conditions by

$$\Delta u = \bar{E}_r \Delta \epsilon_{vd} \quad (9.17)$$

where \bar{E}_r is the rebound modulus and $\Delta \epsilon_{vd}$ is the incremental volumetric strain under drained conditions. The rebound modulus can be expressed as

$$\bar{E}_r = \frac{(\sigma'_v)^{1-m}}{m K_2 (\sigma'_{v0})^{n-m}} \quad (9.18)$$

where σ'_v and σ'_{v0} are the current and initial vertical effective stresses and m , n , and K_2 are experimentally determined from a rebound test in a consolidometer. The incremental volumetric strain is computed as

$$\Delta \epsilon_{vd} = C_1(\gamma - C_2 \epsilon_{vd}) + \frac{C_3 \epsilon_{vd}^2}{\gamma + C_4 \epsilon_{vd}} \quad (9.19)$$

where γ and ϵ_{vd} are the cyclic shear and volumetric strains, respectively, and C_1-C_4 are constants determined from the results of drained cyclic simple shear tests. Martin et al. (1981) developed a procedure for estimation of these constants without laboratory test results. When incorporated into nonlinear ground response analyses, cyclic nonlinear and pore pressure models allow computation of the generation, redistribution, and dissipation of pore pressures. Hence the effective stress conditions throughout a soil deposit can be monitored throughout and even after an earthquake to evaluate liquefaction hazards.

Advanced constitutive models (Section 6.4.4) provide a more rigorous approach to prediction of soil behavior under a wide variety of loading conditions. Such models describe the increments of volumetric and deviatoric strain produced by increments of volumetric and deviatoric stress. By setting the incremental volumetric strain to zero to represent undrained conditions, changes in effective stresses can be computed. Such models can be incorporated into nonlinear ground response and dynamic response analyses. The one-dimensional nonlinear ground response program DYNA1D (Prevost, 1989), for example, uses a nested yield surface constitutive model to account for nonlinear, anisotropic, hysteretic soil behavior to predict the generation, redistribution, and dissipation of excess pore pressure during and after earthquake shaking.

Probabilistic Approach. There are many potential sources of uncertainty in both the loading and resistance aspects of liquefaction problems, and probabilistic approaches have been developed to deal with them. Uncertainties in cyclic loading can be evaluated using the standard probabilistic seismic hazard analyses described in Section 4.4. Uncertainties in liquefaction resistance can be treated in one of two general ways.

One group of methods is based on probabilistic characterization of the parameters shown by laboratory tests to influence pore pressure generation. Haldar and Tang (1979) characterized uncertainty in the parameters of the simplified cyclic stress approach described in Section 9.5.3.1. Fardis and Veneziano (1982) used a similar approach with total stress and effective stress models. Chameau and Clough (1983) described pore pressure generation probabilistically using experimental data and an effective stress model. Each of these methods can compute the probability of liquefaction due to a particular set of loading conditions. Their accuracy depends on the accuracy of the underlying liquefaction/pore pressure model and on how accurately the uncertainty of the model parameters can be determined.

An alternative group of methods are based on in situ test-based characterization of liquefaction resistance (e.g., Christian and Swiger, 1975; Yegian and Whitman, 1978; Veneziano and Liao, 1984; Liao et al., 1988). These methods use various statistical classification and regression analyses to assign probabilities of liquefaction to different combinations of loading and resistance parameters. Liao et al. (1988), for example, analyzed 278 case studies to produce the following expression for the probability of liquefaction:

$$P_L = \frac{1}{1 + \exp [-(\beta_0 + \beta_1 \ln(\text{CSR}) + \beta_2 (N_1)_{60})]} \quad (9.20)$$

where the parameters β_0 - β_2 are shown in Table 9-3. Liquefaction probability curves for the clean and silty sand cases are shown graphically in Figure 9.44.

Example 9.5

Use the approach of Liao et al. (1988) to estimate the probabilities of liquefaction at the site described in Example 9.4.

Solution The σ'_{v0} and τ_{cyc} data from Example 9.4 can be used to compute the cyclic stress ratio (column 4 below). Using this cyclic stress ratio and the $(N_1)_{60}$ values evaluated originally in Example 6.6, probabilities of liquefaction at each depth in the soil profile using equation (9.20) (with the clean sand regression coefficients).

Although the results of this analysis are expressed in terms of a probability of liquefaction rather than a factor of safety against liquefaction (as in Example 9.4), both indicate that

D (m)	τ_{cyc} (kPa)	σ'_{vo} (kPa)	CSR	$(N_1)_{60}$	P_L
1.2	2.28	22.1	0.103	17.3	—
2.2	4.38	36.4	0.120	7.9	0.403
3.2	6.53	47.3	0.138	5.1	0.835
4.2	8.66	58.8	0.147	4.6	0.903
5.2	10.8	70.4	0.153	7.0	0.823
6.2	12.8	82.0	0.156	11.7	0.469
7.2	14.8	93.6	0.158	14.6	0.218
8.2	16.7	105.3	0.159	13.7	0.293
9.2	18.5	116.8	0.158	15.2	0.180
10.2	20.2	128.4	0.157	9.3	0.687
11.2	21.7	140.0	0.155	22.8	0.009
12.2	23.1	151.5	0.152	12.4	0.342
13.2	24.1	163.1	0.148	10.1	0.522
14.2	25.3	174.7	0.145	9.8	0.519
15.2	25.6	186.3	0.137	20.7	0.010
16.2	26.3	197.9	0.133	22.5	0.003
17.2	26.6	209.4	0.127	4.1	0.815
18.2	26.9	221.1	0.122	4.7	0.729
19.2	27.1	232.7	0.116	3.1	0.785
20.2	27.8	244.3	0.114	28.5	0.0001

Table 9-3 Regression Parameters for Calculating Probability of Liquefaction

Data ^a	Number of Cases	β_0	β_1	β_2
All cases	278	10.167	4.1933	-0.24375
Clean sand cases only	182	16.447	6.4603	-0.39760
Silty sand cases only	96	6.4831	2.6854	-0.18190

Source: After Liao et al. (1988).

^a A fines content of 12% is used as the boundary between clean and silty sands.

extensive liquefaction would have been expected at this particular site in the 1964 Niigata earthquake. Widespread liquefaction was indeed observed at sites with soil conditions similar to these in that earthquake.

9.6 EFFECTS OF LIQUEFACTION

Liquefaction phenomena can affect buildings, bridges, buried pipelines, and other constructed facilities in many different ways. Liquefaction can also influence the nature of ground surface motions. Flow liquefaction can produce massive flow slides and contribute to the sinking or tilting of heavy structures, the floating of light buried structures, and to the failure of retaining structures. Cyclic mobility can cause slumping of slopes, settlement of

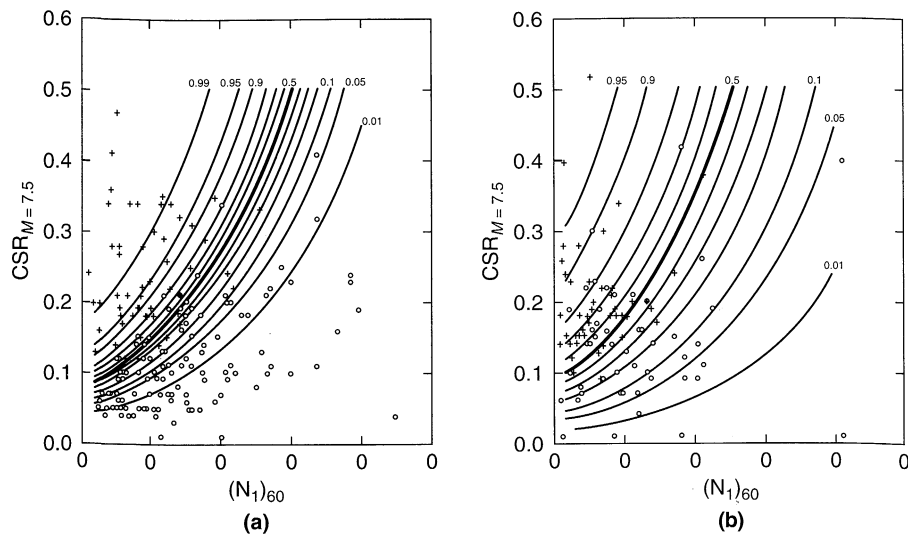


Figure 9.44 Contours of equal probability of liquefaction for (a) clean sand (less than 12% fines), and (b) silty sands (greater than 12% fines). (After Liao et al., 1988. Regression models for evaluating liquefaction probability, *Journal of Geotechnical Engineering*, Vol. 114, No. 4. Reprinted by permission of ASCE.)

buildings, lateral spreading, and retaining wall failure. Substantial ground oscillation, ground surface settlement, sand boils, and postearthquake stability failures can develop at level-ground sites.

The effects of liquefaction can be better appreciated by studying well-documented case histories. In addition to the regularly published journals that deal with geotechnical earthquake engineering, an excellent compilation of case histories can be found in Hamada and O'Rourke (1992).

9.6.1 Alteration of Ground Motion

The influence of the shear modulus and damping characteristics of soils on ground response is well established. Several examples of the effects of these characteristics presented in Chapter 8 showed that soft soil deposits respond differently than stiff soil deposits to the same motion.

The development of positive excess pore pressures causes soil stiffness to decrease during an earthquake. A deposit of liquefiable soil that is relatively stiff at the beginning of the earthquake may be much softer by the end of the motion. As a result, the amplitude and frequency content of the surface motion may change considerably throughout the earthquake. In the most extreme case, the development of very high pore pressures can cause the stiffness (and strength) of even a thin layer to be so low that the high-frequency components of a bedrock motion cannot be transmitted to the ground surface. An example of this effect is shown in Figure 9.45. It is not difficult to identify the point at which liquefaction-induced reduction of the stiffness of the underlying soil took place—the acceleration amplitude and frequency content both changed dramatically about 7 sec after the motion began. The fact

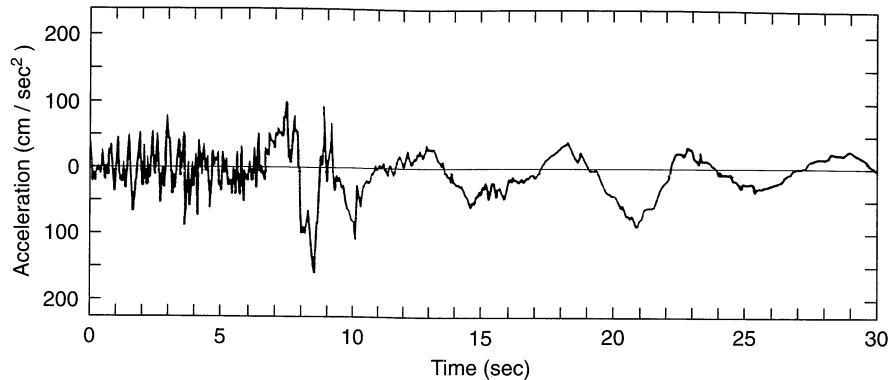


Figure 9.45 Accelerogram from site near apartment building resting on liquefiable soil (shown in Figure 1.6) in 1964 Niigata earthquake. (After Aki, 1988.)

that surface acceleration amplitudes decrease when pore pressures become large does not mean that damage potential is necessarily reduced because low acceleration amplitudes at low frequencies can still produce large displacements. These displacements may be of particular concern for buried structures, utilities, and structures supported on pile foundations that extend through liquefied soils (Figure 9.46).

The occurrence of liquefaction at depth beneath a flat ground surface can decouple the liquefied soils from the surficial soils and produce large, transient ground oscillations. The surficial soils are often broken into blocks (Figure 9.47) separated by fissures that can open and close during the earthquake. Ground waves with amplitudes of up to several feet have been observed during ground oscillation, but permanent displacements are usually small.

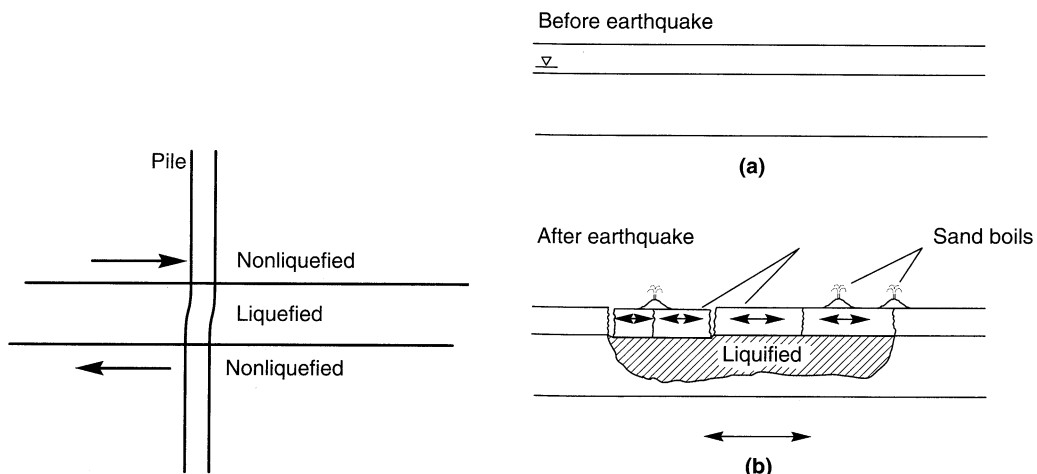


Figure 9.46 Potential effects of subsurface liquefaction on pile foundations. The large strains that may develop in a liquefied layer can induce high bending moments in piles that extend through it.

Figure 9.47 Ground oscillation (a) before and (b) after earthquake. (After Youd, 1984b.)

Youd (1993) attributed to ground oscillation most of the chaotic ground movements that fractured and buckled pavements in the Marina District of San Francisco during the 1989 Loma Prieta earthquake. Prediction of the amplitude of ground oscillation at a particular site is very difficult; even detailed nonlinear ground response analyses can provide only crude estimates.

9.6.2 Development of Sand Boils

Liquefaction is often accompanied by the development of sand boils. During and following earthquake shaking, seismically induced excess pore pressures are dissipated predominantly by the upward flow of porewater. This flow produces upward-acting forces on soil particles [these forces can loosen the upper portion of the deposit and leave it in a state susceptible to liquefaction in a future earthquake (Youd, 1984a)]. If the hydraulic gradient driving the flow reaches a critical value, the vertical effective stress will drop to zero and the soil will be in a *quick* condition. In such cases, the water velocities may be sufficient to carry soil particles to the surface. In the field, soil conditions are rarely uniform so the escaping porewater tends to flow at high velocity through localized cracks or channels. Sand particles can be carried through these channels and ejected at the ground surface to form sand boils. The development of sand boils is a complicated and somewhat random process; it depends on the magnitude of the excess pore pressure; the thickness, density, and depth of the zone of excess pore pressure; and the thickness, permeability, and intactness of any soil layers that overlay the zone of high excess pore pressure. There are pitfalls to reliance upon the presence of sand boils for evidence of liquefaction-related phenomena; liquefaction at great depths or in thin layers may not produce sand boils, but lower excess pore pressures in thick layers at shallow depths may. Also, the low permeability of silty sand may prevent porewater from flowing quickly enough to produce sand boils, even if high excess pore pressures develop. Ishihara (1985) examined the soil conditions associated with various liquefaction-related damage reports from the 1983 Nihonkai-chubu earthquake ($M = 7.7$) and 1976 Tangshan ($M = 7.7$) earthquakes (Gao et al. 1983) and produced estimates of the thickness of the overlying layer required to prevent level-ground liquefaction-related damage (Figure 9.48). These estimates have been validated against a much larger database for sites not susceptible to ground oscillation or lateral spreading, but are insufficient for predicting damage at other sites (Youd and Garris, 1995).

Sand boils are of little engineering significance by themselves, but they are useful indicators of high excess pore pressure generation. Shaking table (Liu and Qiao, 1984) and centrifuge (Fiegel and Kutter, 1992) tests have shown that porewater draining from the voids of the loose layers can accumulate beneath the less pervious layers and form *water interlayers* (Figure 9.49). Sand boils can develop when the water interlayers break through to the ground surface. Some redistribution of soil grains is also likely to accompany the formation of water interlayers; specifically the sand immediately beneath the water interlayer may be loosened by the upward flow of water toward the interlayer. If such conditions develop beneath an inclined ground surface, the presence of the water interlayer and the reduced steady state strength of the loosened sand immediately beneath it can contribute to large flow deformations (Section 9.6.4).

Ground surface settlement results from the volumetric strain that develops as seismically induced pore pressures dissipate. The phenomenon is illustrated for an element of soil

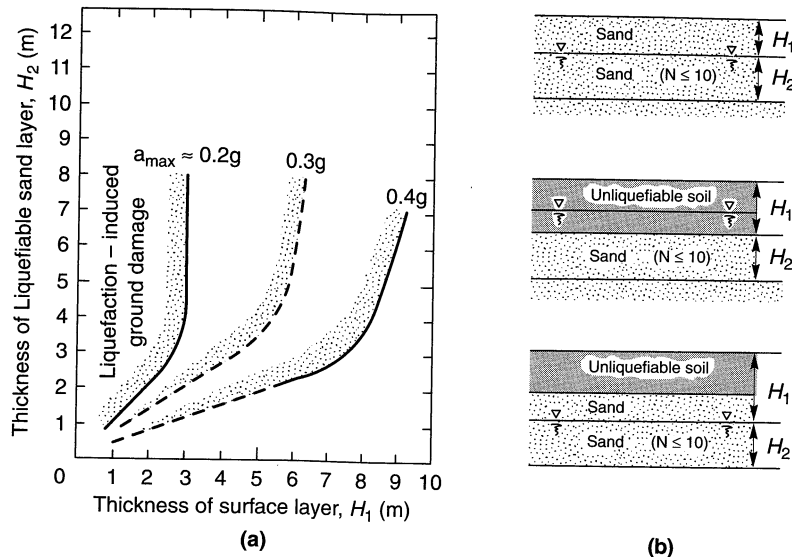


Figure 9.48 (a) Relationship between thickness of liquefiable layer and thickness of overlying layer at sites for which surface manifestation of level-ground liquefaction has been observed, and (b) guides to evaluation of respective layer thicknesses. (After Ishihara, 1985; used by permission of Kluwer Academic Publishers.)

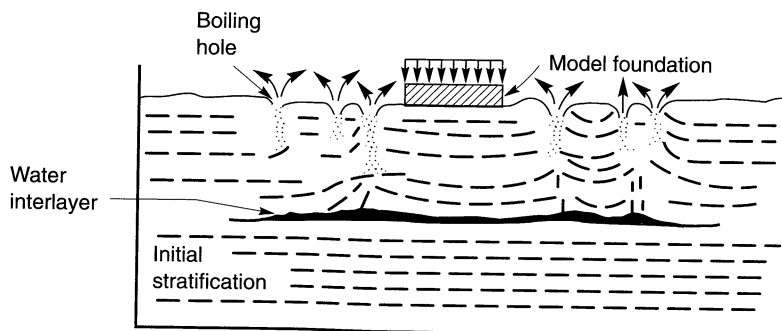


Figure 9.49 Formation of water interlayers in shaking table tests of Liu and Qiao (1984).

in Figure 9.50. Initially, the element is in drained equilibrium (zero excess pore pressure) at point A. Earthquake shaking causes excess pore pressure to build up under undrained conditions, thereby reducing the effective stress to that shown at point B. The excess pore pressure produces a hydraulic gradient that drives the porewater out of the voids. The flow of water reduces the hydraulic gradient until the excess pore pressure has completely dissipated (point C). As the water flows from the voids, the volume of the element decreases. As Figure 9.50 clearly illustrates, the magnitude of the volume change increases with the magnitude of the seismically induced excess pore pressure. Even small excess pore pressures,

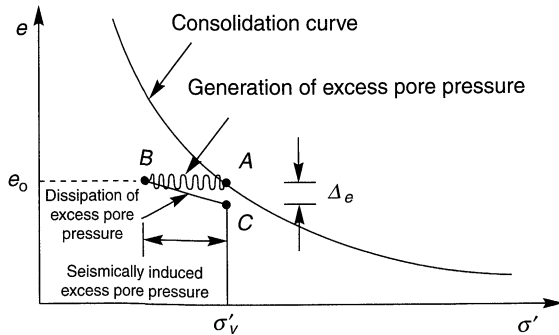


Figure 9.50 Process of earthquake-induced settlement from dissipation of seismically induced excess pore pressure.

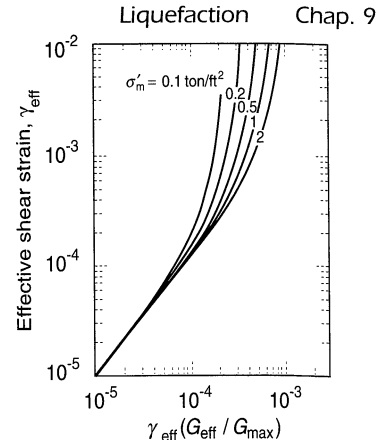


Figure 9.51 Plot for determination of effective cyclic shear strain in sand deposits. (After Tokimatsu and Seed, 1987. Evaluation of settlements in sand due to earthquake shaking, *Journal of Geotechnical Engineering*, Vol. 113, No. 8. Reprinted by permission of ASCE.)

which may not be sufficient to produce flow liquefaction or cyclic mobility, can produce some postearthquake settlement.

9.6.3 Settlement

The tendency of sands to densify when subjected to earthquake shaking is well documented. Subsurface densification is manifested at the ground surface in the form of settlement. Earthquake-induced settlement frequently causes distress to structures supported on shallow foundations, damage to utilities that serve pile-supported structures, and damage to life-lines that are commonly buried at shallow depths.

Dry sands densify very quickly; settlement of a dry sand deposit is usually complete by the end of an earthquake. The settlement of a saturated sand deposit requires more time—settlement can occur only as earthquake-induced pore pressures dissipate. The time required for this settlement to occur depends on the permeability and compressibility of the soil, and on the length of the drainage path—it can range from a few minutes up to about a day.

Estimation of earthquake-induced settlements of sands is difficult. Errors of 25 to 50% are common in static settlement predictions; even less accuracy should be expected for the more complicated case of seismic loading. Nevertheless, the following procedures have been shown to produce results that agree reasonably well with many cases of observed field behavior.

9.6.3.1 Settlement of Dry Sands

The densification of dry sands subjected to earthquake loading depends on the density of the sand, the amplitude of the cyclic shear strain induced in the sand, and the number of cycles of shear strain applied during the earthquake (Silver and Seed, 1971). Settlements

can be estimated using detailed ground response analyses with corrections for the effects of multidirectional shaking (Seed and Silver, 1972; Pyke et al., 1975), or by simplified procedures (Tokimatsu and Seed, 1987). In the simplified procedure, the effective cyclic shear strain, γ_{cyc} , is estimated by a procedure similar to that proposed for the cyclic strain approach to the initiation of liquefaction (Section 9.5.3.2):

$$\gamma_{cyc} = 0.65 \frac{a_{\max}}{g} \frac{\sigma_v r_d}{G(\gamma_{cyc})} \quad (9.21)$$

Since the shear modulus varies with γ_{cyc} , several iterations may be required to calculate a value of γ_{cyc} that is consistent with the shear modulus. Figure 9.51 may be used to estimate γ_{cyc} when G_{\max} is known. The effective cyclic shear strain can then be used, along with the relative density or SPT resistance of the sand, to estimate the volumetric strain due to compaction, ϵ_c , from Figure 9.52. The data from Figure 9.52 are based on 15 cycles of strain, which corresponds to a $M = 7.5$ earthquake. For earthquakes of other magnitudes, the volumetric strain due to compaction can be determined from the volumetric strain ratio presented in Table 9-4.

Following the experimental results of Pyke et al. (1975), the effect of multidirectional shaking is accounted for by doubling $\epsilon_{c,M}$. Pyke et al. (1975) also suggested that the vertical component of ground motion could cause an additional 50% increase in settlement (above that caused by the horizontal components); the effect of vertical motion is not explicitly accounted for in the simplified procedure of Tokimatsu and Seed (1987). Since the stiffness, density, and shear strain amplitudes typically vary with depth, a given soil deposit is usually divided into sublayers, with the settlement of each sublayer computed and summed to obtain the total ground surface settlement.

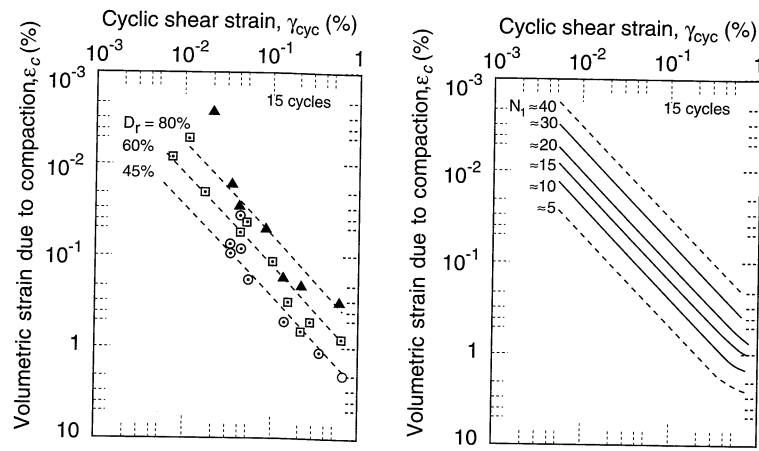


Figure 9.52 Relationship between volumetric shear strain, $\epsilon_{c,M=7.5}$ and cyclic shear strain, γ_{cyc} , in terms of (a) relative density and (b) standard penetration resistance. (After Tokimatsu and Seed, 1987. Evaluation of settlements in sand due to earthquake shaking, *Journal of Geotechnical Engineering*, Vol. 113, No. 8. Reprinted by permission of ASCE.)

Table 9-4 Influence of Earthquake Magnitude on Volumetric Strain for Dry Sands

Earthquake Magnitude	$\frac{\varepsilon_{c,M}}{\varepsilon_{c,M=7.5}}$
5 $\frac{1}{4}$	0.4
6	0.6
6 $\frac{3}{4}$	0.85
7 $\frac{1}{2}$	1.0
8 $\frac{1}{2}$	1.25

Source: After Tokimatsu and Seed, 1987

Example 9.6

The settlement of a 50-ft-thick deposit of loose sand ($D_r = 45\%$) with an average corrected SPT resistance of 9 was estimated for an earthquake of magnitude 6.6 by Seed and Silver (1972) and Tokimatsu and Seed (1987).

Solution The deposit can be divided into a series of layers; six layers are used in this example as illustrated in tabular form below. Based on the given $(N_1)_{60}$ values, G_{\max} can be estimated using the relationship of Ohto and Goto (1976) given in Table 6-6 (column 5 below). This allows estimation of γ_{cyc} (column 6 below) using Figure 9.51. The resulting volumetric strain (for a magnitude 7.5 earthquake) can then be obtained from Figure 9.52 (column 7 below). Using Table 9-5, the volumetric strain in a $M = 6.6$ earthquake should be about 80% of that in a magnitude 7.5 earthquake (column 8 below). Accounting for multidirectional shaking, the volumetric strains are then doubled (column 9 below). Finally, the settlement of each layer can be estimated as the product of the volumetric strain and the thickness of the layer (column 10 below).

(1) Layer Number	(2) Thickness (ft)	(3) D_r (%)	(4) $(N_1)_{60}$	(5) G_{\max} (ksf)	(6) γ_{cyc}	(7) $\varepsilon_{c,M=7.5}$ (%)	(8) $\varepsilon_{c,M=6.6}$ (%)	(9) $2\varepsilon_{c,M=6.6}$ (%)	(10) Settlement (in.)
1	5	45	9	520	0.0005	0.14	0.11	0.22	0.13
2	5	45	9	900	0.0008	0.23	0.18	0.36	0.22
3	10	45	9	1270	0.0012	0.35	0.28	0.56	0.67
4	10	45	9	1630	0.0014	0.40	0.32	0.64	0.77
5	10	45	9	1930	0.0015	0.45	0.36	0.72	0.86
6	10	45	9	2190	0.0013	0.38	0.30	0.60	0.72 3.37

These settlements are consistent with those that were observed at a site with these conditions in the 1971 San Fernando earthquake (Tokimatsu and Seed, 1987). The number of significant figures in this example is intended to facilitate understanding of the calculations, not to suggest that the results are accurate to 0.01 in.

9.6.3.2 Settlement of Saturated Sands

The postearthquake densification of saturated sand is influenced by the density of the sand, the maximum shear strain induced in the sand, and the amount of excess pore pressure

generated by the earthquake. Laboratory experiments have shown that the volumetric strain after initial liquefaction varies with relative density and maximum shear strain. Tokimatsu and Seed (1987) used a correlation between $(N_1)_{60}$ and relative density and an estimate of the shear strain potential of liquefied soil from $(N_1)_{60}$ and cyclic stress ratio (Seed et al., 1984) to produce a chart (Figure 9.53) that allows the volumetric strain after liquefaction in a $M = 7.5$ earthquake to be estimated directly from the cyclic stress ratio and SPT resistance. For earthquakes of other magnitudes, an equivalent cyclic stress ratio, CSR_M , can be determined from equation (9.2) and Table 9-2. Note that the volumetric strain after liquefaction can be as high as 2 to 3% for loose to medium dense sands and higher for very loose sands; a 5-m thick (16 ft) layer of very loose sand produced settlements of 50 to 70 cm (20 to 28 in.) in Hachinohe, Japan following the Tokachioki earthquake ($M = 7.9$) in 1968 (Ohsaki, 1970); settlements of 50 to 100 cm (20 to 39 in.) were observed on Port Island and Rokko Island in Kobe, Japan following the 1995 Hyogo-ken Nanbu earthquake. If sand boils are produced, postearthquake settlements are likely to be irregular. The resulting differential movement can be damaging to structures, pavements, or pipelines on or near the ground surface.

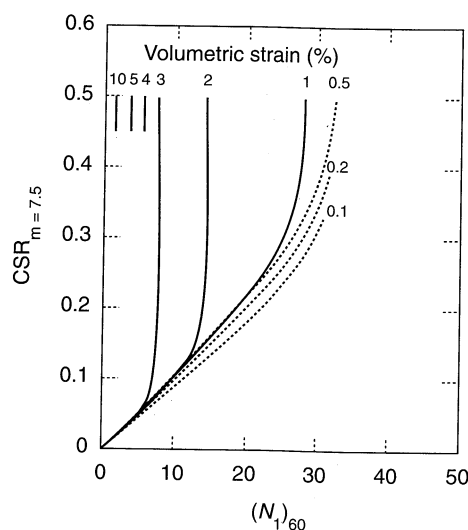


Figure 9.53 Chart for estimation of volumetric strain in saturated sands from cyclic stress ratio and standard penetration resistance. (After Tokimatsu and Seed, 1987. Evaluation of settlements in sand due to earthquake shaking, *Journal of Geotechnical Engineering*, Vol. 113, No. 8. Reprinted by permission of ASCE.)

Example 9.7

Significant settlement was observed in the Marina District of San Francisco following the 1989 Loma Prieta earthquake. Much of this settlement was determined to have resulted from densification of hydraulic fills that were placed to reclaim the area from San Francisco Bay in the 1990s. Subsurface conditions at one location in the Marina District are shown in Figure E9.7 (O'Rourke et al., 1991). Estimate the settlement that would have been expected at this location in the Loma Prieta earthquake. A peak acceleration of $0.20g$ was measured in the vicinity of the Marina District.

Solution The subsurface profile shows measured (uncorrected) SPT resistances. Assuming that the SPT resistances were measured using standard procedures ($E_m = 0.60E_{ff}$), corrected SPT resistances can be computed using equation (6.30) (column 4 below). The simplified procedure of Seed and Idriss (1971) can be used to estimate the cyclic stress ratio (column 5 below).

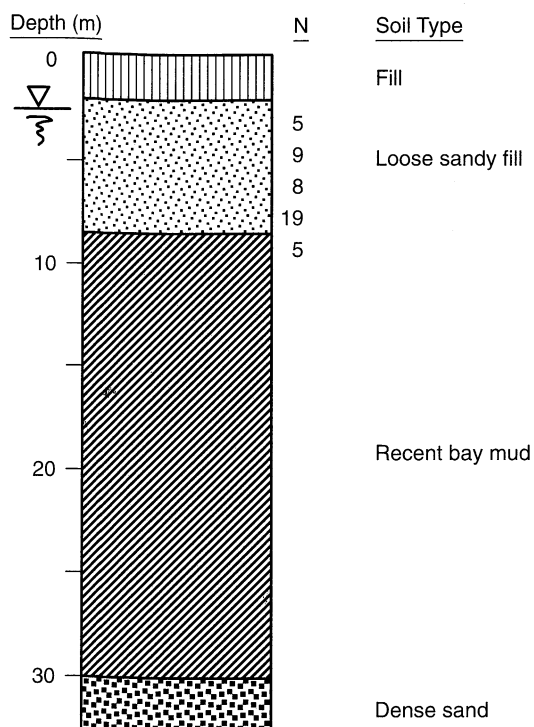


Figure E9.7

(1) Layer	(2) Depth Range (m)	(3) N	(4) $(N_1)_{60}$	(5) CSR	(6) ε_v (%)	(7) ΔH (m)
1	2.5–3.5	5	7.5	0.141	3.0	0.030
2	3.5–5.3	9	11.4	0.165	2.4	0.043
3	5.3–6.8	8	8.6	0.180	2.8	0.042
4	6.8–8.5	19	18.7	0.186	0.2	0.003
						0.118

The volumetric strain can then be estimated using Figure 9.53. The settlement of each layer is then computed as the product of the volumetric strain and the layer thickness.

The actual settlements in the vicinity of this site were on the order of 12 to 15 cm. Some of the actual settlements resulted from densification of the dry soil above the water table; that settlement is not accounted for in this example.

In an alternative approach, either the factor of safety against liquefaction [equation (9.14)] or the maximum cyclic shear strain, and the relative density, SPT resistance, or CPT tip resistance, can be used to estimate postliquefaction volumetric strain (Figure 9.54). Integration of these volumetric strains over the thickness of the liquefied layer produces the ground surface settlement.

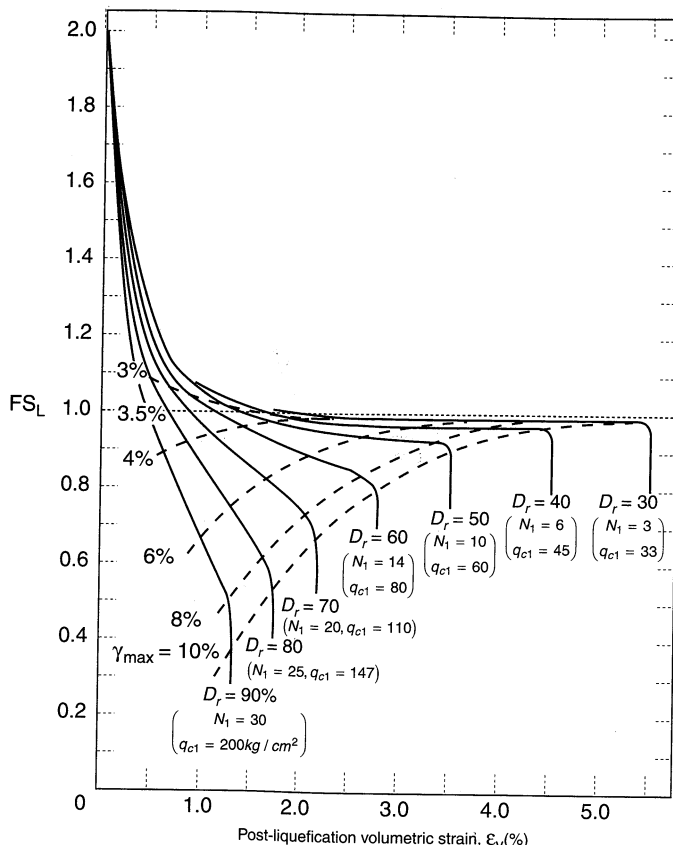


Figure 9.54 Chart for estimating postliquefaction volumetric strain of clean sand as function of factor of safety against liquefaction or maximum shear strain. (After Ishihara and Yoshimine, 1992; used by permission of JSSMFE.)

Example 9.8

Repeat Example 9.7 using the Ishihara–Yoshimine approach.

Solution The Ishihara–Yoshimine approach requires evaluation of the factor of safety against liquefaction. Using the $(N_1)_{60}$ values from Example 9.7 and Figure 9.31, the (magnitude corrected) critical stress ratio required to initiate liquefaction can be determined (column 4 below). Using the CSR values from Example 9.7 and equation (9.11), the factor of safety against liquefaction can be computed for each layer. Then the $(N_1)_{60}$ values must be converted to N_1 values [recall that Japanese SPT procedures typically transmit 20% more energy to the SPT sampler; hence $N_1 \approx 0.833(N_1)_{60}$]. Using the resulting values of and FS_L , Figure 9.54 can be used to estimate the volumetric strain in each layer (column 8 below). Again, the settlement of each layer (column 9 below) is given by the product of the volumetric strain and layer thickness.

The total settlement is calculated as 17.7 cm by the Ishihara–Yoshimine procedure. Hence the Tokimatsu–Seed and Ishihara–Yoshimine procedures both provided good estimates

(1) Layer	(2) Depth Range (m)	(3) $(N_1)_{60}$	(4) CSR_L	(5) CSR	(6) FS_L	(7) N_1	(8) ϵ_v (%)	(9) ΔH (m)
1	2.5–3.5	7.5	0.088	0.141	0.62	6.3	4.4	0.044
2	3.5–5.3	11.4	0.134	0.165	0.81	9.5	3.5	0.063
3	5.3–6.8	8.6	0.102	0.180	0.57	7.2	4.2	0.063
4	6.8–8.5	18.7	0.220	0.186	1.18	15.6	0.4	0.007 0.177

of the observed postearthquake settlement at this site. Ishihara (1993) illustrated the use of the Ishihara–Yoshimine procedure for a nearby site (with a smaller thickness of hydraulic fill) using CPT data; a settlement of 7.3 cm was predicted.

In many cases, strong ground motion produces excess pore pressures that are not sufficient to produce initial liquefaction. These pore pressures will dissipate, however, and may produce some volume change. Tokimatsu and Seed (1987) combined a relationship between normalized stress ratio, CSR/CSR_L , and pore pressure ratio (Tokimatsu and Yoshimi, 1983) and a relationship between pore pressure ratio and volumetric strain (Lee and Albaiza, 1974) to develop the relationship shown in Figure 9.55. Figure 9.55 can be used to estimate the volumetric strain for cases in which the maximum pore pressure ratio is less than 100%. Note that postearthquake volume changes are quite small unless the CSR is greater than 70 to 80% of that required to cause initial liquefaction ($r_u = 100\%$).

The rate at which settlement develops depends on the *reconsolidation* characteristics of the liquefied soil. Reconsolidation generally begins at the bottom of the liquefied soil (Florin and Ivanov, 1961; Heidari and James, 1982) and proceeds upward. Because effective stresses can vary over several orders of magnitude during reconsolidation, nonlinear consolidation models are required to predict settlement rates (Whitman et al., 1982; Scott, 1986).

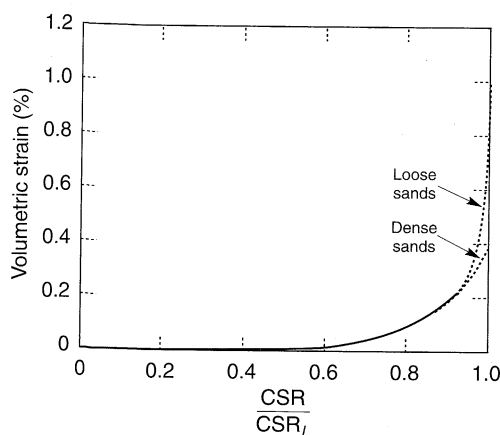


Figure 9.55 Postearthquake volumetric strains for pore pressure ratios less than 100%. (After Tokimatsu and Seed, 1987. Evaluation of settlements in sand due to earthquake shaking, *Journal of Geotechnical Engineering*, Vol. 113, No. 8. Reprinted by permission of ASCE.)

9.6.4 Instability

Liquefaction-induced instabilities are among the most damaging of all earthquake hazards. Their effects have been observed in the form of flow slides, lateral spreads, retaining wall

failures, and foundation failures in countless earthquakes throughout the world. Instability failures can be produced by different liquefaction phenomena, and it is not always clear exactly which is responsible for a given failure. All are strongly influenced, however, by the shear strength of the liquefied soil.

9.6.4.1 Shear Strength of Liquefied Soil

Instability occurs when the shear stresses required to maintain equilibrium of a soil deposit exceed the shear strength of that deposit. The soil then deforms until it reaches a configuration in which the shear stresses do not exceed the shear strength. The amount of deformation required to reach a stable configuration is strongly influenced by the difference between the shear stresses required for equilibrium and the shear strength of the liquefied soil. If the shear strength of the liquefied soil is only slightly lower than the shear stress required for equilibrium, permanent deformations are likely to be small. If the difference between the shear strength and shear stress is large, very large deformations may develop. Accurate evaluation of the effects of liquefaction-induced instability requires accurate estimation of the shear strength of the liquefied soil.

Three different approaches have been developed to estimate the shear strength of liquefied soils. One is based on a program of careful undisturbed sampling and laboratory testing. Another is based on in situ test parameters and interpretation of known liquefaction case histories. The third treats the shear strength of liquefied soil as a normalized strength.

Laboratory Testing Approach: Steady-State Strength. The steady-state strength (defined in Section 9.4.4.2) governs the behavior of liquefied soil. In concept, it is a function solely of the density of the soil, although some experimental studies suggest that it may be influenced by stress path and other factors. For many soils, the steady-state strength is extremely sensitive to density (i.e., small changes in density can result in large changes in steady-state strength).

If cohesionless soils could be sampled "perfectly" (i.e., without any disturbance whatsoever), the steady-state strength, S_{su} , of a given specimen could be measured in a single triaxial test by consolidating the specimen to the in situ stress conditions and then shearing it under undrained conditions following the most appropriate stress path. Unfortunately, the acts of sampling, transportation, handling, and consolidation cause changes in the density of a laboratory specimen by the time it is tested. Given the sensitivity of S_{su} to density, the steady-state strength of a laboratory specimen must be corrected to correspond to the in situ void ratio. Poulos et al. (1985) proposed the following four-step procedure for measurement of in situ steady-state strength. The procedure is illustrated graphically in Figure 9.56.

1. Determine the insitu void ratio from one or more "undisturbed" specimens. This is the most critical, and most difficult, step in the entire procedure. Poulos et al. (1985) suggested three satisfactory sampling procedures: (1) fixed-piston sampling, (2) freezing of the ground and coring, and (3) sampling in test pits. The importance of careful sampling to the success of this procedure cannot be overemphasized.
2. Locate the steady-state line using reconstituted specimens. Since the slope of the SSL is chiefly influenced by grain shape, the SSL from a series of reconstituted specimens should have the same slope as that of the in situ soil. Tests on five or six specimens consolidated to initial states well above the SSL (to ensure contractive behavior) are suggested.

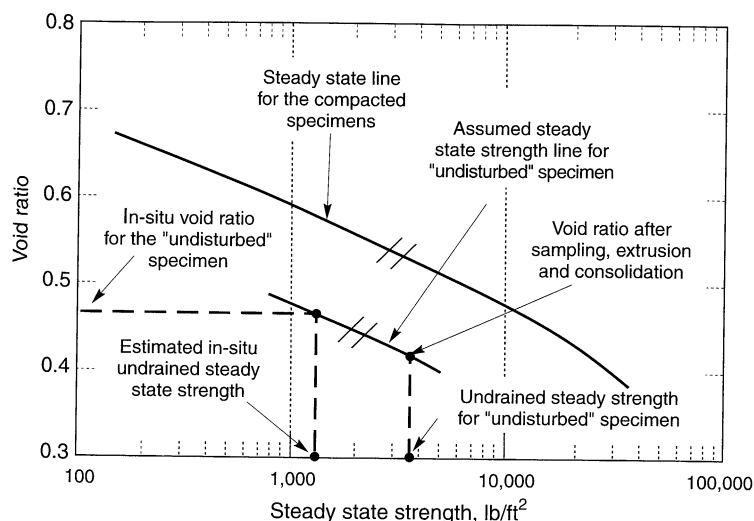


Figure 9.56 Procedure for estimating steady-state shear strength. (After Poulos et al., 1985. Liquefaction evaluation procedure, *Journal of Geotechnical Engineering*, Vol. III, No. 6. Reprinted by permission of ASCE.)

3. Determine the steady-state strength of an undisturbed specimen. A consolidated-undrained triaxial test is performed on a specimen obtained from step 1. To ensure that the steady state is reached at reasonable strain levels, consolidation to elevated effective confining pressures (again, to produce contractive behavior) is suggested.
4. Correct the measured steady state strength to the in situ void ratio. By assuming that the SSL of the undisturbed specimen has the same slope as that of the reconstituted specimens, the in situ steady-state strength can be found by projecting a line through the point describing the undisturbed specimen (from step 3) parallel to the SSL (from step 2) and back to the in situ void ratio (from step 1). The resulting strength is taken as the in situ steady-state strength.

The corrected in situ steady-state strength can then be used to evaluate potential liquefaction hazards. Although this procedure is rational, the user must remain aware of the sensitivity of the results to uncertainties in the input parameters, particularly the in situ void ratio. Kramer (1989) presented a procedure for estimating the uncertainty in S_{su} .

In Situ Testing Approach: Residual Strength. As an alternative to laboratory-based procedures, Seed (1986) developed a correlation between SPT resistance and the apparent shear strength back-calculated from observed flow slides. Since there is no guarantee that all the conditions of the steady state of deformation were satisfied in the case histories—indeed, Stark and Mesri (1992) suggested that partial drainage occurred before some of the flow slides came to rest—the back-calculated strength is termed the *residual strength*. Seed and Harder (1990) reanalyzed many of the flow slides and added new data to

develop a relationship between residual strength and an equivalent clean-sand SPT resistance (Figure 9.57). For sands with more than 10% fines, the equivalent clean-sand SPT resistance is obtained from

$$(N_1)_{60-cs} = (N_1)_{60} + N_{corr} \quad (9.22)$$

where N_{corr} is obtained from Table 9-5.

Table 9-5 Recommended Fines Correction for Estimation of Residual Undrained Strength by Seed-Harder and Stark-Mesri Procedures

Percent Fines	N_{corr} (blows/ft)	
	Seed-Harder	Stark-Mesri
0	0	0
10	1	2.5
15	—	4
20	—	5
25	2	6
30	—	6.5
35	—	7
50	4	7
75	5	7

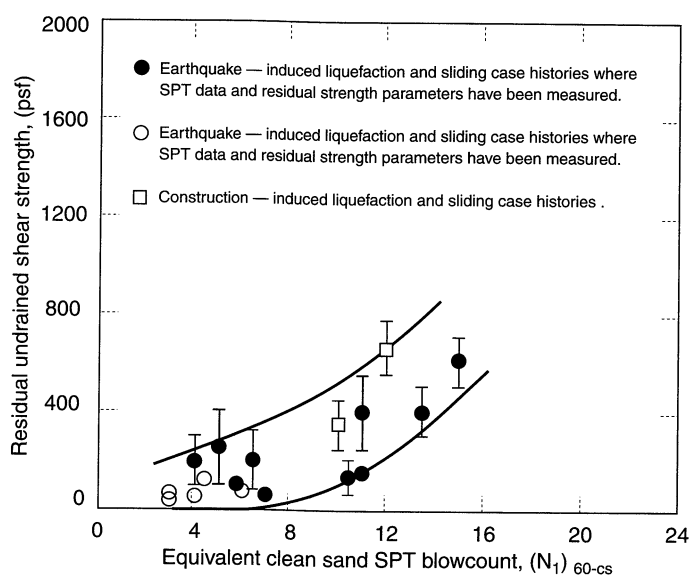


Figure 9.57 Relationship between residual strength and corrected SPT resistance.
(After Seed and Harder, 1990. H. Bolton Seed Memorial Symposium Proceedings, Vol. 2, p. 371. Used by permission of BiTech Publishers, Ltd.)